Semiconductor optical amplifiers for analogue applications

Constable, Julie Ann

Award date:
1993

Awarding institution:
University of Bath

SEMICONDUCTOR OPTICAL AMPLIFIERS FOR ANALOGUE APPLICATIONS

Submitted by Julie Ann Constable
for the degree of PhD
of the University of Bath
1993

J. A. Constable

ProQuest LLC
789 East Eisenhower Parkway
P.O. Box 1346
Ann Arbor, MI 48106-1346

For my parents

Contents

Summary

This dissertation describes a study of the use of semiconductor optical amplifiers in analogue amplitude modulated systems.

Chapter 1 gives a brief introduction to lightwave systems, and to the role of the optical amplifier in future optical networks, while chapter 2 explains the mechanism of optical amplification in a semiconductor, and describes some of the characteristics of optical amplifiers.

The high levels of signal distortion and noise generated by optical amplifiers are a serious disadvantage in analogue systems, where signal quality requirements are high. Before these devices can be used to fulfill analogue applications, therefore, the mechanisms governing distortion must be understood, in order that it may be reduced. To enable this, two computer models have been written to predict the response of an optical amplifier to a variety of stimuli, and these are described in chapter 3.

Chapter 4 defines a process for the design of a low distortion semiconductor optical amplifier, and presents a simulation of its performance.

A novel method of reducing distortion with the use of an electrical negative feedback loop is described in chapter 5, and experimental verification of its performance is presented in chapter 6.

Modulation frequency conversion in an analogue system is investigated in chapter 7, by a variety of electro-optic and all-optical methods. One of these uses a high frequency resonance signal generated by the electronics in the feedback loop to modulate the bias current of the optical amplifier, providing frequency and wavelength conversion. The frequency shift provided by this technique is used to transfer the interference signal at the output of a Mach-Zehnder interferometer from dc, and thus enable successful measurement of the linewidth of a distributed feedback laser.

Final conclusions are presented in chapter 8.

Acknowledgements

Firstly, my thanks to my supervisor, Professor Ian White, for his advice and guidance, and for teaching me that a forty hour week is not enough.

I must also express my gratitude to Dr David Cunningham and Alistair Coles, of Hewlett-Packard Laboratories in Bristol, for their helpful comments and advice, and for the experimental data used to optimise the bulk amplifier theoretical model.

The multi-quantum-well device described in chapter 4 was kindly supplied by Rick Trutna of Hewlett-Packard Laboratories in Palo Alto, California.

My thanks to the members of the optoelectronics group, who helped me to retain a sense of humour. Special thanks to Mehdi Asghari for his assistance with the gain measurements described in chapter 4.

Thanks are also due to the staff in the department for their help and friendship; in particular Brian Ring, Brian Gay, Bob Draper and Debs Pennock, for whom nothing was ever too much trouble.

I must acknowledge the SERC for the provision of a maintenance grant, and Hewlett-Packard Laboratories, Bristol for my CASE award.

Last, but by no means least, my unending gratitude to my parents and grandparents for their moral and financial support over the past three years, and to Paul who put up with a lot.

Publications

1. A N Coles, J A Constable, I H White, D G Cunningham: "Amplitude and phase distortion of analogue intensity modulated signals in semiconductor optical amplifiers", paper SDL10.1, LEOS'91, 4-7 November 1991, San Jose.
2. A N Coles, J A Constable, I H White, D G Cunningham: "Distortion of analogue intensity modulated signals in semiconductor optical amplifiers", *Electron. Lett.* **28**, pp. 1012-1013, 1992.
3. J A Constable, I H White, A N Coles, D G Cunningham: "Harmonic and phase distortion of analogue amplitude-modulated signals in bulk near travelling-wave semiconductor optical amplifiers", *IEE Proc J* **139**, pp. 389-398, 1992.
4. J A Constable, I H White, A N Coles, D G Cunningham: "Enhancement of the harmonic performance of a semiconductor optical amplifier using bias current feedback", *Proc SPIE* **1850**, pp. 363-371, 1993.
5. J A Constable, I H White, A N Coles, D G Cunningham: "Reduction of harmonic distortion and noise in a semiconductor optical amplifier using bias current feedback", *Electron. Lett.* **29**, pp. 2042-2044, 1993.
6. J A Constable, I H White: "Laser linewidth measurement using a Mach-Zehnder interferometer and an optical amplifier", accepted for publication by *Electron. Lett.*
7. J A Constable, I H White: "Frequency translation of optical signals using a semiconductor optical amplifier and resonant electrical feedback", submitted to *IEEE Photon. Technol. Lett.*

Introduction to Lightwave Systems

The replacement of copper coaxial systems with optical fibres is expected to lead to improved communications and entertainment services to the home, and to enhanced computing efficiency. Optical amplification, which may be achieved using rare earth doped fibre amplifiers, or semiconductor laser amplifiers, will play a major role in these future networks. Although present fibre amplifiers are more useful where amplification at a wavelength in the 1.5 μm region is required, semiconductor amplifiers display great versatility, and have potential applications in optical signal processing over a wide range of wavelengths.

1.1 Introduction

Although communications systems have advanced greatly during the last century, it is widely acknowledged that the present electrical systems are reaching the limit of their usefulness. It is predicted that in the future everyone will benefit from services such as high definition television, access to remote video libraries, video telephones and high speed supercomputing. If these are to be realised, the existing copper cable networks will need to be replaced by a medium with greater capacity. With a data-carrying capacity in the terahertz, optical fibre is the best possible solution to the problem. Long distance terrestrial telephone links are already carried by fibre, and optical cable television (CATV) links are already planned. In the future, optical fibre may even extend into every home, supplying a huge range of communications and entertainment services.

Home entertainment is one of the exciting applications of future fibre systems; telephony and computer interconnects are two others. In the next section, the merits of fibre over copper will be briefly discussed for each of these situations. Following this, there will be a brief overview of some of the different methods of modulating and multiplexing signals, and their respective merits. Optical amplification will play an important part in future lightwave systems, and this will be briefly discussed, with reference to both doped fibre and semiconductor optical amplifiers. The bulk of this last section will concentrate on the more exciting applications for the semiconductor devices.

1.2 Fibre Applications

1.2.1 Home Entertainment Systems

Many homes already receive several cable television channels. The future, however, is likely to bring several hundreds of channels with high definition pictures, as well as interactive services such as video broadcast and home shopping. These facilities will require the transmission of huge amounts of data, and the capacity and data rates needed are beyond the capabilities of existing copper coaxial networks.

Thus the most important reason for change is the vastly increased bandwidth available in fibre systems. Present cable television networks, for example, typically carry 450 MHz, consisting of 62 channels, on coaxial cable, which is capable of transmitting little more than 1 GHz [1]. In contrast, single mode fibre systems can already support more than 100 Gbit/s of information [2] using wavelength division multiplexing, and so fibre CATV systems will be capable of supplying many more channels and services than the present copper networks.

The disadvantages of the copper systems stem from the relatively high loss of coaxial cable, 1 dB/100 feet (almost 33 dB/km) [1], as compared with the loss of single mode fibre (SMF), which is 0.2 dB/km at a signal wavelength of 1.5 μm [4]. Current CATV system losses are high, due to the 'root and branch' configuration used [1,3] (figure 1.1), in which signals leaving the head end are repeatedly split throughout the system until each home has been served. Because of the high loss of coaxial cable, and the power loss experienced every time the signal is split, amplifiers are needed every 1000-2000 feet throughout the system [1,3]. Each of these amplifiers introduces noise into the system, also crosstalk (interference between different signal channels). This places limits

on the amount of information the system can carry, and also requires that the amplifiers be very precisely controlled in terms of output power and gain flatness, if signal quality is to be maintained at an acceptable level; this leads to high system maintenance costs. Any increase in the amount of data carried by the system would lead to a worsening of the crosstalk problem, and also to increased loss in the cable due to the higher frequencies being carried.

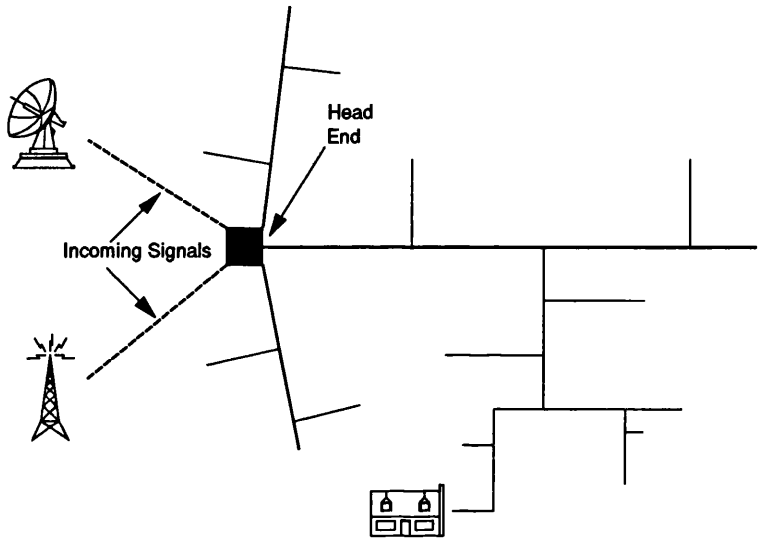

Figure 1.1 Schematic of the 'root and branch' configuration of current electronic CATV systems.

Optical fibres, with their lower loss, can support much larger repeater spacings, and have the considerable advantage that they are insensitive to bit rates; that is, the system data rate may be easily upgraded without increased system loss, although signal dispersion is a problem at very high data rates (in excess of 10 Gbit/s per channel).

The high maintenance cost of copper systems has already been mentioned; as well as the increased reliability and lower failure rate of fibre systems, optical fibre itself is cheaper than copper cable. However, although several city-based trials have been carried out in Europe [5], including a British Telecom trial of a fibre-to-the-home (FTTH) system in Bishops Stortford [6], it is not at present economically viable to replace the entire system, from head end to home, with fibre optic cables. Most houses are already wired

up with coaxial cable which has sufficient capacity to supply the services that one house is likely to require, and the expense of taking fibre into each house and installing optical to electrical conversion circuitry is at present prohibitive.

Several schemes have been proposed, with differing degrees of optical incursion into the electrical network [1,3,6,7,8]. These may be summarised as fibre-to-the-curb (FTTC), fibre-to-the-feeder (FTTF) and fibre backbone (FBB).

In an FTTC network, the optical fibre link continues to the street, and each house is connected by coaxial cable. This has the advantage that it avoids the expense of converting each individual house to fibre, but it does enable this step to be taken later [6].

FTTF systems have a fibre link from the head end to a series of local nodes, each serving 300 - 500 homes which are electrically connected [3].

FBB was first proposed in 1988 [7] to break up the CATV system into a number of smaller systems to reduce the cascade of electrical amplifiers. It is similar to the FTTF system in that each node in the system serves several hundred subscribers with electrical signals, but here the existing coaxial trunk from the head end to the local nodes is overlaid, rather than replaced, by optical fibres. The existing trunk amplifiers are reversed to feed signals back to the head end, and so fewer lasers are required.

Another important consideration is electromagnetic compatibility (EMC), which is becoming a big issue [9,10]. With the proliferation of electrical and electronic facilities in every home, interference between equipment is difficult to avoid. Optical fibre transmission has the added advantage that it produces no electromagnetic interference.

With the increased demand for home services expected in the future, some combination of copper and fibre networks will certainly be required. The level of conversion to fibre will be determined by the capacity demands of the cable operators, and by economic constraints.

Fully interactive home services will not be practical unless the telephone companies are allowed to join with the cable television companies, to provide services such as video telephone in addition to the TV and video channels. In Britain, legislation prevents this happening. In America, where the restriction has recently been lifted, AT&T and Viacom International Inc. have linked up to carry out a trial of fully interactive television and video in California. 1000 homes will be served initially, rising to 4000 over the 18

months of the trial [11]. Although this pioneering experiment will utilise existing copper cable networks, interstate systems must wait for a nationwide high capacity network, which will almost certainly be carried by fibre.

1.2.2 Telecommunications

The transmission rate of current telecommunication systems is limited by the speed of the electronic switching and data processing. An optical broadband integrated services digital network (B-ISDN) is proposed which will enable the transmission of tens of Gbit/s of information, including pictures for videophone [12]. This will make use of all-optical signal processing and switching.

Long-distance terrestrial telecommunications links are already carried by fibre; the next step may be to extend this into the home [5]. The successful trial of an FTTH system in Bishops Stortford [6] demonstrated the provision of telephone signals, along with television and audio channels, using fibre connection to each house in the trial. However, as mentioned before, it is not yet considered economically viable to extend this service nationwide.

Although there have been successful trials of FTTH telephony systems [5,6], too few subscribers were served for final conclusions to be drawn about their feasibility. Again, fibre to the home will almost certainly depend upon a change in the law to become feasible.

1.2.3 Computer Interconnects

As computer networks become more extensive, and computation more powerful, interconnects between mainframes and terminals, and between desktop PCs, will need to become faster and more reliable. Current copper based mainframe interconnects carry 200 Mbit/s per network [13]; systems in which fibre is used as a substitute for copper will be able to carry 622 Mbit/s, 1 Gbit/s or even 2.4 Gbit/s, using multimode fibre (MMF) for short distances (less than 2 km), or single-mode fibre for longer spans [13]. Future all-fibre systems are expected to achieve the Gbit/s per node that will be required by applications in supercomputing and medical imaging. Short haul multimode optical interconnections between personal computers are already available, in the form of plug-in cards, from Hewlett-Packard and IBM.

Present copper systems use time division multiplexing (TDM), in which different channels of information are chopped up into short packets of data, each of which has its own time slot (see section on multiplexing). This transmission scheme is limited in the number of channels it can manage by the speed of the system. Optical networks can, by the use of wavelength division multiplexing (WDM), multiply this number by the number of wavelengths the system can support.

The largest disadvantage of copper based interconnects lies in the hubs which route the signals [13]. These occupy a large volume, dissipate several watts of power and have a short mean time between failures. Most of the cost of the system lies in the cabinet, power supply, fans, electromagnetic screening and floor space required by these hubs. Optical hubs are expected to solve most of the problems of the electronic systems, while delivering greater information-carrying capability.

1.3 Modulation and Multiplexing Techniques

Since this project is concerned with analogue systems, this section will concentrate mainly on the most common analogue modulation and multiplexing techniques.

1.3.1 Amplitude Modulation

Amplitude modulation (AM) is applicable to both analogue and digital signals, but it is in analogue systems that it is most widespread. Current CATV systems use a form of AM known as vestigial sideband [1,3], which will be described later in this section, and so future optical CATV networks may also use this form of AM, for compatibility.

In an (AM) system, the amplitude of a high frequency carrier wave is modulated by the magnitude of the message signal, as shown in figure 1.2(a). The carrier frequency remains unchanged. The transmitted signal $x_c(t)$ may be described by [14]:

$$x_c(t) = A_c\ [1 + \mu\ x(t)]\ \cos\omega_c t \qquad \text{E1.1}$$

where A_c is the unmodulated carrier amplitude, μ is the modulation index such that $\mu \leq 1$, $x(t)$ is the signal waveform, here normalised to an amplitude of $\pm$ 1 and ω_c is the angular frequency of the carrier.

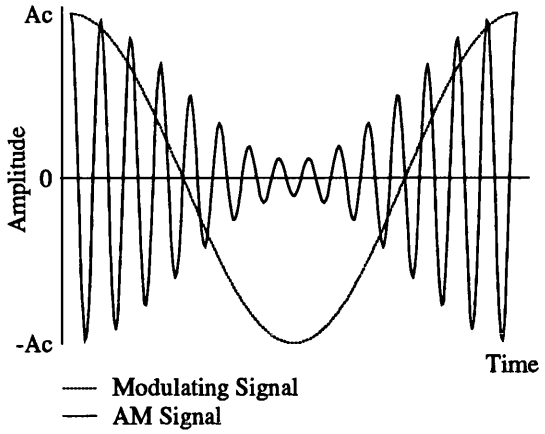

Figure 1.2(a) Amplitude modulation - schematic showing modulating signal and modulated waveform.

This simple form of AM wastes power, since the dc component carries no information. Some systems use double sideband suppressed carrier modulation (DSB-SC), in which the modulation index is set to 1, and the waveform becomes:

$$x_c(t) = A_c\ x(t)\ \cos\ \omega_c\ t \qquad \text{E1.2}$$

Further, because the two sidebands in AM are symmetrical, either one contains all the information in the original signal. Suppressing one sideband along with the carrier halves the bandwidth required to transmit the signal, without loss of information, and is known as single sideband modulation (SSB). However, SSB signals are of poor quality at low frequencies, and so some form of compromise is necessary. This is known as vestigial sideband modulation (VSB), in which the unwanted sideband is partially transmitted. As already mentioned, electrical CATV signals are currently transmitted using AM-VSB modulation [1,3].

AM signals require a small transmission bandwidth, but have poor noise performance when compared to frequency modulation.

1.3.2 Frequency Modulation

In frequency modulation (FM) systems, the frequency of the carrier varies with the magnitude of the message waveform, but its amplitude remains constant (figure 1.2(b)). The frequency of the transmitted wave is described by [14]:

$$f(t) = f_c + f_\Delta\ x(t) \qquad \text{E1.3}$$

Here f_c represents the unmodulated carrier frequency, and f_Δ is the maximum frequency deviation, $x(t)$ being fixed between ± 1 as before. FM signals have a superior noise performance to AM signals, but require a wider bandwidth.

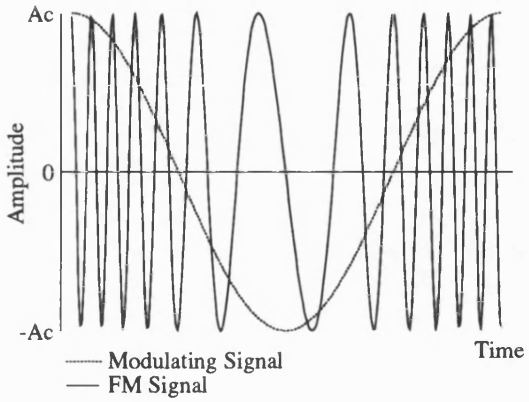

Figure 1.2(b) Frequency modulation - schematic showing modulating signal and modulated waveform.

Where many channels are to be transmitted simultaneously, some form of mixing, or multiplexing, is required. Four techniques are briefly reviewed below.

1.3.3 Frequency Division Multiplexing

As the name implies, frequency division multiplexing (FDM) is the combination of multiple signal channels of different frequencies. Figure 1.3(a) shows three signals, each amplitude modulated in this case, multiplexed to form a baseband signal that will be used to modulate a final carrier before transmission. A typical baseband frequency spectrum is also shown. Although AM signals are used in this example, they could be modulated by some other technique, provided their frequency bandwidths do not overlap. The empty guard band between the signal frequencies reduces system crosstalk, that is interaction between the signal channels.

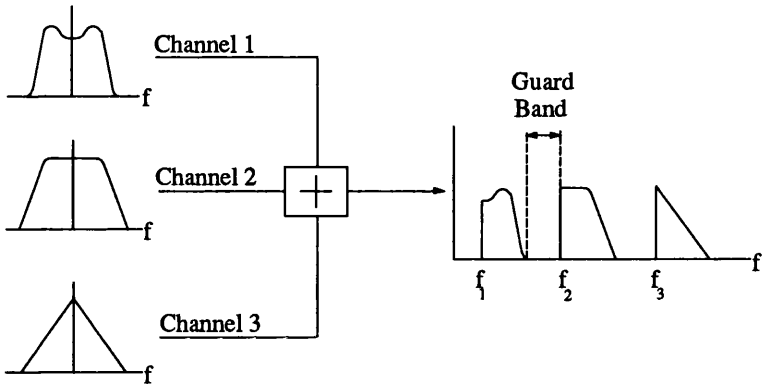

Figure 1.3(a) Frequency division multiplexing - block diagram of system and baseband frequency spectrum.

1.3.4 Wavelength Division Multiplexing

In wavelength division multiplexing (WDM), optical signals of different wavelengths are combined for transmission by fibre. Figure 1.3(b) shows a schematic of a WDM system, together with the optical frequency (wavelength) spectrum obtained. At the detector, the different wavelengths are separated and demodulated separately. Any modulation scheme may be used for the individual signal channels.

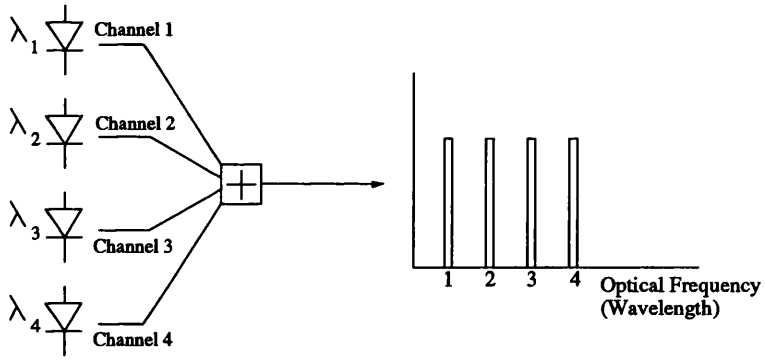

Figure 1.3(b) Wavelength division multiplexing - block diagram of system and optical frequency spectrum.

1.3.5 Time Division Multiplexing

Time division multiplexing (TDM) is prominent in digital systems, most importantly in computer networks. Here, the information from each channel is segmented into short bursts, and the signal channels are accessed sequentially to create the transmitted waveform, as shown in the timing diagram of figure 1.3(c). TDM requires absolute synchronization of the source and detector, to ensure that each channel is accessed at the correct time, and a clock signal is usually sent with the data.

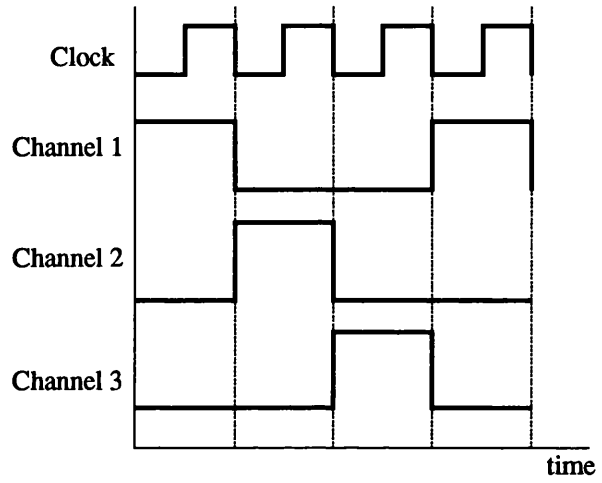

Figure 1.3(c) Time division multiplexing timing diagram for three channels and clock signal.

1.3.6 Subcarrier Multiplexing

When many electrical signals are to be relayed via optical fibre, subcarrier multiplexing (SCM) is often used; future optical CATV systems, for example, are expected to use this technique [8,15,16]. In an SCM system the electrical subcarriers, each modulated by a signal channel, are combined by some multiplexing method. The composite waveform is then used to modulate an optical signal. The principal advantage of this method is that each subcarrier has a narrow bandwidth, and so sophisticated electronics are not required for their generation. Because the subcarriers are narrow band, the individual optical receivers do not need a wide bandwidth, and so their noise is reduced. The use of a single optical beam reduces the number of laser sources required, and relaxes the tight control over emission wavelength required by WDM [8].

These are the basic modulation and multiplexing techniques. Actual communications systems may use more advanced versions of these methods, or even combine two or more of them together [17].

1.4 Optical Amplifiers

Within an optical system there are several applications for optical amplifiers, to increase signal power and enhance system performance. The signal may need boosting before leaving the transmitter [18], particularly if an external modulator has been used, or it may need to be regenerated at intervals along the fibre link due to system losses [2]. In the latter situation, the optical amplifier would replace the electro-optic repeaters currently used, in which the signal is detected with a photodiode, reshaped and retimed electronically, and finally used to modulate a laser to retransmit the signal. Lastly, preamplification before the detector may be required [19,20]. There are two main types of optical amplifiers; doped fibre amplifiers and semiconductor optical amplifiers (SOA), and these will now be discussed.

1.4.1 Doped Fibre Amplifiers

These devices, consisting of a length of optical fibre doped with a rare earth element, typically erbium, rely on optical pumping by a semiconductor laser to provide carriers for stimulated emission. Where simple signal boosting is required, erbium doped fibre amplifiers (EDFA) are very attractive. They may be spliced into fibre systems with little or no coupling loss, and they have high gains, typically greater than 30 dB [21] or even 40 dB [22], high saturation powers [21] and low noise. However, they also have drawbacks; they are expensive and not yet available for wavelengths in the 1.3 μm window, and the long length of fibre used, of the order of several metres, causes significant signal delay. This can be a serious disadvantage in, for example, computer networks [13]. Because of these disadvantages, and the fact that EDFAs cannot be modulated or switched at frequencies greater than kHz, their major use is as gain blocks in 1.5 μm communications systems. Devices operating at 1.3 μm are being developed, but are not yet widely available.

1.4.2 Semiconductor Optical Amplifiers

The second class of optical amplifier, the semiconductor optical amplifier, has a diode laser structure, with the facets AR coated to reduce optical feedback and thus prevent lasing taking place. The operation of these devices will be described in chapter 2.

Although the gain and saturation output power of these amplifiers are not as high as for the EDFA, being typically of the order of 25 dB and +3 dBm respectively [23], they do have several important advantages. As they are based on a laser structure, they can be designed to amplify in any wavelength range. They are small and require little power, being electrically rather than optically pumped, and although they suffer from coupling losses at the interface with the fibre, they have the advantage that they can be integrated on the same wafer as the laser source or the photodiode. The main disadvantage of SOAs lies in the nonlinearity of the optical gain, which can cause phase and harmonic distortion of a modulated optical signal [24].

The SOA's major advantage is its versatility. The same nonlinearity which causes signal distortion enables the device to find applications as for example a switch [25,26,27], a wavelength convertor [28,29,30], a phase modulator [31,32], a multiplexer or demultiplexer [33], a modulation frequency up or downconvertor [34], or a detector [26,35,36].

(i) Switching

Switching has been achieved at speeds of up to 3 GHz [27] by gating the bias current to turn the device on and off; SOAs are particularly suited to this application, as they can completely block an incoming optical signal when switched off. When switched on, however, they can also provide gain to simultaneously boost the signal.

(ii) Wavelength Conversion

Wavelength conversion, using the nonlinear interaction between two optical signals in a process called four wave mixing, has resulted in shifts of up to 4000GHz (30 nm at 1.5 μm) [29]. Using amplifier gain saturation, shifts of several nm have been achieved at data rates of up to 20 Gbit/s [28]. By a different method, workers at British Telecom have succeeded in converting a signal from 1.3 μm to 1.5 μm, for subsequent amplification by a fibre amplifier, using a two section semiconductor amplifier [30].

(iii) Phase Modulation

Modulation of the optical phase of a signal can be achieved by modulating the SOA electrical drive, which modifies the refractive index of the cavity via the carrier concentration.

(iv) Modulation Frequency Conversion

When two signals of different modulation frequencies, for example a signal and a local oscillator frequency, are mixed inside the SOA, several frequency components are emitted, in a process akin to four wave mixing. Among these will be the sum and difference of the two original inputs. Thus the original signal frequency may be up or downconverted by the optical amplifier. This finds applications in preamplified receivers, for downconverting the microwave carrier frequency prior to detection [34].

Thus, although both EDFAs and SOAs perform optical amplification, they are not suitable for the same applications, and therefore they are not in competition. EDFAs are undisputably the most appropriate in situations where signal regeneration at 1.5 μm is required, SOAs at other wavelengths, or where some processing of the signal is required.

1.5 Conclusions

If the enhanced communications, entertainment and computing services planned for the future are to be realised, optical fibre will have to play an important part in future networks. Although long distance links will certainly be carried by fibre, and indeed some already are, it may not be economically viable to extend fibre links into every home.

If long distance optical links are to be efficient, some amplification of the signal will be required, whether by fibre or semiconductor devices. Doped fibre amplifiers are likely to find applications as gain blocks at 1.5 μm; semiconductor amplifiers have lower gain, but greater versatility where signal processing is required.

Because the inherent nonlinearity of SOAs gives rise to significant levels of signal distortion, their behaviour must be understood, with a view to optimisation, before they can be used in analogue systems.

This dissertation describes a study of the nonlinear behaviour of SOAs, both theoretically and experimentally, and also explores the possibility of improving their distortion performance.

1.6 References

1. J A Chiddix, H Laor, D M Pangrac, L D Williamson, R W Wolfe: "AM video on fiber in CATV systems: need and implementation", *IEEE J. Selected Areas in Comms.* **8**, pp. 1229-1239, 1990.
2. T Li: "Next-generation lightwave transmission systems", paper MoC02, *Proc. ECOC '93*, Montreux, Switzerland, September 1993.
3. J A Chiddix, J A Vaughan, R W Wolfe: "The use of fiber optics in cable communications networks", *J. Lightwave Technol.* **11**, pp. 154-166, 1993.
4. A J Seeds: "Microwave optoelectronics", *Opt. Quantum Electron.* **25**, pp. 216-229, 1993.
5. F Sporleder, W Rosenau: "Fiber in the loop - plans and experiences in Europe", paper ThC11.2, *Proc. ECOC '93*, Montreux, Switzerland, September 1993.
6. C E Hoppit, J W D Rawson: "The United Kingdom trial of fibre in the loop", *British Telecommunications Engineering* **10**, pp.48-57, 1991.
7. J A Chiddix, D M Pangrac: "Fiber backbone: a proposal for an evolutionary CATV network architecture", *NCTA '88 Tech. Papers*, 1988.
8. T E Darcie: "Subcarrier multiplexing for lightwave networks and video distribution systems", *IEEE J. Selected Areas in Comms* **8**, pp.1240-1248, 1990.
9. S Linkwitz: "Designers will be paying more attention to EMC testing", *Electronic Design* **40** p117, 1992.
10. A Litauer: "Electromagnetic interference and its effects on telecommunications equipment", *Commutation and Transmission* **14**, pp. 87-94, 1992.
11. AT&T (UK) Ltd. - Private communication, 1993.
12. M Saruwatari: "Ultrahigh speed optical fiber transmission employing all-optical signal processing technology", paper TuC4.1, *Proc. ECOC '93*, Montreux, Switzerland, September 1993.
13. B M Russell: "A computer industry wish-list", Presented at the IEE Colloquium "Optical Switching", June 1993.
14. A Bruce Carlson "Communication Systems", pub McGraw-Hill, 1986 (USA).

15. T E Darcie, G E Bodeep: "Lightwave subcarrier CATV transmission systems", *IEEE Trans. Microwave Theory and Techniques* **38**, pp. 524-533, 1990.

16. R Olshansky, V A Lanzisera, S-F Su, R Gross, A M Forcucci, A H Oakes: "Subcarrier multiplexed broad-band service network: a flexible platform for broad-band subscriber services", *J. Lightwave Technol.* **11**, pp. 60-69, 1993.

17. A S Andrawis, I Jacobs: "A new compound modulation technique for multichannel analog video transmission on fiber", *J. Lightwave Technol.* **11** pp. 49-54, 1993.

18. S Ryu, T Miyazaki, T Kawazawa, Y Namihira, H Wakabayashi: "Field demonstration of 195-km long coherent unrepeatered subcarine cable system using optical booster amplifier", *Electron. Lett.* **28**, pp. 1965-1966, 1992.

19. G R Joyce, V Lanzisera, R Olshansky: "Improved sensitivity of 60 video channel FM-SCM receiver with semiconductor optical preamplifier", *Electron. Lett.* **25**, pp. 499-501, 1989.

20. O K Tonguz, L G Kazovsky: "Theory of direct-detection lightwave receivers using optical amplifiers", *J. Lightwave Technol.* **9**, pp.174-181, 1991.

21. P W France "Optical Fibre Lasers and Amplifiers", pub Blackie, 1991 (UK).

22. R J Mears, S R Baker: "Erbium fibre amplifiers and lasers", *Opt. Quantum Electron.* **24**, pp. 517-538, 1992.

23. J C Simon, B Landousies, Y Bossis, P Doussiere, B Fernier, C Padioleau: "Gain, polarisation sensitivity and saturation power of 1.5 μm near travelling wave semiconductor laser amplifier", *Electron. Lett.* **23**, pp. 332-334, 1987.

24. A N Coles, J A Constable, I H White, D G Cunningham: "Distortion of analogue intensity modulated signals in semiconductor optical amplifiers", *Electron. Lett.* **28**, pp. 1012-1013, 1992.

25. R Fortenberry, A J Lowery, W L Ha, R S Tucker: "Photonic packet switch using semiconductor optical amplifier gates", *Electron. Lett.* **27**, pp. 1305-1307, 1991.

26. K Bertilsson, R Rörgren, P A Andrekson, S T Eng: "Characterization of an InGaAsP semiconductor laser amplifier as a multifunctional device", *J. Lightwave Technol.* **11**, pp. 1147-1150, 1993.

27. P B Hansen, G Raybon, J M Wiesenfeld, C A Burrus, R A Logan, T Tanbun-Ek, H Temkin: "Optical demultiplexing at 6 Gb/s using a semiconductor laser amplifier as an optical gate", *IEEE Photon. Technol. Lett.* **3**, pp. 1018-1020, 1991.

28. B Mikkelsen, M Vaa, R J Pedersen, T Durhuus, C Joergensen, C Braagaard, N Storkfelt, K E Stubkjaer, P Doussiere, G Garabedian, C Graver, E Derouin, T Fillion, M Klenk: "20 Gbit/s polarisation insensitive wavelength conversion in semiconductor optical amplifiers", paper ThP 12.6, *Proc. ECOC '93*, Montreux, Switzerland, September 1993.

29. G Grosskopf, R Ludwig, H G Weber: "140 Mbit/s DPSK transmission using an all-optical frequency convertor with a 4000 GHz conversion range", *Electron. Lett.* **24**, pp. 1106-1107, 1988.

30. P E Barnsley, P J Fiddyment: "Wavelength conversion from 1.3 to 1.55 μm using split contact optical amplifiers", *IEEE Photon. Technol. Lett.* **3**, pp. 256-258, 1991.

31. J Mellis: "Direct optical phase modulation in semiconductor laser amplifier", *Electron. Lett.* **25**, pp. 679-680, 1989.

32. G Grosskopf, R Ludwig, R Schnabel, H G Weber: "Characteristics of semiconductor laser optical amplifier as phase modulator", *Electron. Lett.* **25**, pp. 1188-1189, 1989.

33. R Ludwig, G Raybon: "All-optical demultiplexing using ultrafast four-wave mixing in a semiconductor laser amplifier at 20 Gbit/s", paper ThP 12.2, *Proc. ECOC '93*, Montreux, Switzerland, September 1993.

34. T E Darcie, S O'Brien, G Raybon, C A Burrus: "Optical mixer-preamplifier for lightwave subcarrier systems", *Electron. Lett.* **24**, pp. 179-180, 1988.

35. M Gustavsson, A Karlsson, L Thylén: "Traveling wave semiconductor laser amplifier detectors", *J. Lightwave Technol.* **8**, pp. 610-617, 1990.

36. M Gustavsson, L Thylen, A Djupsjöbacka: "System performance of semiconductor laser amplifier detectors", *Electron. Lett.* **25**, pp. 1375-1377, 1989.

2

Semiconductor Optical Amplifiers

This chapter describes the operation and characteristics of semiconductor optical amplifiers. Optical amplification is explained, with reference to optical absorption and emission, also the confinement of carriers and photons within the active region of the device. Important characteristics of semiconductor optical amplifiers are described, and finally the two main classes of SOA are contrasted. It is concluded that travelling wave type devices are preferable to Fabry-Perot amplifiers. However, they are difficult to fabricate, and it is for this reason that most practical devices are of the near travelling wave variety.

2.1 Introduction

Laser amplifiers were proposed at the same time as semiconductor lasers, in the 1960's [1]. The first semiconductor devices, however, in common with the contemporary lasers, had to be cooled to liquid nitrogen temperatures because of the high bias currents used. SOAs as we know them today have been around since the early eighties, thanks to advanced material growth and device fabrication technology. It was originally hoped that semiconductor optical amplifiers would perform signal regeneration and boosting in future fibre communications systems. However, the nonlinearity of the device gain has led to their being supplanted by rare earth doped fibre amplifiers in 1.5 μm systems, while research has concentrated on more exotic signal processing applications for the

SOA. There are occasions, though, when SOAs are the preferred choice, in 1.3 μm systems for example, or where financial and power budgets are restricted. For this reason, it is important to understand the behaviour of SOAs, and to appreciate their limitations. This chapter provides an introduction to the operation of the semiconductor optical amplifier, and describes some of the characteristics of the device.

Figure 2.1 shows a simple schematic of an SOA. The bias current is injected through the top contact, and the light is emitted perpendicularly, from the edge of the device. SOAs have the same device configuration as semiconductor lasers, namely some variation of a diode structure. The most commonly used structure is based on the Fabry-Perot laser, but has the end facets anti-reflection coated, to reduce optical feedback and prevent lasing from taking place.

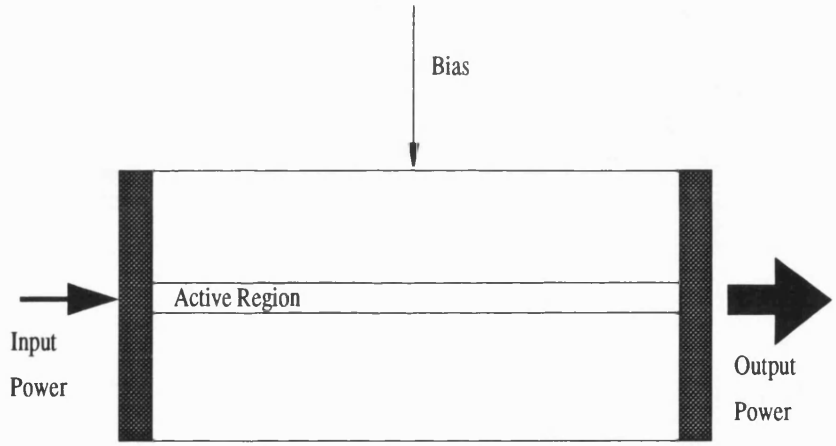

Figure 2.1 Simple schematic of semiconductor optical amplifier

Simple descriptions follow of amplification, and of carrier and light confinement. Residual reflectivity of the end facets of an SOA gives rise to Fabry-Perot resonance, and the effect of this is discussed. The wavelength dependence of the gain is explained, together with the causes of gain saturation, amplifier noise, signal distortion and polarisation sensitivity. The two main types of SOA, travelling wave and Fabry-Perot, are then described and contrasted.

2.2 Optical Amplification

Semiconductor optical amplifiers exhibit absorption, spontaneous emission and stimulated emission, according to the level of electrical pumping employed. These processes are schematically described by figure 2.2, which considers a simple two energy level system, where n_1 is the number of carriers in the lower energy level E_1, and n_2 is the number of carriers in level E_2.

Where there is little or no bias current, ie carriers are not being injected into the device, the system will absorb any light entering the cavity (figure 2.2(a)), using the energy gained to promote electrons to the conduction band, represented by level E_2 on the schematic. These promoted carriers can spontaneously recombine with holes in the valence band, level E_1, emitting photons of light, as shown in figure 2.2(b). The probability of this happening depends upon the proportion of electrons in the upper band, ie upon the degree of population inversion. This process is the origin of the broadband spontaneous emission, which is the principal source of amplifier noise.

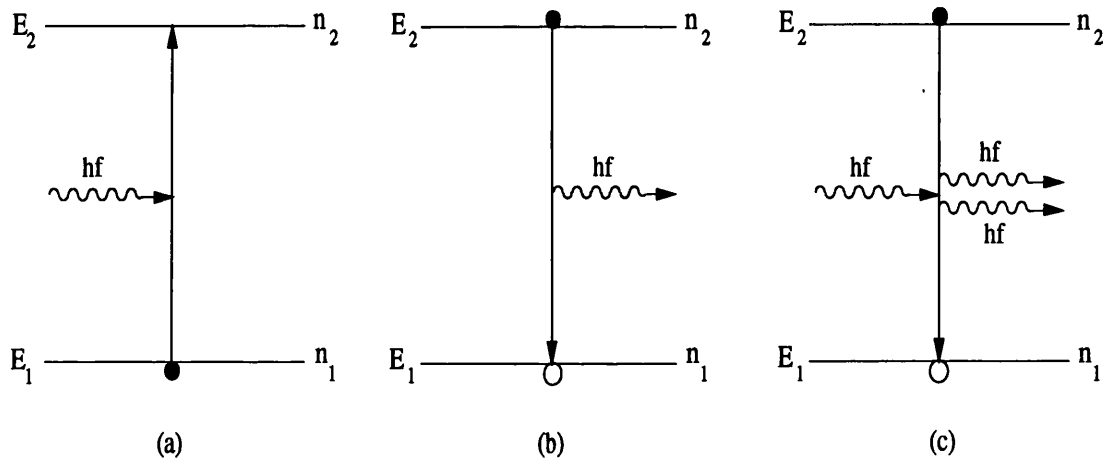

Figure 2.2 Schematic of (a) Absorption (b) Spontaneous emission (c) Stimulated emission in a two level system.

When the bias current is increased, there are more carriers in the conduction band, and the level of spontaneous emission increases. When all of the available states in the conduction band have been filled, the light is no longer absorbed, but is allowed to pass through. The device is now said to be *transparent.*

As the bias current is increased further, the light in the cavity begins to be reinforced by a process called stimulated emission, as shown in figure 2.2(c). In this case, a photon of a particular energy passing through the cavity stimulates an electron in the conduction band to recombine with a hole in the valence band, level E_1, emitting another photon of the same energy and phase as the first. This is the process which provides optical amplification, and ultimately lasing action.

Increasing the bias current further will give a corresponding increase in optical gain, and if the facets of the device are not AR coated, lasing will eventually occur. However, if the facets are coated, there will come a point where the output power cannot continue to increase with bias, and the gain will cease to grow. This is known as saturation.

The recombination of carriers and the emission of light take place in the active region of the device, defined by carrier and light confinement. The next section will briefly explain these concepts, with examples of common confinement methods.

2.3 Optical and Electrical Confinement

For maximum device efficiency, the carriers and light must be confined together in the active region of the device. The end facets give longitudinal definition; transverse and lateral confinement will be discussed in this section. Figure 2.3 illustrates the definitions of the principal axes of the device.

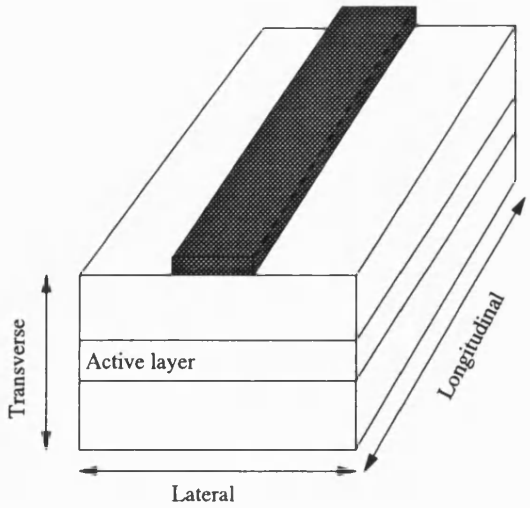

Figure 2.3 Definition of lateral, transverse and longitudinal dimensions of a laser amplifier.

2.3.1 Transverse Confinement - the double heterostructure

Transverse carrier confinement is achieved with the use of band structure engineering. Here, the structure of the conduction and valence bands within the device is controlled during the growth of the material. The use of interfaces between two material layers with different properties is known to create potential barriers to the movement of carriers, and this feature is widely used in the construction of lasers. The double heterostructure, having two heterojunctions, (interfaces between unlike materials), is the most common structure for bulk devices, and will be used here as a model of transverse confinement.

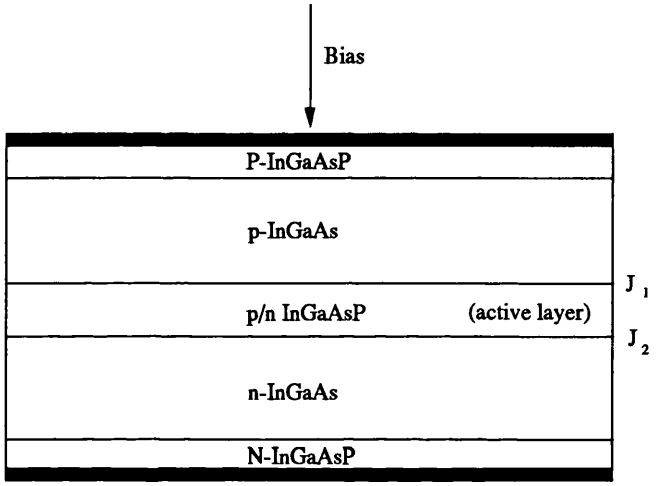

Figure 2.4(a) Double heterostructure device structure.

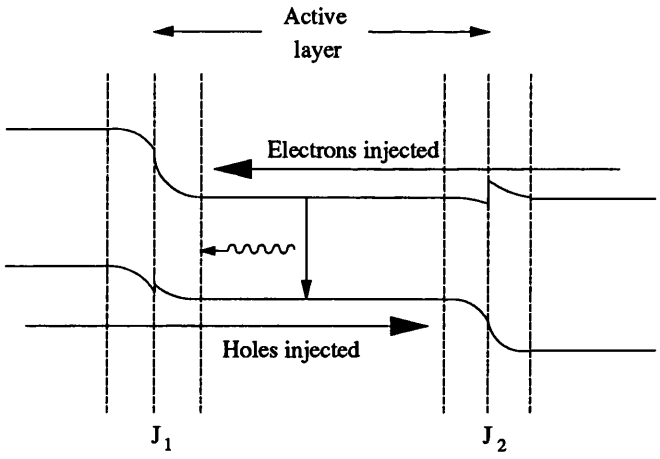

Figure 2.4(b) Energy band diagram showing carrier confinement.

To fabricate a double heterostructure, two different materials are grown in alternate layers, as in figure 2.4(a). As the simplified band diagram in figure 2.4(b) shows, a material of narrow energy bandgap is sandwiched between two layers of wide bandgap material. When the device is biased, electrons flood into the n-type material towards the active region, and flood out of the p-type material leaving holes behind. The injected electrons are prohibited from leaving the active region by the potential gradient at junction 1; the holes are restricted by the barrier at junction 2. Thus, the carriers are kept within the active region, where they recombine to produce light.

Optical confinement is achieved by use of the phenomenon of total internal reflection (TIR), which occurs at the interface between a material of high refractive index and one of low refractive index. For TIR to take place in the DH device, the wide bandgap cladding material must have a lower refractive index than that of the active region. Fortunately, wide bandgap III-V semiconductors do indeed have lower refractive indices than narrower gap materials, and so the double heterostructure provides efficient confinement of both carriers and photons in the transverse direction.

2.3.2 Lateral Confinement - the buried heterostructure

Lateral confinement of carriers and photons is often achieved by the use of a buried heterostructure (BH) configuration, and indeed this is the structure of the SOA with which much of this dissertation is concerned.

To fabricate a BH device, the transverse material structure is laid down using some form of epitaxial growth process. The width of the active region is masked off using photoresist, and then the material on either side is etched away to a prearranged depth. Regrowth is used to fill the gaps thus left with a material of a lower refractive index, again utilising TIR for optical confinement.

Electrical confinement is provided by the interface between the active region and the regrown material, which gives rise to discontinuities in the energy bands. These discontinuities represent potential barriers to the movement of carriers, and provide lateral carrier restraint. The oxide layers on either side of the electrical contact funnel the bias current into the active region.

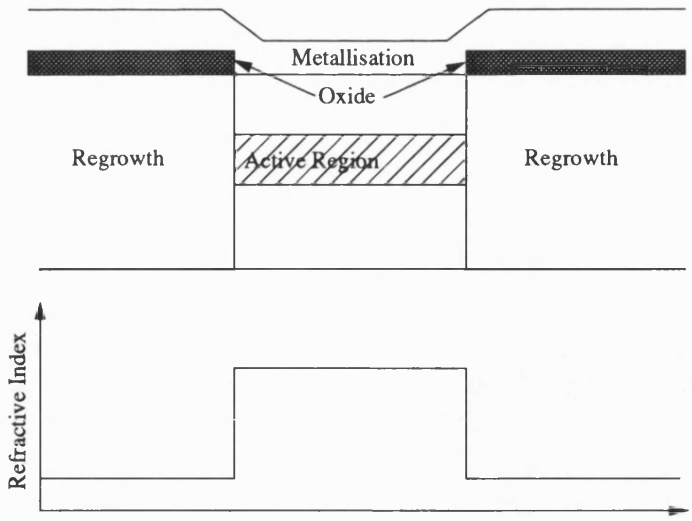

Figure 2.5 (a) Schematic of buried heterostructure (b) Lateral variation of refractive index.

Traditional buried heterostructure devices exhibit efficient guiding of the light in the active region, but are less successful at confining carriers. A high proportion of the current injected into the device can be lost through leakage and diffusion of carriers around the active region [2]. For improved confinement, semi-insulating material can be implanted into the regrown regions to prevent carrier movement within these areas.

Having described the structure and operation of the optical amplifier, some of the characteristics of the device will be briefly described.

2.4 Fabry-Perot Effects

It was stated in section 2.1 that SOAs are based on a semiconductor laser structure, but with the facets AR coated to reduce reflections. The ideal is a pure travelling wave device, with zero facet reflectivity, in which the input signal is amplified in a single pass through the cavity, as illustrated by figure 2.6. However, this is rarely achievable in practice, and some degree of reflectivity always remains.

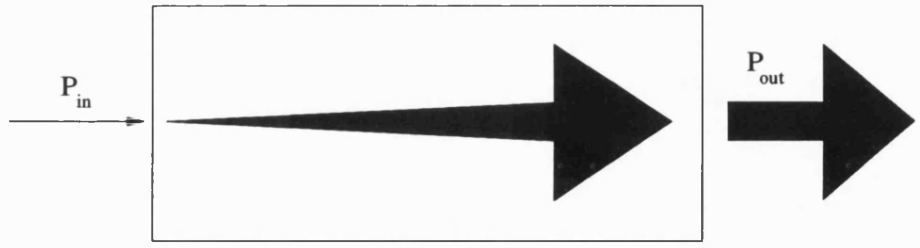

Figure 2.6 Schematic of a travelling wave semiconductor optical amplifier.

Where there is residual reflectivity, a certain proportion of the amplified light does not leave the cavity, but is reflected back by the output facet (figure 2.7). The effect of this is to set up a Fabry-Perot etalon in the cavity.

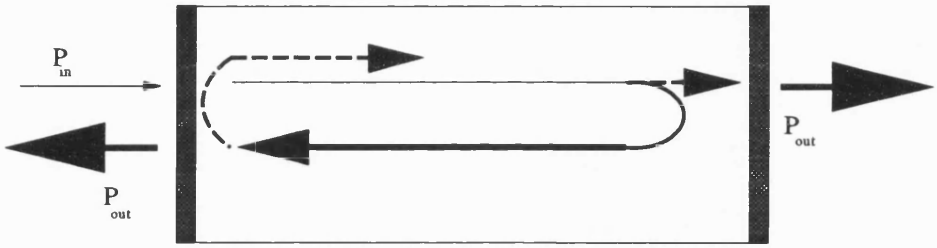

Figure 2.7 Schematic of a Fabry-Perot semiconductor optical amplifier.

The transmitted intensity of a Fabry-Perot etalon is given by:

$$I_t = I_i \frac{(1-R)^2}{(1-R)^2 + 4R\sin^2\phi} \qquad \text{E2.1}$$

where I_i is the input intensity, R is the reflectivity of each facet and ϕ is the optical phase change associated with a single pass throught the cavity. There will be a transmission maximum when an integer number of half wavelengths fit exactly into the cavity, and a minimum when a half integral number fit.

This expression may be applied to an optical amplifier with the inclusion of gain terms:

$$I_{out} = I_i \frac{(1-R_1)(1-R_2)\ G_s}{(1-\sqrt{R_1R_2}\ G_s)^2 + 4\ \sqrt{R_1R_2}\ G_s\ \sin^2\phi} \qquad \text{E2.2}$$

Here, I_{out} is the output intensity, G_s, is the single pass gain and R_1 and R_2 are the power reflectivities of the facets. The facet reflectivities have been considered separately, otherwise the expression is similar to E2.1.

This condition gives rise to a strong wavelength dependence of the device gain, known as ripple, as shown in figure 2.8. The ripple amplitude depends upon the gain of the device, and upon the facet reflectivities, in the following way:

$$\frac{G_{peak}}{G_{trough}} = \left(\frac{1 + \sqrt{R_1\ R_2}\ G_s}{1 - \sqrt{R_1\ R_2}\ G_s} \right)^2 \qquad \text{E2.3}$$

If there is no ripple on the gain curve, the device is said to be travelling wave; if 3 dB or less, it is designated 'near travelling wave'; if 3 dB or more, the device is Fabry-Perot.

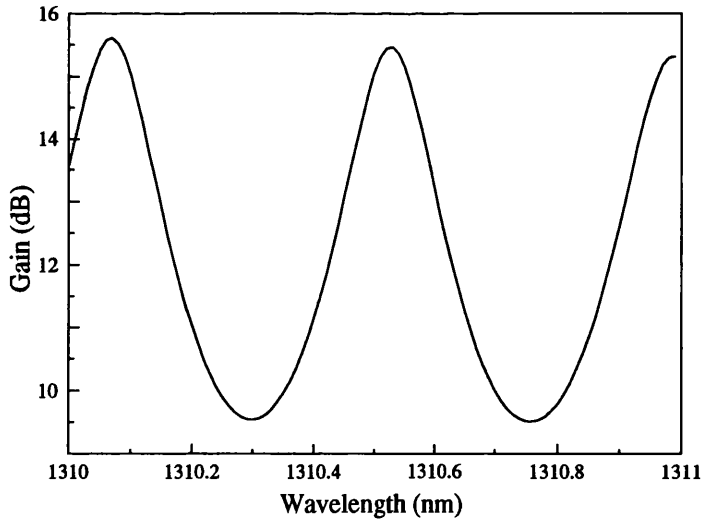

Figure 2.8 Gain of a Fabry-Perot optical amplifier plotted over a short wavelength range, showing the effect of facet reflectivity. Power facet reflectivities 2 %, bias current 60 mA.

Gain ripple is a serious disadvantage of SOAs, and can cause severe signal degradation in high speed optical systems [3]. The variation of device gain with wavelength is a problem in itself, but the situation is worsened by the fact that the ripples are not stationary. If the carrier concentration in the cavity is changed, the interaction between the local electric field and the field of the light is modified. This causes a change in the effective refractive index inside the cavity, altering the effective cavity length and thus its peak transmission wavelength; a shift in the gain ripple with wavelength results. This effect may be caused by a change in input power, bias current or temperature of the device.

2.5 Gain Spectrum

The gain spectrum of the optical amplifier, as depicted schematically in figure 2.9, is approximately parabolic.

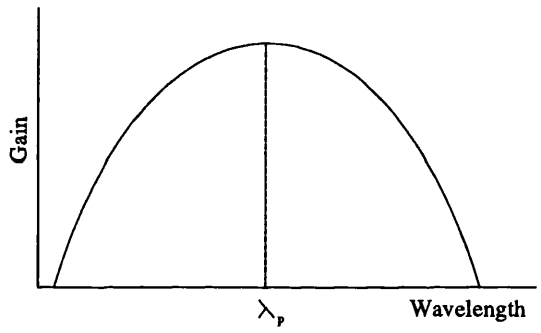

Figure 2.9 Schematic of optical amplifier gain spectrum.

The shape of the spectrum is defined by the energy distribution of the carriers in the material, as shown in fig 2.10 [4]. The lowest energy transition (longest wavelength) corresponds to E_g, the size of the energy gap between the conduction and valence bands. The separation of the quasi-Fermi levels, E_{Fc} and E_{Fv}, defines the highest energy (shortest wavelength) transition [5]. The shape of the spectrum is defined by the energy profile of the carrier density, shown in figure 2.10. There is a lower distribution of carriers near to the band edge, because the available energy states are less dense there. As the energy

increases, the probability of occupancy of a given state, defined by the Fermi function, decreases exponentially. This produces the characteristic gain spectrum depicted schematically in figure 2.9.

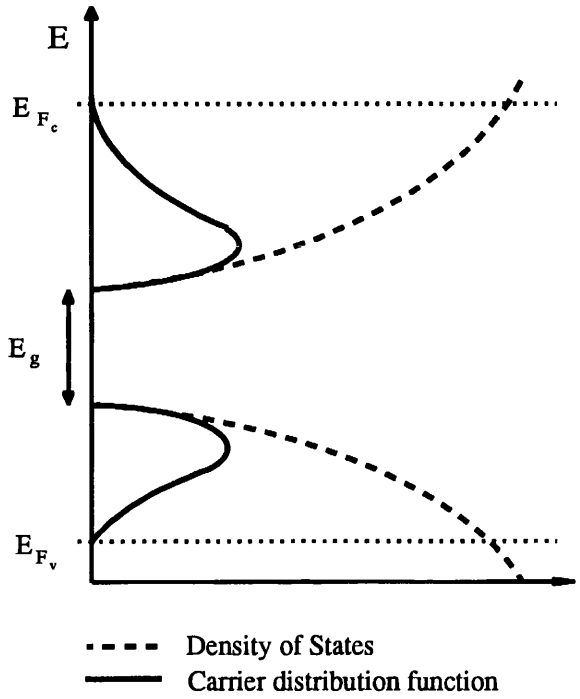

Figure 2.10 Density of states and carrier density in a semiconductor.

Although the gain spectrum is not precisely parabolic, it is usually assumed to be so when the behaviour of the device is being modelled.

The 3 dB optical gain bandwidth is described by $\Delta\lambda = 2(\lambda_p - \lambda_1)$, where λ_p is the peak gain wavelength and λ_1 is the signal wavelength for which the gain is half the peak value. The envelope gain of the device, taking into account the residual facet reflectivity, is defined as the peak value for each wavelength of the single pass gain, G_s:

$$G_e = \frac{(1-R_1)(1-R_2)G_s}{(1-\sqrt{R_1R_2}G_s)^2} \qquad \text{E2.4}$$

It can then be shown that the 3 dB optical bandwidth is given by:

$$\Delta\lambda = 2\sqrt{\frac{ln\left(\frac{2}{1+\xi}\right)}{a_2\,\Gamma L}} \qquad \text{E2.5}$$

where a_2 is a constant which describes the dependence of the gain upon the signal wavelength, Γ represents the proportion of the light confined in the cavity, and is known as the confinement factor, L is the length of the cavity, and

$$\xi = \sqrt{R_1 R_2}\, G_s \qquad \text{E2.6}$$

From equations E2.5 and E2.6, it may be inferred that residual facet reflectivity narrows the gain spectrum.

2.6 Gain Saturation

It was mentioned in section 2.2 that the gain of the device cannot increase indefinitely with electrical pumping. This limitation is imposed by the material structure and the dimensions of the device, which can only support a finite number of carriers, and therefore can only produce a finite amount of light.

Gain saturation is also experienced when the bias current remains constant, and the input power is increased. Here, the gain remains constant until a particular value of input power is attained, and then begins to decrease (figure 2.11). This occurs because the process of stimulated emission depletes the number of carriers available to take part in amplification, and thus prevents the output power from increasing indefinitely with input power. The value of input power at which the gain is half its unsaturated value is known as the saturation input power.

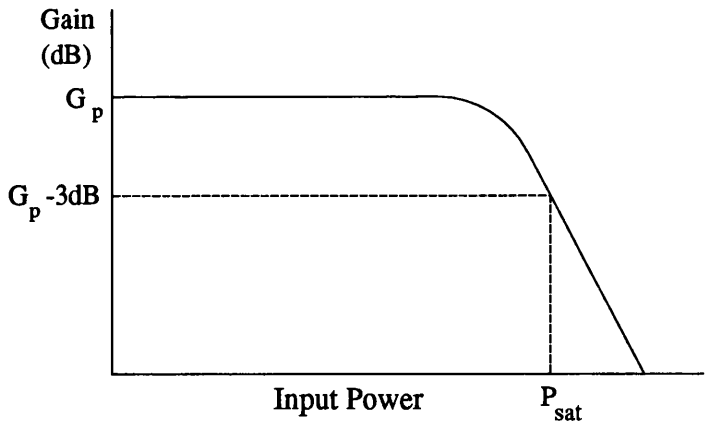

Figure 2.11 Schematic of optical amplifier gain as a function of input power showing the effect of gain saturation.

Gain saturation in an optical amplifier is described by the following equation:

$$g = \frac{g_0}{1 + \frac{P}{P_{sat}}} \qquad \text{E2.7}$$

where g_0 is the peak gain, P is the input signal power and P_{sat} is the saturation input power. Thus when the input signal is small compared with the saturation power, the gain is constant; as P becomes comparable to P_{sat} the gain is reduced by saturation.

Gain saturation presents a severe limitation to the performance of semiconductor optical amplifiers, especially since device nonlinearities and signal distortion are worsened under saturation conditions [6].

2.7 Noise and Amplified Spontaneous Emission

Section 2.2 described the processes of spontaneous and stimulated emission, the latter giving rise to amplification of the input light. However, photons created by spontaneous emission, propagating through the device, may also stimulate the creation of light, and thus be amplified. This amplified spontaneous emission (ASE) is the origin of the noise in the output signal of the SOA.

The expression for optical amplifier noise is derived from the statistical fluctuations in the photon number at the output of the device. The mean number of photons per second emitted by the amplifier is given by:

$$< n > \;=\; G < n_0 > + \gamma(G-1) \qquad \text{E2.8}$$

where G is the average gain of the device, $< n_0 >$ is the mean input photon number, and γ is the degree of population inversion, ie the proportion of electrons in the conduction band. Thus, the first term on the right hand side of E2.8 represents the amplified signal, and the second spontaneous emission.

At the detector, the two optical fields add, and the detector noise is given by the variance in the photon numbers:

$$\sigma^2 \;=\; var\left\{ \left(\sqrt{G n_0} + \sqrt{(G-1)\gamma}\right)^2 \right\} \qquad \text{E2.9a}$$

$$\;=\; var\{G n_0\} + var\{(G-1)\gamma\} + var\{\sqrt{2G(G-1)\gamma n_0}\} \qquad \text{E2.9b}$$

Using the fact that coherent photon streams obey Poisson statistics (E2.10a), and incoherent photon streams obey Bose-Einstein statistics, ie:

$$var\{n\} = < n > \qquad \text{coherent} \qquad \text{E2.10a}$$

$$var\{n\} = < n > + < n >^2 \qquad \text{incoherent} \qquad \text{E2.10b}$$

we can rearrange E2.9b to give the expression for the variance of the photon number at the output of the amplifier [7]:

$$\sigma^2 = \frac{GP}{E} + n_{sp}\,(G-1)\,\Delta f_1 + 2G(G-1)\,n_{sp}\,\chi\,\frac{P}{E} + (G-1)^2\,\Delta f_2\,n_{sp}^2 \qquad \text{E2.11}$$

where P is the average input power and E is the photon energy, such that $\frac{P}{E}$ is the photon number. Δf_1 is the effective shot noise bandwidth, χ is an excess beat noise factor and Δf_2 is the effective beat noise bandwidth.

The four terms on the right hand side of the noise equation correspond to the four sources of amplifier noise; signal shot noise, spontaneous emission shot noise, signal-spontaneous beat noise and spontaneous-spontaneous beat noise respectively. As the name suggests, signal shot noise arises from the amplification of the noise on the input signal; spontaneous shot noise is simply ASE. Since the shot noise is broadband, it will have many frequency components; beat noise is created by the interaction between signal and spontaneous shot noise components, or between different spontaneous noise components. It may be observed from E2.11 that the level of noise produced by the amplifier is dependent upon the size of the average gain; for the case of beat noise, this is a square law dependence.

At the amplifier output the beat noise is typically stronger than the shot noise. Of the two, spontaneous-spontaneous beat noise is dominant at low powers where P is small; this noise can be minimised with the use of a narrow band optical filter. However, signal-spontaneous beat noise, which is strongest at high powers, cannot be removed so easily, because it contains components at the signal wavelength.

Noise places serious limitations upon the usage of SOAs, especially in analogue systems where signal quality is crucial.

2.8 Signal Distortion

Semiconductor optical amplifiers exhibit highly nonlinear behaviour, which can cause significant distortion of optical signals. This presents an obstacle to their use in analogue AM systems, where signal quality is of vital importance. There are three main types of signal distortion; harmonic distortion, crosstalk and intermodulation distortion.

Signal distortion arises because the variation of power in the input signal causes modulation of the carrier density; when the signal power is high, the carriers are depleted, and when the signal power is low the carrier numbers are high. Thus the modulation of the carrier density is out of phase with the modulation of the light in the cavity, and the interaction between the two time-varying quantities gives rise to harmonics of the

modulation frequency, which are emitted along with the fundamental. This is known as harmonic distortion [8]. The modulation of the carrier concentration causes the refractive index of the cavity to vary, and alters the optical phase, delaying the signal by varying amounts as it passes through the device. This gives rise to distortion of the phase of the modulation signal, with respect to the input signal. Gain saturation causes a deterioration of the situation, since the carrier concentration changes rapidly with input power in this regime, and thus is more deeply modulated by the input signal. Figure 2.12 illustrates the modulation of the carrier density in the two gain regimes, above and below saturation.

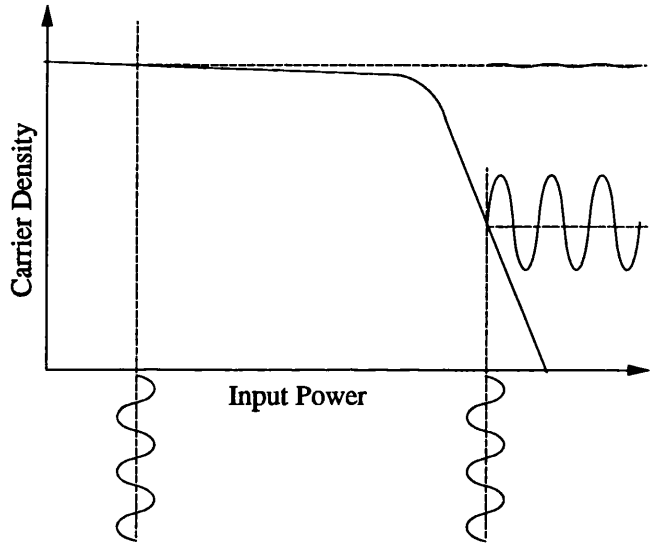

Figure 2.12 Schematic of carrier density as a function of input power, showing the effect of a modulated input signal.

Crosstalk occurs when two or more signals are amplified simultaneously. Because each signal causes modulation of the carrier density, the information contained in each channel can be partially transferred to the others, causing corruption of the data [9].

Intermodulation distortion occurs when two or more WDM signals pass through the cavity. If their optical frequency spacing is of the order of GHz, the carrier density beats at the difference frequency and gives rise to intermodulation products at the output [10].

Because signal quality is so important in analogue systems, it is crucial to understand the mechanisms of distortion, and this dissertation is devoted to the investigation of harmonic distortion, and its minimisation.

2.9 Polarisation Sensitivity

Another feature of SOAs is the dependence of the gain upon the polarisation of the input light. This is due to the shape of the active region of the device, which is generally wider than it is deep. Because of this, TE polarised light is confined more strongly by the cavity than TM light, and experiences a higher gain [11]. This has been a serious problem in the past, not least because the polarisation of a signal can alter significantly while propagating through an optical fibre. A substantial amount of research has concentrated on solving this problem, and some solutions have been proposed. These range from fabricating an active region with a square cross-section [12], to the use of lattice strain, caused by the joining of two materials of different lattice constants [13]. Some workers have proposed system configurations involving two or more amplifiers [14] to equalise the TE and TM gains.

2.10 Travelling Wave and Fabry-Perot Optical Amplifiers

Section 2.4 stated the definitions of TWAs and FPAs as being dependent upon the degree of ripple on the device gain; not surprisingly, they differ in terms of performance, and this section is devoted to a brief comparison of their respective characteristics.

Because of the effect of gain ripple, and its shift with changing carrier concentration, the temperature, bias and input power of an FPA must be very accurately controlled. This is not practical in many systems, and so TWAs are generally preferred.

It has been found that the polarisation dependence of the device gain is stronger in FPAs than in TWAs, since the facet reflectivities are polarisation dependent, and thus the strength of optical feedback also varies [7]. TWAs also generate lower levels of noise than FPAs [15], and have wider gain bandwidths [16], as shown in section 2.5.

The levels of harmonic and phase distortion of the signal are strongly affected by Fabry-Perot resonance, since it causes the gain, and therefore the carrier concentration, to fluctuate. This will be dealt with in detail in a later chapter.

It is evident that FPAs have serious drawbacks, and that TWAs will generally be the preferred option for systems applications. However, true travelling wave behaviour is very difficult to obtain, and most practical devices are of the near-travelling wave type.

2.11 Conclusions

This chapter has described the process of optical amplification, and highlighted some of the limitations of semiconductor optical amplifiers. These include gain saturation, noise and signal distortion. Fabry-Perot resonance, caused by residual reflectivity of the end facets, strongly affects the characteristics of the device, and is therefore a very important effect. Because of the shifting of the Fabry-Perot modes, the bias, input power and temperature of the device must be minutely controlled, which is not possible in many systems. The strong polarisation dependence of the devices, exacerbated by the effects of facet reflectivity, makes them very unattractive for most applications, although solutions to this problem have been proposed. Fabry-Perot ripple also narrows the gain spectrum, and affects the level of signal distortion.

It is evident that, for most commercial applications, travelling wave type amplifiers will be the preferred choice; however, these are very difficult to fabricate, and thus most practical devices retain some degree of facet reflectivity. For this reason, it is important to understand the effects of Fabry-Perot resonance upon the amplification process.

Before SOAs can be considered for analogue optical systems, the causes and effects of signal distortion must be analysed, so that they may be alleviated. To this end, a theoretical model has been devised to predict the behaviour of an SOA under different working conditions, and this will be described in chapter 3.

2.12 References

1. H A Steinberg: "The use of a laser amplifier in a laser communication system", *Proc. IEEE* **51**, p. 943, 1963.
2. N K Dutta, D P Wilt, R J Nelson: "Analysis of leakage currents in 1.3-μm InGaAsP real-index-guided lasers", *J. Lightwave Technol.* **2**, pp. 201-208, 1984.
3. M Z Iqbal, K B Ma, C E Zah, T P Lee, N K Cheung: "Effects of gain ripples in semiconductor optical amplifiers on very high speed lightwave systems", *IEEE Photon. Technol. Lett.* **2**, pp. 48-50, 1990.
4. L Solymar, D Walsh, "Lectures on the Electrical Properties of Materials", pub. Oxford Science Publications, 4ed (Oxford 1988) chapter 8.
5. A Yariv, "Optical Electronics", pub. Saunders College Publishing, 4ed (USA 1991) chapter 15.
6. K Inoue: "Crosstalk and its power penalty in multichannel transmission due to gain saturation in a semiconductor laser amplifier", *J. Lightwave Technol.* **7**, pp. 1118-1123, 1989.
7. M J O'Mahoney: "Semiconductor laser optical amplifiers for use in future fiber systems", *J. Lightwave. Technol.* **6**, pp. 531-544, 1988.
8. J A Constable, I H White, A N Coles, D G Cunningham: "Harmonic and phase distortion of analogue amplitude-modulated signals in bulk near travelling wave semiconductor optical amplifiers", *IEE Proc. J* **139**, pp. 389-398, 1992.
9. I M I Habbab, G P Agrawal: "Asymmetric channel gain and crosstalk in traveling wave optical amplifiers", *J. Lightwave Technol.* **7**, pp. 1351-1369, 1989.
10. S-U Lee, S-Y Shin: "Intermodulation distortion characteristics of a semiconductor laser amplifier in subcarrier multiplexing", *Optics Commun.* **90**, pp. 255-258, 1992.
11. J C Simon: "Polarisation characteristics of a travelling-wave-type semiconductor laser amplifier", *Electron. Lett.* **18**, pp. 438-439, 1982.
12. S Cole, D M Cooper, W J Devlin, A D Ellis, D J Elton, J J Isaac, G Sherlock, P C Spurdens, W A Stallard: "Polarisation-insensitive near-travelling-wave semiconductor laser amplifiers at 1.5 μm", *Electron. Lett.* **25**, pp. 314-315, 1989.

13. M Joma, H Horikawa, C Q Xu, K Yamada, Y Katoh, T Kamijoh: "Polarization insensitive semiconductor laser amplifiers with tensile strained InGaAsP/InGaAsP multiple quantum well structure", *Appl. Phys. Lett.* **62**, pp. 121-122, 1993.

14. G Grosskopf, R Ludwig, G Waarts, H G Weber: "Optical amplfier configurations with low polarisation sensitivity", *Electron. Lett.* **25**. pp. 1387-1388, 1987.

15. J C Simon: "Semiconductor laser amplifier for single mode optical fiber communications", *J. Opt. Commun.* **4**, pp. 51-62, 1983.

16. J Wang, H Olesen, K E Stubkjaer: "Recombination, gain and bandwidth characteristics of 1.3-μm semiconductor laser amplifiers", *J. Lightwave Technol.* **5**, pp. 184-189, 1987.

Modelling Gain and Distortion in Bulk Optical Amplifiers

This chapter describes two computer models, written to simulate the response of a semiconductor optical amplifier to steady state and amplitude modulated optical signals. Comparison of the results obtained from these programs with experimental data shows good agreement, confirming that the major physical mechanisms are satisfactorily described. Harmonic distortion is found to be significant even for input powers substantially below saturation, and to be strongly influenced by the effect of Fabry-Perot resonance. The level of distortion is shown to be directly influenced by the saturation power of the device, and it is concluded that a device with high saturation power is necessary for low distortion operation

3.1 Introduction

Two computer simulations have been formulated to predict the performance of a semiconductor optical amplifier, with the aim of modelling the phase and harmonic distortion generated by the device. Since the response to a steady state signal is different to the response to a modulated signal, two separate programs have been written to cover these two situations. The experimental results in this chapter were provided by Alistair Coles of Hewlett-Packard Laboratories, Bristol.

The optical amplifier used in this study is a commercially available bulk buried heterostructure device, number SOA 3100-1300, manufactured by BT&D Technologies. The device has input and output fibre pigtails, with polarisation control, and an integral temperature controller. The peak gain wavelength is 1302.5 nm for a bias current of 50 mA. The facet reflectivities, which are highly wavelength dependent (figure 3.1), are estimated at 2 % on the long wavelength side of the gain peak, where the measurements were taken. From the spontaneous emission spectrum in figure 3.1, it may be seen that the 3 dB gain bandwidth is approximately 27 nm.

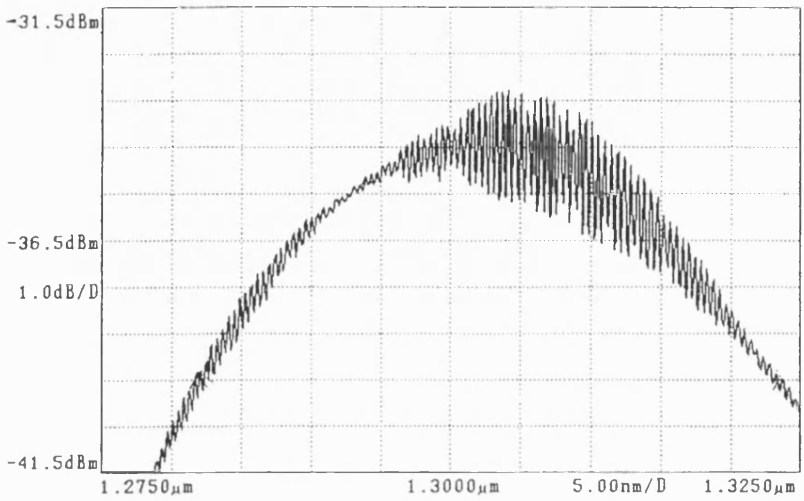

Figure 3.1 Spontaneous emission spectrum of BT&D optical amplifier measured at 50 mA.

Certain effects have been included in the model, while others are less important and hence have been omitted to simplify the computation. The assumptions will be explained initially, then the equations used to model the device will be detailed. The two models will be described, and results presented, following which there will be a discussion about the causes and effects of distortion.

3.2 Inclusions and Assumptions

For the sake of simplicity, physical mechanisms and effects have been incorporated in the models only if their inclusion is essential.

3.2.1 Inclusions

Both the steady state and small signal models include the effects of:

(i) Fabry-Perot resonance

It was stated in chapter 2 that the residual reflectivity of the end facets set up a Fabry-Perot etalon in the cavity of the device. This effect gives rise to ripples in the gain, so that the value of device gain depends upon the wavelength of the input signal. The fluctuations in carrier density caused by the variation in cavity gain also affect gain saturation, and the levels of phase and harmonic distortion, and so this important effect has been taken into account.

(ii) Spontaneous emission

Spontaneous emission is the origin of broadband noise, as mentioned in chapter 2; more importantly, amplified spontaneous emission contributes to gain saturation by depleting the carriers needed for amplification.

(iii) Nonradiative and Auger recombination

Not all electron-hole recombinations result in the emission of photons at the lasing energy. Defects in the material can give rise to localised states with energies in the material bandgap; recombination at one of these sites results in the absorption of the liberated energy by the lattice, or in the emission of a phonon, and is designated non-radiative. Auger recombination occurs when two electrons and a hole collide. The energy freed when the hole recombines with one of the electrons is immediately absorbed by the second electron. This carrier may then be promoted to a state deep in the conduction band, returning to the bottom of the band with the emission of a phonon. The carrier recombination lifetime is strongly influenced by these two effects, and thus they are both included.

(iv) Gain spectral dependence

The gain spectrum of the device shifts in wavelength due to changes in carrier density, through movement of the quasi Fermi levels. This has important implications for device performance, since gain saturation depends upon the position of the signal wavelength relative to the unsaturated gain peak [1,2]. As the input signal increases in power, and the carriers are depleted, the gain peak moves towards higher wavelengths. Thus, a

signal positioned on the long wavelength side of the gain peak will experience enhanced gain and therefore not saturate at such a low input power as one on the low wavelength side of the gain spectrum.

(v) Current leakage and diffusion

The commercial device used to develop the theory has a buried heterostructure configuration, and so suffers from the effects of current leakage and diffusion caused by nonoptimal layer thicknesses or doping levels. Because of this, a relatively small proportion of the bias current is actually injected into the active region, and so this effect is important to the model.

(vi) Electrical heating

The injection of bias current into the device causes heating in the active region. The main effect of this is to reduce the gain, contributing to gain saturation at high values of bias current.

3.2.2 Assumptions

(i) Lumped cavity

During amplification, the optical power in the cavity increases exponentially with distance from the input facet, and the carrier density suffers a corresponding decrease due to depletion. Thus, when very fast optical effects are to be simulated, the cavity is generally divided into short sections, and the behaviour of carriers and light solved for each separately [3]. The simulations to be described in this chapter, however, are concerned with events which take place on a relatively long timescale, and so it is valid to average the photon and electron densities along the length of the cavity.

(ii) Monomode emission

The assumption that the input and output signals are monomode permits the use of a single rate equation to describe the behaviour of the device. Because of this, the spontaneous emission at the signal wavelength only is considered.

(iii) Parabolic gain spectrum

It was stated in chapter 2 that the gain spectrum is often assumed to be parabolic; this simplification is used here also.

(iv) TE input signal

The input polarisation is assumed to be optimised for maximum gain.

(v) Constant facet reflectivity

Although figure 3.1 showed the power reflectivities of the facets to vary considerably across the wavelength spectrum, the computer simulations are concerned with a narrow wavelength range, of the order of a few nanometres. Because of this, the facet reflectivities are assumed constant.

(vi) Constant length

Although temperature effects can cause the length of the device to vary, this effect has been neglected.

Comparison between experimental results and theoretical data confirm that the above assumptions are valid in this case.

3.3 Amplifier Equations

This section details the equations used by both models to predict the behaviour of the bulk semiconductor optical amplifier used in this study.

Any representation of a laser or laser amplifier begins with one or more rate equations to describe the interaction between carriers and photons. Because this study assumes monomode radiation only within the cavity, the photon and carrier numbers are directly linked, and so one combined rate equation suffices. This is adapted from Kawaguchi's theory of bistability in laser amplifiers [4]:

$$\frac{dn}{dt} = \frac{J_a}{qd} - \frac{n}{\tau_s} - \frac{g_m I_{av}}{E} - \beta g_m S \qquad \text{E3.1}$$

The first term on the right hand side of E3.1 represents bias current injection, the second term carrier recombination, the third gain, and the fourth amplified spontaneous emission. The parameters are defined as follows: n is the carrier concentration in the active region; J_a is the current density in the active region, being equal to the current divided by the surface area of the active region, WL; q is electronic charge; d is the

thickness of the active region; τ_s is the carrier recombination lifetime; g_m is the material gain; I_{av} is the average optical intensity inside the cavity; E is the photon energy; β is the spontaneous emission coupling coefficient for the single amplified mode; S is the spontaneous photon density, averaged over the whole spectrum.

Taking into account nonradiative, bimolecular and Auger recombination (constants A, B and C respectively in the following equation), the recombination lifetime is given by:

$$\tau_s = \frac{1}{A + Bn + Cn^2} \qquad \text{E3.2}$$

Since this device has non-zero facet reflectivities, the effects of Fabry-Perot resonance have been taken into account when calculating the optical intensity inside the cavity [4]:

$$I_{av} = I_{in} \frac{(1 + R_2\, e^{gL})(e^{gL} - 1)(1 - R_1)}{gL\left\{(1 - \sqrt{R_1 R_2}\, e^{gL})^2 + 4\sqrt{R_1 R_2}\, e^{gL} \sin^2\phi\right\}} \qquad \text{E3.3}$$

Here, I_{in} is the intensity of the input signal, being equal to the input power divided by the area of the facet, Wd; $g = \Gamma g_m - \alpha$ is the net material gain per unit length, Γ being the optical confinement factor. α represents the effective optical loss per unit length, and thus e^{gL} is the single pass gain of the device. Similarly, the overall device gain is given by:

$$\frac{I_{out}}{I_{in}} = \frac{(1 - R_1)(1 - R_2)\, e^{gL}}{(1 - \sqrt{R_1 R_2}\, e^{gL})^2 + 4\sqrt{R_1 R_2}\, e^{gL} \sin^2\phi} \qquad \text{E3.4}$$

The nonlinear phase change in a single pass of the cavity, ϕ, is calculated from:

$$\phi = \frac{2\pi L}{\lambda}\left(N_r + \Gamma n_p \frac{dN}{dn}\right) + \frac{2\pi L \Gamma (n - n_p)}{\lambda}\frac{dN}{dn} \qquad \text{E3.5}$$

where the first term on the right hand side represents the constant detuning of the signal wavelength from the gain peak, and the second term represents the variation in phase due to the changing gain in the cavity. The symbols are defined as follows: L is the cavity length; λ is the signal wavelength; N_r is the refractive index of the material; n_p is the value of carrier concentration for zero input power, at 50 mA, the bias current which is used to define the reference value for the peak gain wavelength; $\frac{dN_r}{dn}$ is the rate of change of refractive index with carrier concentration.

$\frac{dN_r}{dn}$ quantifies the effect which causes the FP modes to shift when the carrier concentration changes, and it is calculated from [5]:

$$\frac{dN_r}{dn} = \frac{-\alpha_H \lambda a_1}{4\pi} \qquad \text{E3.6}$$

Here, α_H is the linewidth broadening factor and a_1 is the principal material gain constant, sometimes written $\frac{dg_m}{dn}$.

It has already been stated that the gain spectrum is assumed to be parabolic; the material gain of the device is thus described by [6]:

$$g_m = a_1 (n - n_0) - a_2(\lambda - \lambda_p)^2 \qquad \text{E3.7}$$

where a_2 is a gain constant, n_0 is the carrier concentration required for transparency, and λ_p is the peak gain wavelength for the value of bias current used. This is defined by [6]:

$$\lambda_p = \lambda_0 - a_3(n - n_p) \qquad \text{E3.8}$$

Here, a_3 is a third gain constant and λ_0 is the peak gain wavelength at 50 mA, the bias current which defines n_p.

The spontaneous emission photon density is calculated from [7]:

$$S = \frac{R_{sp}}{g}\left\{\frac{(e^{gL}-1)\ [(1-R_1)(1+R_2e^{gL}) + (1-R_2)(1+R_1e^{gL})]}{gL\ (1-R_1R_2\ e^{2gL})} - 2\right\} \qquad \text{E3.9}$$

where R_{sp} is the spontaneous emission recombination rate. Since only bimolecular emission is radiative, this is given by Bn^2.

The effects of current leakage and diffusion are calculated from the following expression [8] for the current injected into the active region, I_a:

$$I_a = \frac{\eta_0\{I_{bias} - I_0\}}{1 + \frac{\eta_0(I_{bias} - I_0)}{I_n}} \qquad \text{E3.10}$$

The parameters are defined as follows: I_{bias} is the terminal current, η_0 is the effective current injection efficiency, I_0 is the leakage current and I_n is a curve fitting parameter. Once calculated, I_a is immediately converted to current density by the program.

The effects of electrical heating, which tend to diminish the gain, have been addressed by including the temperature dependence of the constants a_1 and n_0 [6]:

$$a_1 = a_1(T_0) + \frac{da_1}{dT} R_{th}VI \qquad \text{E3.11a}$$

$$n_0 = n_0(T_0) + \frac{dn_0}{dT} R_{th}VI \qquad \text{E3.11b}$$

where $a_1(T_0)$ and $n_0(T_0)$ are reference values at a known temperature, and $\frac{da_1}{dT}$ and $\frac{dn_0}{dT}$ describe the temperature dependence of the two constants. $R_{th}VI$ defines the effective change in temperature in the active region, being the product of the thermal resistance and the dissipated electrical power.

These are the equations used by the two computer models to predict the response of the device to a variety of stimuli. The values of the physical constants used by the programs are shown in table 3.1, at the end of this chapter. These have been estimated from published figures [eg 6,8], and then adjusted by comparison between theoretical data from the steady state program and experimental results. The experimental results were obtained using a small signal modulated input signal, which to some extent invalidated their use for this purpose. However, the close agreement between experimental and theoretical small signal results (section 3.5) supports the approach taken.

3.4 Steady State Model

3.4.1 Model Description

The steady state model is written in Microsoft Quickbasic release 4.5, and has three sections, providing values of output power and gain versus: bias current for up to eight values of wavelength; input power for up to eight values of wavelength; wavelength for up to eight values of input power.

The program is menu-driven, allowing the user to choose the gain-dependence required, and to input the measurement conditions. Figure 3.19, at the end of this chapter, shows a simplified flow chart explaining the operation of the program, using the section on bias current dependence as an example.

The output power and gain are obtained by solving the rate equation in steady state, using a simple iteration to determine the value of carrier concentration for each set of conditions.

The following subsections contain results obtained from the steady state program. Device gain is plotted as a function of bias current, input power and wavelength.

3.4.2 Results of Bias Current Dependence

This section compares an experimental measurement of device gain as a function of bias current with a corresponding theoretical plot.

Figure 3.2 shows a schematic of the measurement system. The input signal is supplied by a Toshiba TOLD 335S distributed feedback (DFB) laser, with its temperature precisely controlled, both to tune the signal wavelength and to prevent it from drifting. The

isolator immediately after the laser prevents reflections from the input facet of the SOA from entering the laser and affecting its operation. The attenuator is used to set the value of input power, so that the laser bias remains the same throughout. The optical switch routes the laser output signal; either straight to the optical spectrum analyser (OSA) to measure the input power, or to the SOA for the gain measurement. The polarisation rotator allows the orientation of the input light to be optimised for maximum gain. Finally, the second isolator prevents reflections from the grating in the OSA from re-entering the output facet of the SOA.

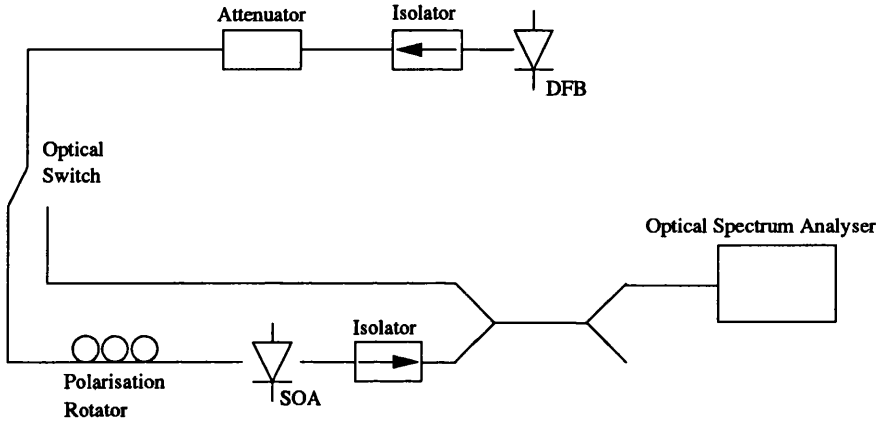

Figure 3.2 Schematic of steady state measurement system

At high bias currents, there is a significant amount of amplified spontaneous emission, which can distort the gain measurement. There are several methods by which this can be avoided; for example an optical bandpass filter, centred around the signal wavelength can be used to remove most of the ASE, or a polarising filter, optimised to the signal polarisation, can be used to filter out that ASE which is differently polarised. The method which has been used here comprises three separate measurements. First, the input power is measured using the optical spectrum analyser, then the ASE at the SOA output is measured without the input signal present. Finally, the total power output from the SOA is measured with the input signal present. The dc gain of the device is then given by:

$$G = \frac{\text{Total Power} - \text{ASE}}{\text{Input Power}} \qquad \text{E3.12}$$

This method is only appropriate for low values of input power. High input powers saturate the ASE and reduce its value; thus the ASE produced while the signal is present will not be the same as that measured with no optical input signal

Figure 3.3(a) shows an experimental plot of gain as a function of bias current measured under these conditions: the fibre input power is -30 dBm, corresponding to a chip input power of -35 dBm, and the different lines on the graph were generated at different wavelengths between 1311.11 nm and 1311.43 nm. Figure 3.3(b) shows a theoretical plot generated by the computer program under the same conditions. There is good agreement between the two plots.

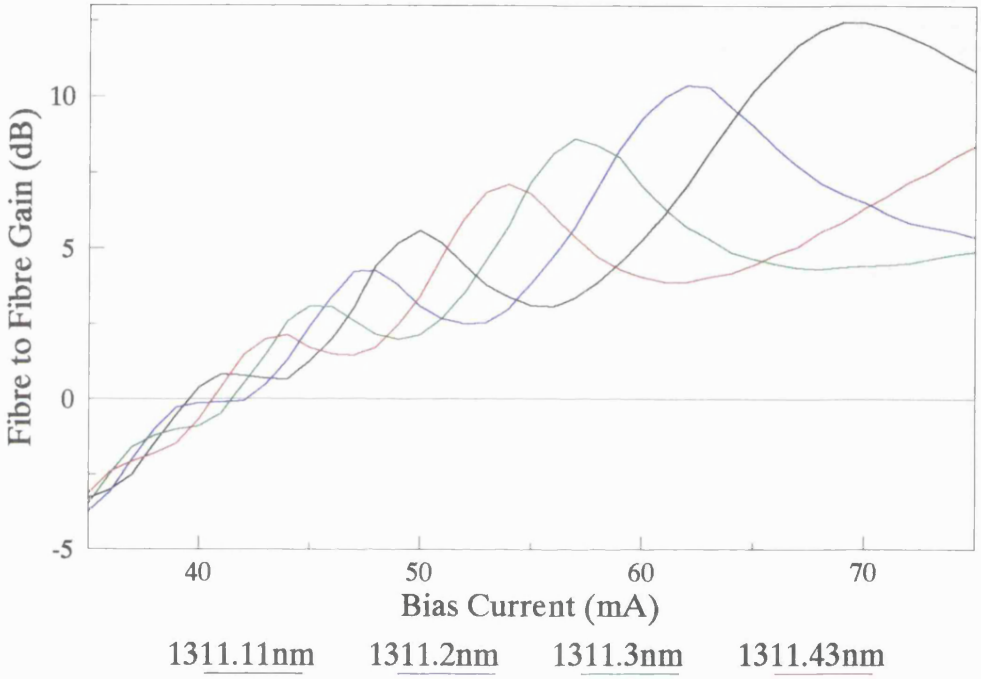

Figure 3.3(a) Experimental dependence of fibre to fibre amplifier gain on bias current for fibre input power -30 dBm and signal wavelengths 1311.11 nm, 1311.2 nm, 1311.3 nm, 1311.43 nm.

At low bias currents, ie less than 45 mA, the device gain is not sufficient to overcome the internal device losses, and those due to fibre coupling, and the fibre to fibre gain is negative. The effect of saturation may be observed at high currents; this effect is strongly influenced by the effects of electrical heating, and current leakage.

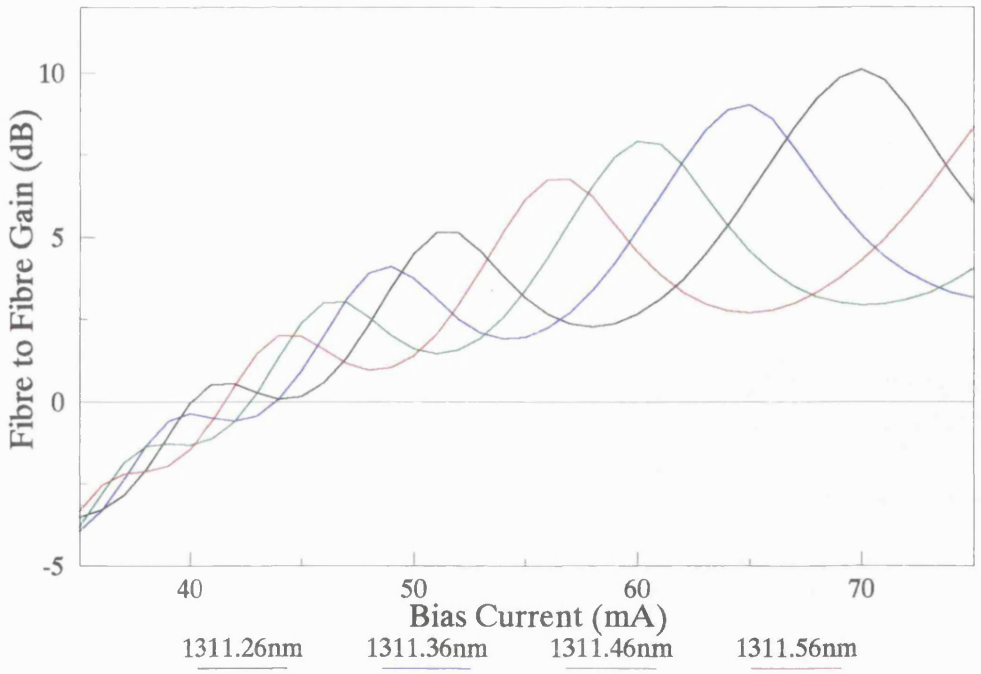

Figure 3.3(b) Theoretical dependence of fibre to fibre amplifier gain on bias current for fibre input power -30 dBm and signal wavelengths 1311.26 nm, 1311.36 nm, 1311.46 nm, 1311.56 nm.

The effects of the FP resonance are clearly evident in this result. As the bias current is increased and the carrier concentration rises, the refractive index falls. This causes the FP ripples to shift down in wavelength. If the signal wavelength is kept constant, it will experience rising and falling gain as the ripples move across it. This is the cause of the undulations in the gain curve.

3.4.3 Results of Input Power Dependence

Figure 3.4 shows the dependence of the fibre to fibre gain on the fibre input power, calculated for a bias current of 50 mA, and four signal wavelengths as before. Again the twin effects of FP resonance and gain saturation are evident. At low powers, where the carrier concentration changes little, there is no shifting of the gain ripple, and the gain for a given wavelength is constant. As the amplifier begins to saturate at high powers, the carrier concentration is rapidly depleted, shifting the ripple to higher wavelengths and producing the distinctive oscillations in the gain.

The saturation input power, defined as the value of input power for which the gain at the peak of the FP resonance is 3 dB below the peak gain, is -7.5 dBm fibre input, or -12.5 dBm chip input.

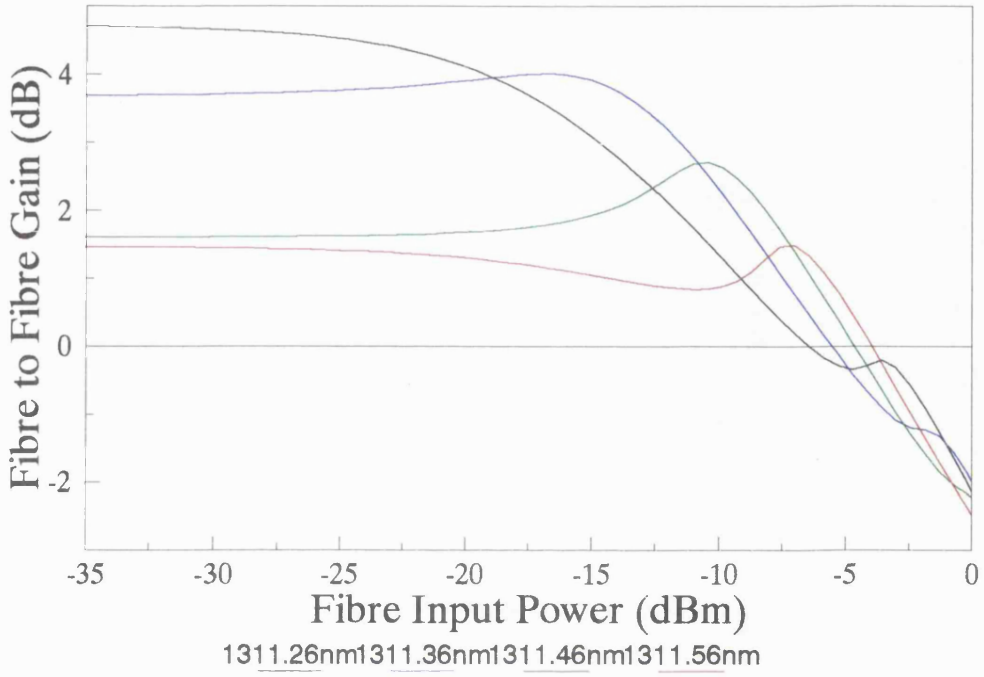

Figure 3.4 Theoretical dependence of fibre to fibre gain upon fibre input power. Bias current 50 mA, signal wavelengths 1311.26 nm, 1311.36 nm, 1311.46 nm, 1311.56 nm.

3.4.4 Results of Wavelength Dependence

The FP ripple may be directly observed in figure 3.5, which shows a theoretical plot of gain as a function of wavelength for a bias current of 50 mA, and four different fibre input powers. The shift of the gain ripple to higher wavelengths, and the compression of the gain by saturation effects, are clearly evident in this plot.

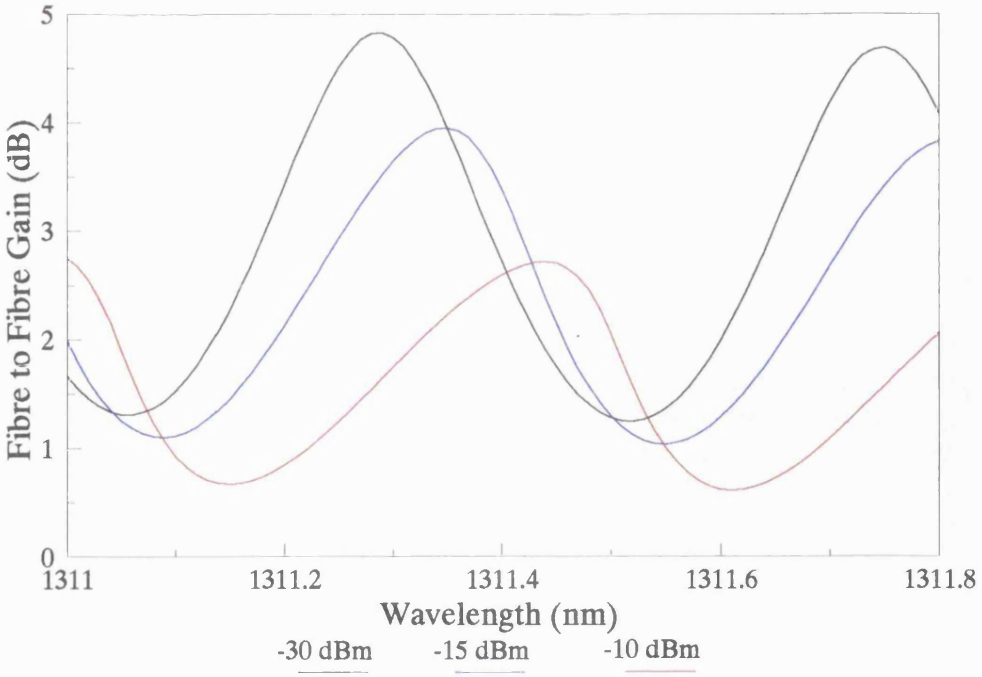

Figure 3.5 Theoretical dependence of fibre to fibre gain upon signal wavelength for a bias current of 50 mA and fibre input powers of -30 dBm, -15 dBm, -12 dBm, -10 dBm.

The results obtained from this computer model agree well with the experimental measurements of device gain.

3.5 Small Signal Model

3.5.1 Model Description

This program analyses the response of the amplifier to an optical input which is amplitude modulated with a sine wave. It provides gain, phase distortion and harmonic distortion values as a function of: bias current for up to eight wavelengths; input power for up to eight wavelengths; wavelength for up to eight input powers; modulation frequency for up to eight input powers.

Again the program is menu-driven, with the user prompted to input: choice of independent variable; values (or ranges) of input power, bias current, wavelength, modulation frequency; optical modulation index (omi); level of harmonic distortion, if any, present in the input signal.

The time dependent response of the amplifier to a sinusoidally modulated optical input is obtained using an incremental method, and a simple Fourier series representation is used to calculate the gain, and the phase and harmonic distortion.

The figure of merit for harmonic distortion used here is the ratio between the power in the first harmonic and that in the second; it is known as the harmonic ratio (HR).

The phase distortion is defined as the phase difference between the modulation of the input signal and that of the fundamental component of the output signal.

Sample results from the model are presented below.

3.5.2 Results of Time Dependence

Before the gain and distortion figures can be calculated, the time dependence must be known. Figure 3.6 shows the input power, carrier concentration and output power as a function of time. The modulation frequency is 120 MHz, the omi is 0.7 (70 %), the bias current is 50 mA and the fibre input power is -10 dBm (-15 dBm chip input power).

During the first few modulation periods, the value of carrier concentration is settling from n_1 to its correct value, and the calculated values are inaccurate. The high value of input power used results in a high level of signal distortion, which can be observed in the flattened form of the output signal. The phase distortion can be seen also, in the offset between the input and output signals.

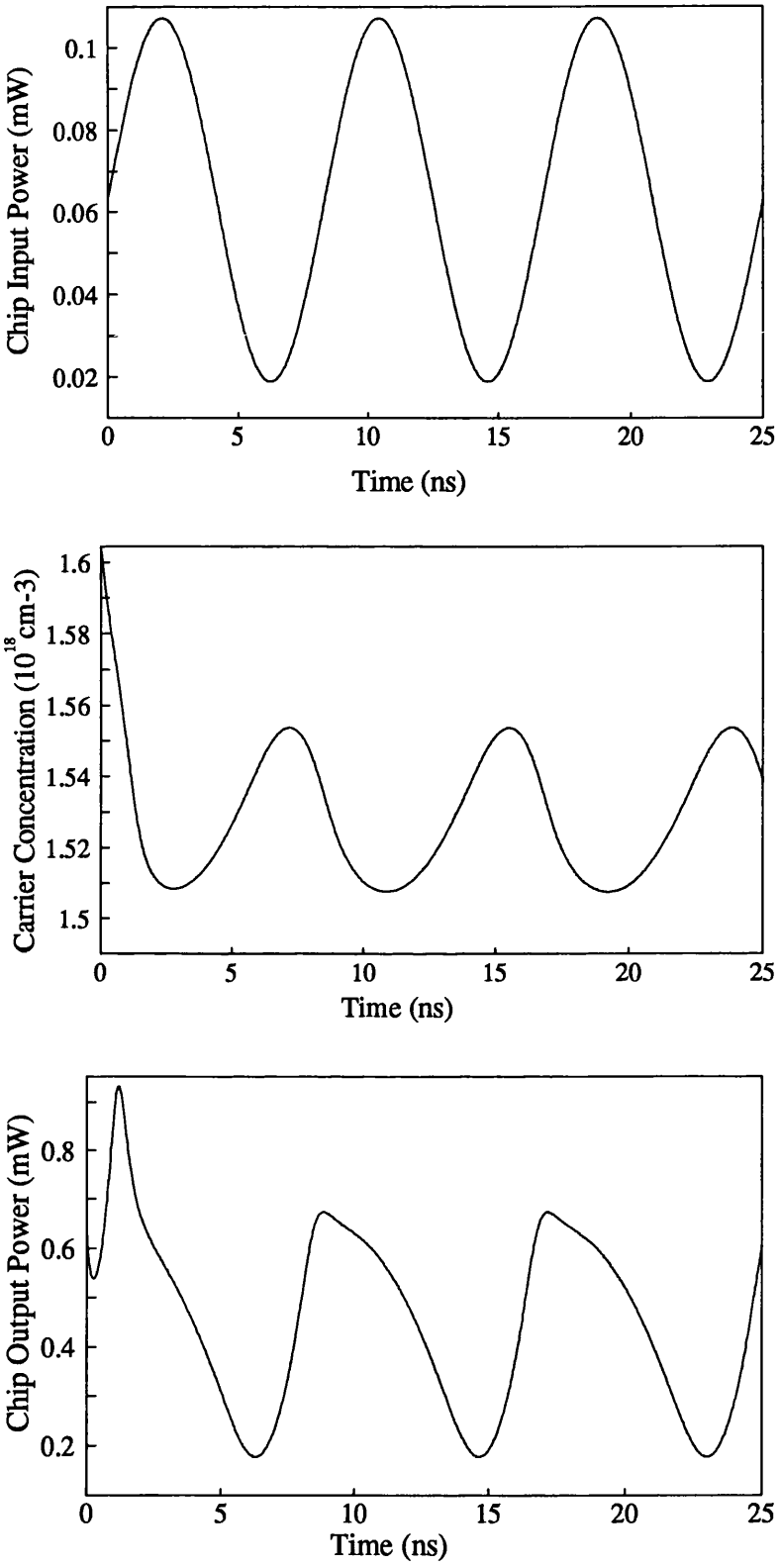

Figure 3.6 Modelled time dependence of input power, carrier concentration and output power. Bias current 50 mA, fibre input power -10 dBm, modulation frequency 120 MHz, modulation index 70 %.

3.5.3 Experimental Techniques

This section describes the techniques used to measure the modulated gain and the two types of distortion.

(i) Gain and Harmonic Ratio

Figure 3.7 shows the system used to measure the modulated gain and the harmonic ratio. It is similar to that used to measure dc gain vs bias (figure 3.3), but here the signal is modulated using an external modulator, with a signal supplied by an rf oscillator. The dc bias to the modulator is adjusted to maximise the harmonic ratio of the input signal, a value of 35 dB optical being achieved. The optical power measurements are carried out using a lightwave signal analyser, comprising an optical head and an electrical spectrum analyser.

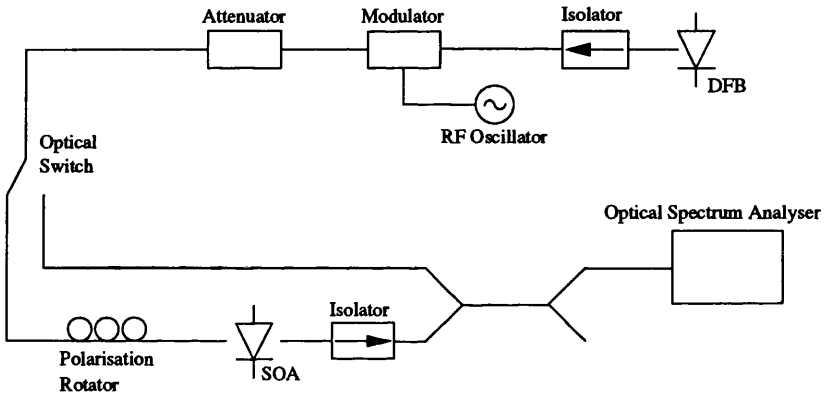

Figure 3.7 Gain and harmonic ratio measurement system

The system used to measure phase distortion is shown in figure 3.8.

Here, the modulating signal is mixed with the SOA output signal, producing an output at twice the modulation frequency, and one at dc. The latter is proportional to the phase difference between the two signals. Since this is is expected to change linearly with frequency, any deviation from linearity is phase distortion.

The following subsections present theoretical and experimental results of the investigation into signal distortion. Some of these have been published [9,10].

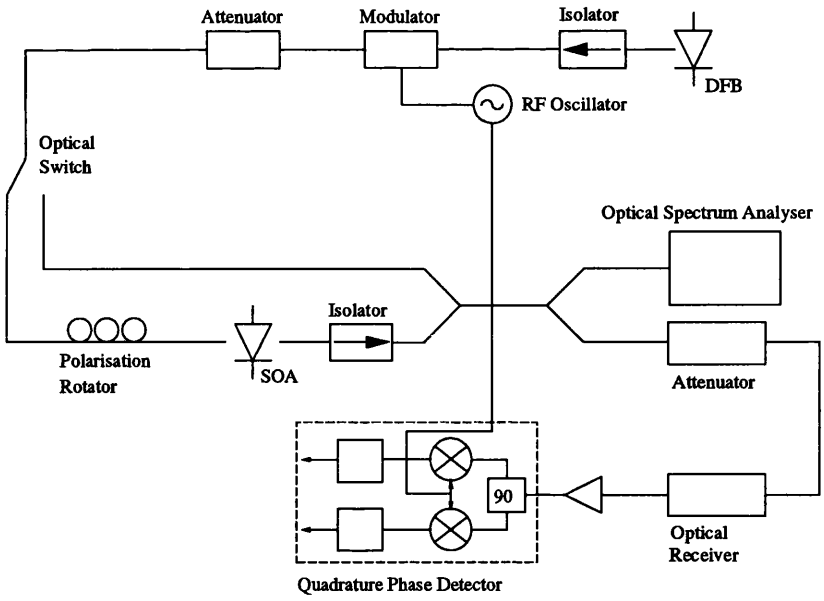

Figure 3.8 Phase distortion measurement system

3.5.4 Results of Bias Current Dependence

The rf gain is plotted in figure 3.9 as a function of bias current, using experimental and theoretical data. The conditions are: SOA temperature 20 °C, average fibre input power -10 dBm, modulation frequency 120 MHz, omi 70 %, four signal wavelengths across a Fabry-Perot ripple pitch. The saturation of the gain at high bias currents is clearly much deeper than in the steady state plot in figure 3.4. This is due partly to the high value of input power used, but also to the high level of spontaneous emission produced at these bias currents, which is modulated by the carrier density fluctuations. These are almost exactly out of phase with the signal modulation, and the ASE follows them. When the amplifier output is detected, the vector sum of the signal and ASE appears smaller than the signal alone. This causes the device to appear to be deeply saturated. This effect can be reduced by the use of a polarising or bandpass filter, but cannot be completely removed.

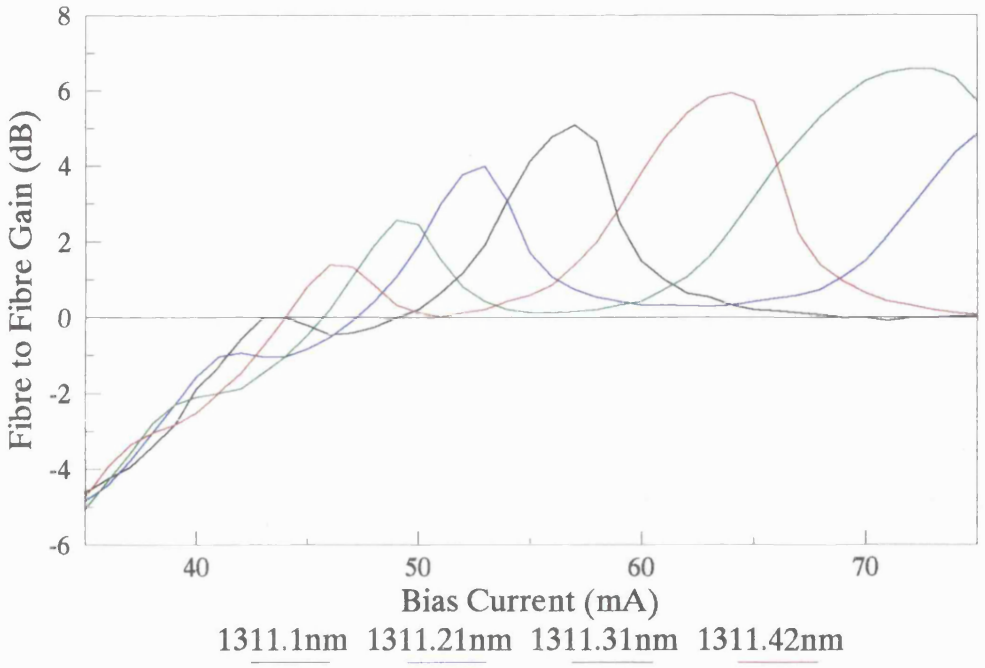

Figure 3.9(a) Experimental variation of rf gain with bias current. Fibre input power -10 dBm, modulation frequency 120 MHz, omi 70 %, signal wavelengths 1311.11 nm, 1311.2 nm, 1311.3 nm, 1311.43 nm.

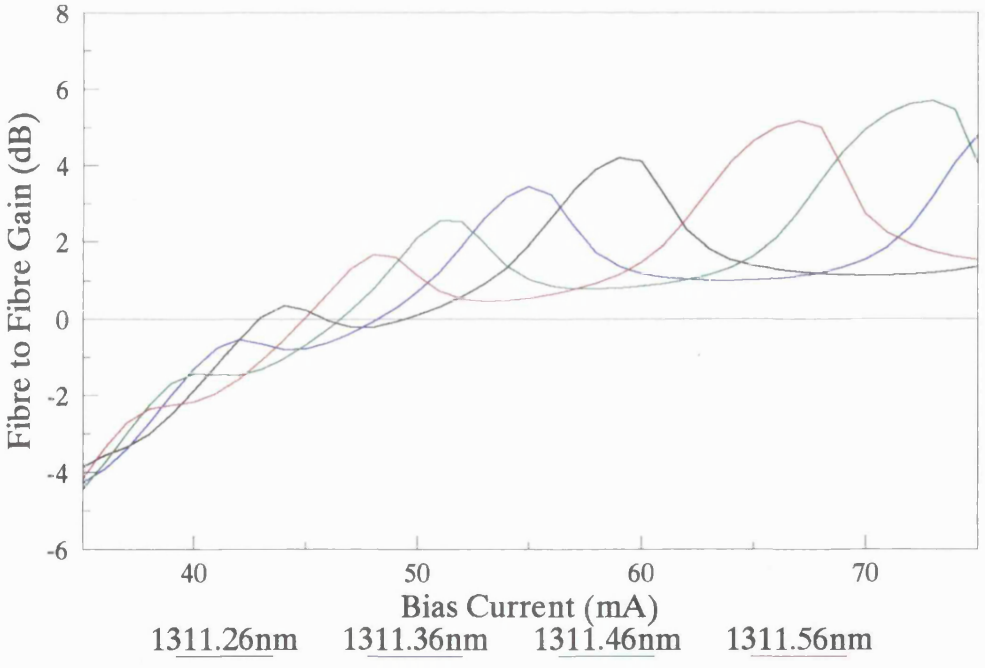

Figure 3.9(b) Theoretical variation of rf gain with bias current. Fibre input power -10 dBm, modulation frequency 120 MHz, omi 70 %, signal wavelengths 1311.26 nm, 1311.36 nm, 1311.46 nm, 1311.56 nm.

The dependence of the phase distortion upon the bias current (figure 3.10) shows strong evidence of FP resonance. Good agreement is obtained between experiment and theory.

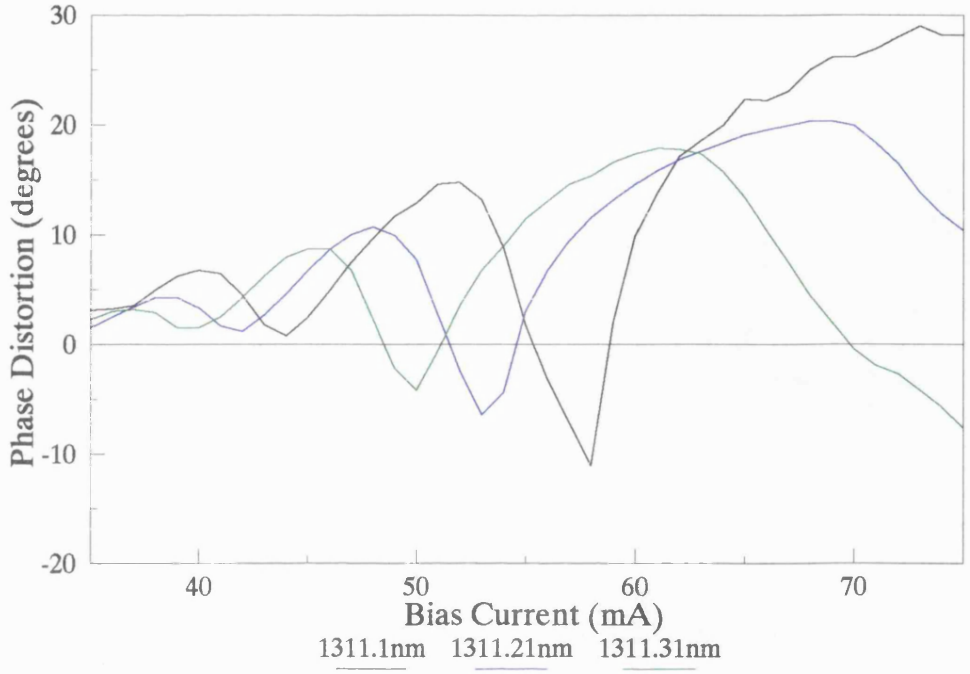

Figure 3.10(a) Experimental variation of phase distortion with bias current. Conditions as figure 3.9(a).

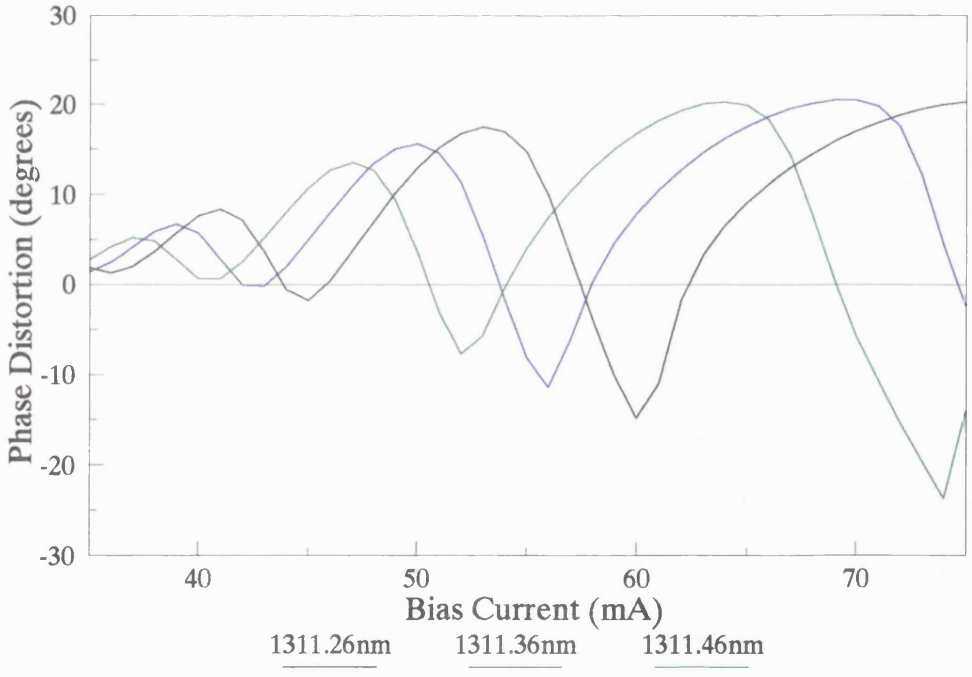

Figure 3.10(b) Theoretical variation of phase distortion with bias current. Conditions as figure 3.9(b).

The variation of the harmonic ratio with current (fig 3.11) again experiences very strong FP influence.

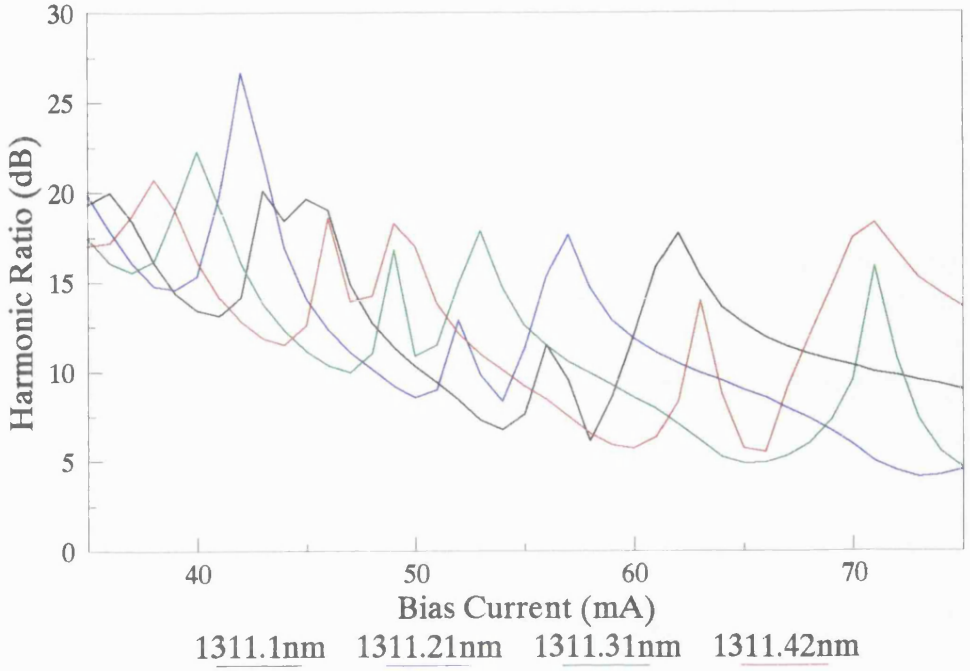

Figure 3.11(a) Experimental variation of harmonic ratio with bias current. Conditions as figure 3.9(a).

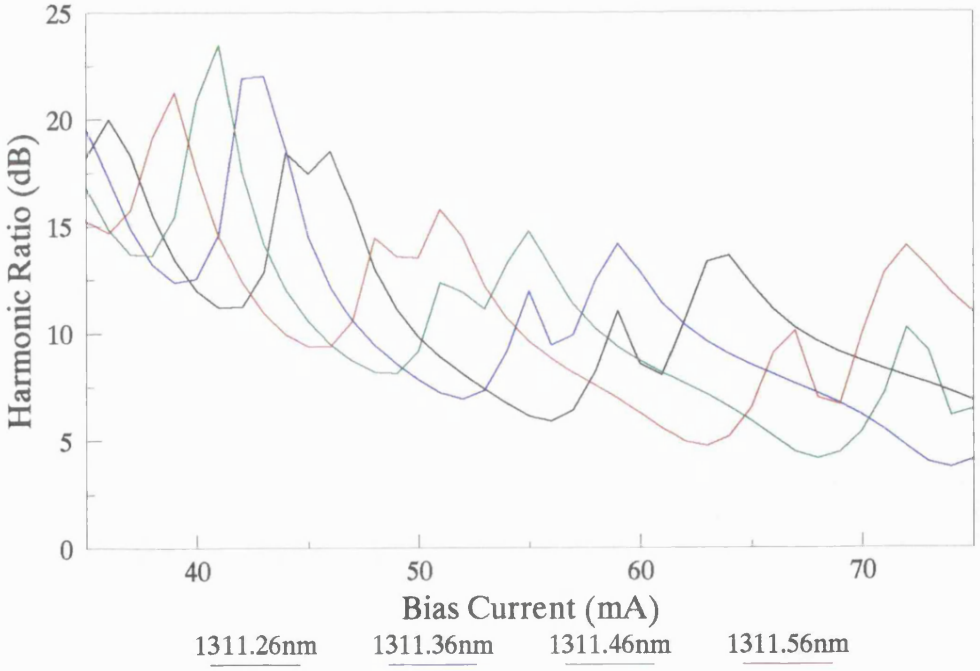

Figure 3.11(b) Theoretical variation of harmonic ratio with bias current. Conditions as figure 3.9(b).

3.5.5 Results of Input Power Dependence

The input power dependences of the rf gain, phase distortion and harmonic ratio are shown in figure 3.12. The experimental and theoretical data have been overlaid; the lines represent theoretical results, the symbols experimental results. The bias current is 50 mA, the modulation frequency 120 MHz and the omi 0.7; four wavelengths across a FP resonance period have been plotted, as shown in the inset. There is excellent agreement between experiment and theory, although the curves deviate slightly in the saturation regime.

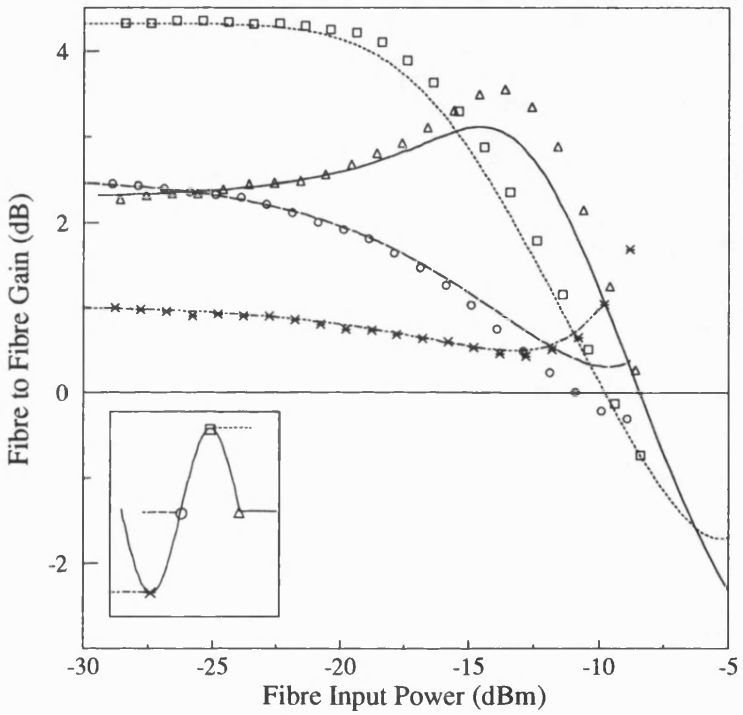

Figure 3.12(a) Theoretical and experimental dependence of rf gain upon fibre input power. Bias current 50 mA, modulation frequency 120 MHz, omi 0.7. Lines = theoretical, symbols = experimental. Wavelengths as inset.

The input saturation power for a modulated signal is slightly lower than for a cw input, although this is not obvious from figure 3.12(a). This is again due to the phase mismatch between the modulation on the input power and that on the carrier concentration, as described in the previous section.

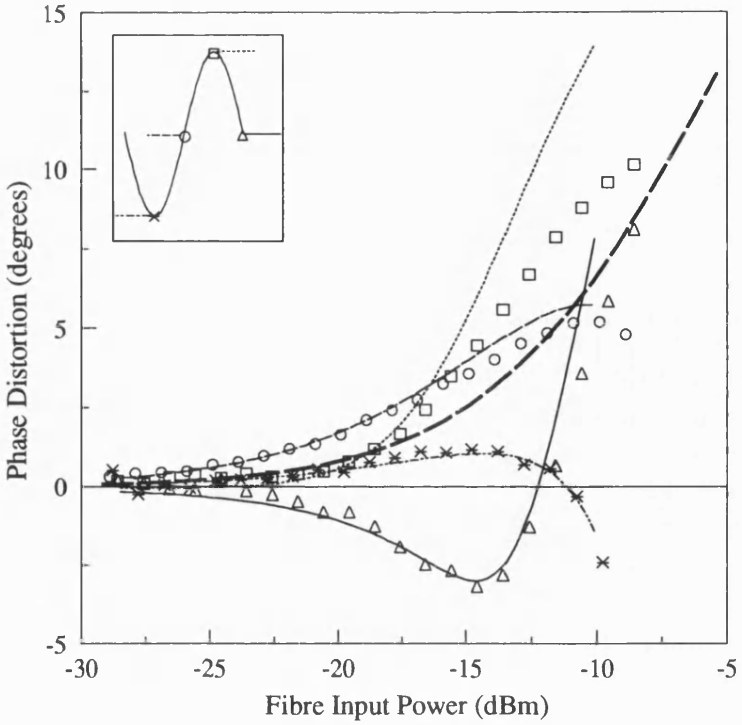

Figure 3.12(b) Theoretical and experimental dependence of phase distortion upon fibre input power. Conditions as for 3.12(a), wavelengths as inset. The heavy dashed line represents a pure travelling wave device.

As the device saturates, the carrier concentration decreases rapidly; this causes the refractive index, and thus the signal delay, to increase, raising the level of phase distortion. The effects of FP resonance are evident in the phase distortion plot. The ripple causes a large variation in the level of distortion at a given value of input power, and necessitates careful control of the bias current and temperature of the device, as mentioned in chapter 2. The heavy dotted line on the plot represents the theoretical response of a pure travelling wave device, ie zero facet reflectivities. It may be observed that the phase distortion corresponding to a trough wavelength is lower than that of the pure travelling wave device. This implies that the FP amplifier could perform better than a pure travelling wave device, albeit with a lower gain; however, the precise control required renders this impractical.

It is interesting to note that the phase distortion curves cross the axis (zero distortion condition) at wavelengths close to gain peaks and troughs. This is due to the twin effects of gain saturation and Fabry-Perot resonance. Gain saturation tends to reduce the device

gain by carrier depletion; this change in carrier concentration causes the gain ripple to shift in wavelength, altering the gain. If the shift in gain ripple causes an increase in gain which balances the decrease due to saturation, a situation arises in which the gain becomes momentarily constant with input power or wavelength, and the distortion is reduced. A similar effect has been observed for crosstalk in multi-wavelength systems [11].

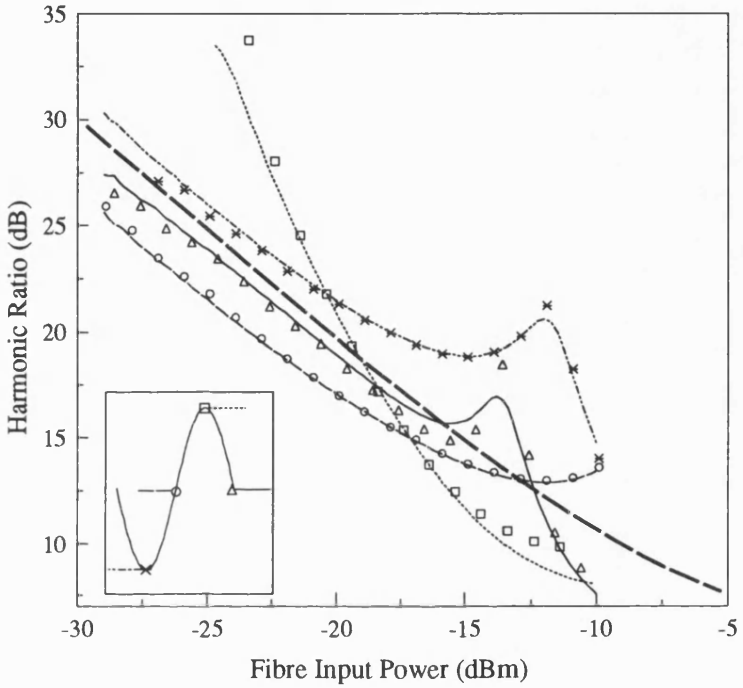

Figure 3.12(c) Theoretical and experimental dependence of harmonic ratio upon fibre input power. Conditions as for 3.12(a), wavelengths as inset. The heavy dashed line represents a pure travelling wave device.

Gain saturation also increases the level of harmonic distortion, as may be observed from the fall in HR in figure 3.12(c). This is due to the increased depth of carrier density modulation experienced by the device in saturation, as explained in chapter 2. Again, FP resonance is evident, and again the FP device has the potential to outperform the travelling wave device (heavy dashed line on plot). It must be noted that distortion levels are significant even at low input powers, and that the value of HR for a given value of input power is strongly wavelength dependent.

In common with the phase distortion, a minimum in harmonic distortion (peak HR) almost corresponds to a peak or trough in gain.

3.5.6 Results of Wavelength Dependence

The effects of FP resonance are clearly evident in figure 3.13, which shows the experimental and theoretical wavelength dependence of the rf gain for three different values of input power.

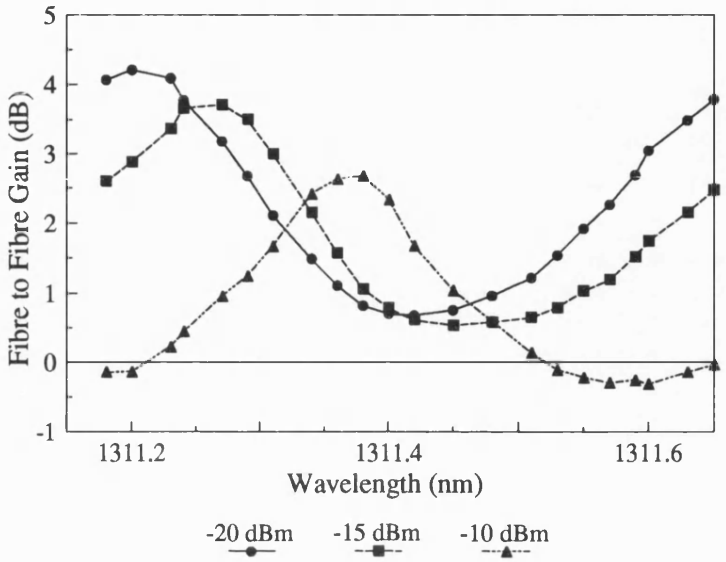

Figure 3.13(a) Experimental dependence of rf gain upon signal wavelength. Bias current 50 mA, modulation frequency 120 MHz, omi 0.7, input power as shown.

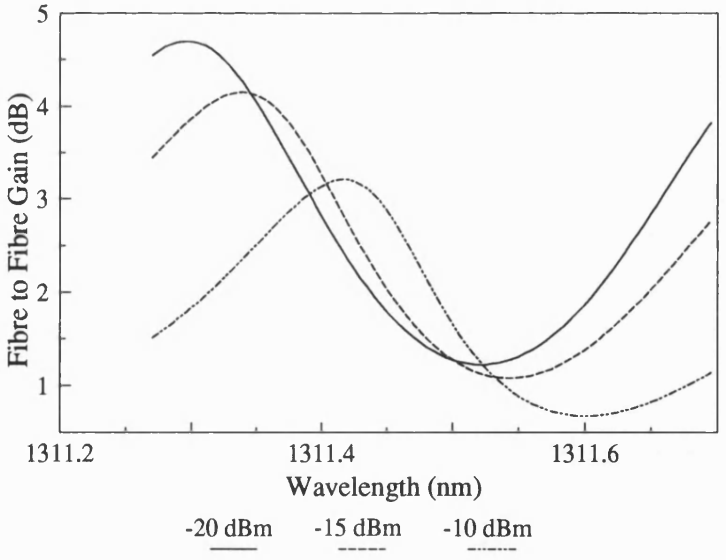

Figure 3.13(b) Theoretical dependence of rf gain upon signal wavelength. Conditions as for 3.13(a).

In common with the plot of cw gain vs wavelength (figure 3.5), the FP ripples shift up in wavelength as the device saturates and the carrier concentration falls. Good agreement is achieved between experimental and theoretical data.

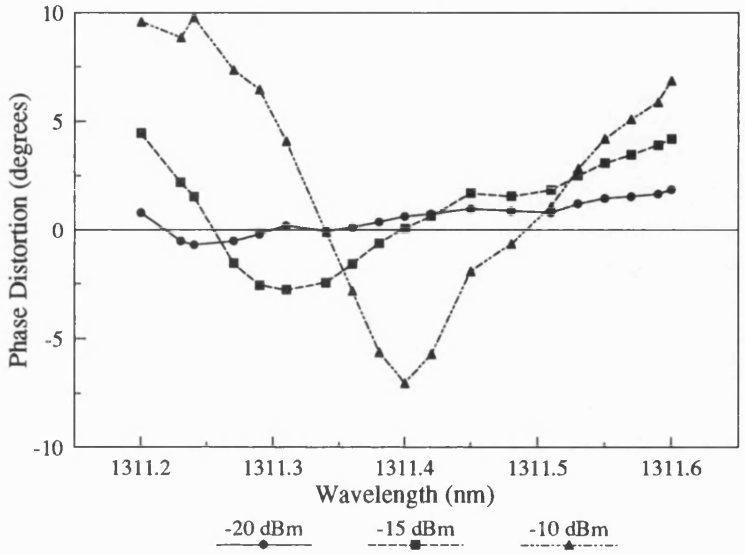

Figure 3.14(a) Experimental dependence of phase distortion upon signal wavelength. Conditions as for 3.13(a).

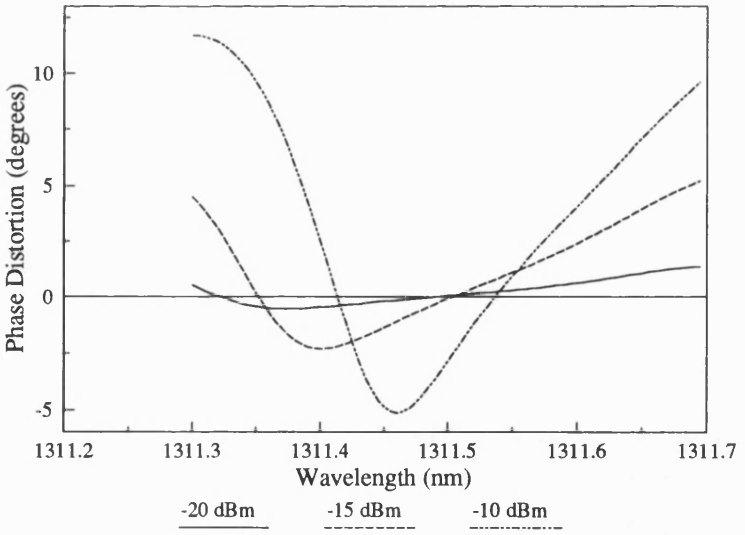

Figure 3.14(b) Theoretical dependence of phase distortion upon signal wavelength. Conditions as for 3.13(b).

Again, it may be noted that the phase distortion is strongly wavelength-dependent. In common with the power-dependent plots in the previous section, a zero phase condition almost corresponds to a Fabry-Perot gain peak or trough.

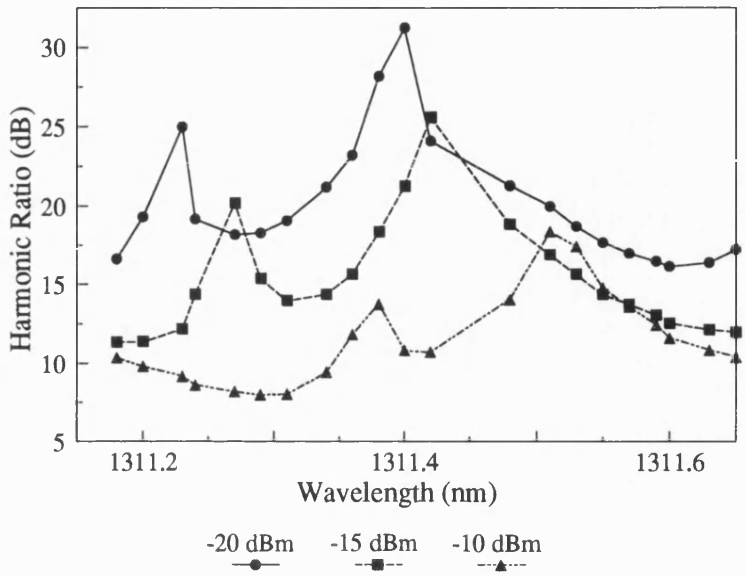

Figure 3.15(a) Experimental dependence of harmonic ratio upon wavelength. Conditions as figure 3.13(a).

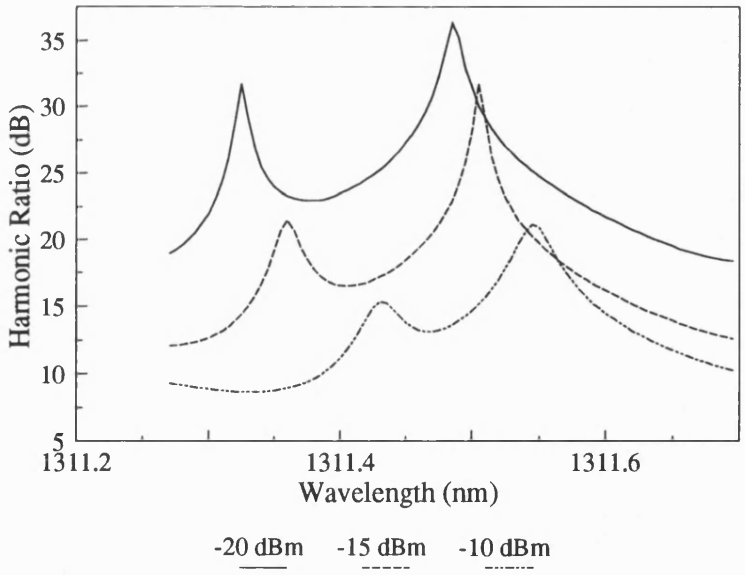

Figure 3.15(b) Theoretical dependence of harmonic ratio upon wavelength. Conditions as figure 3.13(b).

Again the effect of the facet reflectivity is clear. At -20 dBm, the amplifier experiences a variation of up to 15 dB in HR with wavelength.

3.5.7 Results of Modulation Frequency Dependence

Figure 3.16 shows the dependence of the rf gain upon the modulation frequency, for 4 values of wavelength.

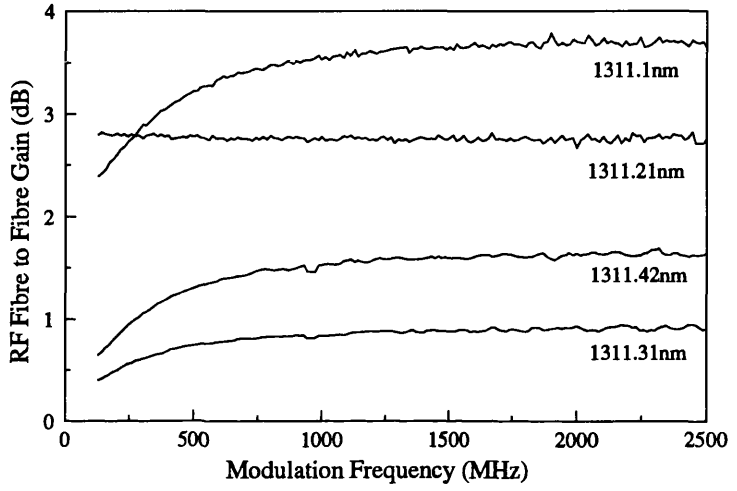

(a)

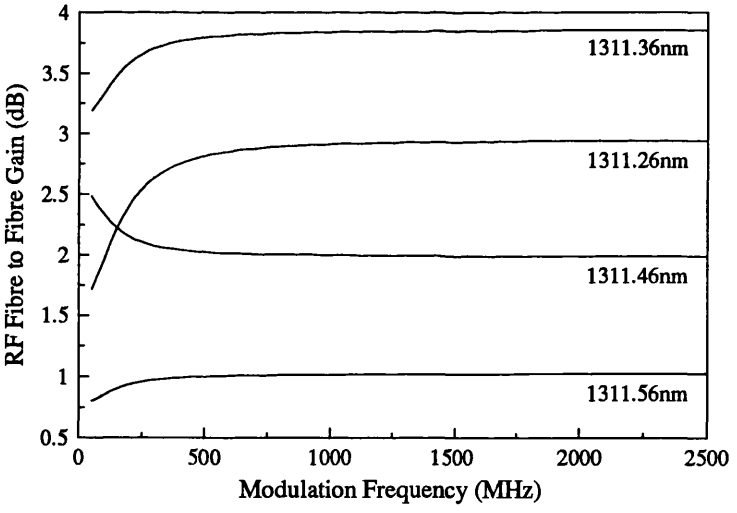

(b)

Figure 3.16 Dependence of rf gain upon modulation frequency. Bias current 50 mA, fibre input power -15 dBm, omi 0.7. (a) Experimental results for signal wavelengths 1311.1 nm, 1311.2 nm, 1311.31 nm, 1311.42 nm (b) theoretical results for signal wavelengths 1311.26 nm, 1311.36 nm, 1311.46 nm, 1311.56 nm.

It may be seen that in both the experimental and theoretical plots the gain generally rises with frequency, effectively raising the saturation power. The reduction in saturation power due to modulation of the carrier concentration and ASE was explained in section 3.5.4. At high modulation frequencies, the modulation of the ASE is limited by the spontaneous recombination rate, Bn^2, and thus its modulation depth decreases.

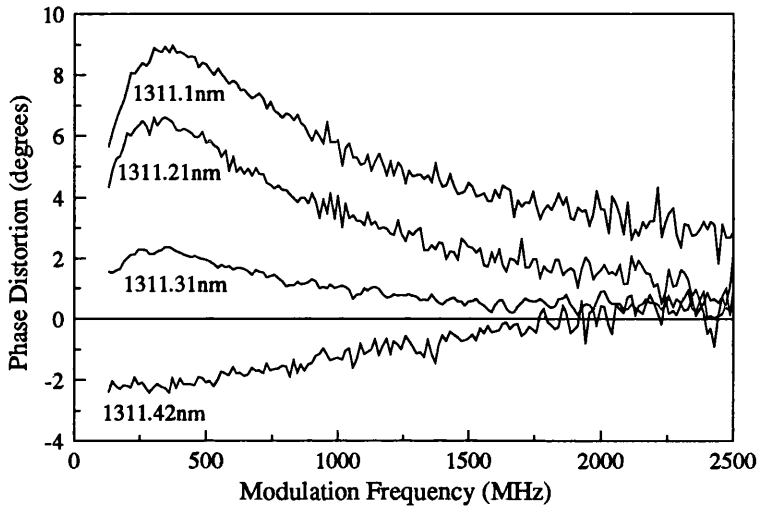

(a)

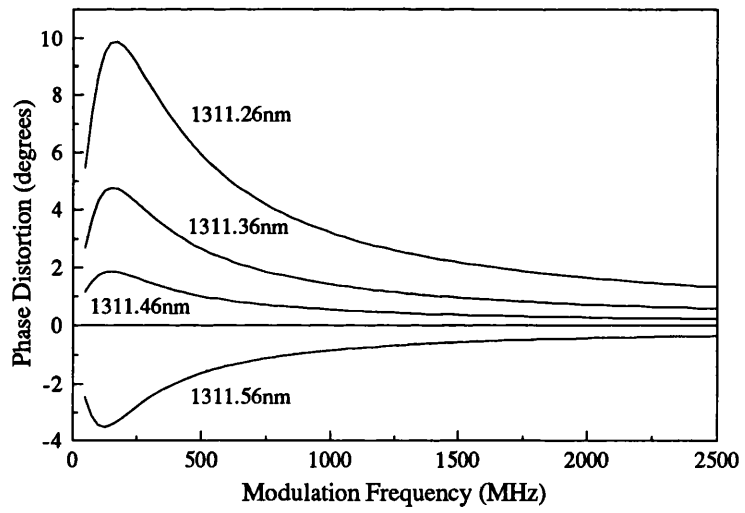

(b)

Figure 3.17 Dependence of phase distortion upon modulation frequency. (a) Experimental (b) theoretical. Conditions as figure 3.16.

The phase distortion (figure 3.17) has a very interesting frequency dependence. It can be shown that for low frequencies it is proportional to ω, the angular frequency of

modulation, while for high frequencies it depends upon $\frac{1}{\omega}$. The peak in phase distortion increases in height and frequency as the input power is increased. The modelled results do not agree precisely with the experimental plot, but the frequency dependence of the phase is very sensitive to the values of carrier concentration and cavity power

There are no experimental results for the dependence of the harmonic ratio upon the modulation frequency; theoretical results are presented in figure 3.18. The harmonic ratio, like the rf gain, rises with modulation frequency. Again this is due to the inability of the carriers to follow the fast modulation, limited as they are by the recombination lifetime. Because the carrier concentration is modulated less deeply, its interaction with the modulation on the input signal gives rise to less distortion.

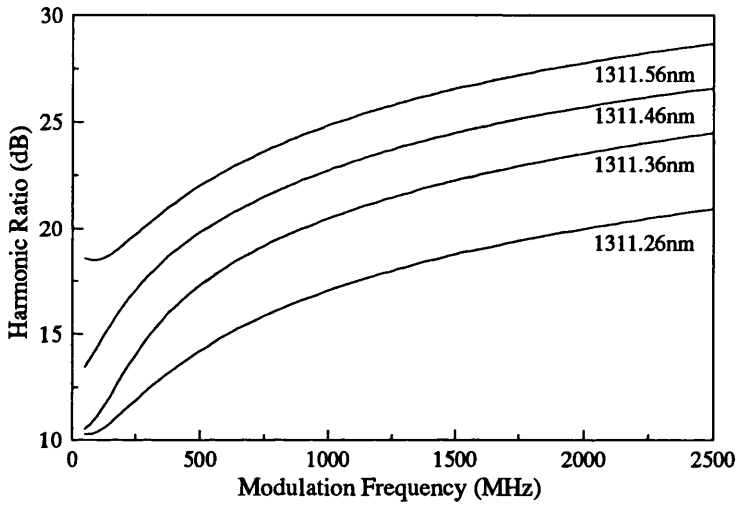

Figure 3.18 Theoretical dependence of harmonic ratio upon modulation frequency. Conditions as figure 3.16.

A simple mathematical analysis of the rate equation demonstrates the effect of the carrier recombination lifetime in reducing the carrier density modulation at high frequencies. The calculation is detailed below.

The rate equation, E3.1, can be expressed as:

$$\frac{dn}{dt} = \frac{j_a}{qd} - \frac{n}{\tau_s} - \frac{(n_x - n_0)P_{av}}{\Gamma \tau_s P_{sat}} \qquad \text{E3.13}$$

Here, the material gain has been expressed as $a_1(n - n_0)$, and the saturation power as:

$$P_{sat} = \frac{1}{\Gamma a_1 \tau_s} \qquad \text{E3.14}$$

For dimensional correctness, P_{av}, the average power in the cavity, has the dimensions of $\frac{I}{E}$ here.

The input signal, modulated by a sine wave of angular frequency ω, modulates the light and carriers inside the cavity. Simplified forms of cavity power and carrier concentration are assumed:

$$P_{av} = P_x + P_y \sin \omega t + P_z \sin(2\omega t + \phi) \qquad \text{E3.15a}$$

$$n = n_x - n_y \sin \omega t \qquad \text{E3.15b}$$

Here, the subscript x refers to dc, y to the fundamental frequency and z to the second harmonic frequency. It should be noted that harmonic distortion of the input is included, also that the carrier density modulation is assumed to be exactly out of phase with that of the signal inside the cavity.

Substituting for carrier concentration and power in the rate equation, and collecting terms in ωt, we obtain the following expression for n_y, the depth of modulation of the carrier density:

$$n_y = \frac{P_y(n_x - n_0)}{\Gamma \tau_s P_{sat}} \cdot \frac{1}{\omega + \frac{1}{\tau_s} + \frac{P_x}{\Gamma \tau_s P_{sat}}} \qquad \text{E3.16}$$

At low frequencies, where $\omega \ll \frac{1}{\tau_s}$, this can be simplified to:

$$n_y \approx \frac{P_y(n_x - n_0)}{\Gamma P_{sat}} \cdot \frac{1}{1 + \frac{P_x}{\Gamma P_{sat}}} \qquad \text{E3.17}$$

This may be seen to be approximately constant for fixed values of average and modulated input power. At high frequencies, however:

$$n_y \approx \frac{P_y(n_x - n_0)}{\Gamma \tau_s P_{sat}} \cdot \frac{1}{\omega + \frac{P_x}{\Gamma \tau_s P_{sat}}} \qquad \text{E3.18}$$

Here it may be clearly seen that the carrier density modulation depth decreases as the modulation frequency increases, and the recombination lifetime begins to limit its response to the input signal.

3.6 Discussion - Distortion issues

The study of signal distortion has revealed some important issues. Firstly, that signal distortion is significant even for input powers substantially below saturation, and must be taken into account for every SOA application. Secondly, that FP resonance has a significant effect on the level of distortion, causing a variation with wavelength of up to 15 dB at low input powers, for a given value of input power and of bias current. The FP effect can be a serious disadvantage, since it requires precise control of the SOA's operating conditions. It can be reduced either by more efficient coating of the facets, or by driving the device with a lower bias current to reduce the gain, and therefore the gain ripple. In addition, chapter 5 outlines a method for reducing distortion using an electrical feedback circuit to reduce the carrier density modulation.

While these measures can reduce the distortion to some extent, for some applications it may be necessary to design a device specifically for low distortion operation. An analysis carried out by the author has ascertained that the level of harmonic distortion generated by a semiconductor optical amplifier is directly related to the saturation power of the device. The proof is detailed below.

3.6.1 Relationship Between Saturation Power and Distortion

This analysis is very much simplified, but gives an insight into the cause of distortion. To begin, the rate equation is expressed as in equation E3.13.

Once again, simplified forms of cavity power and carrier concentration are assumed:

$$P_{av} = P_x + P_y \sin \omega t + P_z \sin(2\omega t + \phi) \qquad \text{E3.19a}$$

$$n = n_x - n_y \sin \omega t \qquad \text{E3.19b}$$

For low modulation frequencies, ie where the modulation period is greater than the carrier recombination lifetime, this can be shown to give the following expression for the rf signal power inside the cavity:

$$P_y = \frac{n_1(\Gamma P_{sat} + P_x)}{(n_x - n_0)} \qquad \text{E3.20}$$

A similar treatment of the $2\omega t$ terms yields the following for the power in the second harmonic:

$$P_z = \frac{n_1 P_y}{2(n_x - n_0)} \qquad \text{E3.21}$$

Combining E3.20 and E3.21 gives the following expression for harmonic ratio:

$$\frac{P_y}{P_z} = \frac{2(\Gamma P_{sat} + P_x)}{P_y} \qquad \text{E3.22}$$

This is an important result, confirming as it does that the HR at all values of input power is actually determined by the saturation power of the amplifier. This follows from the result derived in the previous section, which shows that the depth of carrier density modulation is approximately inversely proportional to the saturation input power.

Thus it is clear that, for acceptable distortion performance in most applications a device with high input saturation power is required. This may be achieved for example with the use of a multi-quantum-well structure, and chapter 4 deals with the design of such a device.

3.7 Conclusions

Two computer programs, written to examine the performance of a semiconductor optical amplifier, have been described in this chapter. They include the effects of Fabry-Perot resonance due to residual facet reflectivity, spontaneous emission, nonradiative and Auger recombination, the spectral dependence of the gain, current leakage under the buried heterostructure, and electrical heating. Several assumptions are made to simplify the calculations and shorten the run-time. However, the close agreement between the experimental and theoretical results presented in this chapter confirms that the major physical effects are adequately described by the model.

This study has established some important issues to be addressed when using SOAs in analogue amplitude modulated systems.

Firstly, that distortion levels are significant, and may be unacceptable for some applications, at input powers substantially below saturation. Also that the effect of shifting FP resonance causes a large variation in phase and harmonic distortion as the carrier concentration fluctuates. This large variation in distortion means that an FP SOA can in theory outperform a TWA, although this is not practical since it requires very precise control over the operating conditions of the device. It has also been discovered that the gain and saturation power appear to be reduced when a modulated input signal is applied. This is due to the modulation of the spontaneous emission in the cavity, which tends to be out of phase with the signal modulation. This effect diminishes as the modulation frequency is increased, and the ASE modulation becomes limited by the recombination lifetime.

Signal distortion may be reduced by a decrease in FP resonance, either by efficient coating of the device facets, or by a reduction in device gain. However, if distortion is to be minimised, specially optimised devices are required. It has been shown in this

chapter that the device saturation power has a direct effect on the level of harmonic distortion generated by the SOA. Chapter 4 describes a process for the design of a high saturation power multi-quantum-well device intended for low distortion operation.

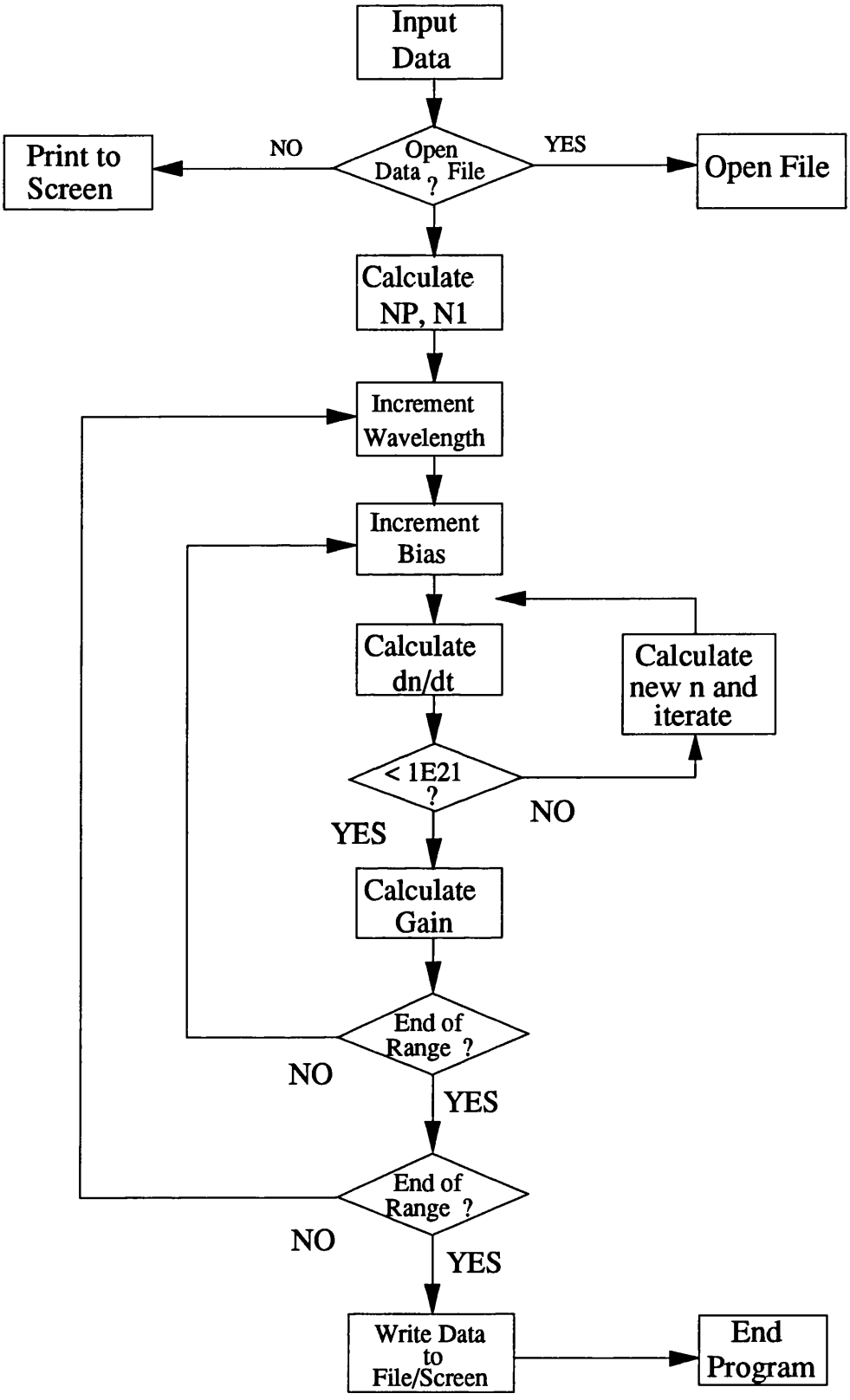

Figure 3.19 Flowchart explaining the operation of the steady state computer program.

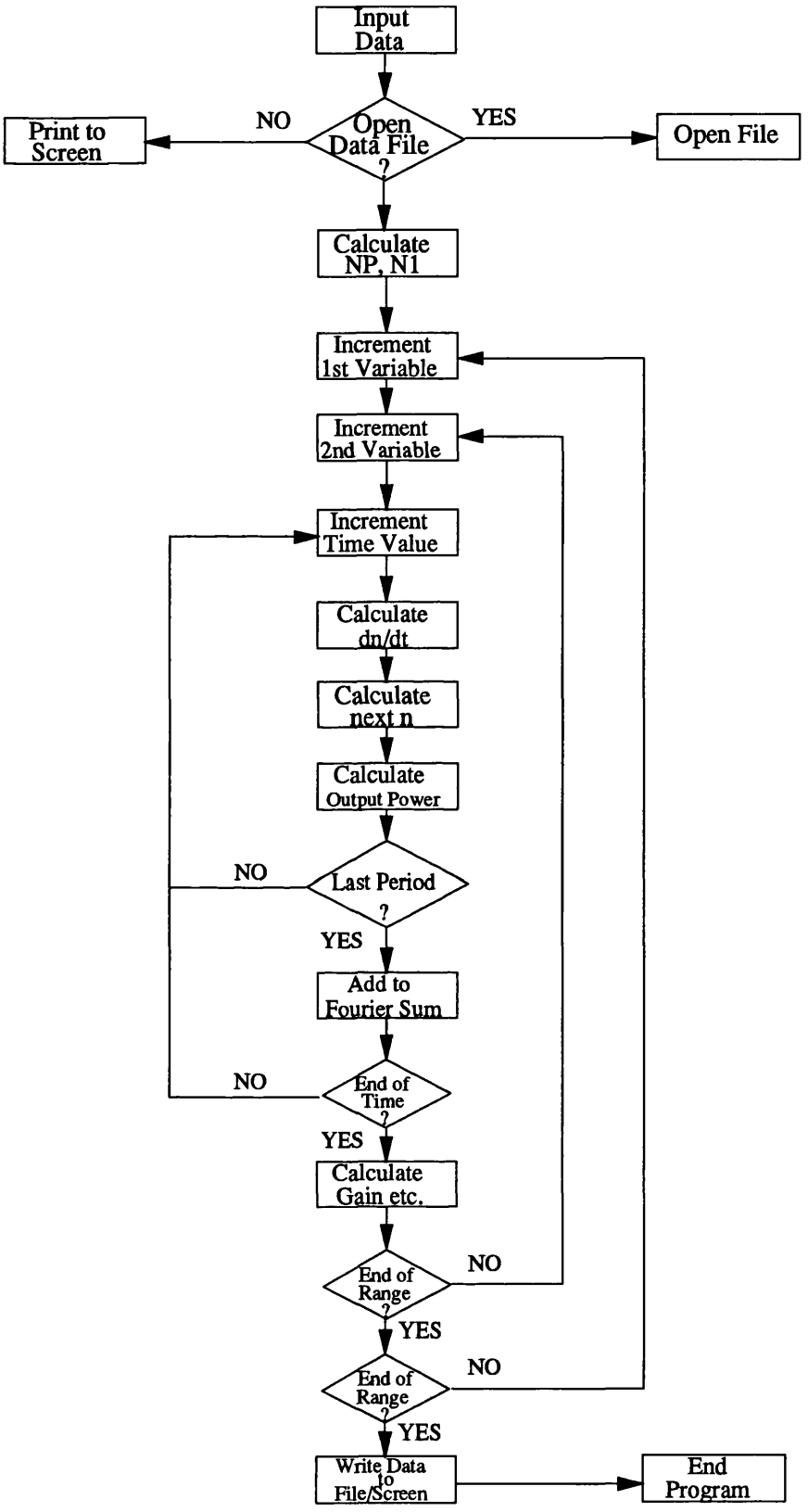

Figure 3.20 Flowchart explaining the operation of the small signal computer model.

Constant	Description	Value
W	Width of active region	1.8 μm
d	Depth of active region	0.2 μm
L	Length of cavity	510 μm
Γ	Confinement factor	0.58
R_1, R_2	Facet reflectivity	2 %
A	Nonradiative recombination constant	10^8 s^{-1}
B	Bimolecular recombination constant	8×10^{-11} cm^3 s^{-1}
C	Auger recombination constant	4×10^{-29} cm^6 s^{-1}
α	Effective optical losses	25 cm^{-1}
$a_1(T_0)$	Material gain constant at T_0	3.5×10^{-16} cm^2
$\frac{da_1}{dT}$	Temperature dependence of a_1	-9.5×10^{-19} cm^2 K^{-1}
a_2	Material gain constant	0.12 cm^{-1} nm^{-2}
a_3	Material gain constant	1.21×10^{-17} cm^3 nm
$n_0(T_0)$	Transparency carrier density at T_0	1.1×10^{18} cm^{-3}
$\frac{dn_0}{dT}$	Temperature dependence of n_0	6.1×10^{15} cm^{-3} K^{-1}
$\frac{dN_r}{dn}$	Change in refractive index with carrier density	-2×10^{-20} cm^3
β	Spontaneous coupling coefficient	2×10^{-3}
λ_0	Peak gain wavelength at 50 mA	1302.5 nm
I_0	Leakage current	9.5 mA
I_n	Curve fitting parameter	35 mA
η_0	Effective current injection efficiency	0.7
α_H	Linewidth enhancement factor	6
R_{th}	Thermal resistance	300 K W^{-1}
V	Junction voltage	0.955 V
	Total coupling loss	7 dB

Table 3.1 Values of physical constants used to model the bulk buried heterostructure optical amplifier.

3.8 References

1. I D Henning, M H Adams, J V Collins: "Performance predictions from a new optical amplifier model", *IEEE J. Quantum Electron.* **21**, pp. 609-613, 1985
2. K Inoue, T Mukai, T Saitoh: "Gain saturation dependence on signal wavelength in a travelling wave semiconductor laser amplifier", *Electron. Lett.* **23**, pp. 328-329, 1987
3. A M Lomax, I H White: "Modulation of picosecond pulses using semiconductor laser amplifiers", *IEE Proc. J* **138**, pp. 178-184, 1991.
4. H Kawaguchi: "Absorptive and dispersive bistability in semiconductor injection lasers", *Opt. Quantum Electron.* **19**, pp. S1-S36, 1987.
5. M J Adams, H J Westlake, M J O'Mahoney: "Optical bistability in semiconductor laser amplifiers", *Optical nonlinearities and instabilities in semiconductors*, ed H Haug (Academic Press, San Diego 1988)
6. J Wang, H Olesen, K Stubkjaer: "Recombination, gain and bandwidth characteristics of 1.3 μm semiconductor laser amplifiers", *J. Lightwave Technol.* **5**, pp. 184-189, 1987.
7. M J Adams, J V Collins, I D Henning: "Analysis of semiconductor laser optical amplifiers", *IEE Proc. J* **132**, pp. 58-63, 1985.
8. J O Binder, G D Cormack: "Prediction of the gain versus injection-current characteristic of individual semiconductor laser amplifiers", *J. Lightwave Technol.* **8**, pp. 1055-1063, 1990.
9. A N Coles, J A Constable, I H White, D G Cunningham: "Distortion of analogue intensity modulated signals in semiconductor optical amplifiers", *Electron. Lett.* **28**, pp. 1012-1013, 1992.
10. J A Constable, I H White, A N Coles, D G Cunningham: "Harmonic and phase distortion of analogue amplitude-modulated signals in bulk near travelling-wave semiconductor optical amplifiers", *IEE Proc. J* **139**, pp. 389-398, 1992.
11. H E Lassen, P B Hansen, K E Stubkjaer: "Crosstalk in 1.5 μm InGaAsP optical amplifiers", *J. Lightwave Technol.* **6**, pp. 1559-1565, 1988.

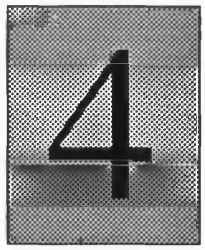

Multi-Quantum-Well Amplifiers

This chapter describes an investigation into the design of a high saturation power multi-quantum-well optical amplifier. The effect upon the saturation power of changing each of the physical dimensions is examined, and the required compromise between cavity length and electrical thickness quantified. It is concluded that the optimum device will have a wide ridge, thick heterostructure, and a short, thick cavity. Modelled results for a device having these attributes confirm its superior performance. Experimental gain measurements performed upon an MQW laser with coated facets support the conclusion that high performance optical amplifiers must be designed specially, and that laser structures are not in general suitable for amplifier applications.

4.1 Introduction

If SOAs are to fulfil their potential in analogue systems, the signal distortion they introduce must be minimised. Although adjustment of the operating conditions may bring some improvement, and chapters 5 and 6 describe a method of doing so, many applications call for a specially designed device to give optimum performance. The relationship between distortion levels and the device saturation power was demonstrated in chapter 3, where it was shown that it was desirable to have the highest possible saturation power. This may be achieved simply by enlarging the optical volume of the cavity to give a higher saturation output power for a given intensity. In a general systems application, however, there may be other requirements; for instance high gain, a broad wavelength spectrum or a wide electrical modulation bandwidth.

Multi-quantum-well (MQW) amplifiers are known to have large gains, in excess of 20 dB [1], high saturation powers, of up to +16 dBm [2], wide spectral bandwidths, of the order of 100 nm [3], and large modulation bandwidths. This last is due to the small carrier recombination lifetime, which in turn results from the large carrier concentration present in the small active volume [4].

These advantages encourage the use of MQW amplifiers in analogue systems; however, the high gain devices generally have small saturation powers and vice versa. Some criteria are needed to aid in developing a compromise design, with sufficient gain to be useful, but with a high saturation input power. An analysis of the design process has led to the determination of the effect of changing the physical dimensions of the device upon the saturation power, and upon the bias current required for a given peak gain, resulting in the proposal of an optimum amplifier design for low distortion operation.

This chapter details the differences between bulk and MQW device theory, and describes the design process for a high saturation power MQW amplifier. An optimised device is proposed, and its distortion performance is compared with that of the bulk device already studied. Experimental measurements of the gain of an MQW amplifier are described, and compared with theoretical data for the same structure. Its performance is explained with reference to the device structure, and conclusions are drawn about the use of MQW optical amplifiers in analogue systems.

4.2 Device Theory

A schematic diagram of the device under consideration is shown in figure 4.1. It is a separate-confinement-heterostructure (SCH), ridge waveguide (RWG), MQW amplifier. SCH refers to the fact that the quantum well active region is isolated by thick cladding layers, which provide waveguiding in the transverse direction (figure 4.1b). This structure also allows the optical cavity to be enlarged without affecting the electrical confinement (see over). A ridge waveguide is chosen as it provides good lateral guiding, along with a wider optical cavity than in BH devices. In a RWG, the mode is more weakly guided than in a BH structure, and is therefore broader. Because of this, RWGs can be made wider than BHs without incurring multiple lateral modes.

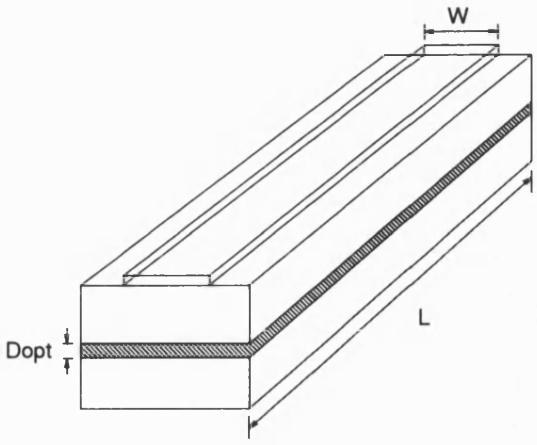

(a)

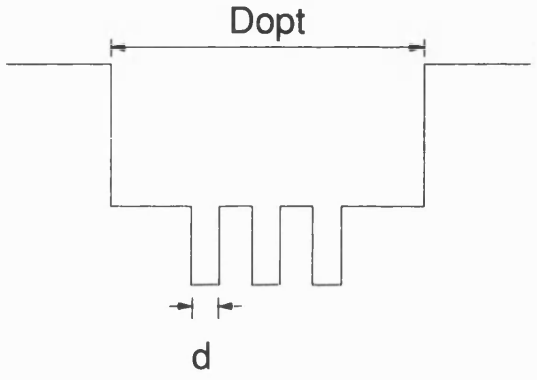

(b)

Figure 4.1 (a) Schematic of SCH-RWG MQW amplifier (b) conduction band diagram.

The MQW amplifier can be approximately described by the electron rate equation:

$$\frac{dn}{dt} = \frac{j_a}{qN_w d_w} - \frac{n}{\tau_s} - \frac{g_m I_{av}}{E_{ph}} - \beta g_m S \qquad \text{E4.1}$$

The terms are as defined in chapter 3, with the exception of the electrical thickness which is now defined as the number of quantum wells, N_w, multiplied by the well thickness, d_w. Also, the conversion of optical power to intensity now involves the width of the

ridge, W and the optical thickness, D_{opt}, as defined in figure 1. From this it may be seen that the optical depth of the cavity may be enlarged without affecting the electrical volume, which is a great advantage of this structure.

The carrier recombination lifetime may again be described by the expression E3.2, although there have been reports of carriers in the barrier layers around the quantum well region, which may modify the device dynamics [5]. Quantum well devices have a high level of Auger recombination; the large value of C, together with the high carrier concentration, in the equation leads to a short recombination lifetime, of the order of 0.2 ns, which gives the device its wide electrical modulation bandwidth.

The major difference between the operation of bulk and MQW amplifiers lies in the dependence of the material gain upon the carrier concentration. From experimental assessment of a range of 1.5 μm MQW laser devices [6,7], it has been shown that the material gain for an MQW device (independent of well number) can be fitted to a logarithmic dependence on the threshold current density [8], unlike the bulk device which has a linear expression for g_m. Using a fit obtained by Greene et al [7], and substituting for j, the following expression is used to obtain values of g_{m_w}, the material gain per well:

$$g_{mw} = g_{m_1}\left\{1+\ln\left(\frac{nqd_w}{g_{m_2}\tau_s}\right)\right\} \qquad \text{E4.2}$$

g_{m1} and g_{m2} are constants whose values are given in table 4.1 at the end of this chapter.

The total gain is therefore obtained by multiplying by the total confinement factor, Γ_t, so that the total gain times length product for the optical filament is given by:

$$gL = \Gamma_t\, g_{mw}\, L - \alpha\, L \qquad \text{E4.3}$$

The confinement factor is smaller in an MQW device than in a bulk structure, typically by an order of magnitude, due to the small dimensions of the quantum well region. There is an approximately linear relationship between Γ_t and the number of quantum wells [8].

These changes have been incorporated into the computer models described in chapter 3, and the validity of the equations and constants verified by fitting published results [4].

4.3 Device Design

4.3.1 Equations

Two numerical analyses have been carried out to discover the effect upon the saturation power of changing the various physical dimensions of the device. In both cases, steady state operation has been assumed. The amplified spontaneous emission term is neglected for the purposes of the numerical analysis, and the facet reflectivity has been set to zero for simplicity. One study investigates the variation of input saturation power and bias current, with fixed peak gain, for different values of various device dimensions; for the other, in order to provide design trends, the ridge width, heterostructure thickness and bias current are fixed, and contours of constant peak gain and constant input saturation power are plotted on axes of device length and electrical thickness ($N_w d_w$).

Since we are interested primarily in increasing the input saturation power of the device, equation E4.1 has been rewritten in terms of $(I_{av})_{3dB}$, the average cavity intensity at 3 dB gain saturation, as:

$$(I_{av})_{3dB} = \frac{E_{ph}}{(g_m)_{3dB}} \left(\frac{j}{N_w \, q d_w} - \frac{n_{3dB}}{\tau_{s3dB}} \right) \qquad \text{E4.4}$$

in steady state. Here, $(g_m)_{3dB}$ is the material gain corresponding to a device gain of half the peak value, and n_{3dB} and τ_{s3dB} are the corresponding carrier concentration and carrier lifetime values.

The first analysis has been carried out at a chosen constant peak gain, G_{peak}, to enable a direct comparison to be made between different hypothetical devices. As any system is likely to require a net gain of at least 10 dB, this has been set at 18 dB (facet to facet), allowing 8 dB total coupling losses.

For an ideal travelling-wave device ($R_1 = R_2 = 0$), the gain is given by:

$$G = e^{gL} \qquad \text{E4.5}$$

Thus it is simple to obtain $(gL)_{peak}$, in turn allowing $(g_m)_{peak}$ to be found from

$$(g_m)_{peak} = \frac{(gL)_{peak} + \alpha L}{\Gamma L} \qquad \text{E4.6}$$

$(g_m)_{3dB}$ can thus be found using E4.6 and the 3 dB value of gL. However, if the average cavity intensity is to be calculated from E4.4, $\frac{j}{N_w\, q\, d_w}$ must be known. This is equal to $\frac{n_1}{\tau_s}$, which can be found by rearranging expression E4.2 for peak material gain:

$$\frac{n_1}{\tau_s} = \frac{g_{m2}}{qd} \exp\left(\frac{(g_m)_{peak}}{g_{m1}} - 1\right) \qquad \text{E4.7}$$

$\frac{n_{3dB}}{\tau_{s3dB}}$ can also be determined, using E4.7 reformulated for $(g_m)_{3dB}$.

Thus the 3dB cavity intensity can be calculated from the following expression:

$$(I_{av})_{3dB} = \frac{E_{ph}}{(g_m)_{3dB}}\left(\frac{n_1}{\tau_s} - \frac{n_{3dB}}{\tau_{s3dB}}\right) \qquad \text{E4.8}$$

But this is also given by the following equation, adapted from [9] for the zero reflectivity case:

$$(I_{av})_{3dB} = (I_{in})_{3dB}\left[\frac{(e^{gL} - 1)}{gL}\right]_{3dB} \qquad \text{E4.9}$$

So that, given $(I_{av})_{3dB}$ and $(gL)_{3dB}$, $(I_{in})_{3dB}$ is easily obtained.

The bias current required for a given gain and saturation power can be readily found using

$$I_{bias} = \frac{n_1}{\tau_s} q \; d_w \; N_w \; L \; W \qquad \text{E4.10}$$

where L is the device length, and W is the effective ridge width.

The equations listed above have been used to carry out the two analyses described earlier in this section. The results are detailed in the following two subsections.

4.3.2 Constant Peak Gain Analysis

In order to assess overall structural requirements for an optimised device, the 3dB saturation input power and bias current have been investigated for constant peak gain by varying the following parameters; well thickness (d_w), well number (N_w), ridge width (W), total heterostructure thickness (D_{opt}) and device length (L). Values of the confinement factor were calculated using a full complex waveguide model kindly made available by Professor White.

(i) Well Thickness Variation

Figure 4.2 shows the results of the analysis for the case where the well thickness is varied, all other parameters remaining constant. Here the 3dB saturation input power, and the current required to achieve a peak gain of 18 dB, are plotted against well thickness. The values of the independent variables are as follows: ridge width 4 μm; cavity length 500 μm; well number 4; heterostructure thickness, D_{opt}, 0.6 μm. The ridge width is chosen to be as wide as possible without multimode operation resulting; the cavity length is a typical value; the number of wells is average for an MQW amplifier; the heterostructure thickness is chosen to be large to increase the saturation power, but growth and carrier transport restrictions are considered.

The results in figure 4.2 demonstrate that the best saturation performance is obtained for the thinnest wells, though the highest bias current is required to maintain 18 dB peak gain under these conditions.

The relationship between input saturation power and well thickness can be explained in the following way. From E4.6, it can be seen that, for constant $(gL)_{peak}$, g_m varies as $\frac{1}{\Gamma}$ (ie approximately as $\frac{1}{d}$). From equation E4.7 therefore,

$$\left(\frac{n_1}{\tau_s}-\frac{n_{3dB}}{\tau_{s3dB}}\right) \propto \frac{1}{d}\exp\left(\frac{X_1}{\Gamma}-1\right)\left[1-\exp\left(\frac{-X_2}{\Gamma}\right)\right] \qquad \text{E4.11}$$

Combining this with the dependence of equation E4.8, we have

$$(P_{av})_{3dB} \propto \frac{\Gamma}{d}\exp\left(\frac{X_1}{\Gamma}\right)\left[1-\exp\left(\frac{-X_2}{\Gamma}\right)\right] \qquad \text{E4.12}$$

where
$$X_1 = \frac{(gL)_{peak} + \alpha L}{g_{ml} L} \qquad \text{E4.13a}$$

and
$$X_2 = \frac{\ln 2}{g_{ml}\, L} \qquad \text{E4.13b}$$

Since Γ varies approximately linearly with d [8], the term $\frac{\Gamma}{d}$ remains approximately constant. Therefore the relationship between the well thickness and input saturation power is an exponential one showing that, by reducing Γ, an exponential growth in saturation power can be achieved. It may be concluded that the logarithmic nature of the gain is a major influence on the well thickness dependence of saturation power.

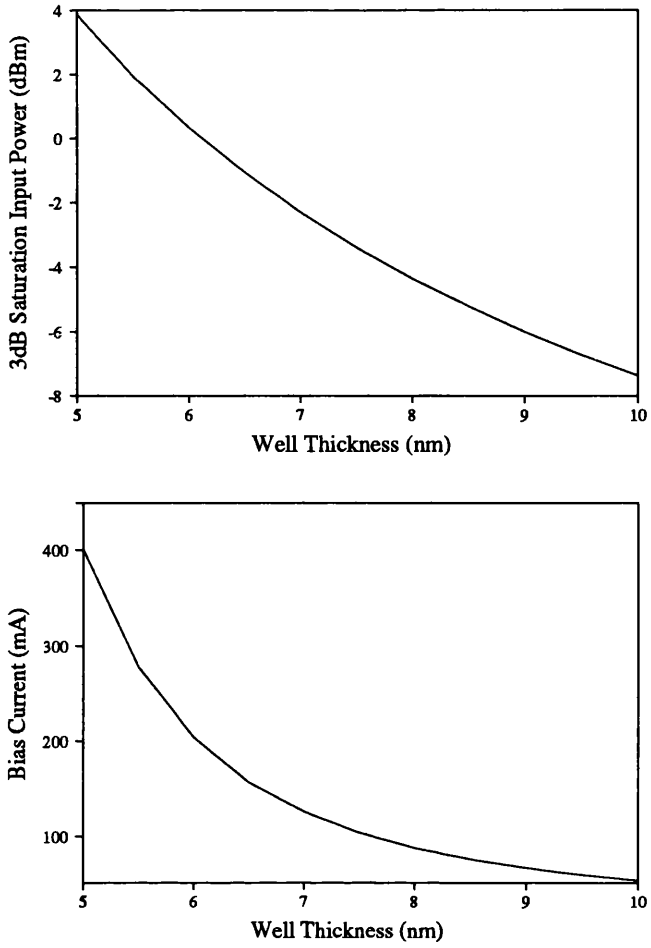

Figure 4.2 Variation of input saturation power and bias current with quantum well thickness for a fixed peak gain of 18 dB.

(ii) Well Number Variation

Again the peak gain is fixed at 18 dB, but here the required bias current and 3 dB input saturation power have been plotted, in figure 4.3, as a function of the number of quantum wells. The independent variables are as before, with the addition of the well thickness which is 8 nm.

Once again the highest saturation powers are obtained for the smallest electrical thicknesses, corresponding this time to the lowest number of quantum wells, but again these are the conditions which require the highest bias currents. The dependence of $(P_{in})_{3dB}$ on the well number is approximately the same as that for well thickness, since for the purposes of this study the two methods of altering the electrical thickness are considered

approximately equivalent in terms of confinement factor [8]. From this it may be inferred that the optimum device should have a small electrical thickness, provided the required current is not too high.

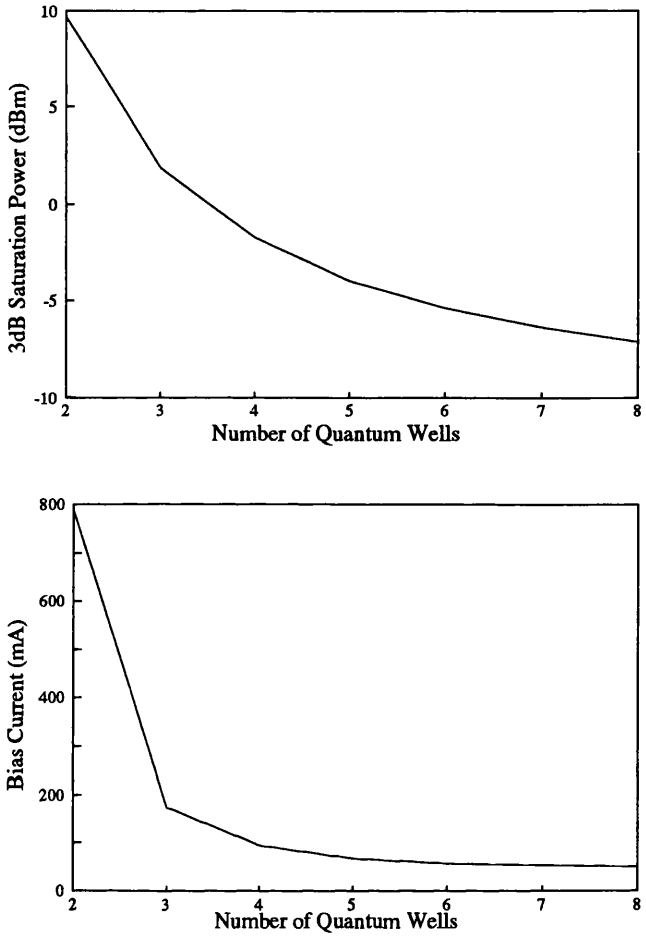

Figure 4.3 Variation of input saturation power and bias current with well number for a peak gain of 18 dB.

(iii) Ridge Width Variation

For this study, current leakage and diffusion have been neglected. As figure 4.4 shows, there is a linear dependence of both the input saturation power in mW and the required bias current on the ridge width.

This may be easily understood. Since the peak gain is fixed, so is the 3 dB gain. This means that $(g_m)_{3dB}$ is also fixed, since Γ, α and L are constants. As g_m does not depend on the ridge width, $\frac{n_1}{\tau_s}$ is also independent. From E4.10, it can be seen that the bias current

therefore increases linearly with W, as the effective electrical volume increases. If $(g_m)_{3dB}$ and $\frac{n_{3dB}}{\tau_{s3dB}}$ are both constant, it follows from E4.4 that $(I_{av})_{3dB}$ is also constant with changing ridge width. Because $(P_{in})_{3dB} = \{(I_{in})_{3dB}\ WD_{opt}\}$, the 3 dB input saturation power, plotted in mW, also rises linearly with ridge width.

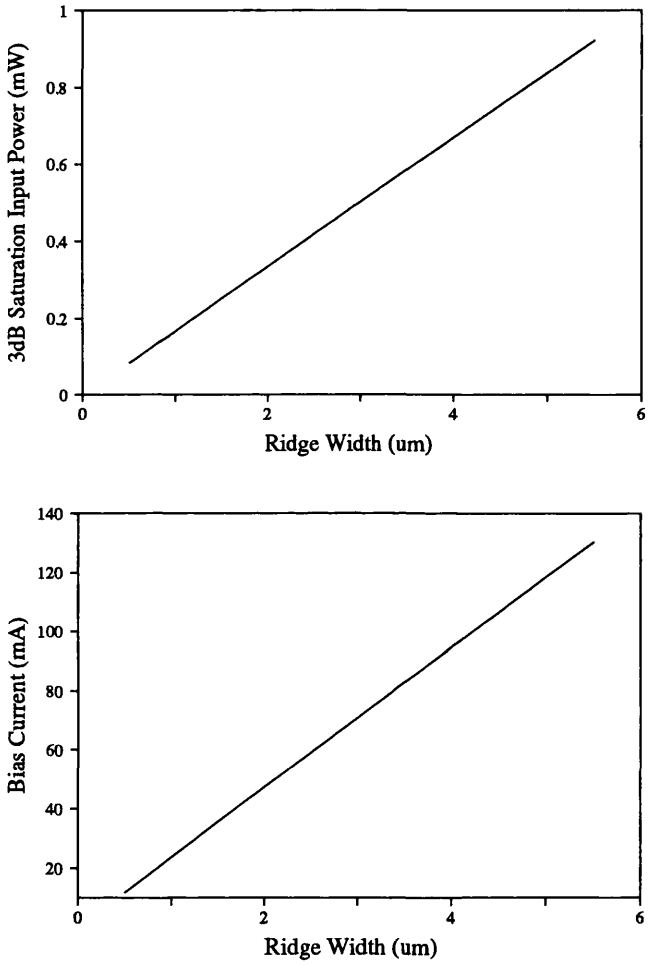

Figure 4.4 Variation of input saturation power and bias current with ridge width for peak gain of 18 dB.

(iv) Heterostructure Thickness Variation

Increasing the heterostructure thickness D_{opt} , that is widening the barrier layers around the quantum wells, has a strong effect on the total confinement factor, as figure 4.5 shows. Γ rises at first and peaks at $D_{opt} = 0.4$ μm, before falling again.

From E4.6, for constant $(gL)_{3dB}$, $(g_m)_{3dB}$ varies as $\frac{1}{\Gamma}$. As a result, the dependence of g_m on the heterostructure thickness is the inverse of figure 4.5. The bias current dependence (figure 4.6) is similar to the material gain dependence. But the cavity intensity also depends on $\left(\frac{n_1}{\tau_s} - \frac{n_{3dB}}{\tau_{3dB}}\right)$, which depends on the difference $[(g_m)_{peak} - (g_m)_{3dB}]$. Rearranging E4.6 and substituting for $(gL)_{peak}$ and $(gL)_{3dB}$, leads to an expression for the difference $[(g_m)_{peak} - (g_m)_{3dB}]$, being given by $\frac{\ln 2}{\Gamma L}$. This therefore has a D_{opt} dependence similar to that of g_m , that is a dip at $D_{opt} = 0.4\ \mu m$. Combining the profiles of $\left(\frac{n_1}{\tau_s} - \frac{n_{3dB}}{\tau_{3dB}}\right)$ and $\frac{1}{(g_m)_{peak}}$ with the linear relationship between P_{in} and D_{opt} , gives the final result shown in figure 4.6 for three wells. All other dimensions are as before

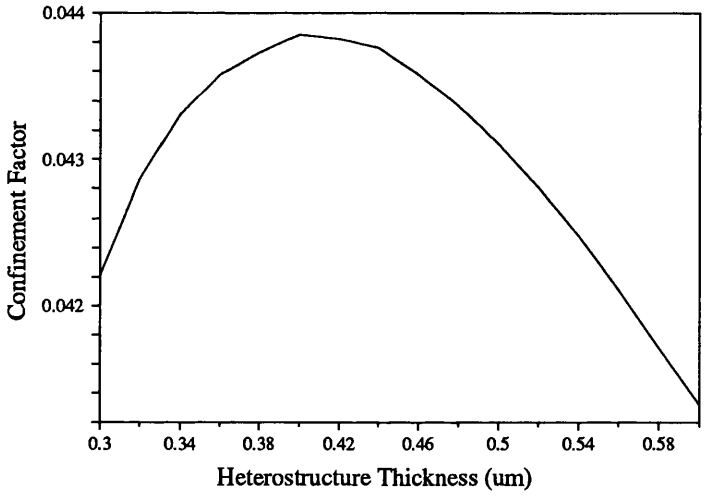

Figure 4.5 Variation of total confinement factor with heterostructure thickness for three quantum wells.

One method of increasing the input saturation power is to reduce Γ by some means to decrease the gain [4]. It is evident from figure 4.5 that increasing D_{opt} above 0.4 μm will achieve this, as well as reducing the input intensity by enlarging the cavity.

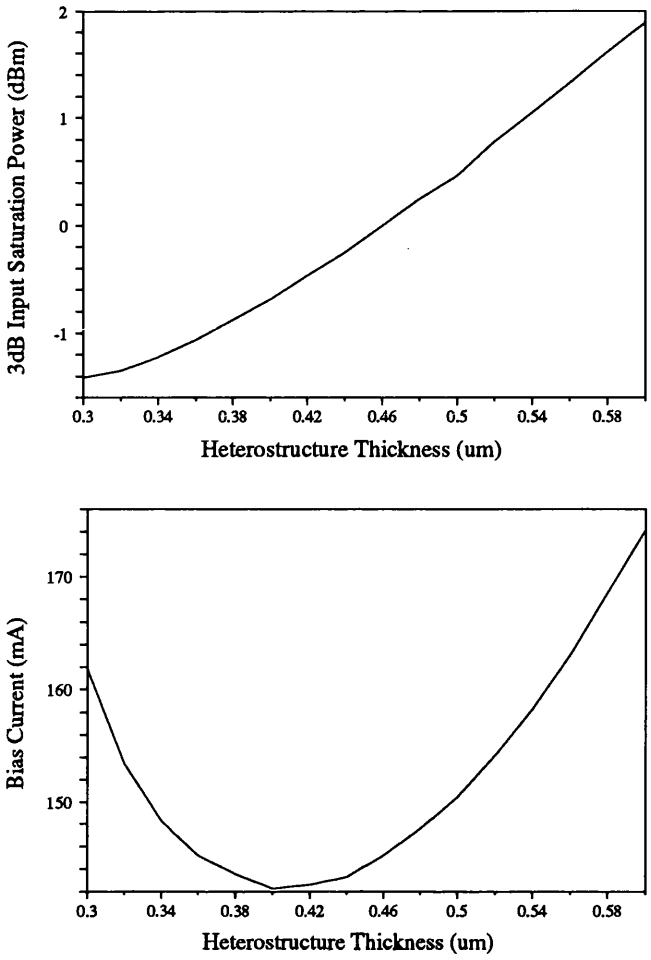

Figure 4.6 Variation of input saturation power and bias current with heterostructure thickness for peak gain of 18 dB.

(v) Device Length Variation

The relationship between saturation input power and device length obtained in this study (figure 4.7) is similar to that reported by Eisenstein et al [10].

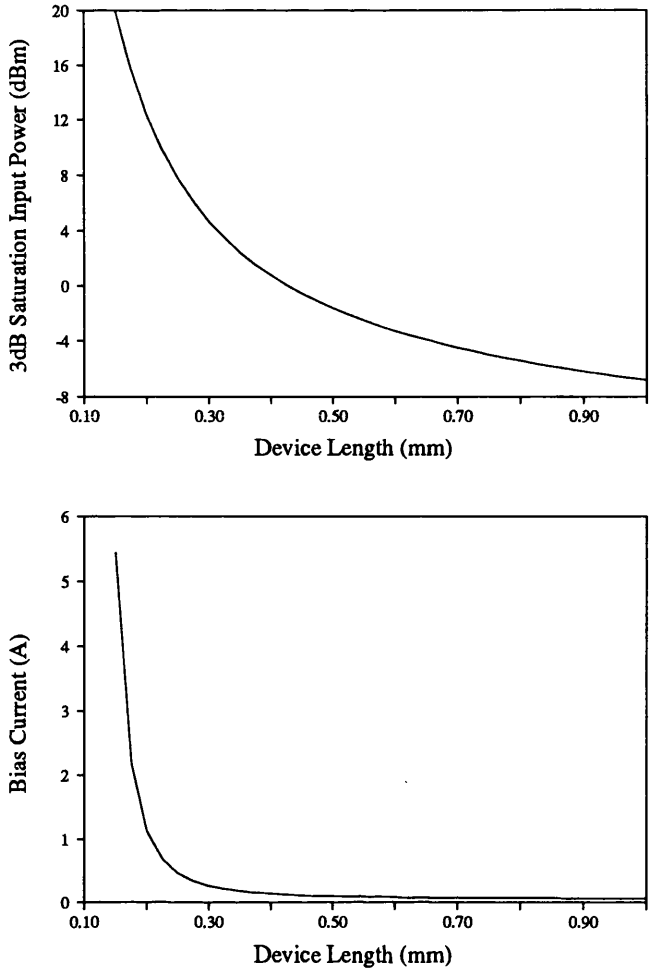

Figure 4.7 Variation of input saturation power and bias current with cavity length for a peak gain of 18 dB.

Rearranging E4.7 and substituting yields an approximate $\exp\left(\frac{X_2}{L}\right)\left[1-\exp\left(\frac{X_3}{L}\right)\right]$ dependence for $\left(\frac{n_1}{\tau_s}-\frac{n_{3dB}}{\tau_{s3dB}}\right)$. Thus the relationship between $(P_{in})_{3dB}$ and the device length has the form

$$(P_{in})_{3dB} \propto \left(\frac{L}{X_1+\alpha L}\right)\exp\left(\frac{X_2}{L}\right)\left(1-\exp\left(\frac{X_3}{L}\right)\right) \qquad \text{E4.14}$$

where

$$X_1 = gL - \ln 2 \qquad \text{E4.15a}$$

$$X_2 = \frac{gL}{g_{m1}\Gamma} \qquad \text{E4.15b}$$

$$X_3 = \frac{\ln 2}{g_{m1}\Gamma} \qquad \text{E4.15c}$$

As a result, an increase in length, whilst leading to an increase in gain, results in an exponential decrease in saturation power.

4.3.3 Gain and Saturation Power Contour Plots

It would seem from studying the above results that, to get the best saturation performance, a device must be designed with the following characteristics:

1. A low number of wells
2. Narrow wells
3. A wide ridge
4. Thick barrier layers around the quantum well region
5. A short cavity

There are, however, limitations on these parameters, not least the fact that the conditions which give high saturation power also require very high bias current levels. However, there are other constraints to the dimensions. The well-width is limited by the fact that very narrow wells are difficult to fabricate accurately, and can also have unpredictable characteristics. The ridge width is really limited to about 4 μm if multimode operation is to be avoided, and D_{opt} should be kept to a reasonable limit to keep the growth time to a reasonable length; for example 0.6 μm. A large value for D_{opt} may also cause device modulation bandwith limitations due to delays in carrier transport across the heterostructure.

Any design therefore needs to be a compromise. A single narrow well with wide ridge and thick cladding layers may need to be offset by a long cavity to obtain the required gain, if excessively high bias currents are to be avoided.

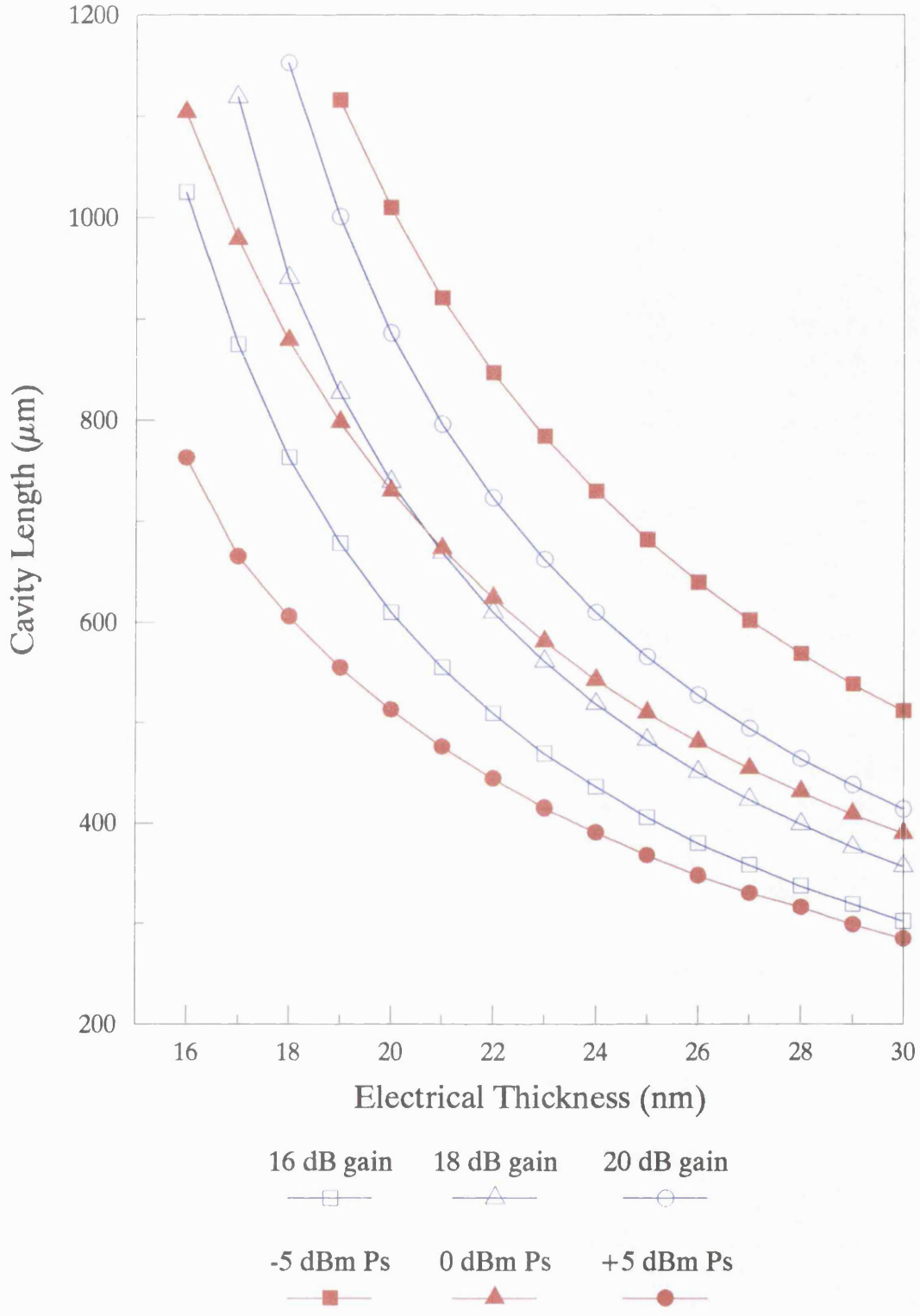

Figure 4.8 Contours of constant gain and saturation power for a device current of 150 mA plotted on axes of device length and electrical thickness. Ridge width 4 μm, heterostructure thickness 0.6 μm.

For insight into design tolerances and trends, contour plots have been drawn for gain and saturation power vs the length and electrical thickness (well width multiplied by well number). Here, the ridge width and heterostructure thickness are kept constant at 4 μm and 0.6 μm respectively. The current is also fixed, at 150 mA. On a graph of device length vs electrical thickness ($N_w d_w$), contours of constant gain and constant saturation power have been drawn, to enable the trade-off between length and thickness to be assessed.

Figure 4.8 shows such a plot for a bias current of 150mA. It may be seen that the higher gains are obtained from the longer/thicker devices, while the higher saturation powers require short/thin designs.

It may be observed from this contour plot that, for a given peak gain value, the best saturation power is obtained from the lower end of the gain contour. That is, large electrical thickness and short device length.

4.3.4 Proposal of optimum device

Using the results of the investigation described above, a design is proposed for a device having a peak gain of 18 dB, and an input saturation power of +1.9 dBm. Its dimensions are as follows: electrical thickness of 30 nm, comprising three wells of 10 nm each; ridge width 4 μm; heterostructure thickness 0.6 μm; cavity length 350 μm; total confinement factor 0.0501. The facet reflectivity is assumed negligible. The gain peak is at 1520 nm, in order for it to be compatible with future fibre systems which are expected to use this wavelength region.

Using the adapted computer model, the gain and harmonic ratio have been calculated, and the results are shown in figure 4.9. In figure 4.9(a) the steady state and small signal gains have been plotted as a function of input power. The modulation frequency is 100 MHz, the optical modulation index 70 %, and the wavelength 1520 nm. It may be observed that the reduction in saturation power due to the modulation of the spontaneous emission is very significant for the MQW device. Thus, while the steady state saturation power is very close to the design value, at +1.7 dBm, the small signal saturation power is reduced to -1.9 dBm. The peak gain is calculated to be 17.8 dB.

The harmonic ratio, defined in chapter 3, has been plotted as a function of facet input power in figure 4.9(b), with the corresponding values for a pure travelling wave bulk device of the same structure as in chapter 3. The enhancement is evident, with an improvement of the order of 12 dB being achieved below saturation.

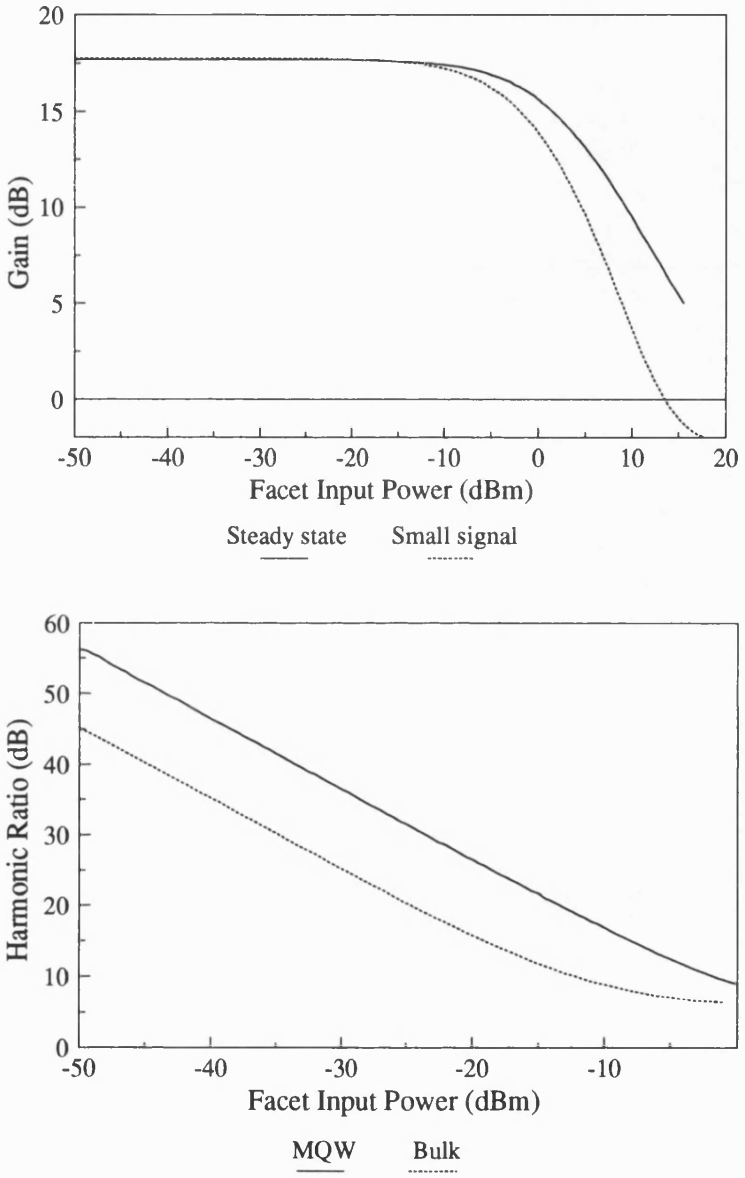

Figure 4.9 (a) Steady state and small signal gains plotted against facet input power for the MQW device. DC bias 150 mA, signal modulation 100 MHz, omi 70 %, wavelength 1520 nm. (b) Harmonic ratio plotted against facet input power for the MQW and bulk devices. Conditions as (a) except bulk amplifier bias 50 mA, wavelength 1311 nm

4.4 Verification of Theory

To test the accuracy of the adapted computer model, and of the design criteria described above, gain measurements were carried out on an MQW laser device with coated end facets, supplied by Hewlett-Packard.

The device has a SCH-RWG structure with 3 wells of 8.5 nm each, a heterostructure thickness of 0.2 μm, a 3 μm ridge, and a cavity length estimated to lie between 500 - 600 μm. Data supplied by Hewlett-Packard gives a value of 0.6 % for the facet reflectivity. For the purposes of modelling the steady state gain, these values are unchanged with the exception of the length, for which a value of 480 μm has been found to give the best fit. The confinement factor for this structure is calculated to be approximately 0.04, the change in refractive index with carrier density used by the model is -3.6×10^{-20} cm^3 [11], and a value of 15 cm^{-1} is used for the effective losses. Otherwise, all constants are as stated in table 4.1.

4.4.1 Experimental Details and Results

The gain measurements were carried out using the system depicted in figure 4.10.

The input signal is supplied by a dfb laser with an emission wavelength of 1489 nm, close to the amplifier gain peak at 1490 nm. The signal is split by a 3 dB optical coupler so that the input power can be monitored using the first optical head. The polarisation controller optimises the orientation of the light; this is particularly important where MQW devices are concerned, as their gain is very sensitive to signal polarisation. Since the optical amplifier is not packaged, the input light is guided into the facet by a fibre lens; the output light is gathered by a bulk lens to prevent large losses. The beamsplitter divides the signal once again, this time enabling the image of the facet to be observed using an infra-red camera while the gain is measured using the second optical head. The use of the camera aids in positioning the fibre and bulk lenses to ensure that the laser signal is not simply passing around or above the amplifier. The slits in front of the second optical head limit the amount of scattered light detected, and also prevent saturation of the detector.

In order to minimise the influence of the ASE on the results, the following method has been adopted. The bias currents to the laser and amplifier are pulsed, as shown in the schematic of figure 4.11, the SOA pulse being delayed with respect to that of the source. The output power thus consists of three components: the first is the laser light scattered around the amplifier; the second, where the two bias pulses coincide, is the SOA gain; the third is the spontaneous emission produced by the amplifier. The actual gain of the amplifier is then given by

$$G = \frac{\text{total output - spontaneous emission - deflected laser light}}{\text{input power}} \qquad \text{E4.16}$$

the input light being measured by the first optical head.

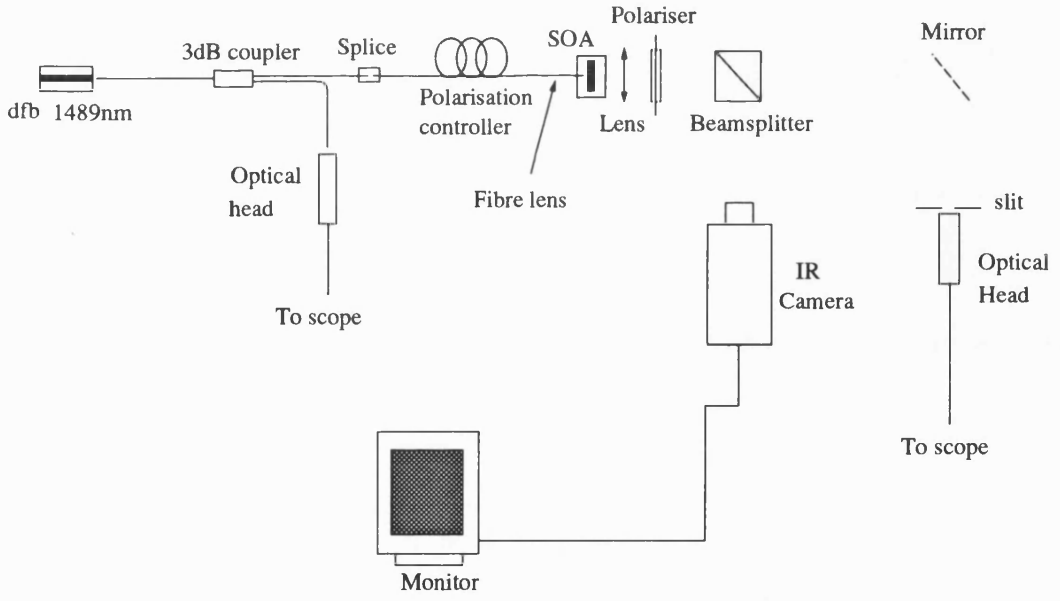

Figure 4.10 Experimental system used to measure the gain of the MQW device.

This method does not give accurate results at high input powers, where the ASE is saturated, but is more effective than a simple ratio of output power to input power, since this device generates large quantities of spontaneous emission.

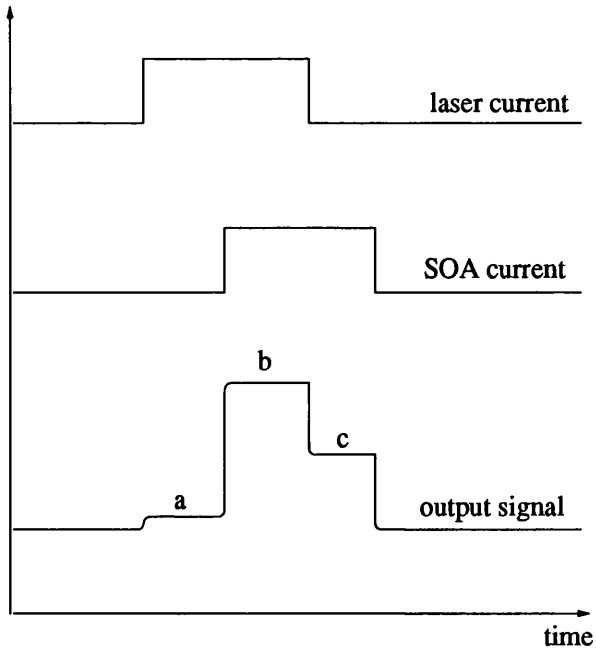

Figure 4.11 Schematic time dependence of laser bias, SOA bias pulse and output from optical head showing (a) scattered laser light, (b) SOA output and (c) spontaneous emission.

Figure 4.12 shows the dc gain of the device, compared with modelled data, for the following conditions: SOA current 90 mA, pulsewidth 1.8 ms, pulse period 18 ms, wavelength 1489 nm. Reasonable agreement is achieved. Modelling a wavelength range from 1488.8 to 1489.5 nm predicts a peak gain of 16.2 dB, and an input saturation power of -5.3 dBm for this device; it was not possible to saturate it experimentally. The gain ripple is estimated by the model to be 3 dB, indicating that the facet coatings are still not good enough.

4.4.2 Discussion

The chip gain and input saturation power of this device are both low, at 16.2 dB and -5.3 dBm respectively. This may be attributed to the structure of the device, which was designed for laser operation. Contrary to the finding that the highest saturation power is achieved using a short thick cavity, the electrical thickness is 25.5 nm, against a cavity length of approximately 500 μm. The small optical cavity, with a total heterostructure thickness of 0.2 μm, contributes to the low saturation power, and also to the strong polarisation sensitivity of the device.

These results confirm that high performance optical amplifiers need to be specially designed, and that laser structures are not generally suitable for amplification purposes.

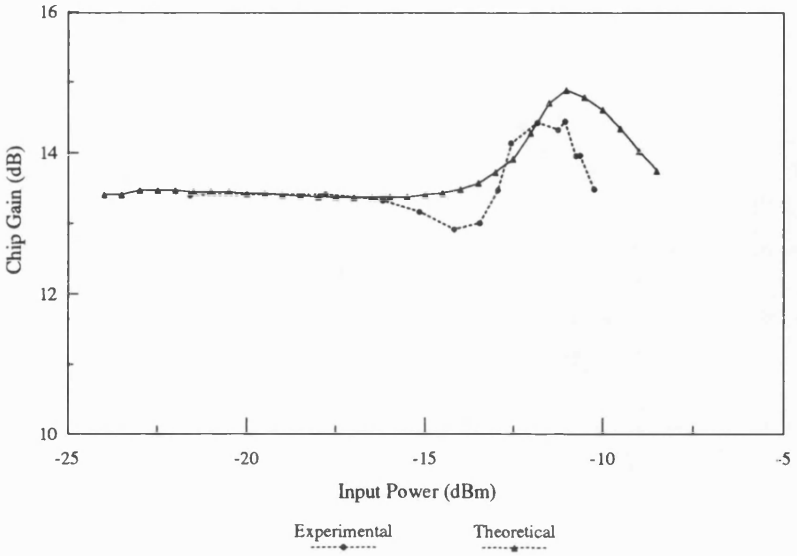

Figure 4.12 Experimental and theoretical gain of MQW device for bias current of 90 mA at a signal wavelength of 1489 nm.

4.5 Conclusions

A simple process for the design of multi-quantum-well optical amplifiers has been described. The effect of changing the physical dimensions of the cavity upon the saturation input power, and upon the bias current needed to achieve a given peak gain, has been investigated. The conditions which enable the highest saturation power to be achieved also demand high bias current injection to provide the required value of gain. The use of contour plots enables the compromise between gain and saturation power to be made effectively by the adjustment of the cavity length and electrical thickness of the device, and shows that a device with high saturation power requires a short, thick structure.

Using this information, a design has been proposed for a high saturation power device, having 18 dB peak chip gain and +19 dBm input saturation power. Modelled results indicate a peak gain of 17.8 dB, and steady state and small signal input saturation powers

of +1.7 dBm and -1.9 dBm respectively. The proposed MQW device has a harmonic performance far superior to that of the bulk amplifier described in chapter 3, with 12 dB improvement in HR being achieved.

Measurement of the gain of an MQW laser with AR coated facets confirms that a large optical volume and short cavity are necessary for high saturation power, also that a thick electrical region is required for high gain. It may be concluded from this that laser structures in general are not suitable for the fabrication of optical amplifiers, and that specially designed devices are required for low distortion operation.

Constant	Description	Value
W	Ridge width	4 μm
d_w	Well thickness	8 nm
N_w	Well number	4
D_{opt}	Optical thickness	0.6 μm
L	Cavity length	500 μm
R_1, R_2	Facet reflectivity	0
A	Nonradiative recombination constant	10^{8} s^{-1}
B	Bimolecular recombination constant	10^{-10} cm^{3} s^{-1}
C	Auger recombination constant	1.3×10^{-28} cm^{6} s^{-1}
α	Effective optical losses	15 cm^{-1}
g_{m1}	Material gain constant	675 cm^{-1}
g_{m2}	Material gain constant	236 C cm^{-2} s^{-1}
β	Spontaneous coupling coefficient	2×10^{-5}

Table 4.1 Constants used in the numerical analysis of the design process.

4.6 References

1. G Eisenstein, U Koren, G Raybon, J M Wiesenfeld, M Wegener: "Gain and gain saturation spectra in 1.5μm multiple quantum well optical amplifiers", *Appl. Phys. Lett.* **57**, pp. 333-335, 1990.

2. M Bagley, G Sherlock, D M Cooper, L D Westbrook, D J Elton, H J Wickes, P C Spurdens, W J Devlin: "Broadband operation of InGaAsP-InGaAs GRIN-SC-MQW BH amplifiers with 115 mW output power", *Electron. Lett.* **26**, pp. 512-513, 1990.

3. K Magari, S Kondo, H Yasaka, Y Noguchi, T Kataoka, O Mikami: "A high gain GRIN-SCH MQW optical semiconductor laser amplifier", *IEEE Photon. Technol. Lett.* **2**, pp. 792-793, 1990.

4. G Eisenstein, U Koren, G Raybon, T L Koch, J M Wiesenfeld, M Wegener, R S Tucker, B I Miller: "Large and small-signal gain characteristics of 1.5 μm multiple quantum well optical amplifiers", *Appl. Phys. Lett.* **56**, pp. 1201-1203, 1990.

5. G Eisenstein, J M Wiesenfeld, M Wegener, G Sucha, D S Chemla, S Weiss, G Raybon, U Koren: "Ultrafast gain dynamics in 1.5 μm multiple quantum well optical amplifiers", *Appl. Phys. Lett.* **58**, pp. 158-160, 1991.

6. J E A Whiteaway, G H B Thompson, P D Greene, R W Glew: "Logarithmic gain/current-density characteristic of InGaAs/InGaAlAs/InP multi-quantum-well separate-confinement-heterostructure lasers", *Electron. Lett.* **27**, pp. 340-342, 1991.

7. P D Greene, J E A Whiteaway, G D Henshall, R W Glew, C M Lowney, B Bhumbra, D J Moule: "Optimisation and comparison of InP-based quantum well lasers incorporating InGaAlAs and InGaAsP alloys", *Institute of Physics Conference Series* **112**, pp. 555-560, 1990.

8. P W A McIlroy, A Kurobe, Y Uematsu: "Analysis and application of theoretical gain curves to the design of multi-quantum-well lasers", *IEEE J. Quantum Electron.* **21**, pp. 1958-1963, 1985.

9. H Kawaguchi: "Absorptive and dispersive bistability in semiconductor injection lasers", *Opt. Quantum Electron.* **19**, pp. S1-S36, 1987.

10. G Eisenstein, N Tessler, U Koren, J M Wiesenfeld, G Raybon, C A Burrus: "Length dependence of the saturation characteristics in 1.5-μm multiple quantum well optical amplifiers", *IEEE Photon. Technol. Lett.* **2**, pp. 790-791, 1990.

11. J Jacquet, P Brosson, A Olivier, A Perales, A Bodere, D Leclerc: "Carrier-induced differential refractive index in GaInAsP-GaInAs separate confinement multi-quantum well lasers", *IEEE Photon. Technol. Lett.* **2**, pp. 620-622, 1990.

5

Reducing Signal Distortion Using Bias Current Feedback

This chapter proposes a novel method of reducing analogue signal distortion, using an electrical feedback circuit. The carrier density modulation may be detected through fluctuations in the terminal voltage and, with the use of a negative feedback loop, reduced in depth. Since the carrier density modulation is less deep at low input powers and high modulation frequencies, the signal distortion is lower, and the feedback signal is smaller. This does, however, mean that the response of the electronics will only need to be as fast as the carrier lifetime, of the order of 3 ns. Mathematical analysis, and theoretical results from a modified form of the computer model described in chapter 3, predict significant improvement in harmonic performance using this method. Specifically, it is demonstrated that the rf gain may be increased, due to an enhancement of 3.25 dB in input saturation power, the phase distortion reduced by up to three orders of magnitude, and the HR raised by more than 15 dB.

5.1 Statement of Problem and Proposal of Solution

There are two problems to be overcome before semiconductor optical amplifiers can achieve widespread use in analogue amplitude modulated systems; these are the effective reduction in gain and saturation power experienced by the device, and the relatively high levels of signal distortion introduced into the system. Both effects are caused by the

deep modulation of the carrier concentration, and therefore of the cavity gain and spontaneous emission, by the modulated input signal. Simply stated, the solution is to vary the rate of carrier injection, and thus to maintain the carrier concentration at an approximately constant level. The result of this is expected to be an increase in input saturation power, and a decrease in signal distortion.

The carrier density modulation may be detected through the terminal voltage, which represents the conditions inside the cavity [1-4]. Delaying the voltage fluctuations with respect to the signal, and adding them to the dc bias in such a way that the feedback signal destructively interferes with the voltage at the terminals of the device, reduces the depth of modulation of the carrier concentration. Modulation of the bias current has previously been used to reduce intermodulation distortion in multichannel systems [5], but in the system proposed here the amplifier provides its own modulation signal.

In the next section, the approximate magnitude of the terminal voltage fluctuations is calculated, following which the changes to the small signal computer model are detailed. The theoretical effect of the feedback circuit on the time-dependent response of the device is described, along with analysis of the increase in gain and harmonic ratio expected. Finally, theoretical gain and distortion figures are presented as confirmation of the benefits of this system. Experimental verification is given in chapter 6.

5.2 Calculation of Terminal Voltage

The calculation of the terminal voltage of an optical amplifier, and the fluctuations due to a modulated input signal, follows the method outlined in reference [1]. The terminal voltage of an SOA may be calculated from:

$$U_F = \frac{1}{q} \cdot (E_{FC} + E_{FV} + E_g) \qquad \text{E5.1}$$

where q is electronic charge, E_g is the bandgap of the material, and E_{FC} and E_{FV} are the quasi-Fermi energies measured from the edges of the conduction and valence bands respectively. Thus the expression inside the brackets gives the quasi-Fermi level separation, which is calculated using the electron and hole effective masses for InP [6].

The variation of the terminal voltage is calculated using values of carrier concentration provided by the computer model; sample results are shown in figure 5.1. Here, the change in junction voltage due to a steady state optical signal has been plotted as a function of the fibre input power, for a bias current of 50 mA. The dark junction voltage at this current is calculated to be 975.16 mV, corresponding to a carrier concentration of 1.606×10^{18} cm^{-3}. For a device having a typical diode series resistance of approximately 3 Ω, the dark terminal voltage will be approximately 1.125 V under these conditions.

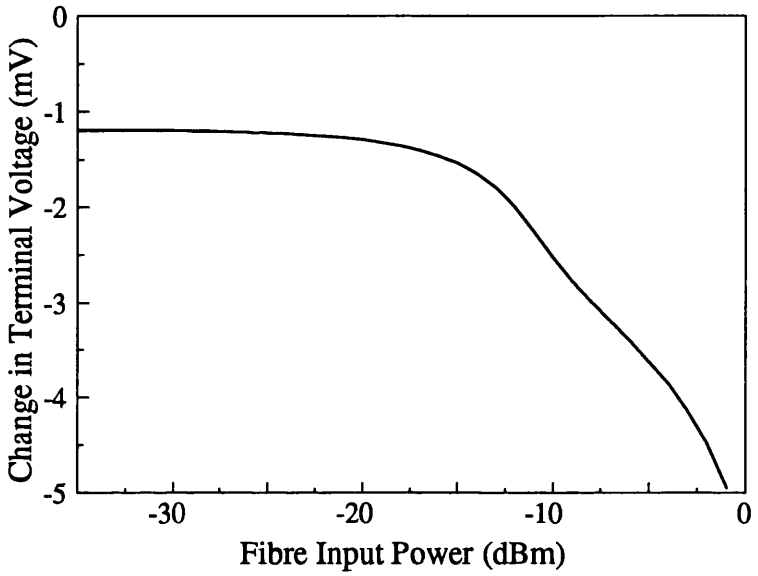

Figure 5.1 Calculated change in terminal voltage due to optical signal. Bias current 50 mA, 1311 nm.

It may be observed from figure 5.1 that there is an initial drop of just over 1 mV when the optical input signal is applied, following which the terminal voltage remains approximately constant until the device begins to saturate and the carriers are depleted. The effect of Fabry-Perot ripple on the cavity gain and carrier concentration may be seen in this plot.

If the modulation depth of the terminal voltage is to be calculated, the small signal variation of voltage with input power must be known; this may be calculated using a simple small signal equivalent circuit for the amplifier [1], as shown in figure 5.2.

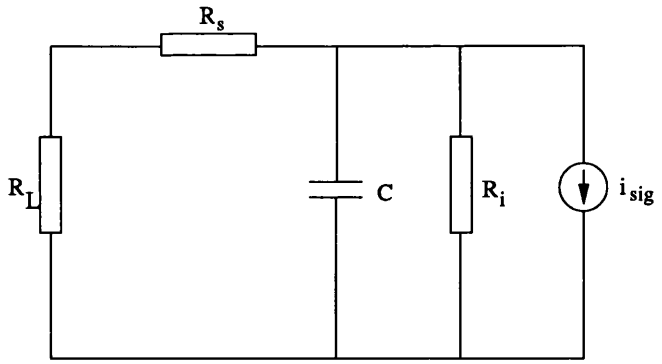

Figure 5.2 Small signal equivalent circuit for optical amplifier

Using this representation, the magnitude of the terminal voltage variation across a load resistance of R_L, due to a small signal modulated optical input, may be calculated from [1]:

$$\frac{u}{P} = R_i\, R_L\, \frac{i_{sig}}{P}\, \frac{\sqrt{(R_i+R_L+R_s)^2 + (\omega R_i C(R_L+R_s))^2}}{(R_i+R_L+R_s)^2 + (\omega R_i C(R_L+R_s))^2} \qquad \text{E5.2}$$

Here, P is the small signal input power, R_i is the differential diode resistance of the amplifier, i_{sig} is the small signal photocurrent, R_s is the diode series resistance, ω is the angular frequency of modulation and C is the diffusion capacitance. These parameters are calculated according to the method detailed in reference [1]. The last term on the right hand side of E5.2 represents a low pass filter function, and its effect can be seen in figure 5.3, which shows the calculated peak to peak voltage ripple as a function of modulation frequency. Two fibre input powers are considered, one above and one below saturation. The voltage ripple increases with increasing input power, and decreases with increasing modulation frequency. This is consistent with the behaviour of the signal distortion as reported in chapter 3. The limiting effect of the carrier lifetime may be observed from this plot; the bandwidth of an amplifier-detector would be limited to a few hundred megahertz even for high input powers.

Since the feedback signal originates in the terminal voltage ripple, it may be inferred that the feedback method will be less effective at high frequencies. This is in fact the

case, but under these conditions the signal distortion is also low, and so less electrical feedback is needed. This method is primarily designed to extend the usable bandwidth of the device to lower frequencies.

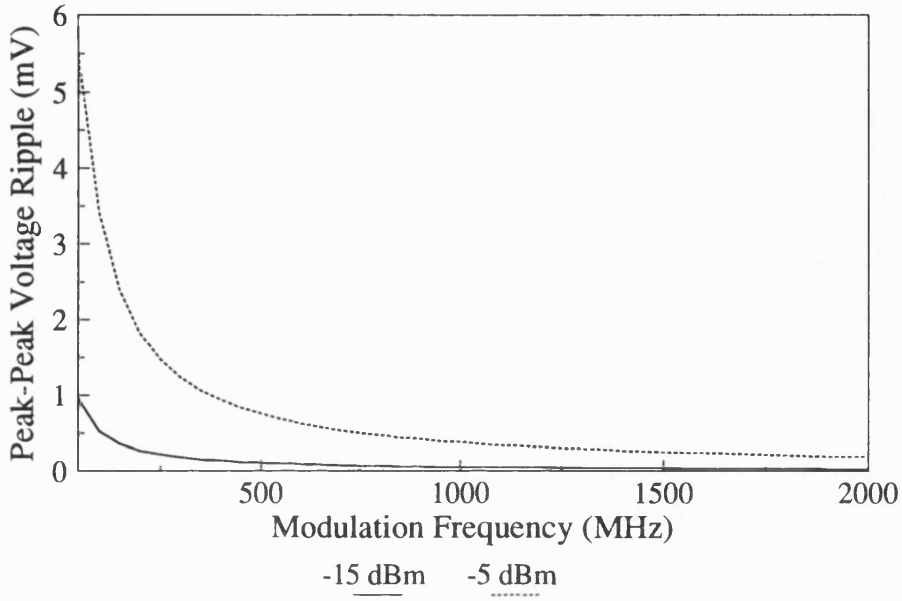

Figure 5.3 Calculated variation of depth of photovoltage ripple with modulation frequency. 50 mA, 70 % modulation, 1311 nm.

5.3 Theoretical Analysis of Feedback

5.3.1 Changes to the Model

Although the feedback signal is in reality generated by the terminal voltage, for ease of computation the theoretical model feeds back the value of carrier density modulation. The carrier density fluctuations are monitored, and three constants quantified. These are n_{2f}, the maximum value of carrier concentration, n_{1f}, the minimum value and n_{xf}, the average value. The calculation is modified by the addition of a feedback term to the expression for $\frac{j_a}{qd}$ in the rate equation:

$$\frac{j_a'}{qd} = \frac{j_a}{qd}\left(1 - 100K\left(\frac{n - n_{xf}}{n_{xf}}\right)\right) \qquad \text{E5.3}$$

where K is the feedback variable. The factor of 100 is used to limit the value of K to a value between 0 and 1.

5.3.2 Mathematical Analysis

The type of feedback considered is ac-coupled, that is the dc drop in terminal voltage due to the application of the input signal is filtered out before the feedback loop. Thus the addition of the feedback signal does not compensate for carrier depletion due to the average input signal, but is designed to reduce the magnitude of the carrier density ripple due to the input signal modulation.

Mathematical analyses of the effect of bias current feedback upon the gain and harmonic ratio of the device demonstrate the beneficial effect of this method.

With the application of ac coupled feedback, the rf device gain may be shown to be:

$$g = a_1 \left[\frac{n_1 \left(1 + K \left(\frac{(n_{xf} - n_0)}{n_{xf}} \right) \right) - n_0}{1 + K \left(\frac{n_1}{n_{xf}} \right) + \frac{P_{av}}{\Gamma P_{sat}}} \right] \qquad \text{E5.4}$$

Comparing this with the conventional gain expression, E2.7, the increase in modulated gain due to feedback may be clearly seen. At low input powers, where n_x is not strongly depleted, the feedback terms are small; when the device begins to saturate, greatly reducing n_x, the feedback terms begin to dominate the gain. Since the numerator feedback term is larger than that in the denominator by a factor of $(n_x - n_0)$, this gives an increase in saturated gain.

The expression for harmonic ratio is modified by the addition of feedback to become:

$$\frac{P_y}{P_z} = \frac{2 \left(\Gamma P_{sat} \left(1 + K \frac{n_1}{n_{xf}} \right) + P_x \right)}{P_y} \qquad \text{E5.5}$$

By comparing E5.5 with E3.23, it may be observed that the HR will always increase, provided the feedback is negative (ie K is positive). It may also be seen that the increase is dependent upon the values of K (amount of feedback) and n_x (level of carrier depletion).

It can be shown that dc-coupled feedback, which raises the average value of n, as well as reducing its modulation, gives a larger increase in rf gain. However, the improvement in HR is no greater than for the case where the feedback is ac-coupled, and a large increase in dc bias current would be generated by the feedback signal.

5.4 Theoretical Results

5.4.1 Time Dependence

The effect of bias current feedback upon the bias current, carrier concentration and output power can be seen in the theoretical plot of figure 5.4. The conditions are as follows: SOA bias current 50 mA; average fibre input power -5 dBm; modulation frequency 100 MHz; modulation index 70 %; wavelength 1311 nm; feedback variable 1. Before the feedback is switched in, it may be observed that the sinusoidally modulated input signal causes modulation of the carrier density, and that this modulation is almost completely out of phase with the input power. The harmonic distortion of the output power is demonstrated by the flattened shape, the phase distortion by the phase shift between the input and output signals. When the feedback signal is switched in, at t = 30 ns, a sinusoid is added to the bias current, and the modulation on the carrier density is much reduced and forced into exact antiphase with the input signal. The output power is increased and brought into phase with the input; its harmonic distortion is visibly reduced.

5.4.2 Input Power Dependence

The effect of bias current feedback on the rf gain, and on the phase and harmonic distortion, has been calculated using the computer model, modified as described in section 5.3.1.

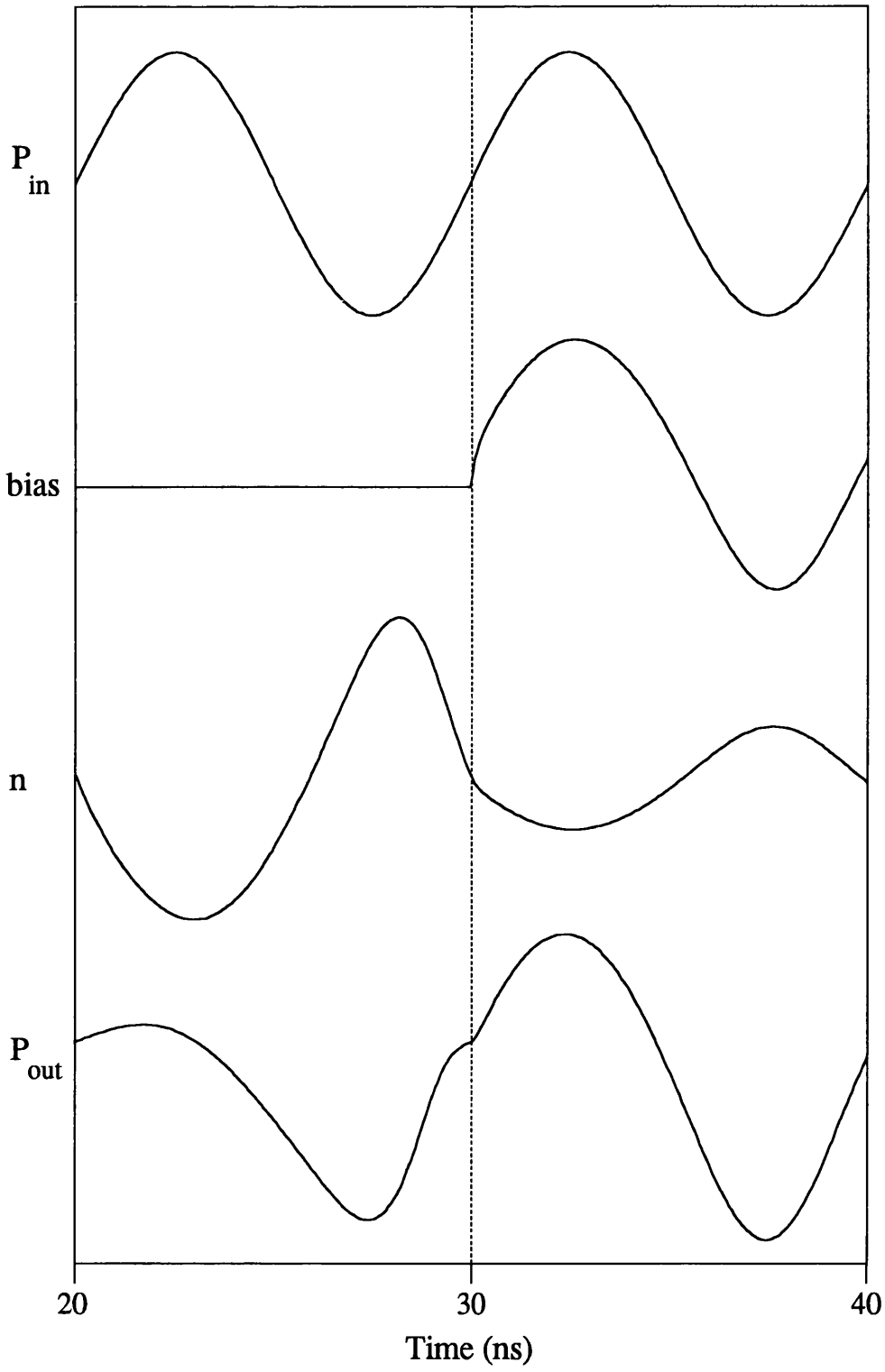

Figure 5.4 Calculated time dependence of input power, bias current, carrier concentration and output power, showing the effect of adding bias current feedback. DC Bias current 50 mA, fibre input power -5 dBm, modulation frequency 100 MHz, omi 70 %, 1311 nm, K=1.

Figure 5.5(a) shows the rf gain, with and without feedback, as a function of input power for conditions as in figure 5.4. At low input powers, there is little change in the gain due to feedback, but at high powers the gain is increased, due to the shift of the gain curve towards higher powers caused by an effective increase of 3.25 dB in the input saturation power.

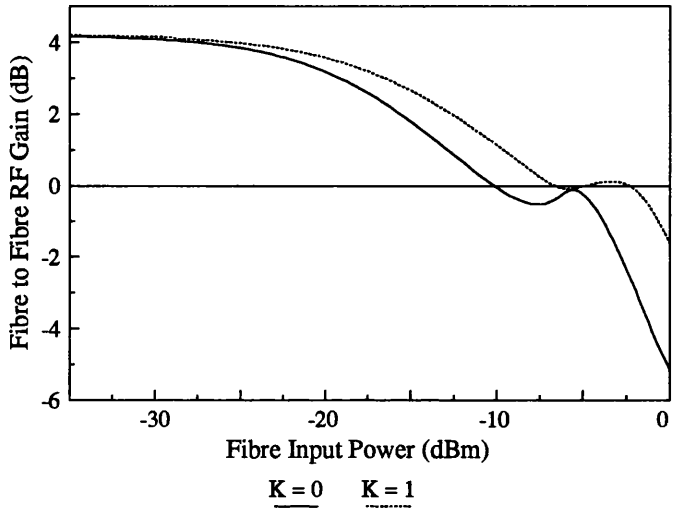

Figure 5.5(a) Input power dependence of rf gain with and without feedback. Bias current 50 mA, modulation frequency 100 MHz, omi 70 %, 1311.23 nm.

The phase distortion is plotted in figure 5.5(b). The improvement is immediately evident, as is the shift towards higher powers.

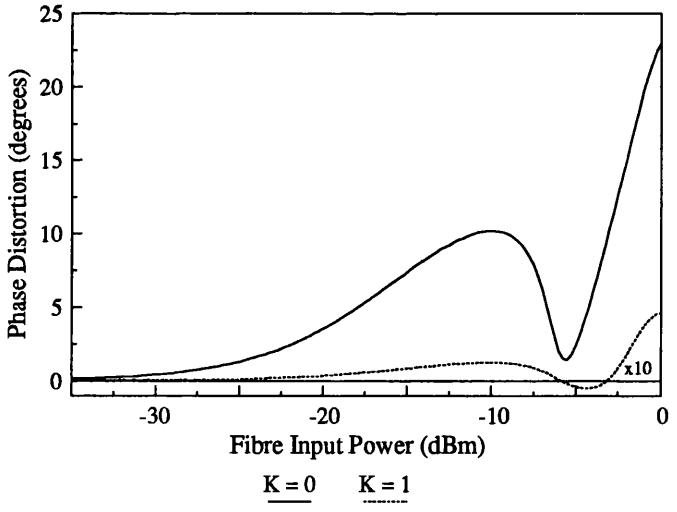

Figure 5.5(b) Input power dependence of phase distortion with and without feedback. Conditions as figure 5.5(a).

The harmonic ratio, as shown in figure 5.5(c), shows an increase of 16 dB at lower powers. The effective increase in input saturation power may be seen in the shift of the curve to higher powers with respect to the dc curve.

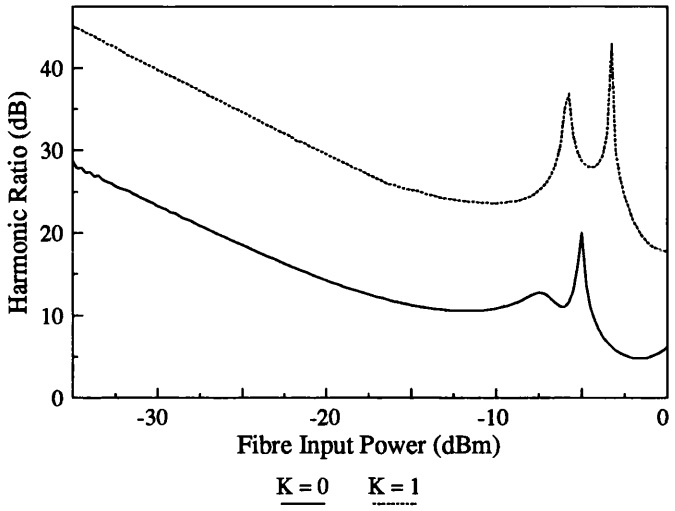

Figure 5.5(c) Input power dependence of harmonic ratio with and without feedback. Conditions as figure 5.5(a).

5.4.3 Modulation Frequency Dependence

The frequency dependences of the rf gain, phase and harmonic distortion have been plotted, with and without feedback, in figure 5.6. The facet reflectivity has been reduced to zero for these plots. Two values of input power have been considered, one below saturation, and one at saturation. A value of 0.2 has been used for K to show the trends.

From figure 5.6(a), it may be seen that the effect of feedback on the rf gain is less at low powers and high frequencies. The increase in gain obtained at saturation is as much as 1.5 dB.

The effect of the bias current feedback upon the phase distortion is to remove entirely the peak seen at low frequencies. As the frequency increases, and the carrier density modulation decreases in depth, the phase distortion with feedback approaches that without. The use of a value of 1 for K results in a totally flat frequency response for phase distortion.

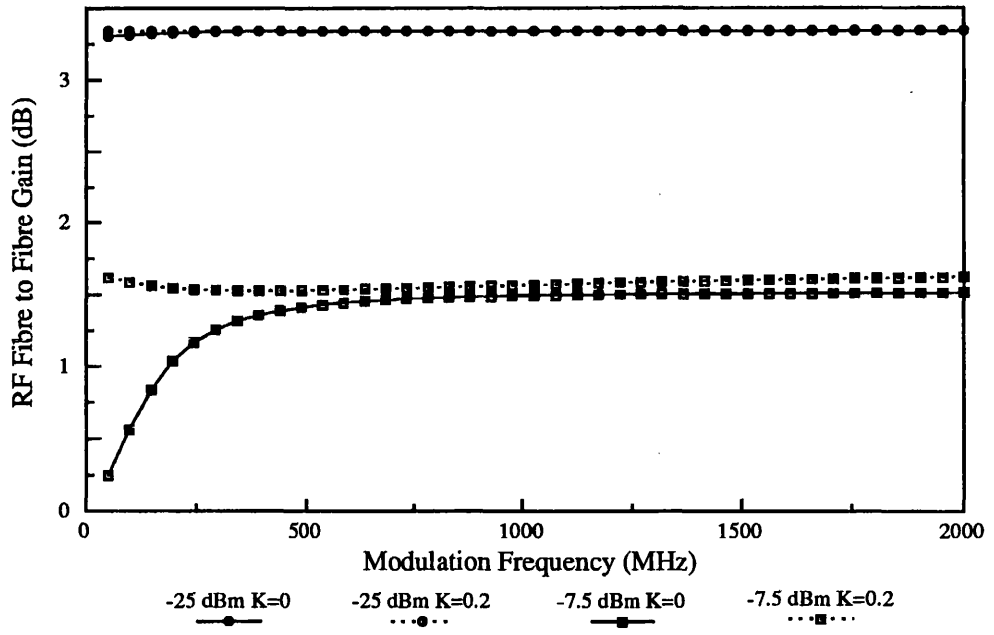

Figure 5.6(a) Modulation frequency dependence of rf gain, with and without feedback, for fibre input powers of -25 dBm and -7.5 dBm. Bias current 50 mA, omi 0.7, 1311 nm, zero facet reflectivity.

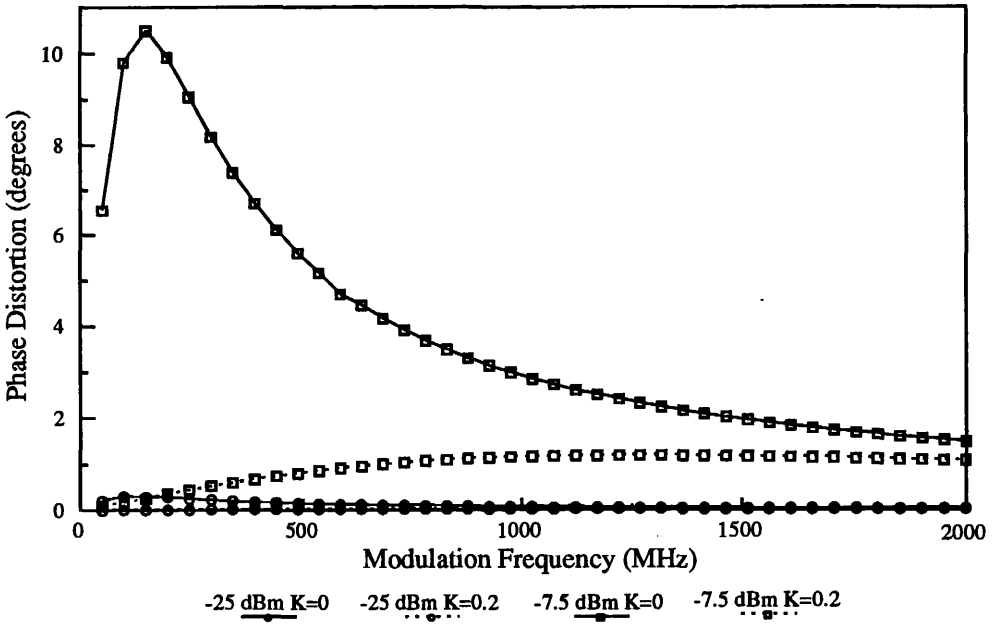

Figure 5.6(b) Modulation frequency dependence of phase distortion, with and without feedback, for fibre input powers of -25 dBm and -7.5 dBm. Conditions as figure 5.6(a).

The harmonic ratio is plotted as a function of modulation frequency in figure 5.6(c), for the same conditions as before. Again, the greatest increase occurs at low frequencies.

Greater improvement is observed at low input powers. This is due to the greater value of P_x at high input powers, which reduces the effect of the feedback term in the numerator, although n_x is smaller in this case.

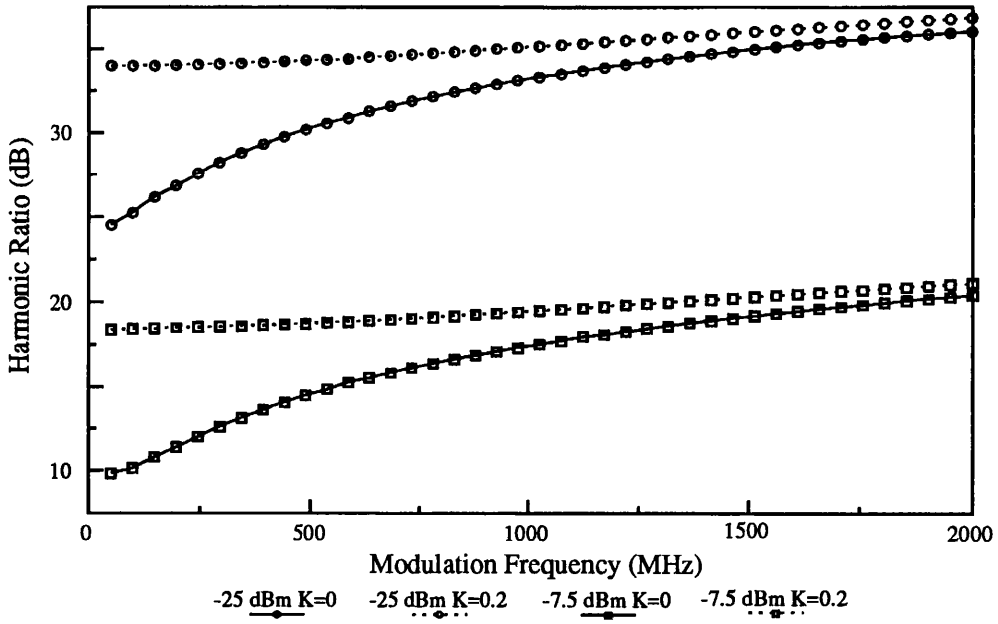

Figure 5.6(c) Modulation frequency dependence of harmonic ratio, with and without feedback, for fibre input powers of -25 dBm and -7.5 dBm. Conditions as figure 5.6(a).

5.4.4 K Dependence

To quantify the achievable enhancement in performance, the rf gain and the distortion have been investigated with varying values of feedback variable. In figure 5.7(a), the improvement in gain has been plotted as a function of K for the values of average input power used in figure 5.6. It may be seen that the increase in gain at the lower value of input power saturates almost immediately at less than 0.1 dB, while for -7.5 dBm input power the gain is still increasing at K=1. The greater increase in gain experienced for the higher input power is due to the larger depth of carrier density modulation, which produces a larger feedback signal. The improvement saturates at high values of K because of the way in which the feedback is applied. Since the device produces its own feedback signal, proportional to the depth of modulation of the carrier density, the magnitude of the feedback signal decreases as the carrier density modulation decreases. Because of

this, the carrier concentration modulation depth will approach zero, but never reach it. It does mean, however, that the extra SOA bias current required to implement the feedback technique will not be large (see figure 5.8).

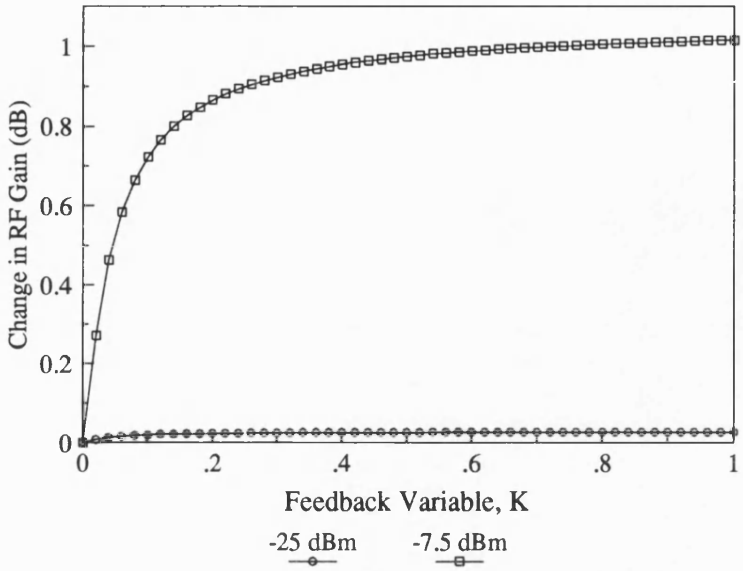

Figure 5.7(a) Change in rf gain as a function of feedback variable for fibre input powers of -25 dBm and -7.5 dBm. Bias current 50 mA, modulation frequency 100 MHz, omi 0.7, 1311 nm, zero facet reflectivity.

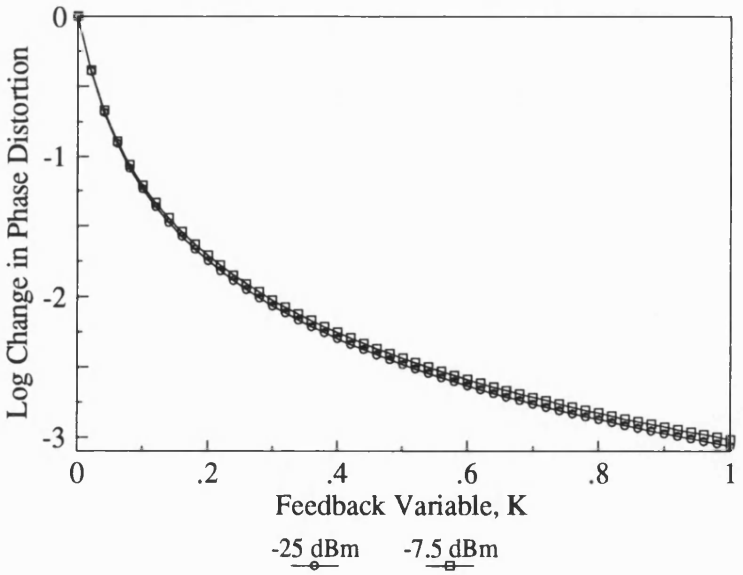

Figure 5.7(b) Log of phase distortion as a function of feedback variable for fibre input powers of -25 dBm and -7.5 dBm. Conditions as figure 5.7(a).

The log of the change in phase distortion has been plotted in figure 5.7(b), since the numbers involved are so small. The improvement obtained is very significant, up to three orders of magnitude. It is interesting to note that the reduction obtained is approximately equal for the two values of input power.

Figure 5.7(c) shows the change in harmonic ratio as a function of feedback variable, for the same two values of input power. Again, it may be seen that the greatest enhancement is obtained at lower input powers, for the reason explained earlier. Again the improvement may be seen to be levelling off at high values of K.

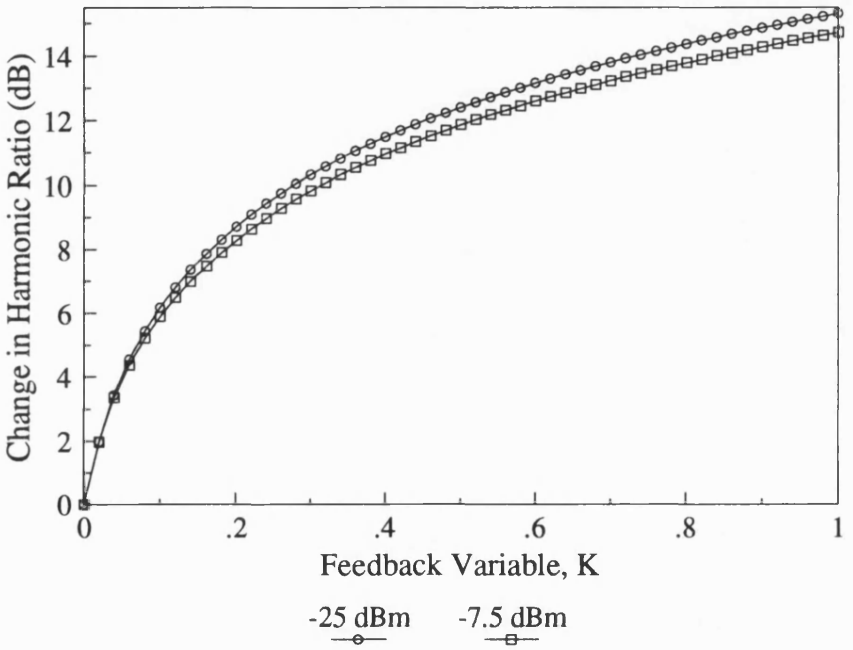

Figure 5.7(c) Change in harmonic ratio as a function of feedback variable for fibre input powers of -25 dBm and -7.5 dBm. Conditions as figure 5.7(a).

To demonstrate that this method does not require the injection of large bias currents, the peak injection current has been calculated as a function of K; this is plotted in figure 5.8. It may be seen that an increase of less than 8% in bias current is required for $K = 1$ at -7.5 dBm input.

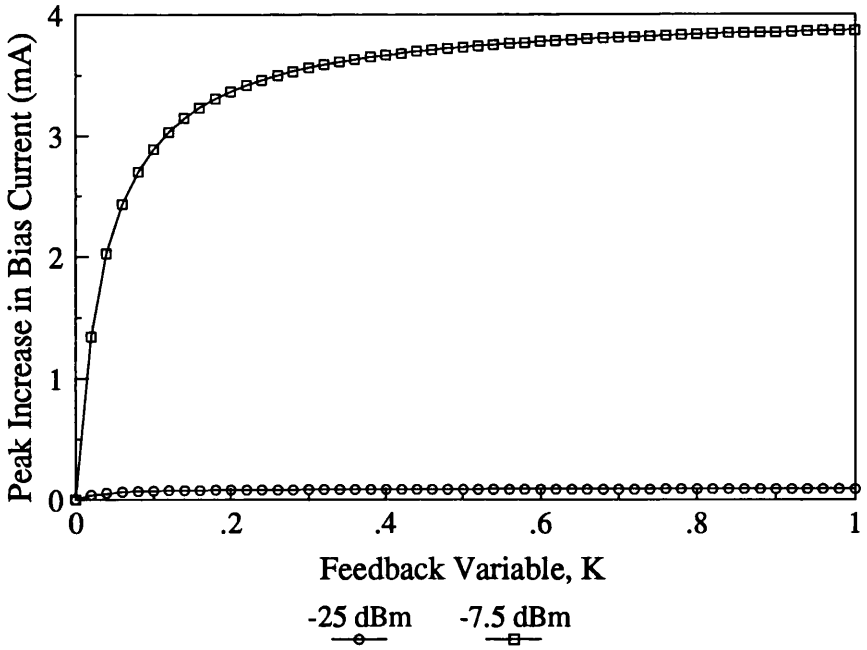

Figure 5.8 Dependence of peak bias current upon feedback variable for fibre input powers of -25 dBm and -7.5 dBm. DC bias current 50 mA, modulation frequency 100 MHz, omi 0.7, 1311 nm, zero facet reflectivity.

5.5 Conclusions

A method of improving the performance of an optical amplifier in an analogue amplitude modulated system has been proposed. This scheme uses an electronic feedback loop to monitor the carrier density modulation via the terminal voltage, and to provide negative feedback to compensate for the modulation of the carrier density. Since the modulation of the carrier concentration is less at high modulation frequencies, the loop will be less effective here; the purpose of this method is to extend the bandwidth of the device to lower frequencies. Reducing the carrier density modulation is expected to lead to higher input saturation power, and therefore higher rf gain, and lower phase and harmonic distortion.

Mathematical analysis of the feedback method confirms that there will always be an improvement in device performance, provided the feedback is always negative. Theoretical data from the computer model, modified to take account of the effect of feedback, predicts typical increases of 3.25 dB in saturation power, and of more than 15 dB in HR, and decreases of up to three orders of magnitude in phase distortion.

5.6 References

1. M Gustavsson, A Karlsson, L Thylen: "Traveling wave semiconductor laser amplifier detectors", *J. Lightwave Technol.* **8**, pp. 610-617, 1990.
2. V V Luc, P G Eliseev, M A Manko, G T Mikaelian: "Electrical diagnostics of the amplifier operation and a feasibility of signal registration on the basis of the voltage saturation effect in junction laser diodes", *IEEE J. Quantum Electron.* **19**, pp. 1080-1083, 1983.
3. R M Fortenberry, A J Lowery, R S Tucker: "Up to 16 dB improvement in detected voltage using two-section semiconductor optical amplifier", *Electron. Lett.* **28**, pp. 474-476, 1992.
4. K L Hall, E P Ippen, G Eisenstein: "Bias-lead monitoring of ultrafast nonlinearities in InGaAsP diode laser amplifiers", *Appl. Phys. Lett* **57**, pp. 129-131, 1990.
5. A A M Saleh, R M Jopson, T E Darcie: "Compensation of nonlinearity in semiconductor optical amplifiers", *Electron. Lett.* **24**, pp. 950-952, 1988.
6. S M Sze "Physics of Semiconductor Devices", pub Wiley, (New York 1981).

6

Experimental Verification of Feedback Technique

The feedback technique proposed in the previous chapter has been investigated experimentally. The fluctuations in amplifier terminal voltage, due to an optical signal, are easily detectable, and slightly larger than those calculated in the previous chapter. Direct modulation of the amplifier bias current is shown to reduce harmonic distortion by up to 17.75 dB, and to increase the modulated gain by up to 2.8 dB. A simple, non-optimised feedback loop has been found to reduce harmonic distortion by up to 18 dB, and also to reduce the noise power at the signal frequency by up to 15 dB. The rf gain may be increased by up to 5.5 dB. An RF resonance signal at 2.37 GHz is present in the feedback loop, and the presence of feedback in the loop has been confirmed.

6.1 Introduction

Chapter 5 proposed a novel method of reducing the modulation of the carrier density, and thus decreasing signal distortion, by means of an electrical feedback loop. Theoretical analysis of the technique suggests that this method will have a beneficial effect on the performance of the device.

An experimental investigation of the influence of bias current feedback will be described in this chapter. Firstly, measurements of the photovoltage are described, under various experimental conditions. Following this, results are presented to demonstrate the

beneficial effect of direct modulation of the bias current on the harmonic performance of the device. Finally, the use of an electrical feedback loop is shown to reduce harmonic distortion, and also noise.

6.2 Measurement of Terminal Voltage

6.2.1 Experimental Details and Results

The system used to measure the photovoltage is shown in figure 6.1. The laser is a multimode diode laser, with its gain peak around 1300 nm, pulsed to allow measurement of the change in SOA voltage due to the optical input signal. The diode in the laser circuit is for reverse-bias protection, the 47 Ω resistor for impedance matching; the pulses are negative with respect to earth. The SOA is dc biased using a current source, and its temperature automatically controlled by an ILX Lightwave LDT-5910 temperature controller unit; the two photodiodes monitor input and output power.

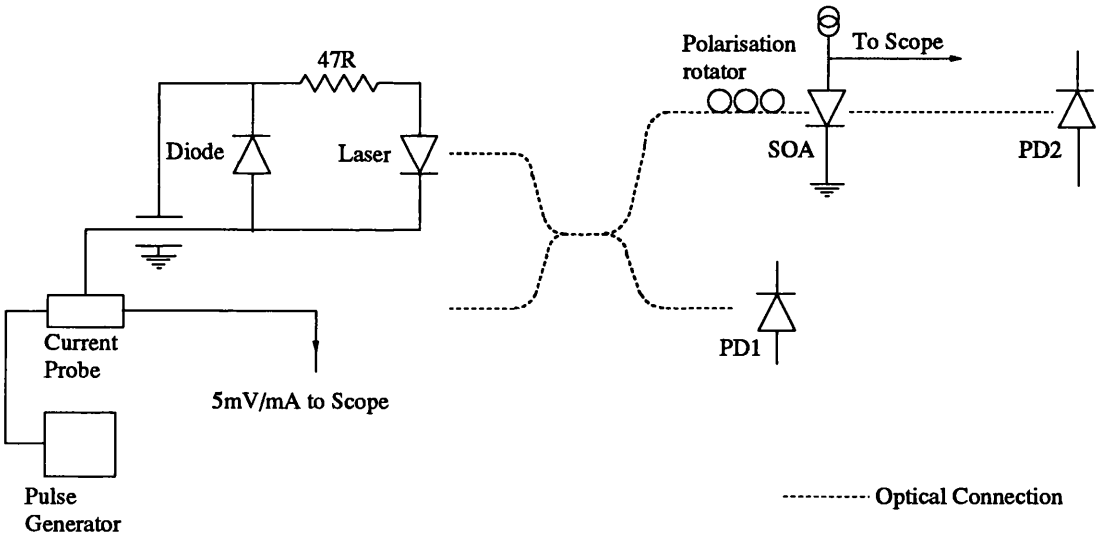

Figure 6.1 Experimental system for the measurement of the SOA photovoltage.

Figure 6.2 shows the dark current-voltage characteristic of the SOA. The voltage was measured using a Keithley 177 digital multimeter. The expected diode relationship is obtained; there is good agreement between the value of 1.14 V measured at 50 mA and the value of 1.125 V calculated in chapter 5.

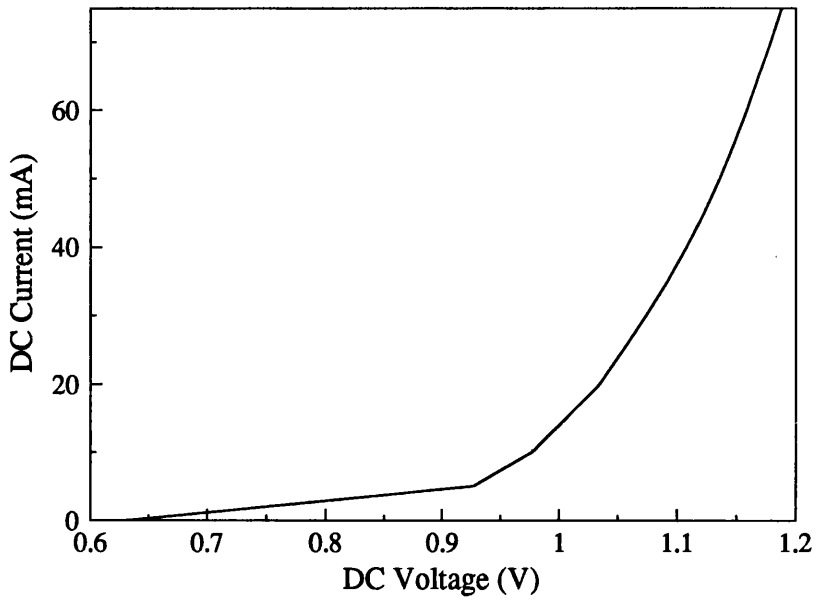

Figure 6.2 Dark current-voltage characteristic.

The change in terminal voltage due to an optical input signal has been plotted in figure 6.3, for a bias current of 50 mA. The pulse width and period are as before, and the voltage is measured into 50 Ω. The voltage variation is in good general agreement with that calculated in chapter 5.

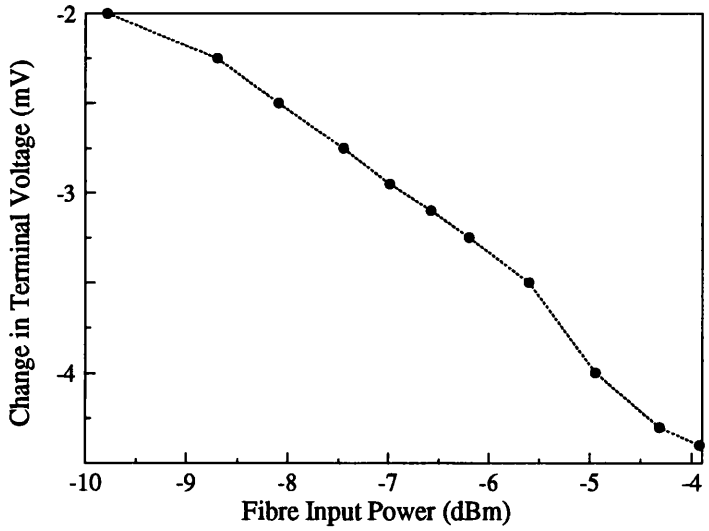

Figure 6.3 Change in terminal voltage as a function of fibre input power for 50 mA dc bias.

Figure 6.4 shows the photovoltage vs amplifier dc bias. The change of sign observed at a bias current of approximately 33 mA occurs at transparency [1,2], as the amplifier switches from absorption to emission. Three values of fibre input power are considered; -8.7 dBm, -5.1 dBm, and -2.73 dBm. The inset, which magnifies part of the scale around transparency, shows that the current at which transparency occurs decreases slightly as the input power is increased, and absorption aids in the creation of the required population inversion.

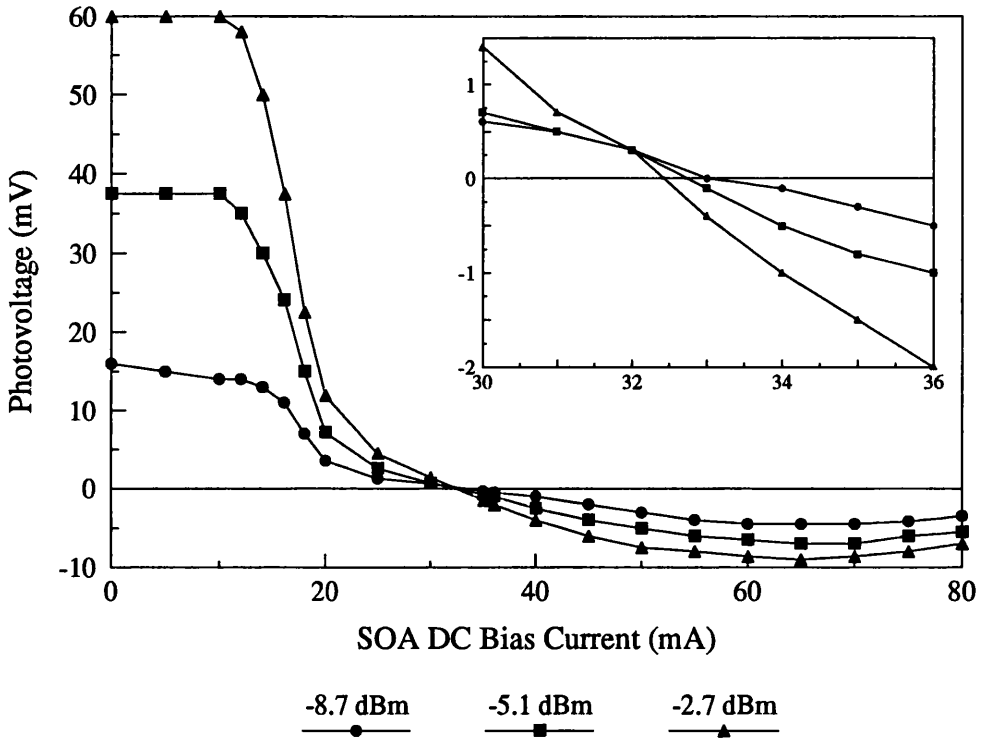

Figure 6.4 Photovoltage as a function of SOA dc bias for three values of fibre input power. Inset showing magnified section of main graph to demonstrate the dependence of the transparency current upon the input power.

From the information in figure 6.4, the responsivity may be calculated as a function of bias current; this is plotted in figure 6.5. The form of the graph agrees well with the theoretical results published by Gustavsson et al [3].

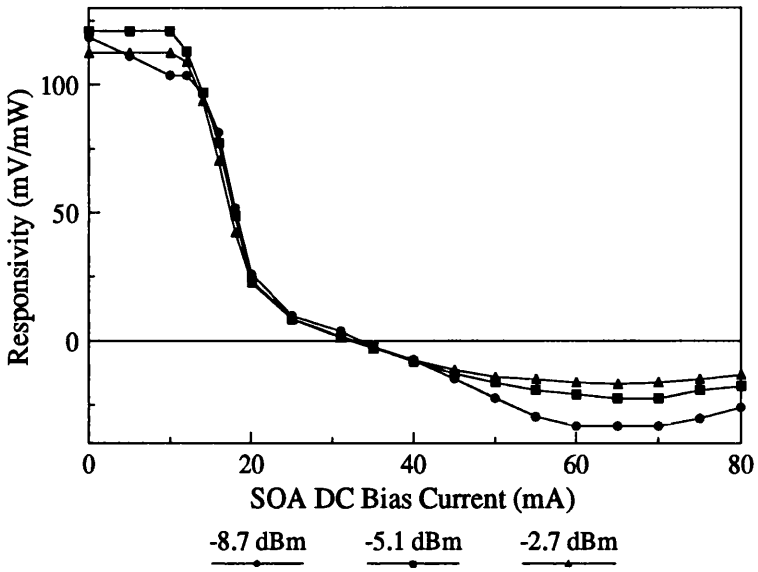

Figure 6.5 Variation of responsivity with amplifier dc bias current for three values of input power as figure 6.4.

6.2.2 Discussion

The results of these measurements show that the calculations presented in the previous chapter, while not precise, are of the right order. Further, they demonstrate that the photovoltage fluctuations are large enough to detect.

6.3 Use of Bias Current Modulation to Reduce Distortion

6.3.1 Experimental Details and Results

The effect of adding a sinusoid to the amplifier dc bias has been investigated by modulating the SOA and laser with the same rf oscillator. This uses the same principle that Saleh et al employed to reduce intermodulation distortion [4]. The experimental system is shown in figure 6.6.

In this system, the laser and amplifier are both modulated by the signal from an HP8350B sweep oscillator, via specially made bias tees; their dc biases are provided by stabilised voltage supplies via limiting resistors. The cable lengths are kept constant, and the phase difference between the modulation on the optical input signal and that on the amplifier bias is tuned by varying the modulation frequency. The input and output optical powers

are measured by a Hewlett-Packard HP11982A lightwave convertor, which contains a fast photodiode and a high frequency electrical amplifier; the frequency spectrum is observed using an HP8593A spectrum analyser.

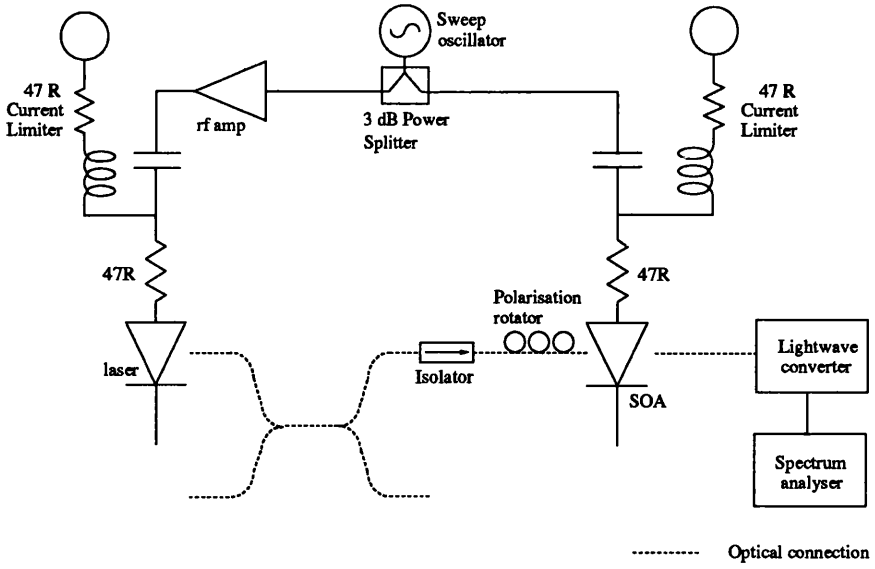

Figure 6.6 Experimental system used to investigate the effect of directly modulating the amplifier bias.

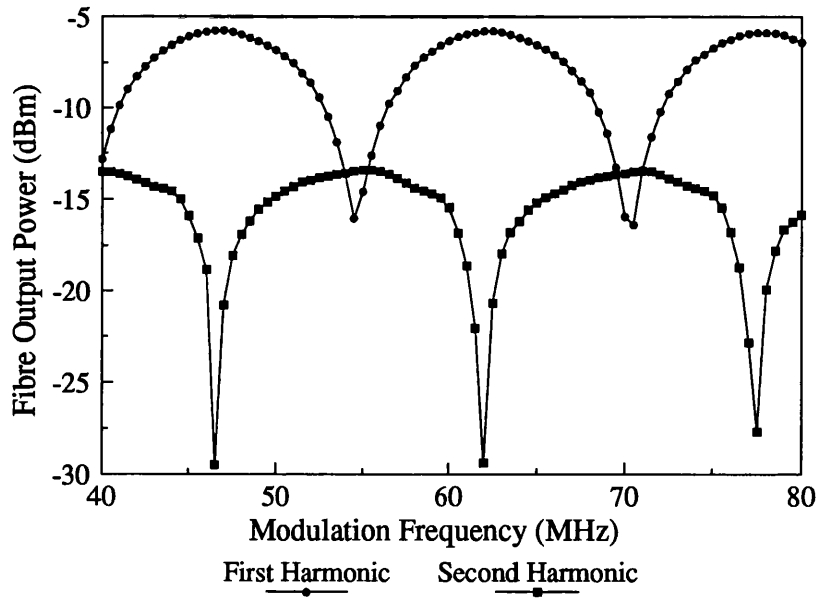

Figure 6.7 Experimental variation of first and second harmonic powers as a function of modulation frequency (phase) for dc bias 55 mA, rf current 8.5 mA pp, fibre input power -10 dBm, omi 56 %.

Figure 6.7 shows the measured first and second harmonic powers at the output of the amplifier for the following conditions: dc bias 55 mA, temperature 20 °C, average fibre input power -10 dBm, modulation index 56 %, input harmonic ratio 12.5 dB, rf modulating current 8.5 mA peak to peak. Over the range of frequencies considered, the HR of the amplifier when dc biased varies by less than 1 dB.

The periodicity of the phase response may be clearly seen. This characteristic gives rise to the dependence of the change in HR with modulation frequency (phase) shown in figure 6.8.

A maximum increase of 17.75 dB has been achieved using this method; this represents a situation where the second harmonic is buried below the noise floor, and thus the real figure may be even higher. At worst, the HR may be reduced by 9 dB, resulting in a negative figure for this quantity, that is, the second harmonic is more powerful than the first. It may be seen that the phase of the modulation signal with respect to the optical input is very crucial around the HR peak. As figure 6.9 shows, the rf gain may be increased by up to 2.8 dB under the conditions which give the peak in HR. Under least optimum phase conditions, the gain is reduced by almost 8 dB.

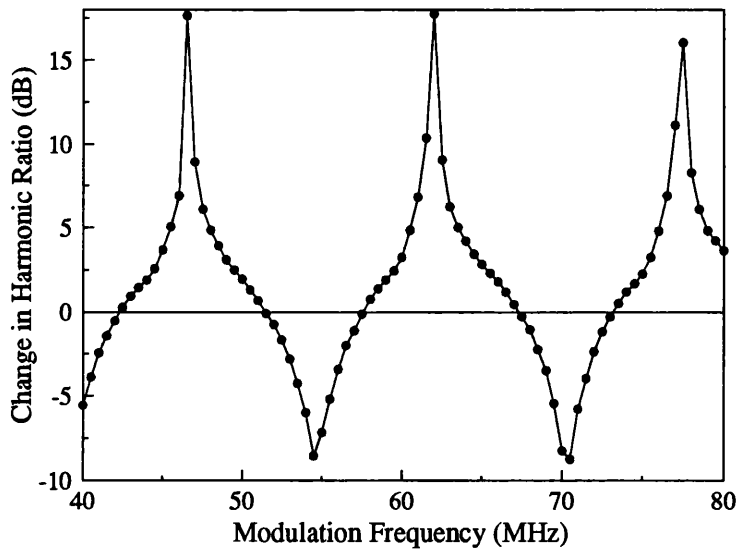

Figure 6.8 Experimental variation of harmonic ratio with modulation frequency for conditions as figure 6.7.

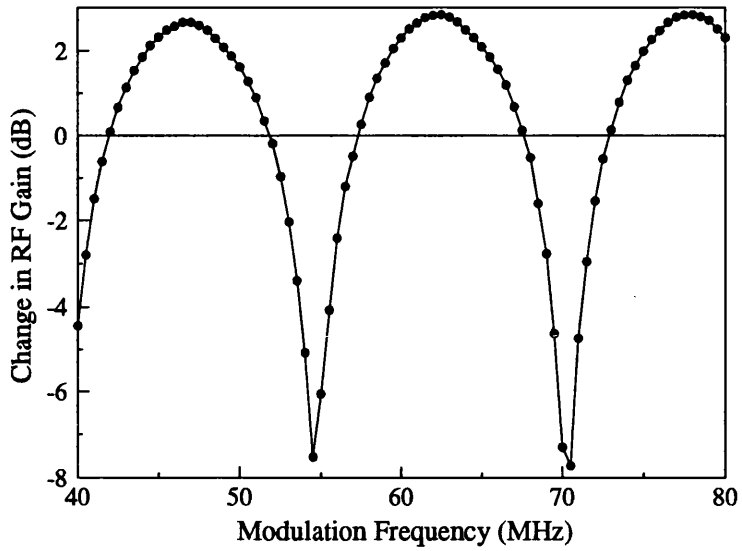

Figure 6.9 Experimental variation of rf gain with modulation frequency for conditions as figure 6.7.

Modifications to the small signal computer model have enabled the simulation of these results. To simplify the changes to the model, the multimoded input signal is taken into account via a decrease in effective power facet reflectivities from 2 % to 0.1 %. One mode only is considered inside the cavity. Figures 6.10(a) and (b) show the theoretical plots corresponding to figures 6.8 and 6.9. Excellent agreement between experiment and theory is obtained, despite the simplifications employed.

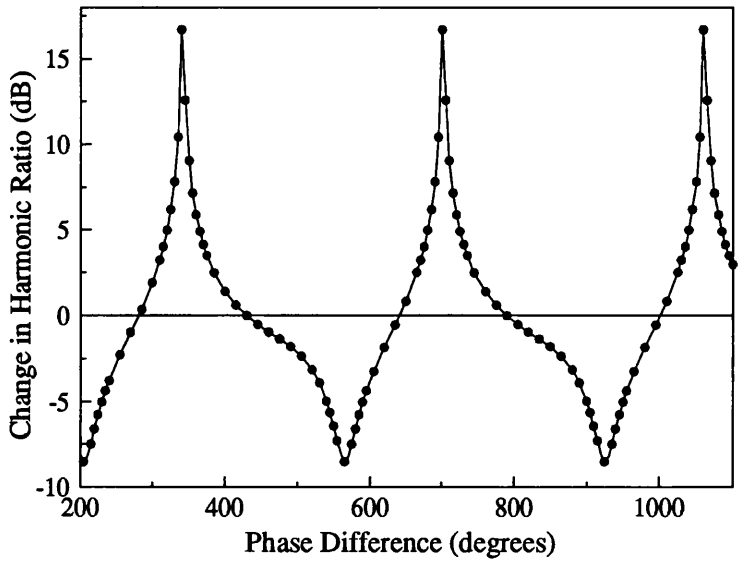

Figure 6.10(a) Theoretical variation of harmonic ratio with modulation frequency for conditions as figure 6.7.

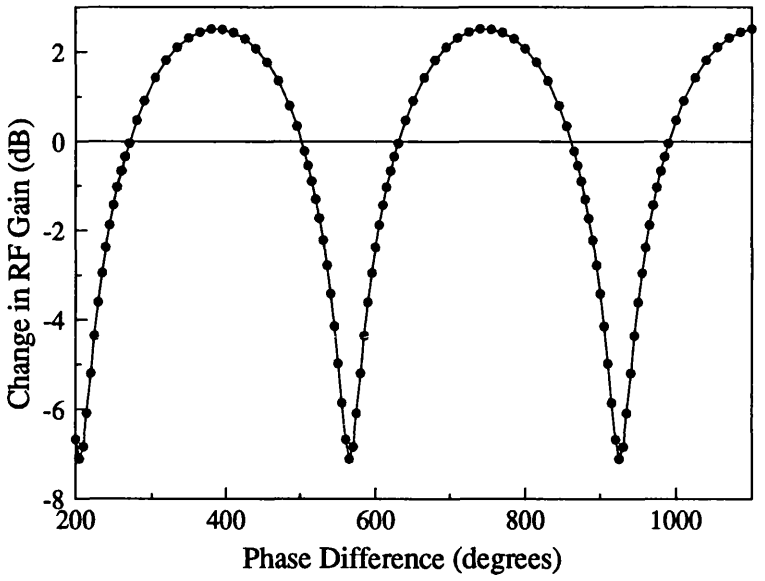

Figure 6.10(b) Theoretical variation of rf gain with modulation frequency for conditions as figure 6.7.

Figure 6.11 shows sample frequency spectra of the output from the amplifier. The conditions are as before, except that the modulation frequency is 62 MHz; the top trace was taken with dc bias, the bottom one with an rf modulation of 12.5 mA. The traces have been displaced for clarity. In the second spectrum, it may be seen that the second harmonic is below the noise floor; an increase of 1 dB in the device rf gain is obtained under these conditions.

To quantify the maximum possible improvement using this method, the HR has been calculated for various values of rf modulating current, and this is plotted in figure 6.13. The conditions are; -7 dBm fibre input power, input HR 12.5 dB opt., 60 MHz modulation frequency, 60 % optical modulation index, 55 mA dc current, 1300 nm. The phase difference between the optical and electrical modulation is optimised to give a maximum increase in HR. It may be seen that there is a peak in HR at an rf current of 7.5 mA peak to peak. Below this value, the bias current modulation is not sufficiently deep to compensate for the carrier density modulation; above 7.5 mA, it may be inferred that the modulated bias current is itself modulating the carriers.

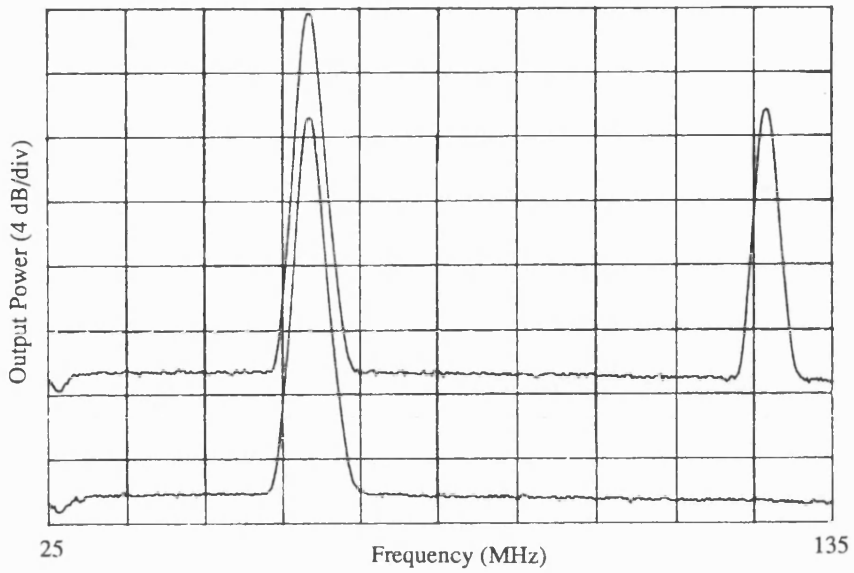

Figure 6.11 Frequency spectra of output power with dc bias (top trace) and rf modulation (bottom trace); SOA dc bias 55 mA, temperature 20 °C, average fibre input power -10 dBm, rf modulation frequency 62 MHz, omi 56 % and rf modulating current 12.5 mA pp. The traces have been vertically displaced for clarity.

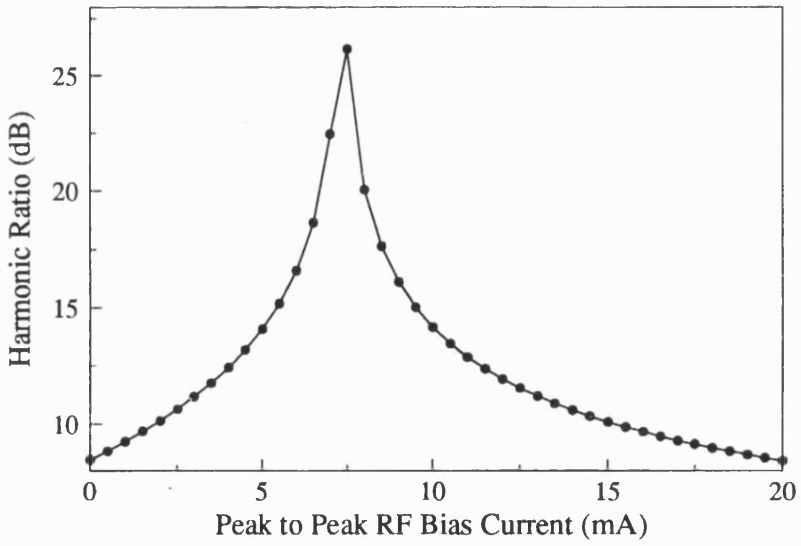

Figure 6.12 Simulated dependence of harmonic ratio upon rf modulating current. SOA dc bias 55 mA, temperature 20 °C, average fibre input power -7 dBm, modulation frequency 60 MHz, omi 60 %, input HR 12.5 dB, 1300 nm.

6.3.2 Discussion

The success of this experiment, in achieving an improvement of 17.75 dB in HR, effectively removing the second harmonic, and an increase of 2.8 dB in rf gain, demonstrates the advantages of modulating the SOA bias current. These results are very encouraging, as the improvement in performance obtained using this method is even higher than that predicted for the feedback method in chapter 5.

6.4 Verification of Feedback Method

6.4.1 Experimental Details and Results

The experimental system used to assess the feedback method is shown in figure 6.13. The multimode laser described earlier is used for some measurements; others are obtained using the dfb used to obtain the experimental results reported in chapter 3. The dfb has automatic temperature control provided by the ILX Lightwave temperature controller; when the dfb is used, the SOA temperature is controlled manually with the use of a current source and a multimeter. For these experiments, the laser is directly modulated by a Systron-Donner 1702 signal generator. The feedback loop itself contains a -10 dB directional coupler. This samples a fraction of the SOA terminal voltage, and directs the rf current around the feedback loop, preventing reflections from the SOA, which the rf signal perceives as a short-circuit. Amplification is provided by two Mini-Circuits rf amplifiers, with combined amplification of approximately 49 dB. Their 1 dB gain compression frequencies are 2 GHz and 4.2 GHz, respectively. There is no phase control in the loop.

Sample frequency spectra are shown in figure 6.14. *These traces have not been spatially displaced.* The conditions are as follows: SOA dc bias 80 mA; SOA temperature 17 °C; average input power -8.57 dBm; modulation frequency 140 MHz; modulation index 55 %; input HR 15.7 dB; dfb laser temperature 16.8 °C, corresponding to a wavelength of approximately 1311.04 nm. It is immediately evident that the higher harmonics have all been reduced in power, and that the low frequency noise floor has been lowered. At this wavelength the rf gain is reduced slightly, however increases of up to 5.55 dB have been achieved using this method. The reduction in HR under these conditions is 12.1 dB, the decrease in noise 12.5 dB. The maximum increase in HR achieved using this method is 18 dB. The decrease in noise is caused by a reduction in the average gain of

the SOA; since both shot and beat noise terms are proportional to the average gain or its square, this results in a significant reduction in noise. Theoretical analysis of the experimental results confirm this to be the noise reduction mechanism, and experimental observation of the optical spectrum, described in chapter 7, endorses this explanation. A maximum reduction of 15 dB has been obtained for the noise power at 100 MHz.

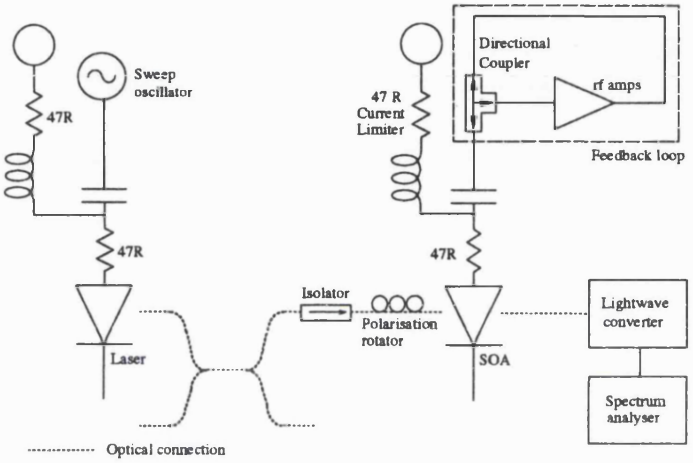

Figure 6.13 Experimental system used to assess the bias current feedback technique.

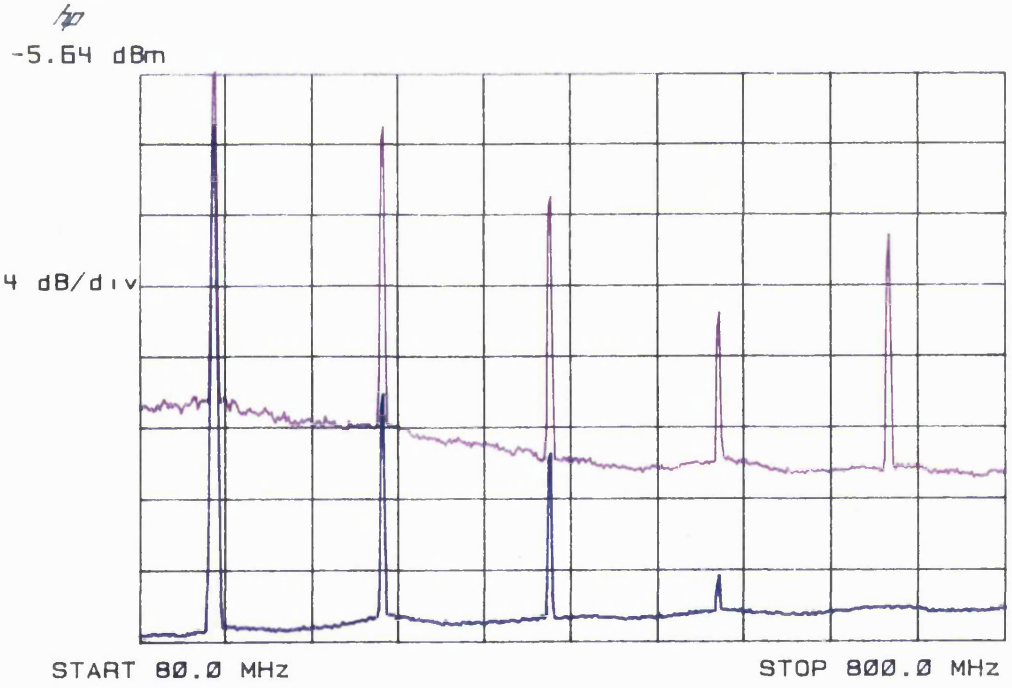

Figure 6.14 Frequency spectra taken with and without feedback. SOA dc bias 80 mA, temperature 17 °C, input power -8.57 dBm, modulation frequency 140 MHz, omi 55 %, input HR 15.7 dB, laser temperature 16.8 °C.

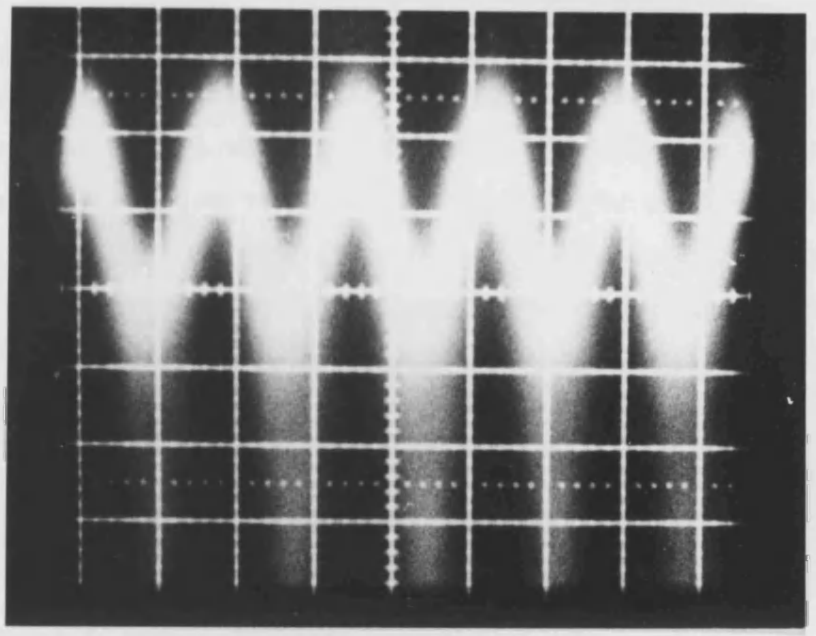

Figure 6.15(a) Photograph of oscilloscope trace. SOA dc bias 80 mA, 17 °c, input power -8.51 dBm, modulation frequency 120 MHz, omi 29 %, dc bias.

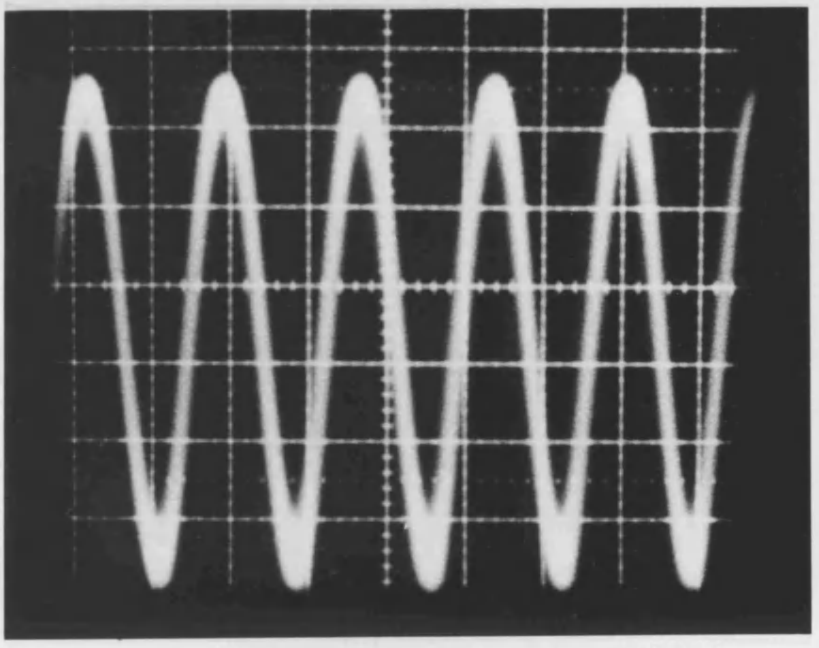

Figure 6.15(b) Photograph of oscilloscope trace. SOA dc bias 80 mA, 17 °c, input power -8.51 dBm, modulation frequency 120 MHz, omi 29 %, with bias current feedback.

The improvements in both noise and distortion are demonstrated by the photographs in figure 6.15. These were taken from the screen of an oscilloscope, the vertical and horizontal scales being the same for both. The conditions are as follows: SOA dc bias 80 mA; temperature 17 °C; average fibre input power -8.51 dBm; modulation frequency 120 MHz; omi 29 %. The source for this observation was the multimode diode laser. The trace in figure 6.15(a), taken with dc bias, shows a high level of noise and also signal distortion, the trace being almost triangular in shape. When the feedback is added (figure 6.15(b)), the modulation has become sinusoidal in form, the noise is visibly reduced, and the rf power is increased.

The modulation depth dependence of the improvement in noise and distortion has been investigated, using the multimode laser as the source. The results are shown in figure 6.16 for the following experimental conditions: SOA dc bias 80 mA; SOA temperature 17 °C; average input power -8.5 dBm; modulation frequency 120 MHz. The omi is varied between 20 % and 55 %. The change in noise and harmonic distortion may be seen to have the same dependence upon the modulation index; a reduction is experienced by both as the modulation index is increased to 46 %. Above this value, it may be inferred that the feedback signal is not strong enough to overcome the deep modulation of the carriers.

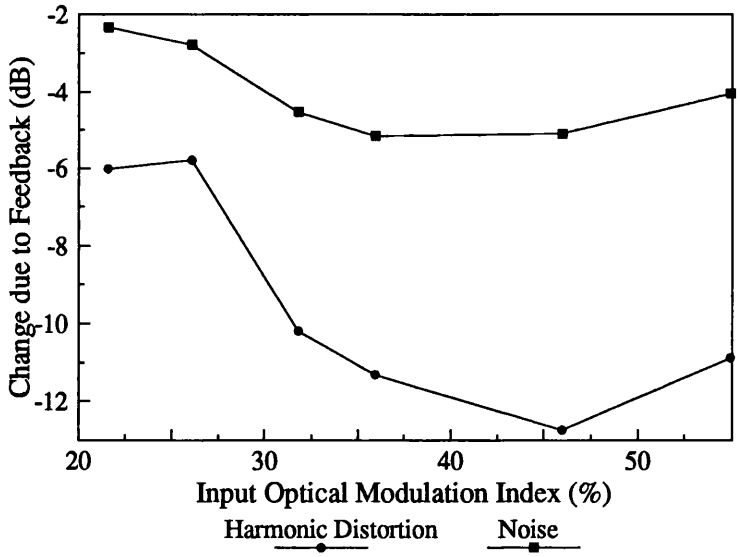

Figure 6.16 Variation of the change in noise and harmonic distortion with input optical modulation index. SOA dc bias 80 mA, temperature 17 °C, average input power -8.5 dBm, modulation frequency 120 MHz.

6.4.2 Confirmation of the Presence of Feedback

Present in the non-optimised electrical feedback loop is a resonance signal at 2.37 GHz, generated by the directional coupler and rf amplifiers. This signal is independent of the optical amplifier, and is present even when the SOA is disconnected from the loop. The result of this is modulation of the optical amplifier bias at 2.37 GHz, in addition to the low frequency optical modulation. Applications of this high frequency modulation signal will be explored in chapter 7.

A detailed theoretical and experimental evaluation of the effect of the feedback loop has been carried out, to confirm the presence of feedback of the low frequency modulation signal. Using the dfb, and tuning its temperature to vary the wavelength, the wavelength dependences of the change in rf gain, harmonic ratio and noise have been measured, using both feedback and direct modulation of the SOA bias. These results have also been simulated using the computer model, suitably modified.

The high frequency 2.37 GHz resonance signal has been measured at +12.1 dBm electrical, equivalent to a peak rf bias of 25.5 mA. It is estimated that approximately 9.1 dBm, equivalent to 18 mA peak, actually enters the SOA. To ascertain whether high frequency modulation is the dominant effect, the amplifier bias is directly modulated with an rf signal of equal power and frequency for comparison.

Figure 6.17(a) shows the measured rf gain, as a function of wavelength, for dc bias, for resonant feedback and for direct modulation of the bias at 2.37 GHz. The SOA dc bias is 80 mA, its temperature is 17 °C, the average input power is -8.6 dBm, the modulation frequency 140 MHz, the omi 57 %. Figure 6.17(b) shows simulated results for the same conditions, using a value of 0.4 for K.

In the theoretical plot, it may be seen that the rf gain is almost unchanged by the addition of direct rf modulation to the bias current. Here, the two plots agree well. For the case of the resonant feedback, however, the theoretical plot shows a shift in the FP resonance, along with an increase in gain. The shift in the maximum transmission wavelength of the cavity is due to the change in refractive index caused by the change in average cavity gain (see figure 6.21). In the experimental plot, the FP ripple is greatly reduced in amplitude, but the wavelength shift predicted theoretically is not observed.

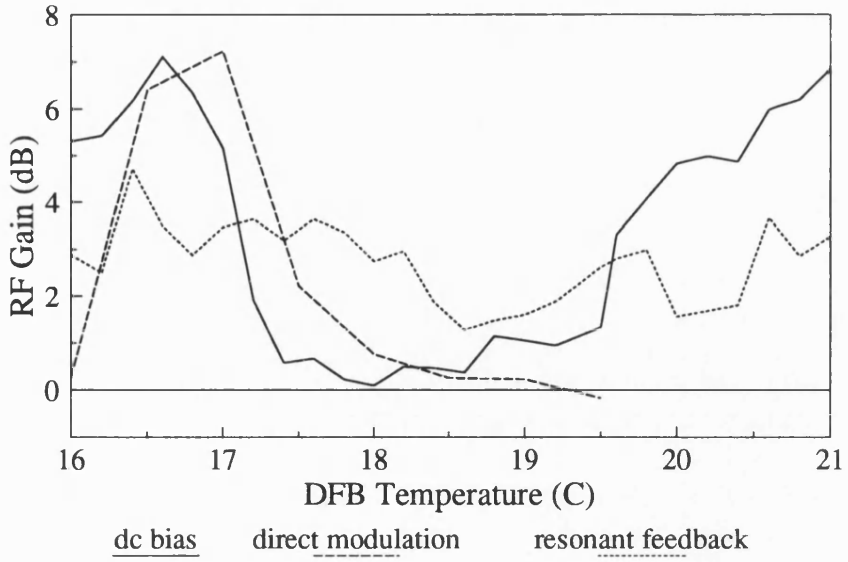

Figure 6.17(a) Experimental rf gain under conditions of dc bias, direct bias current modulation and resonant feedback. SOA dc bias 80 mA, temperature 17 °C, average input power -8.6 dBm, modulation frequency 140 MHz, omi 57 %.

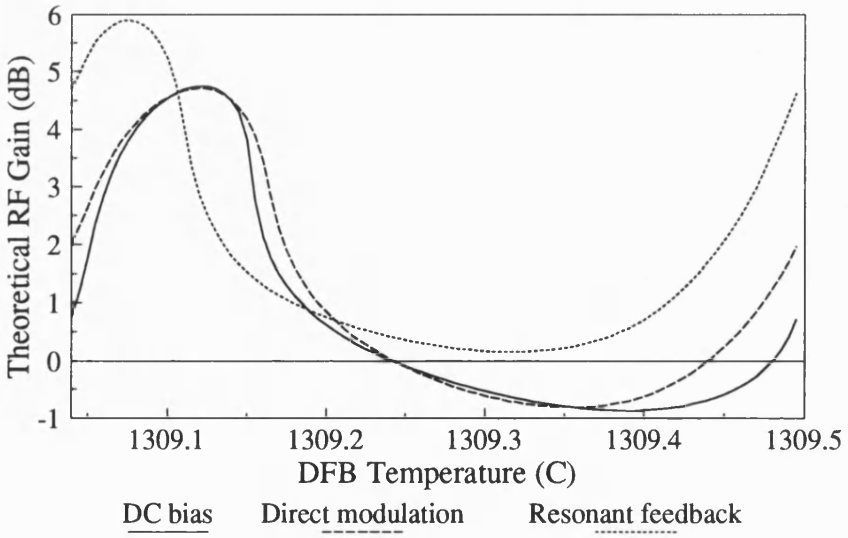

Figure 6.17(b) Theoretical rf gain under conditions of dc bias, direct bias current modulation and resonant feedback. Conditions as figure 6.17(a) except K=0.4.

Figure 6.18 shows the change in rf gain for the same conditions.

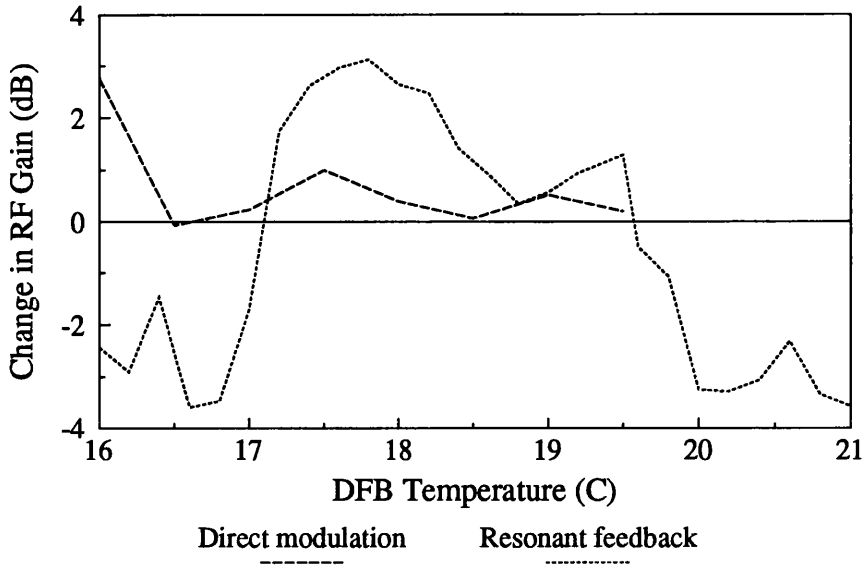

Figure 6.18(a) Experimental change in rf gain due to direct bias current modulation and resonant feedback. Conditions as figure 6.17(a)

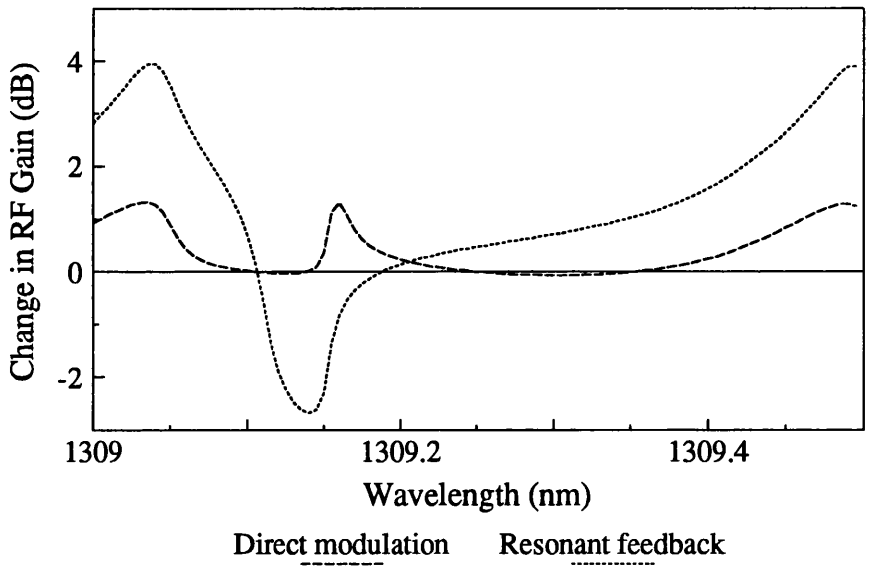

Figure 6.18(b) Theoretical change in rf gain due to direct bias current modulation, and resonant feedback. Conditions as figure 6.17(b).

In both plots, the gain in the case of resonant feedback is increased over the larger part of the wavelength range. For the direct modulation condition, a small increase in rf gain is experienced, but the change is zero for most of the wavelength range. The largest

increase and decrease are both experienced with resonant electrical feedback. The values of the experimental and theoretical change in rf gain agree well for both measurement conditions.

The HR is plotted in figure 6.19, for the same conditions as before. Again there is little change for the case of direct bias, when compared with the dc case. As the theoretical plot shows, the effect of resonant feedback is a wavelength shift, also a rise in peak HR. Again the experimental plot does not exactly agree.

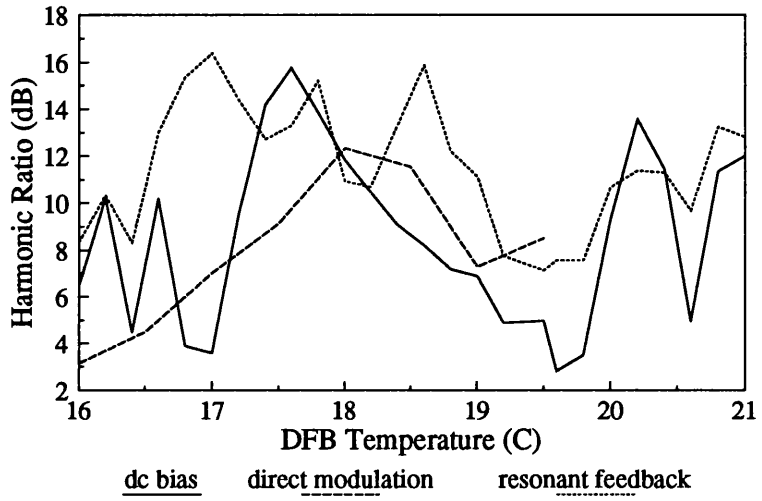

Figure 6.19(a) Experimental harmonic ratio under conditions of dc bias, direct modulation and resonant feedback. Conditions as figure 6.17(a).

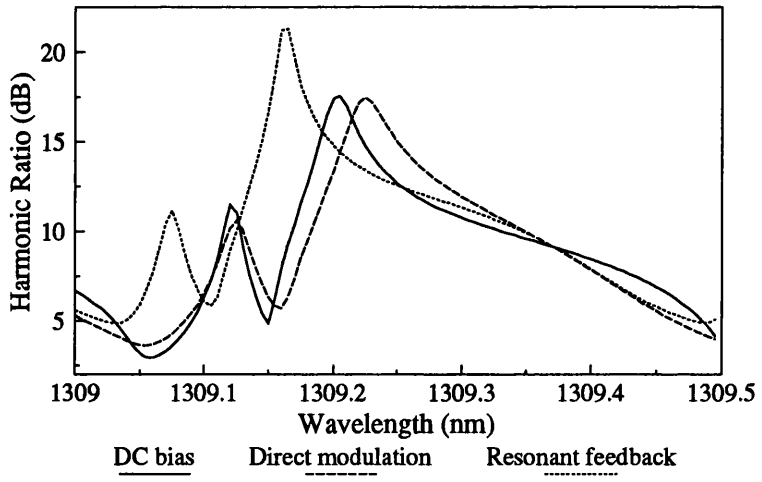

Figure 6.19(b) Theoretical harmonic ratio under conditions of dc bias, direct modulation and resonant feedback. Conditions as figure 6.17(b).

The change in harmonic ratio due to the two bias conditions is plotted in figure 6.20, for experimental and theoretical results. There is good general agreement between figures 6.20(a) and 6.20(b), with the greatest increase in HR being achieved for the case of resonant feedback, the greatest reduction for direct modulation.

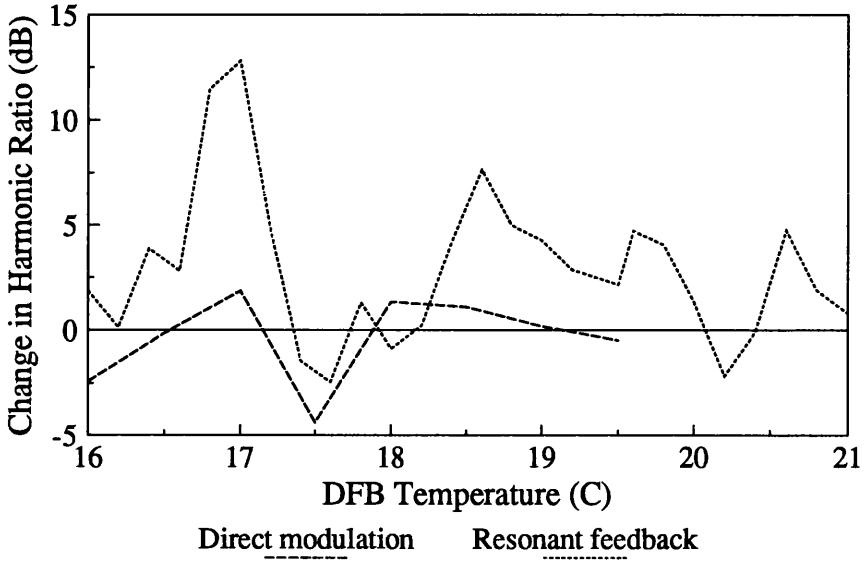

Figure 6.20(a) Experimental change in harmonic ratio due to direct modulation and resonant feedback respectively. Conditions as for figure 6.17(a).

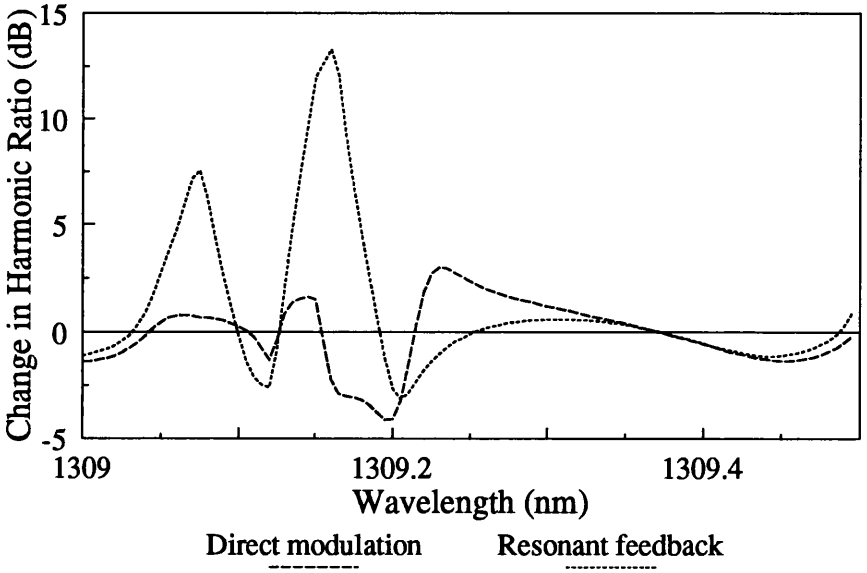

Figure 6.20(b) Theoretical change in harmonic ratio due to direct modulation and resonant feedback respectively. Conditions as for figure 6.17(b).

In figure 6.21(a), the experimentally measured change in noise power at 100 MHz has been plotted against wavelength for the two bias conditions. The theoretical data in figure 6.21(b) is of the change in the time-averaged gain of the device. Since the noise power is proportional to the average gain, the two may be compared qualitatively although not quantitatively. Good agreement is obtained between experiment and theory in this case; there is confirmation that the mechanism of noise reduction is indeed reduction of the average gain, also that it is due to the feedback, and not to the high frequency modulation.

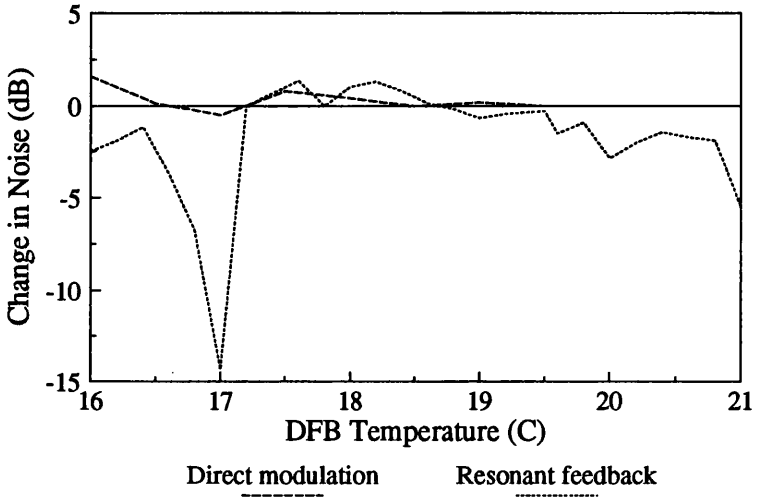

Figure 6.21(a) Experimental change in noise power measured at 100 MHz, due to direct modulation and resonant feedback respectively. Conditions as for figure 6.17(a).

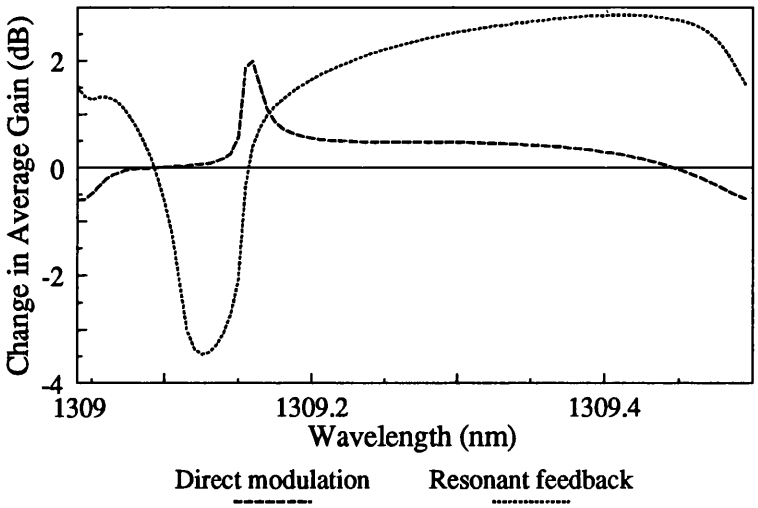

Figure 6.21(b) Theoretical change in time-averaged gain, due to direct modulation and resonant feedback respectively. Conditions as for figure 6.17(b).

6.4.3 Discussion

The feedback method has been shown to provide significant improvement in the performance of the bulk SOA. The harmonic distortion has been reduced by up to 18 dB, the low frequency noise power by up to 15 dB. The improvement is wavelength-dependent, as could be expected from a Fabry-Perot device, in which the carrier concentration and cavity gain are wavelength-dependent. There is not exact agreement between theoretical and experimental data for the wavelength dependence of the rf gain and the harmonic ratio. This could be due to inaccuracy or oversimplification of the model, or possibly to drifting of the SOA temperature during the measurement. The response of the device is very temperature sensitive.

Although the loop is resonating, and producing a high power electrical signal at 2.37 GHz, comparison of the effect of direct modulation with that of the feedback loop confirms that feedback is taking place.

6.5 Conclusions

This chapter has described an experimental investigation of the effect of bias current feedback on the harmonic performance of an SOA.

Measurements of the deviation in photovoltage due to an optical signal reveal that its input power dependence is similar to that calculated in the previous chapter. The measured variation is of a similar order to that calculated.

A preliminary study, involving direct modulation of the SOA bias at the same frequency as the laser, has produced an increase of up to 17.75 dB opt in harmonic ratio, and up to 2.8 dB in rf gain. Theoretical analysis shows that there is an optimum value of rf modulating current; for a dc current of 55 mA and fibre input power of -7 dBm, this is calculated to be 7.5 mA peak to peak.

Use of a simple feedback loop has resulted in increases of up to 18 dB in HR and up to 5.55 dB in modulated gain, and decreases of up to 15 dB in noise. Although there is a high frequency electrical resonance signal in the feedback loop, experimental and theoretical investigation has confirmed that feedback is taking place.

6.6 References

1. K L Hall, E P Ippen, G Eisenstein: "Bias-lead monitoring of ultrafast nonlinearities in InGaAsP diode laser amplifiers", *Appl. Phys. Lett.* **57**. pp. 129-131, 1990.
2. V V Luc, P G Eliseev, M A Manko, G T Mikaelian: "Electrical diagnostics of the amplifier operation and a feasibility of signal registration on the basis of the voltage saturation effect in junction laser diodes", *IEEE J. Quantum Electron.* **19**, pp. 1080-1083, 1983.
3. M Gustavsson, A Karlsson, L Thylén: "Traveling wave semiconductor laser amplifier detectors", *J. Lightwave Technol.* **8**, pp. 610-617, 1990.
4. A A M Saleh, R M Jopson, T E Darcie: "Compensation of nonlinearity in semiconductor optical amplifiers", *Electron. Lett.* **24**, pp. 950-952, 1988.

7

Frequency Conversion

This chapter explores the use of a semiconductor optical amplifier as a modulation frequency convertor. Frequency upconversion is achieved through direct modulation of the bias current, or by the use of the resonant electrical feedback loop described in chapter 6, in conjunction with a modulated optical input. It is found that the efficiency of the conversion depends upon the optical signal wavelength, and the magnitude of the rf modulating current. The resonant feedback method is found to give efficient modulation of the SOA at 2.37 GHz, with harmonics generated up to 14.22 GHz. Wavelength conversion is observed, with shifts of up to 7.11 GHz achieved using resonant feedback. Frequency downconversion is demonstrated using both electro-optic and all-optical methods. The frequency change provided by the resonant feedback method is used to shift the output from a Mach-Zehnder interferometer, and thus enable measurement of the linewidth of a distributed feedback laser.

7.1 Introduction

There are many situations in which the modulation frequency of an optical signal may need to be converted by some method; for example the upconversion of a subcarrier to the carrier frequency prior to transmission, or the downconversion of a microwave carrier prior to signal processing. This may be done electronically, but it is often advantageous to perform the frequency mixing optically, for example using an optical amplifier. When two signals, modulated at different frequencies, enter the amplifier, by electrical or optical injection, they modulate the carrier density in the cavity. The combination of

the two frequencies gives rise to the generation of mixing terms at the sum and difference frequencies ($f_2 \pm f_1$), ($f_2 \pm 2f_1$) etcetera, as well as higher harmonics of the two original frequencies. It was first suggested by Darcie et al in 1988 that a semiconductor optical amplifier might be suitable for frequency conversion applications [1], and an investigation of this idea is described in this chapter.

This chapter is split into four sections. The first covers modulation frequency upconversion, using direct modulation of the amplifier bias current; the signal wavelength and rf modulating current are varied, and the amplifier response investigated experimentally and theoretically. The second section examines frequency upconversion using the 2.37 GHz electrical resonance signal present in the feedback loop. Electrical and optical spectra, taken under various conditions, are presented in this section. In the third section, the possibility of using an SOA for frequency downconversion of a microwave carrier is investigated. Lastly, the upconversion due to the resonance signal is used to frequency shift the output from a Mach-Zehnder interferometer, enabling the linewidth of a dfb laser to be measured as a function of output power.

7.2 Frequency Upconversion Using Bias Current Modulation

7.2.1 Introduction and Experimental Details

The experimental system is similar to that used to investigate bias current feedback, described in the previous chapter, but here the amplifier bias current is modulated using an HP rf sweep oscillator. A Picosecond Pulse Labs 20 GHz bias tee is used in the investigation of the modulation frequency dependence, with a 47 Ω impedance matching circuit in the rf line. Where experimental temporal plots are shown, they have been obtained with the use of a high frequency sampling scope, and a Thurlby DSA 524 digital storage adaptor.

The optical input signal to the amplifier is modulated to simulate the subcarrier, and the bias current is modulated with the carrier frequency. The subcarrier spectrum is to be shifted up to the carrier frequency.

7.2.2 Modulation Frequency Dependence

In this section, the frequency response of the amplifier to an electrical modulation signal is investigated, as the optical input modulation is kept constant at 140 MHz, and the SOA bias current is modulated at frequencies between 200 MHz and 3.8 GHz. Because of the high loss of the impedance matching circuit, it has not been possible to maintain constant rf power outside this frequency range.

Figure 7.1 shows two sample frequency spectra of the output signal from the SOA, taken under the following conditions: SOA dc bias 80 mA; SOA temperature 17 °C; SOA bias rf modulation 18.05 mA peak, equivalent to that provided by the resonance signal from the feedback loop; average input power -8.6 dBm; optical modulation frequency 140 MHz; optical modulation depth 68 %; laser temperature 18.5 °C. The signal wavelength corresponds to an FP gain trough. In figure 7.1(a) the electrical modulation (carrier) frequency is 800 MHz; all other conditions are as described above. The output power obtained at 800 MHz is -4.17 dBm, compared with -9.56 dBm obtained at the signal frequency of 140 MHz. The closeness of the two frequencies gives rise to many mixing terms in the frequency range shown. In figure 7.1(b) the carrier frequency is 3.8 GHz, all other conditions as before. Here the power obtained at the carrier frequency is only -12.25 dBm, due to the limiting effect of the carrier lifetime which prevents deep modulation of the carrier density at this frequency. However, the 140 MHz spectrum is shifted to the carrier frequency, and the power obtained at the sum and difference frequencies is approximately -24 dBm, compared with -20 dBm for a carrier at 800 MHz. Thus, effective frequency shifting is obtained, even when the modulation frequency is several times that suggested by the carrier recombination lifetime.

Figure 7.2 shows the frequency dependence of the 140 MHz component of the SOA output, for dc and modulated bias, also the power in the high frequency component. The 140 MHz fundamental is shown to be unchanged by the addition of electrical modulation, except for electrical modulation frequencies below 1 GHz, where there is considerable mixing between the two forms of modulation. The response to the high frequency modulation may be seen to be in the form of a low pass filter; the peaks are caused by phase effects, due to the fixed length of the cables.

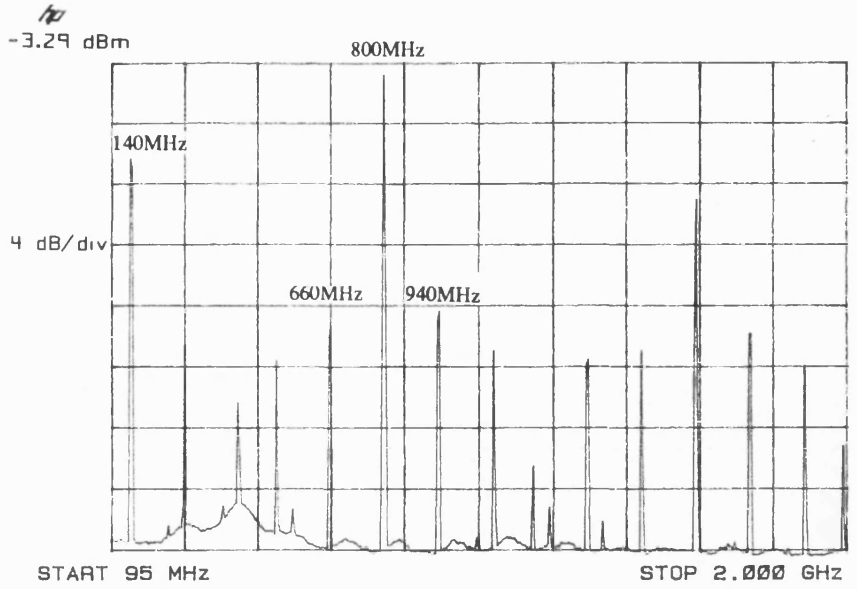

(a)

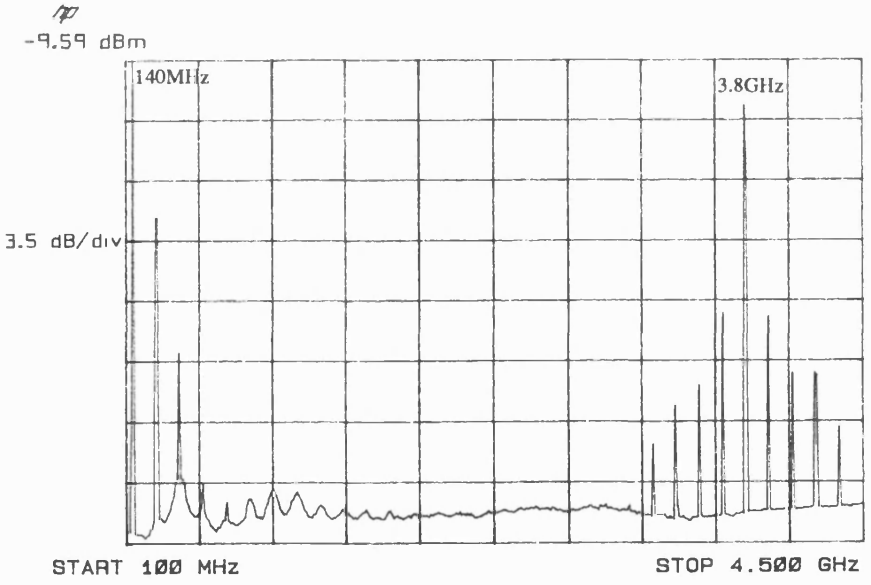

(b)

Figure 7.1 Frequency spectra of the SOA output showing electro-optic frequency mixing. SOA dc bias 80 mA, temperature 17 °C, rf modulation current 18.05 mA peak, average input power -8.6 dBm, optical modulation frequency 140 MHz, omi 68 %, dfb temperature 18.5 °C. Electrical modulation frequency (a) 800 MHz (b) 3.8 GHz.

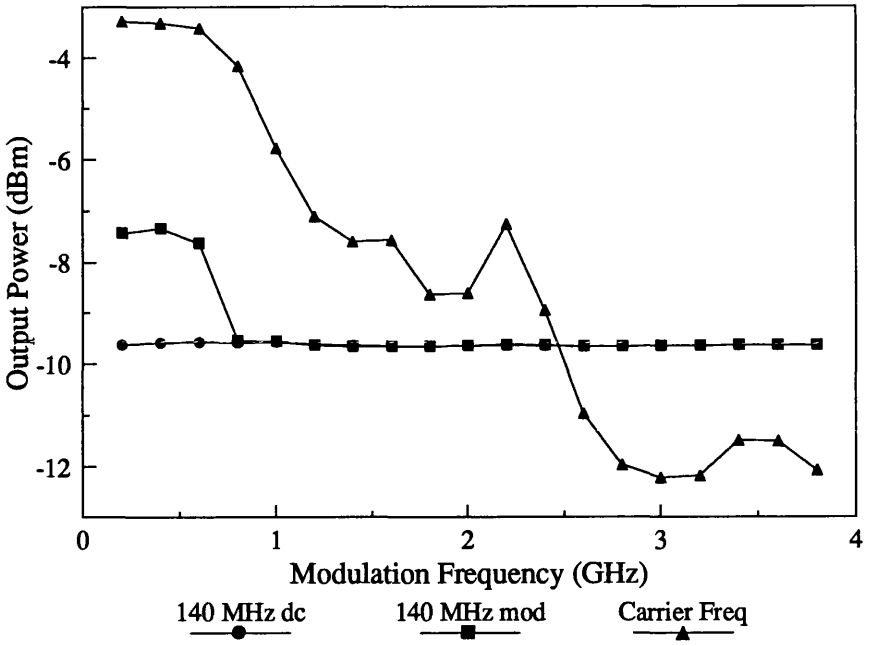

Figure 7.2 Electrical modulation frequency dependence of the SOA output power at 140 MHz and at the electrical modulation frequency. SOA dc bias 80 mA, SOA temperature 17 °C, average input power -8.6 dBm, optical modulation frequency 140 MHz, omi 68 %, dfb temperature 18.5 °C.

The output power in the high frequency component is 3 dB down at a frequency of approximately 1.2 GHz; this could be increased with the use of phase control in the bias modulation circuit. The output power at the electrical modulation frequency exceeds that at 140 MHz up to a frequency of 2.5 GHz; this is because the optical gain at this wavelength is reduced by Fabry-Perot effects. The wavelength at which this measurement was taken corresponds to low optical gain. For this reason, at low modulation frequencies, the output power due to the electrical modulation is considerably higher than that due to the modulation on the optical input signal.

7.2.3 RF Power Dependence - 2.37 GHz

The rf modulation power dependence of the SOA response has also been investigated, using an electrical modulation signal at 2.37 GHz to match that produced by the feedback loop resonance. Two laser temperatures have been used; 16.5 °C corresponding approximately to an FP gain peak, and 19 °C corresponding approximately to an FP gain

trough. The other experimental conditions are as follows: SOA dc bias 80 mA; SOA temperature 17 °C; average input power -8.43 dBm; optical modulation frequency 140 MHz; optical modulation index 58 %.

Figure 7.3 shows the output power at 140 MHz and 2.37 GHz, for dc bias and rf modulation, for the two wavelengths.

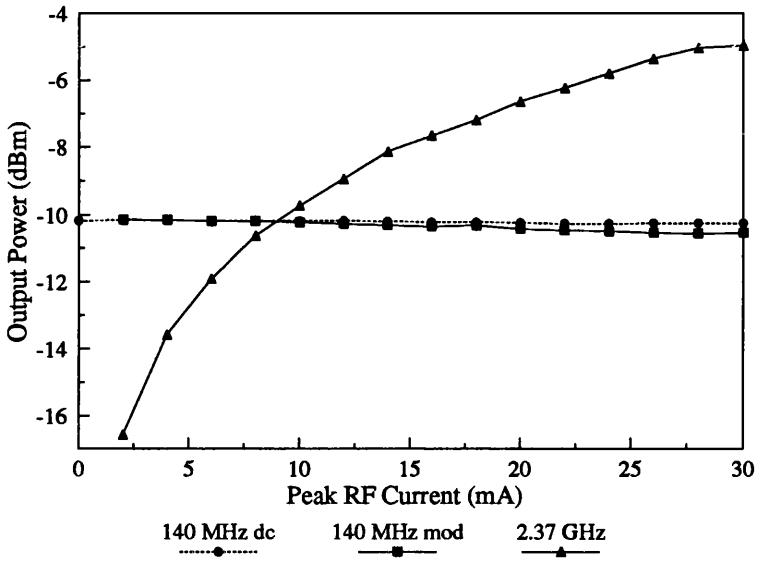

(a)

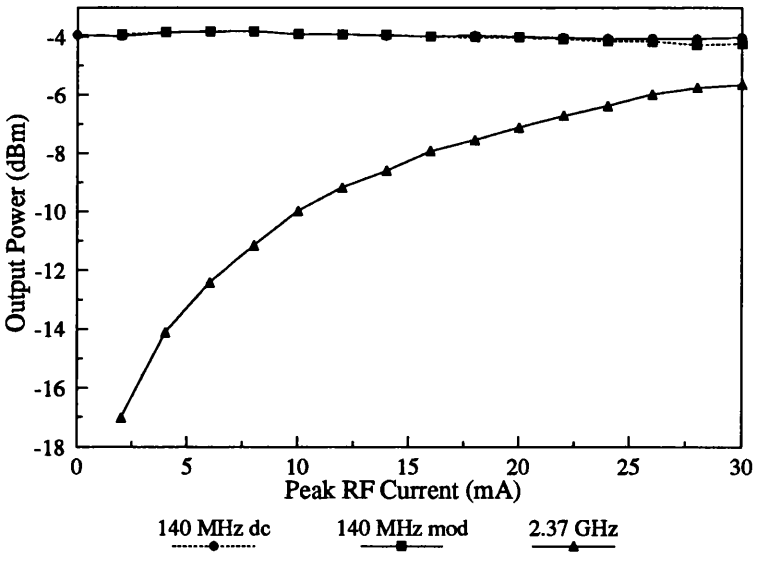

(b)

Figure 7.3 Dependence upon rf modulating current of the output powers at 140 MHz and 2.37 GHz, with the output at 140 MHz with dc bias for comparison. SOA dc bias 80 mA, temperature 17 °C, average input power -8.43 dBm, optical modulation frequency 140 MHz, omi 58 %, dfb temperature (a) 19 °C (b) 16.5 °C.

It may be observed in both cases that the addition of the high frequency electrical modulation signal has little or no effect on the fundamental output at 140 MHz. For both wavelengths, the power in the 2.37 GHz component shows signs of saturation as the modulation current is increased. The effect of the Fabry-Perot resonance may be seen in the fact that at a laser temperature of 16.5 °C, the power at 2.37 GHz never equals that at 140 MHz; at 19 °C, the power at 2.37 GHz exceeds that at 140 MHz for a peak rf current of 8 mA, or 10 % modulation. There is little difference between the output powers at 2.37 GHz at the two signal wavelengths.

Sample frequency spectra for the two wavelengths demonstrate the effect of FP resonance upon the modulation response of the amplifier. Figure 7.4(a) shows a spectrum taken for a laser temperature of 19 °C. All experimental conditions are as figure 7.3(a), except that the rf modulation current is 10 mA peak. The frequency component at 2.37 GHz is clearly dominant in this spectrum. Because this is a gain trough wavelength, and the optical gain is low, there are few harmonics of the 140 MHz signal; those harmonics which are present are reproduced around the 2.37 GHz peak, to form the sum and difference frequency components. Although the low frequency spectrum is not exactly replicated about the 2.37 GHz component, since the second harmonic has been almost completely removed, there is potential for the method of electro-optic frequency conversion proposed by Darcie [1], here used possibly for multiplexing a subcarrier with the microwave carrier wave.

The spectrum for a laser temperature of 16.5 °C, shown in figure 7.4(b), has an rf modulating current of 8 mA peak, no spectrum being available for 10 mA modulation current. The 140 MHz frequency component is clearly dominant in this spectrum, although the 2.37 GHz peak may be distinguished. Since this wavelength corresponds to an FP gain peak, there are many strong harmonics of the 140 MHz optical signal. These mix with the harmonics around the 2.37 GHz electrical signal to produce the frequency spectrum shown in figure 7.4(b).

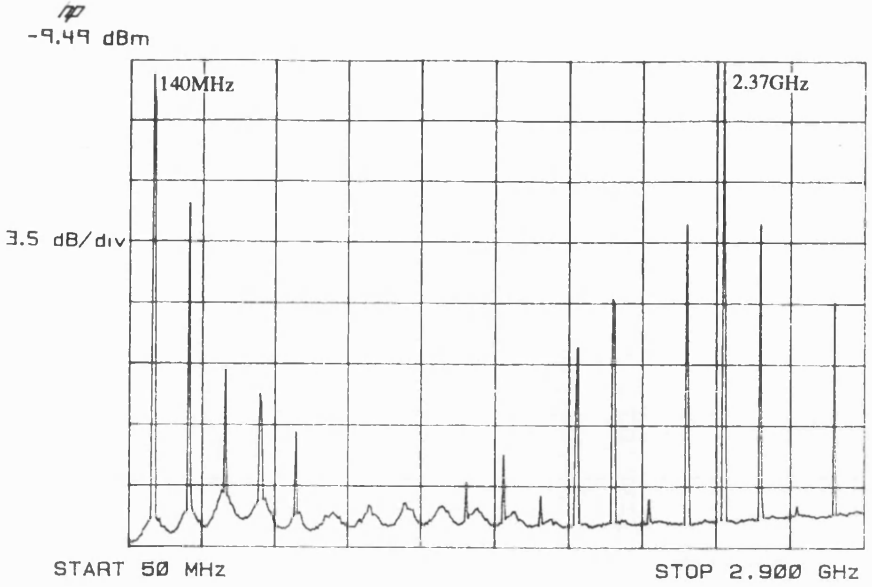

(a)

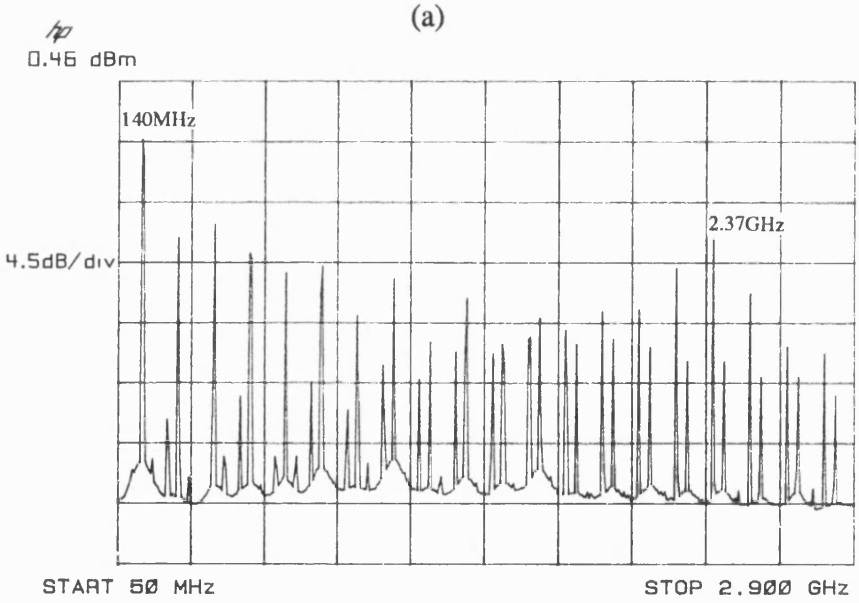

(b)

Figure 7.4 Electrical frequency spectra showing electro-optic frequency mixing. (a) Conditions as figure 7.3(b) except rf modulating current 8 mA peak (b) conditions as figure 7.3(b) except rf modulating current 8 mA peak.

7.2.4 Wavelength Dependence - 2.37 GHz

To investigate the wavelength dependence of the rf response due to the FP resonance, the output power at 140 MHz and 2.37 GHz has been measured over a range of dfb temperatures corresponding to almost one period of the gain ripple. These results are

shown in figure 7.5, for the following conditions: SOA dc bias 80 mA; SOA temperature 17 °C; rf modulation current 18.05 mA peak; average input power -8.3 dBm; optical modulation frequency 140 MHz; omi 57 %.

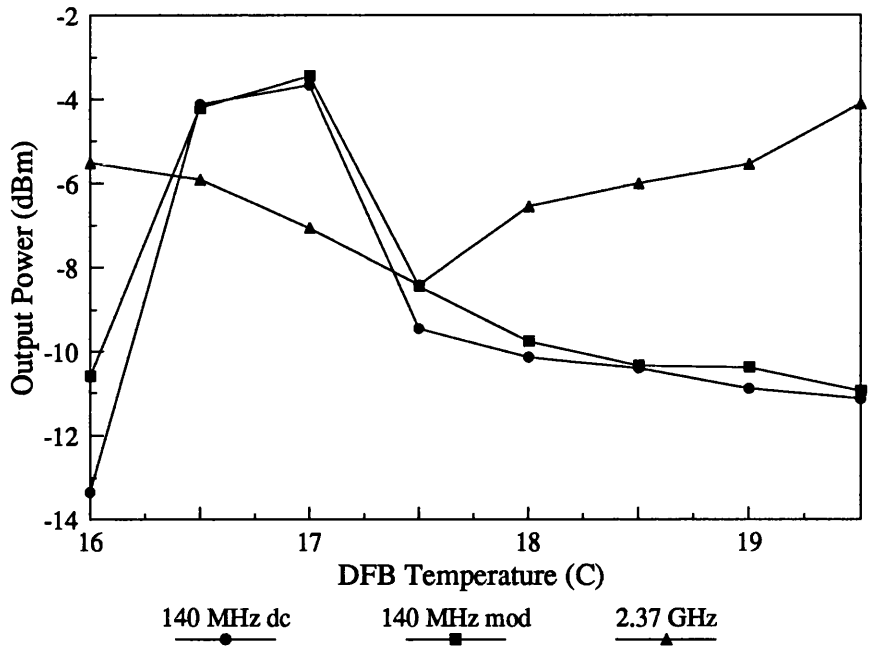

Figure 7.5 Wavelength dependence of SOA output power at 140 MHz and 2.37 GHz for dc bias and rf modulation. SOA dc bias 80 mA, temperature 17 °C, SOA modulating current 18.05 mA peak, average input power -8.3 dBm, optical modulation frequency 140 MHz, omi 57 %.

Again, it may be seen that the application of high frequency electrical modulation has little effect upon the 140 MHz fundamental output signal. The wavelength dependence of the output power at 2.37 GHz is approximately out of phase with that at 140 MHz, for the reason given earlier. There is little variation with wavelength in the output power at 2.37 GHz.

7.2.5 Wavelength Dependence - 1 GHz

An additional study has been carried out to compare the theoretical and experimental time dependence of the SOA output power with its electrical frequency spectrum, for different values of source wavelength. An electrical modulation frequency of 1 GHz has been used, since this is the highest frequency that the sampling scope is able to trigger on satisfactorily.

To investigate the effect of signal wavelength, the time and frequency spectra have been measured for four laser temperatures, corresponding to a wavelength range of 3 nm. The time dependences have been simulated, and theoretical results are also shown.

Figures 7.6 - 7.9 show the time and frequency spectra for the following conditions: SOA dc bias 80 mA; SOA temperature 17 °C; rf modulation current 18 mA peak; average input power -8.47 dBm; optical modulation frequency 140 MHz; omi 60 %; dfb temperature 17 °C, 18 °C, 19 °C and 20 °C respectively. The simulated results were obtained at wavelengths of 1311.25 nm, 1311.35 nm, 1311.45 nm and 1311.55 nm respectively.

The experimental and theoretical results agree well for the four wavelengths. At 17 °C, which represents a peak optical gain wavelength, the high frequency modulation is poorly defined in the temporal plots. Correspondingly, the frequency spectrum shows many frequency components between 140 MHz and 1 GHz. At 18 °C and 19 °C, both corresponding to trough wavelengths, the 1 GHz modulation is better defined, and the electrical spectra are cleaner, with fewer harmonics and mixing terms. At 20 °C, where the optical gain is beginning to rise again, the time spectra are less well defined, and the electrical frequency spectrum shows strong frequency mixing.

7.2.7 Discussion

This section, which investigates electro-optic frequency upconversion, shows that an SOA may be modulated through its bias current at frequencies up to 3.8 GHz; the 3 dB frequency is approximately 1.2 GHz.

The output power obtained at the electrical modulation frequency depends upon the optical signal wavelength, as does the purity of the modulated waveform. At a wavelength corresponding to a Fabry-Perot gain peak, the electrical modulation frequency component is less powerful than the component at the optical modulation frequency, for all values of modulating current up to 30 mA peak. At a trough wavelength, where the gain for the optical input signal is low, the power in the high frequency electrical modulation component exceeds that in the low frequency optical modulation component for a modulating current of only 8 mA peak.

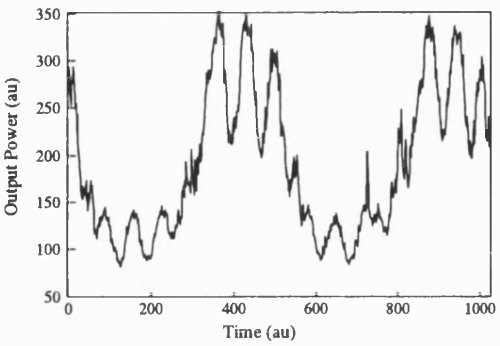

(a)

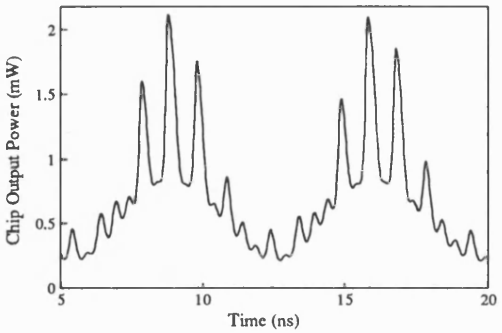

(b)

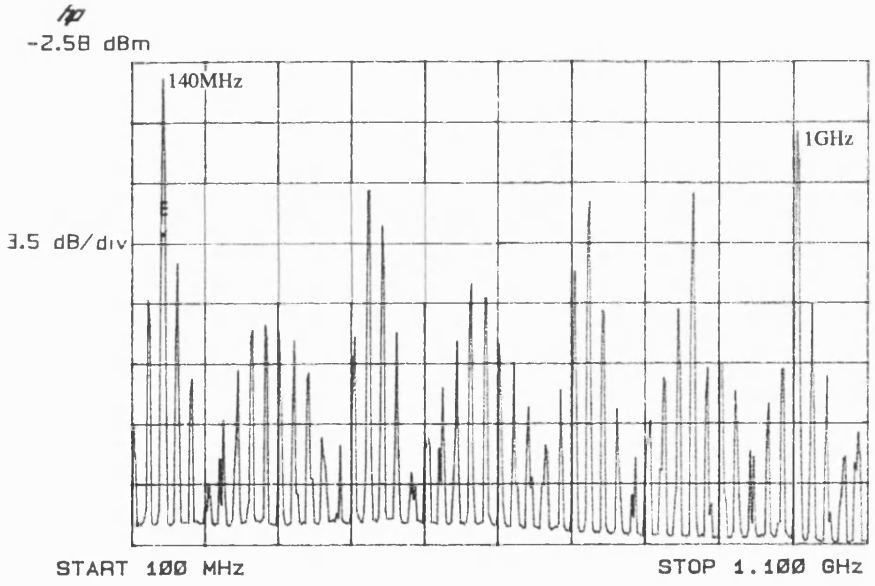

(c)

Figure 7.6 (a) Experimental time dependence of output power, (b) theoretical time dependence of output power, (c) experimental frequency spectrum. SOA dc bias 80 mA, SOA temperature 17 °C, rf modulation current 18 mA peak at 1 GHz, average input power -8.47 dBm, optical modulation frequency 140 MHz, omi 60 %, dfb temperature 17 °C, theoretical wavelength 1311.25 nm.

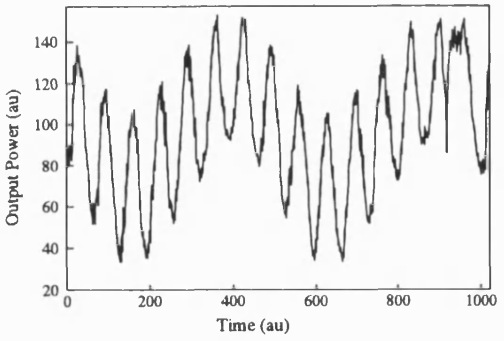

(a)

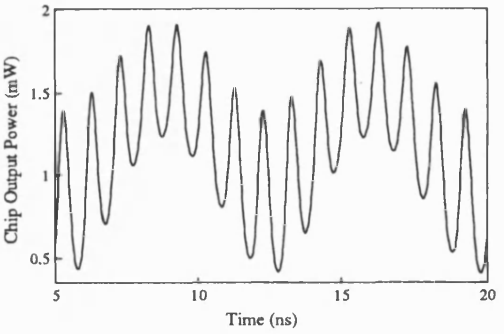

(b)

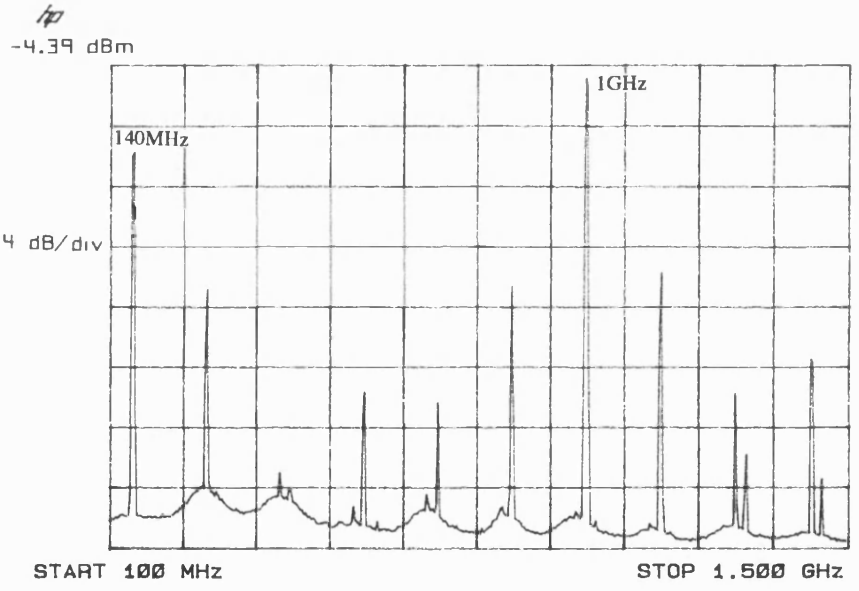

(c)

Figure 7.7 (a) Experimental time dependence of output power, (b) theoretical time dependence of output power, (c) experimental frequency spectrum. Conditions as for figure 7.6 except dfb temperature 18 °C, theoretical wavelength 1311.35 nm.

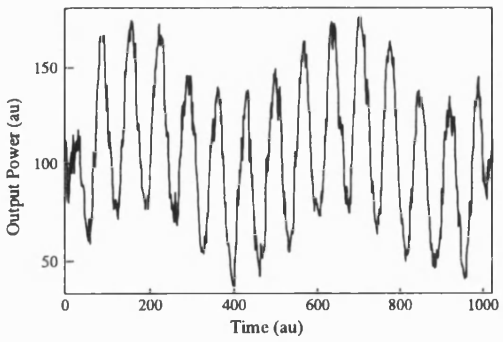

(a)

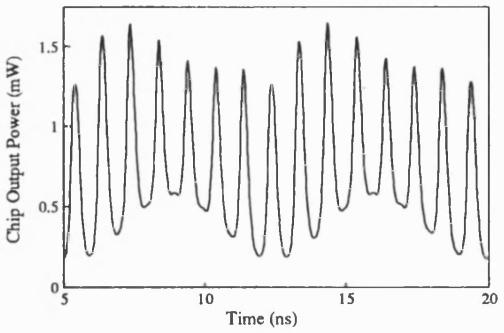

(b)

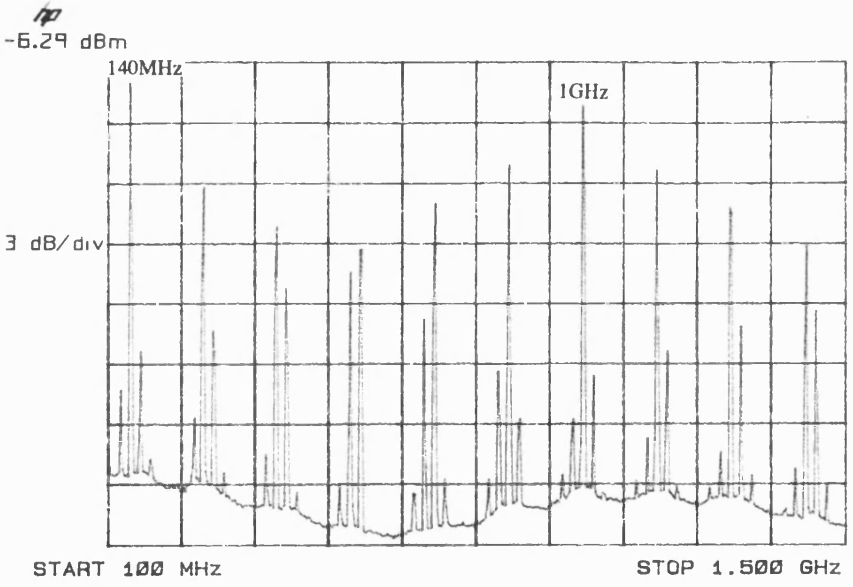

(c)

Figure 7.8 (a) Experimental time dependence of output power, (b) theoretical time dependence of output power, (c) experimental frequency spectrum. Conditions as for figure 7.6 except dfb temperature 19 °C, theoretical wavelength 1311.45 nm.

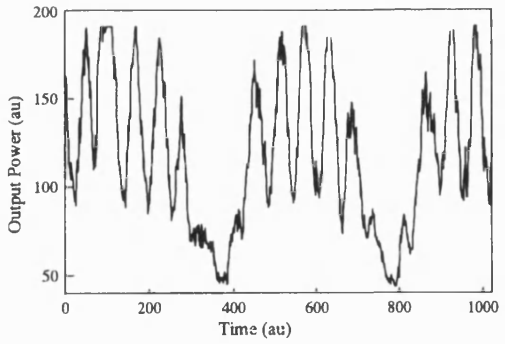

(a)

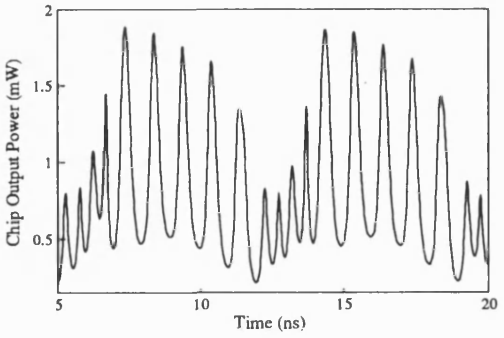

(b)

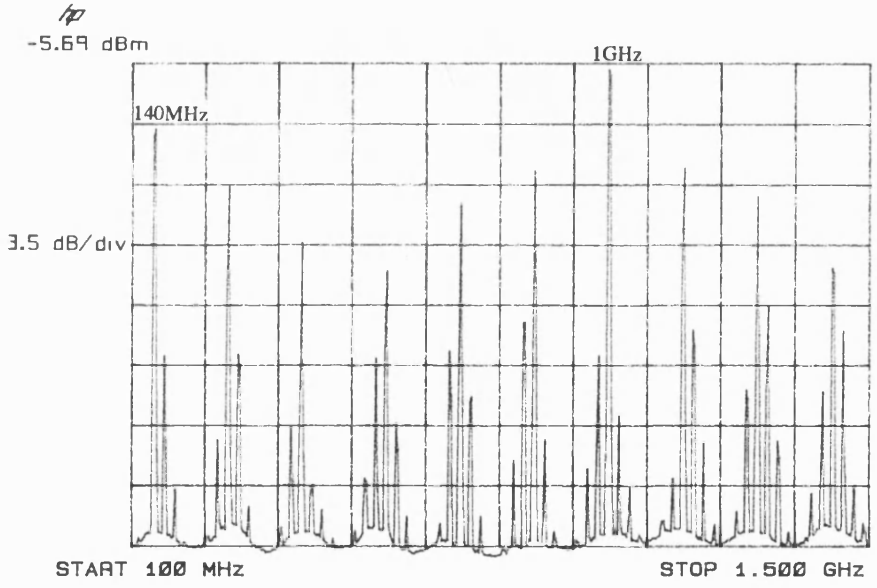

(c)

Figure 7.9 (a) Experimental time dependence of output power, (b) theoretical time dependence of output power, (c) experimental frequency spectrum. Conditions as for figure 7.6 except dfb temperature 20 °C, theoretical wavelength 1311.55 nm.

7.3 Frequency Upconversion Using Resonant Electrical Feedback

7.3.1 Introduction and Experimental Details

The 2.37 GHz electrical resonance signal produced by the bias current feedback loop gives rise to efficient modulation of the amplifier bias current. This can be used to provide frequency mixing, in conjunction with a modulated optical input signal, and this section investigates this effect, using electrical and optical measurements.

The experimental system is identical to that described in chapter 6 for the investigation of the feedback technique; in addition, the optical spectra presented in subsection 7.3.3 have been obtained using a scanning Fabry-Perot interferometer with a finesse of approximately 25.

7.3.2 Electrical Spectra

Figure 7.10 shows two frequency spectra, taken with and without bias current feedback, covering the range 100 MHz to 2.8 GHz, for the following conditions: SOA dc bias 80 mA; SOA temperature 17 °C; average input power -8.57 dBm; optical modulation frequency 140 MHz; omi 55 %; dfb laser temperature 16.8 °C. The lighter coloured spectrum has been obtained with the SOA dc biased, the darker spectrum under feedback conditions. Two effects are evident in this spectrum: firstly the effect of the high frequency electrical modulation, which reproduces the low frequency spectrum as sum and difference components around 2.37 GHz; secondly the feedback, which reduces the harmonic distortion, completely removing all frequency components above the fourth harmonic, and flattens the noise floor. In this case, although the rf gain has been reduced by 1.7 dB, the harmonic distortion and low frequency noise have been decreased by 11.4 dB and 15.4 dB respectively. The power in the 2.37 GHz frequency component is -8.5 dBm, which compares favourably with the -7.75 dBm in the 140 MHz component.

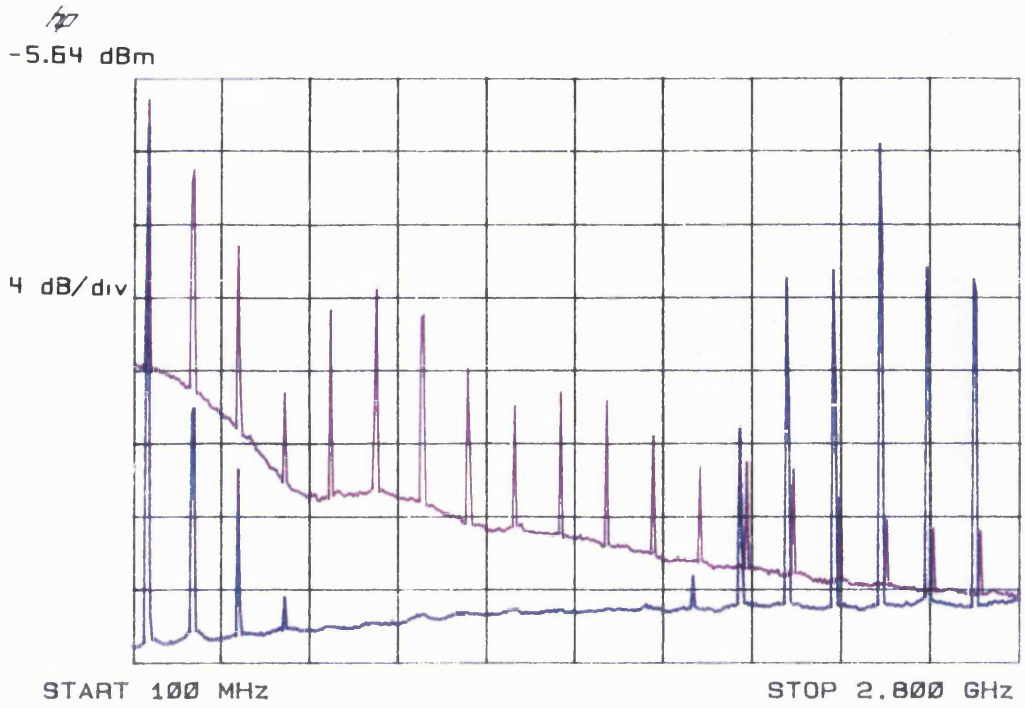

Figure 7.10 Electrical frequency spectra, with and without bias current feedback. SOA dc bias 80 mA, temperature 17 °C, average input power -8.57 dBm, optical modulation frequency 140 MHz, omi 55 %, laser temperature 16.8 °C.

Figure 7.11 shows the wavelength variation of the power at 2.37 GHz, compared with the power at 140 MHz, and with the power obtained at 2.37 GHz under direct bias modulation (from figure 7.5). Here it may be seen that, while the application of direct bias current modulation leaves the 140 MHz component unchanged, the effect of feedback is to effectively flatten the Fabry-Perot gain ripple, as reported in chapter 6. Where the 2.37 GHz frequency component is concerned, both modulation methods cause the wavelength dependence to be out of phase with that at 140 MHz; the power obtained with resonant feedback is, however, higher than that obtained through direct modulation, and shows a greater variation with wavelength. This is almost certainly due to the reinforcing effect of the feedback loop, which is feeding back signals at both 140 MHz and 2.37 GHz.

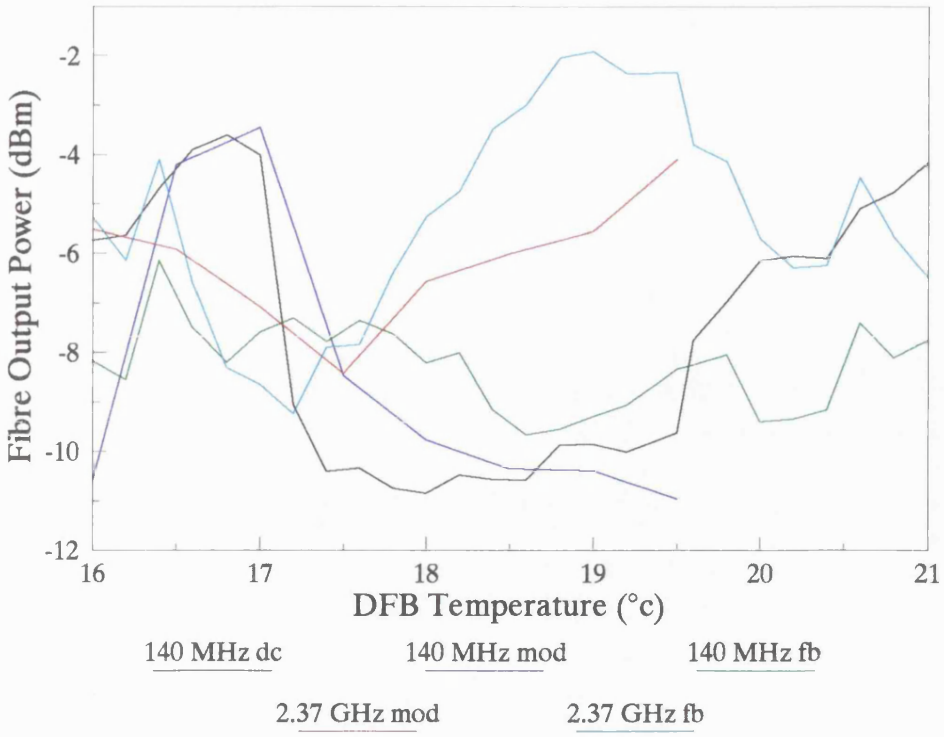

Figure 7.11 Wavelength variation of output power at 140 MHz and 2.37 GHz under conditions of dc bias, resonant feedback and direct bias current modulation. SOA dc bias 80 mA, temperature 17 °C, SOA rf modulation current 18 mA peak, average input power -8.3 dBm, optical modulation frequency 140 MHz, omi 57 %.

A further study was undertaken, to discover the power available in the higher harmonics of the 2.37 GHz feedback resonance signal. The wavelength dependence of the power in the first six harmonics is plotted in figure 7.12, for the following conditions: SOA dc bias current 80 mA; SOA temperature 17 °C; average input power -8.6 dBm; optical modulation frequency 140 MHz; omi 53 %. Wavelength dependence may be observed, due to the high facet reflectivities of the device. The maximum power obtained at 2.37 GHz is -2.2 dBm, 6.4 dB higher than the average input power. A maximum of -20 dBm is generated in the sixth harmonic, at 14.22 GHz. The upconversion of the 140 MHz signal, as demonstrated in figure 7.10, is repeated up to a centre frequency of 14.22 GHz; the high frequency roll-off of the SOA modulation response, and the rising noise floor of the spectrum analyser, prevent the accurate measurement of higher harmonics.

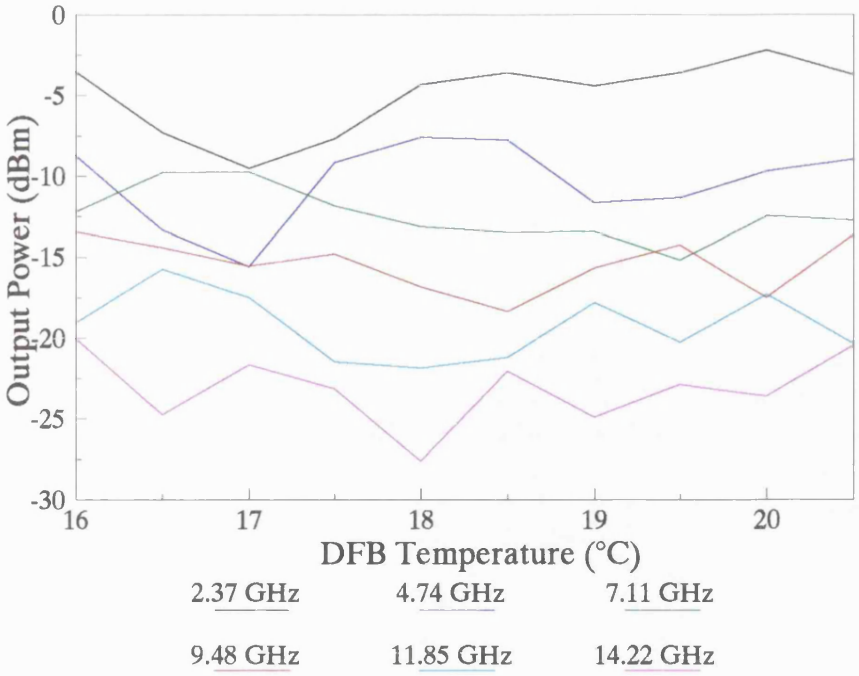

Figure 7.12 Wavelength dependence of the output power in the first six harmonics of 2.37 GHz feedback resonance signal. SOA dc bias 80 mA, temperature 17 °C, average input power -8.6 dBm, optical modulation frequency 140 MHz, omi 53 %.

7.3.3 Optical Spectra

The sidebands generated in the electrical spectrum, at 2.37 GHz spacing, may be expected to appear in the optical spectrum; this is in fact the case. This effect has possible applications in densely packed WDM systems, in which the channels may only be spaced by a few gigahertz, and so the wavelength shift provided by the feedback technique should suffice.

Optical spectra have been measured for a variety of laser wavelengths, with and without feedback, and sample results are presented in figures 7.13 - 7.16, for laser temperatures between 17 °C and 20 °C. The measurement conditions are as follows: SOA dc bias 80 mA; SOA temperature 17 °C; average input power -8.6 dBm; optical modulation frequency 140 MHz; omi 12.5 %. The low modulation index was necessary to prevent laser chirp obscuring the effect of the feedback resonance. Although the vertical axes are labelled in arbitrary units, they are all plotted to the same scale, and may be compared

directly. The finesse of the Fabry-Perot interferometer does not permit the sidebands at 140 MHz separation to be distinguished, but three sets of 2.37 GHz sidebands are visible on all plots.

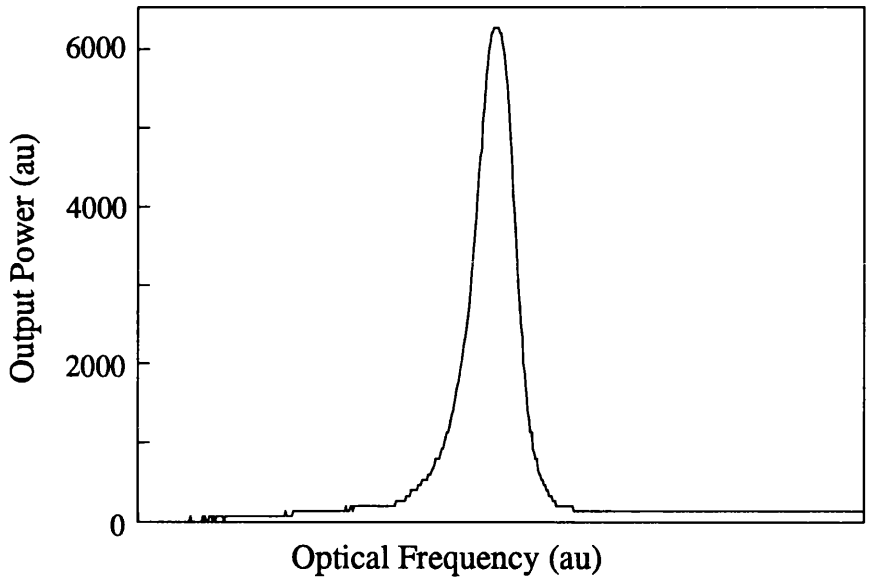

(a)

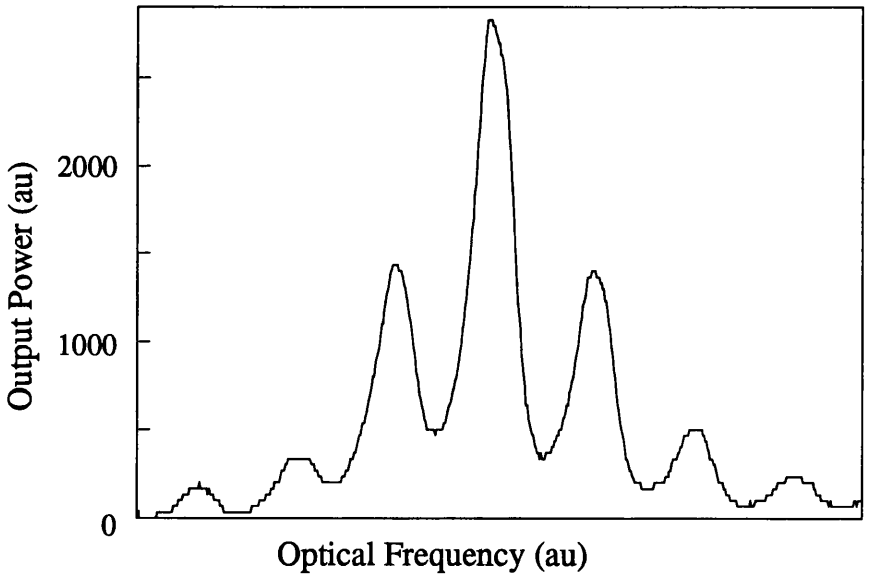

(b)

Figure 7.13 Optical spectra of SOA output power (a) with dc bias (b) with resonant feedback. SOA dc bias 80 mA, temperature 17 °C, average input power -8.6 dBm, optical modulation frequency 140 MHz, omi 12.5 %, laser temperature 17 °C.

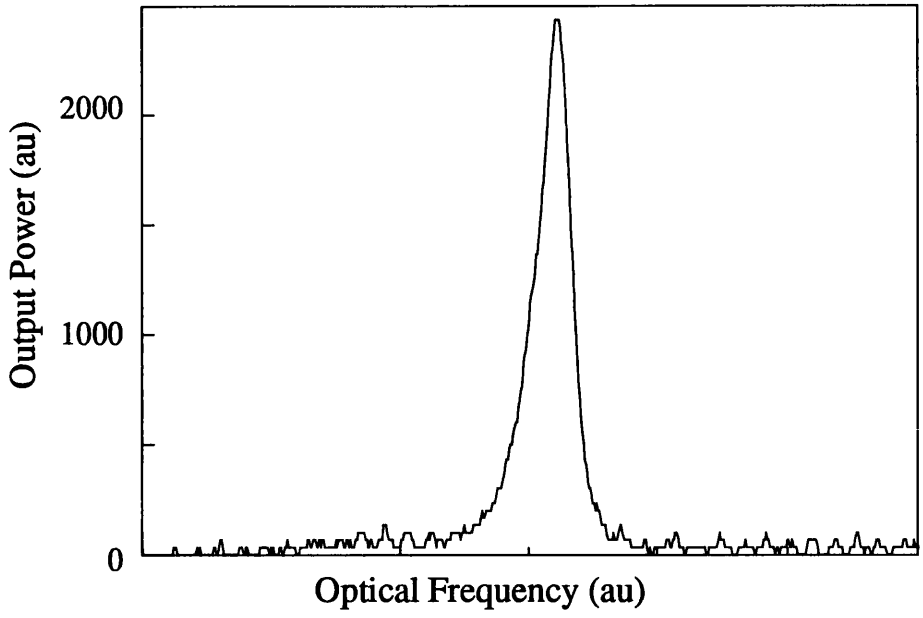

(a)

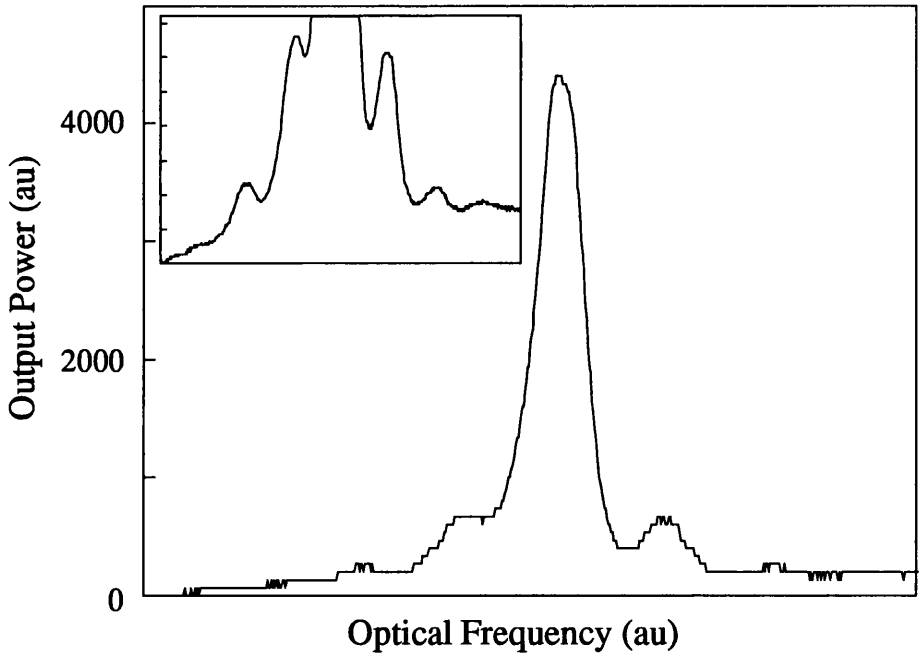

(b)

Figure 7.14 Optical spectra of SOA output power (a) with dc bias (b) with resonant feedback, inset showing detail of sidebands. Conditions as figure 7.13 except laser temperature 18 °C.

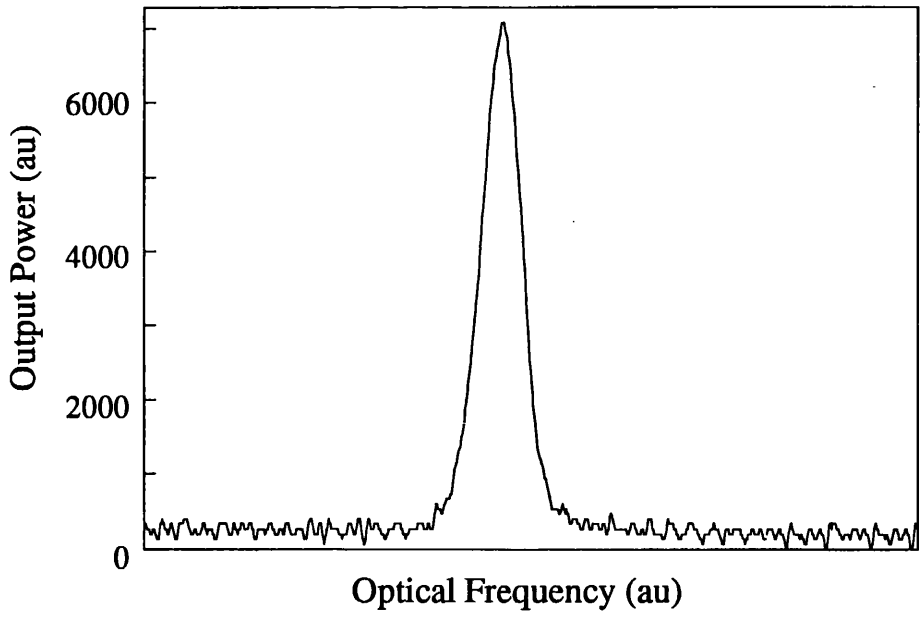

(a)

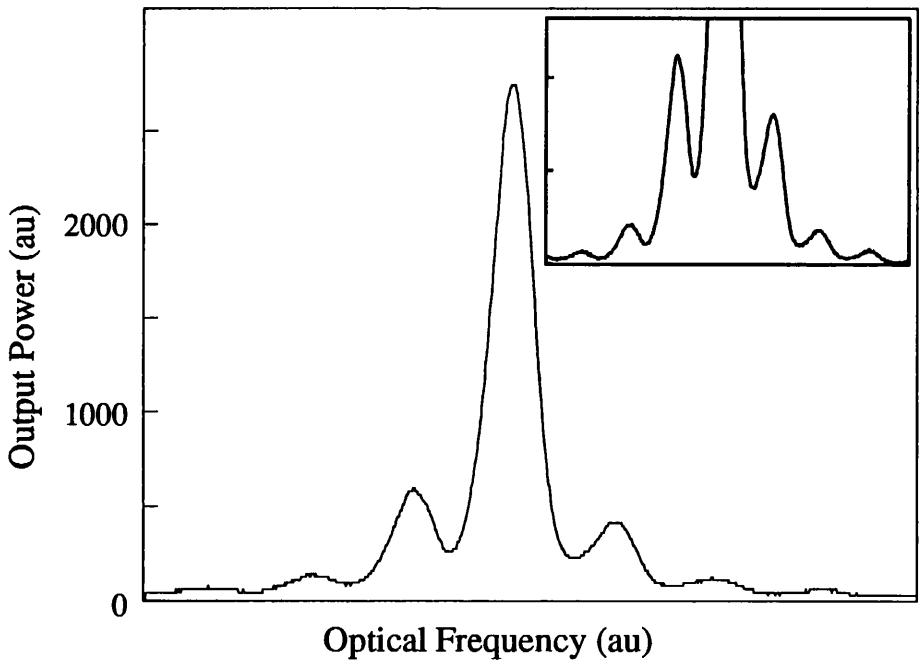

(b)

Figure 7.15 Optical spectra of SOA output power (a) with dc bias (b) with resonant feedback, inset showing detail of sidebands. Conditions as figure 7.13 except laser temperature 19 °C.

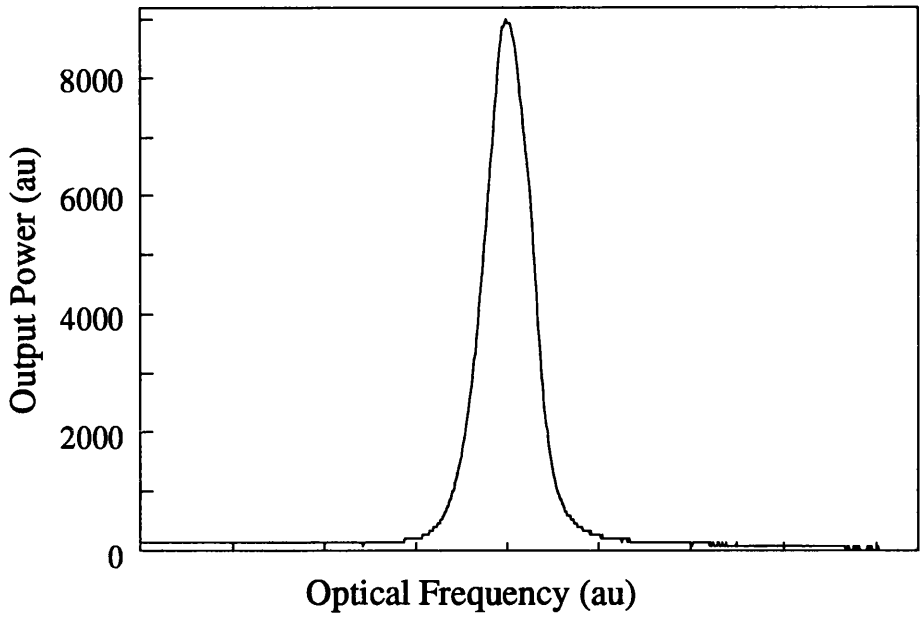

(a)

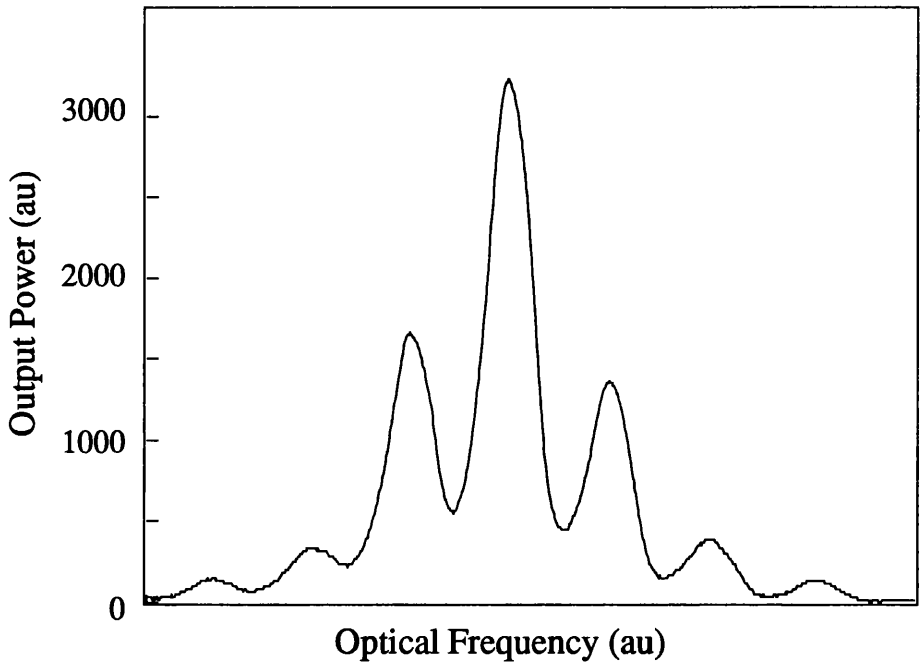

(b)

Figure 7.16 Optical spectra of SOA output power (a) with dc bias (b) with resonant feedback. Conditions as figure 7.13 except laser temperature 20 °C.

The reduction in average gain, previously quoted as the mechanism for noise reduction, may be seen here in the form of dc carrier suppression. The wavelength dependence of the optical carrier suppression has been measured, and compared with the change in electrical noise, for the conditions described above, and the results are presented in figure 7.17. The correlation between optical carrier suppression and electrical noise reduction is clear, confirming that the noise reduction is caused by a decrease in time averaged gain.

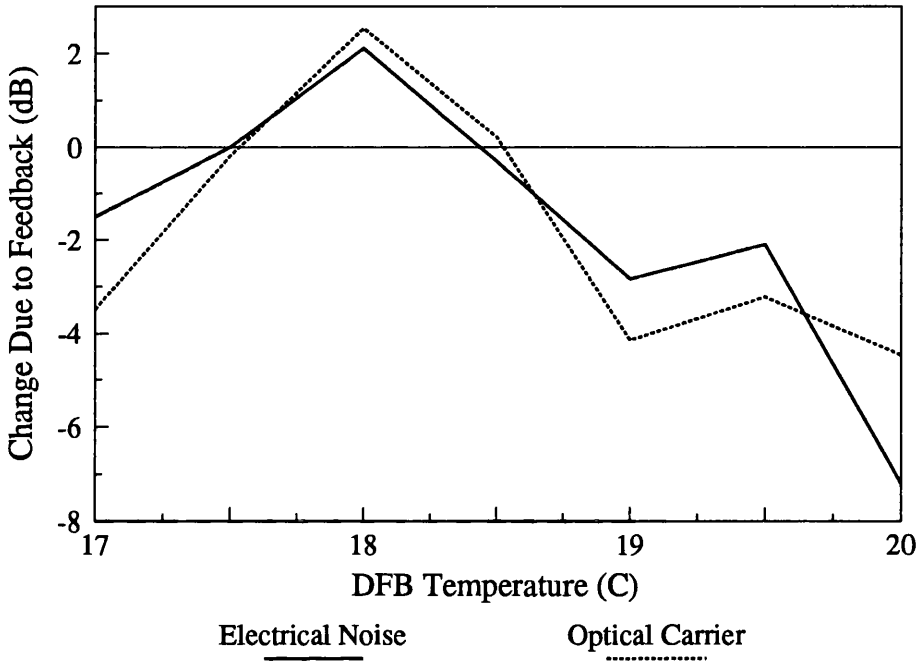

Figure 7.17 Correlation between optical carrier suppression and electrical noise reduction due to resonant bias current feedback. Conditions as figure 7.13.

Figure 7.18 shows an optical spectrum in which the dc carrier has been strongly suppressed by the feedback-induced sidebands. This spectrum was taken using a laser wavelength of 18.5 °C and an SOA dc bias of 35.5 mA, but the same result is attainable under different conditions.

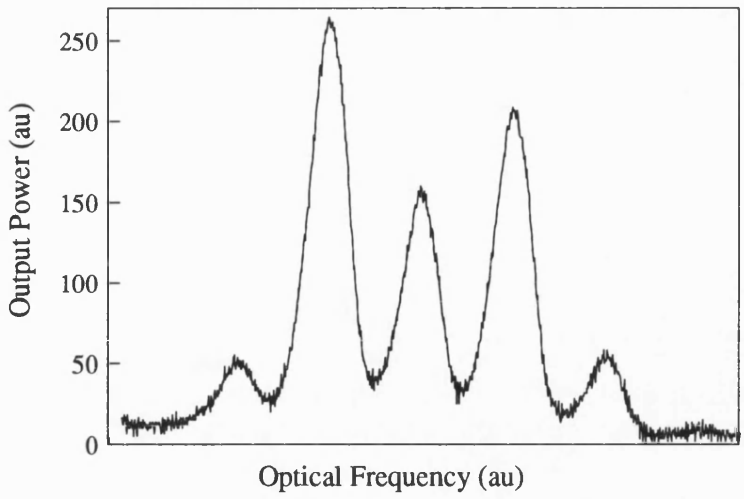

Figure 7.18 Optical spectrum obtained with resonant feedback showing dc carrier suppression. SOA dc bias 35.5 mA, temperature 17 °C, average input power -8.8 dBm, optical modulation frequency 140 MHz, omi 13 %, laser temperature 18.5 °C.

To show that this method of resonant electrical feedback modulates the SOA more effectively than direct bias current modulation, figure 7.19 is an optical spectrum taken under the same conditions as figure 7.13, but with direct modulation of the bias current. No optical sidebands are visible on this plot.

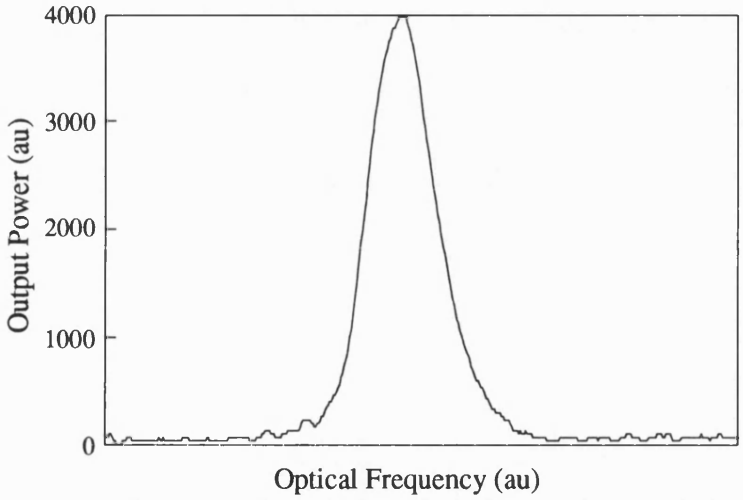

Figure 7.19 Optical spectrum taken with direct modulation of the SOA bias current at 2.37 GHz. SOA dc bias 80 mA, temperature 17 °C, modulating current 18 mA peak, average input power -8.6 dBm, optical modulation frequency 140 MHz, omi 12.5 %, laser temperature 17 °C.

7.3.4 Discussion

The high frequency modulation of the SOA is found to be more effective when aided by electrical feedback. Effective modulation frequency conversion is obtained up to a centre frequency of 14.22, the sixth harmonic of the feedback resonance signal. Successful wavelength conversion is demonstrated using the resonant feedback circuit; no such conversion is observed when direct modulation is employed. The mechanism of noise reduction is confirmed as suppression of the dc gain of the SOA.

7.4 Frequency Downconversion for Subcarrier Multiplexing Applications

7.4.1 Introduction and Experimental Details

The optical carriers used in subcarrier multiplexed systems are modulated at frequencies of the order of gigahertz. It may thus be necessary to downconvert the carrier frequency prior to detection and demultiplexing, and this is investigated here as a possible application for semiconductor optical amplifiers.

Two methods of frequency mixing are considered; electro-optic, in which the SOA bias current is directly modulated to produce mixing with the modulated optical input, and all-optical, in which two laser sources are used, modulated at different frequencies. The experimental systems are shown in figures 7.20 and 7.21. In figure 7.21, the biasing arrangements for the lasers and the SOA have been omitted for simplicity; as before, they are biased and modulated via bias tees.

The two sources used are the dfb and multimode lasers described before; where the dfb is used, it is directly modulated using a Gigatronics rf source; the multimode laser is modulated using the Hewlett-Packard rf sweep oscillator used in chapter 6; the SOA is modulated by the Systron-Donner source. The fibre immediately after the dfb is wound around a section of plastic pipe, to simulate the losses experienced in a fibre system.

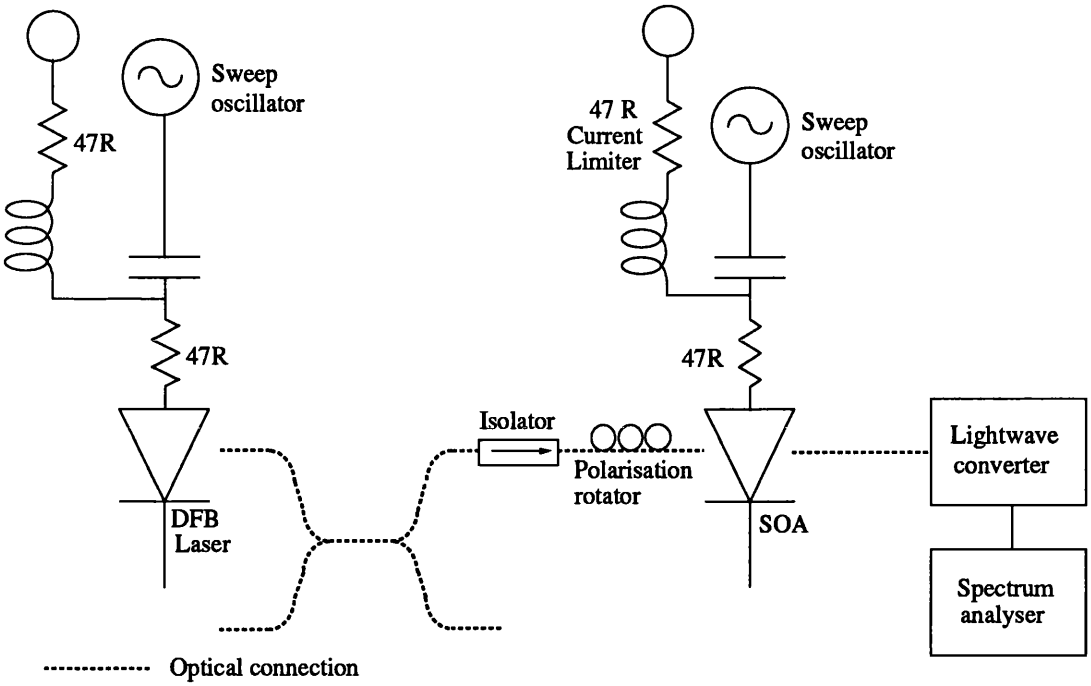

Figure 7.20 Experimental system used to investigate electro-optic modulation frequency mixing in an optical amplifier.

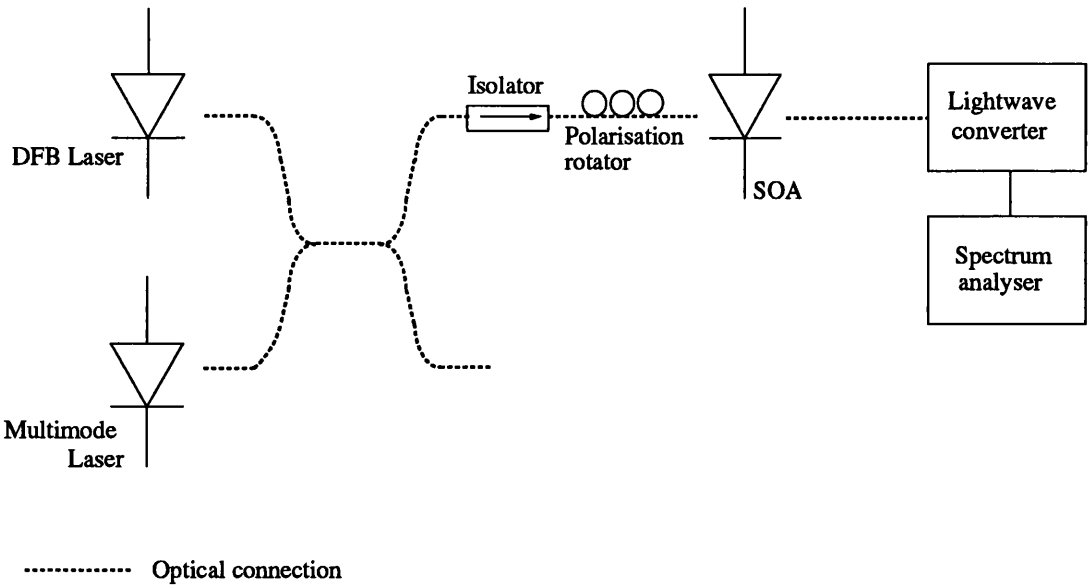

Figure 7.21 Experimental system used to investigate all-optical modulation frequency mixing in an optical amplifier.

7.4.2 Electro-Optic Frequency Downconversion

In this experiment, the dfb is used as the source, modulated at 2 GHz to represent the optical carrier; the SOA bias is modulated at 1.5 GHz, the local oscillator (LO) frequency, f_{lo}. The difference frequency, $f_c - f_{lo}$, of 0.5 GHz is required at the output.

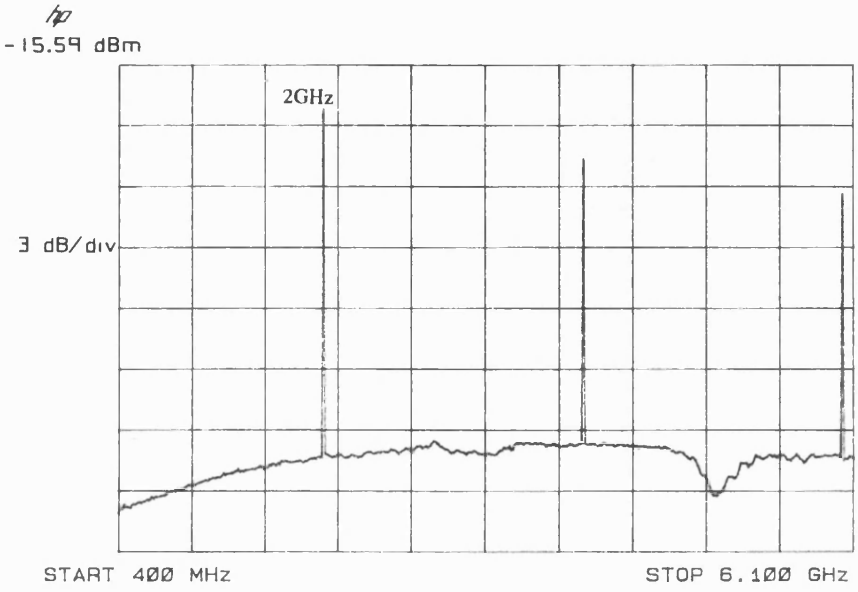

(a)

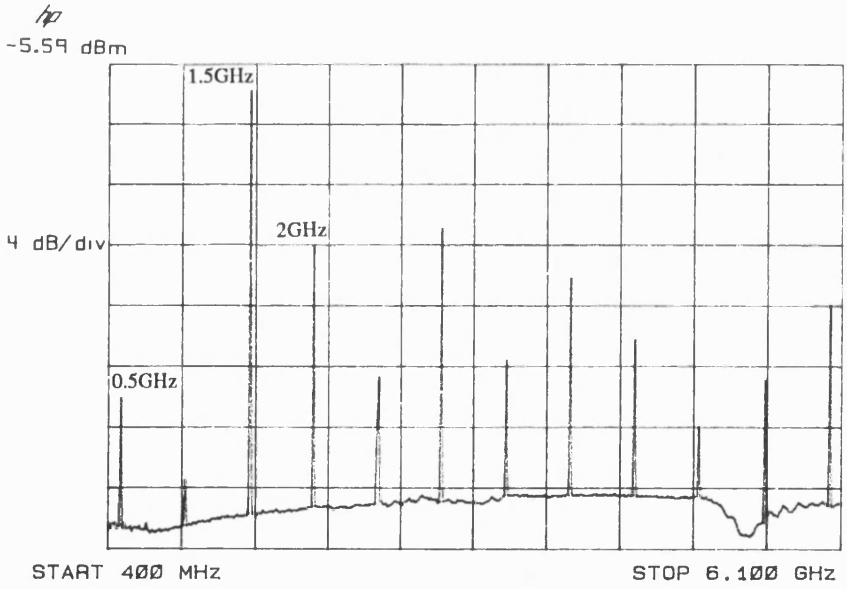

(b)

Figure 7.22 Electrical spectra of (a) SOA output power dc biased (b) SOA output with rf modulation of 30 mA peak. SOA dc bias 80 mA, temperature 17 °C, rf modulating current 30 mA peak, average input power -22.07 dBm, carrier frequency 2 GHz, omi 70.7 %, LO frequency 1.5 GHz, laser temperature 16.5 °C.

Two frequency spectra are presented in figure 7.22 to show the effect of electro-optic frequency mixing. The conditions are as follows: SOA dc bias 80 mA; SOA temperature 17 °C; rf modulation current 30 mA peak; average input power -22.07 dBm; omi 70.7 %; laser temperature 16.5 °C, corresponding to a gain trough at this value of input power. Figure 7.23 shows the corresponding spectra for a laser temperature of 18.5 °C, corresponding to a peak gain wavelength.

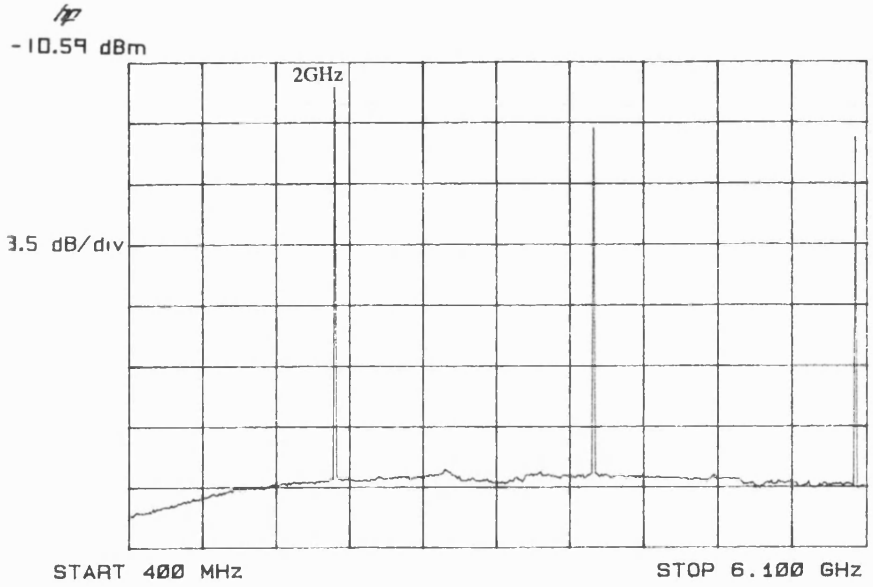

(a)

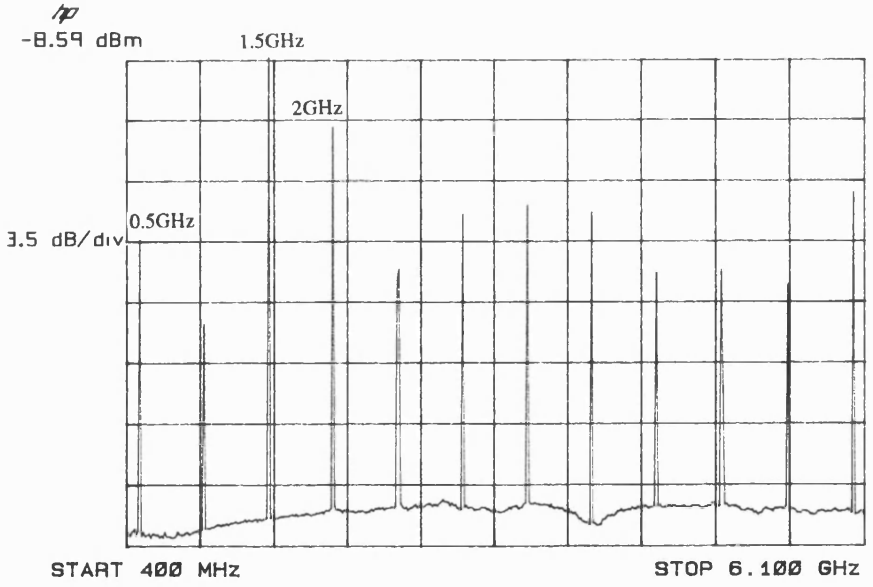

(b)

Figure 7.23 Electrical spectra of (a) SOA output power dc biased (b) SOA output with rf modulation of 30 mA peak. Conditions as figure 7.22 except laser temperature 18.5 °C.

It may be observed that there is more power available in the difference frequency component at the peak gain wavelength, although there is slightly less power at 1.5 GHz than for the trough wavelength, as expected.

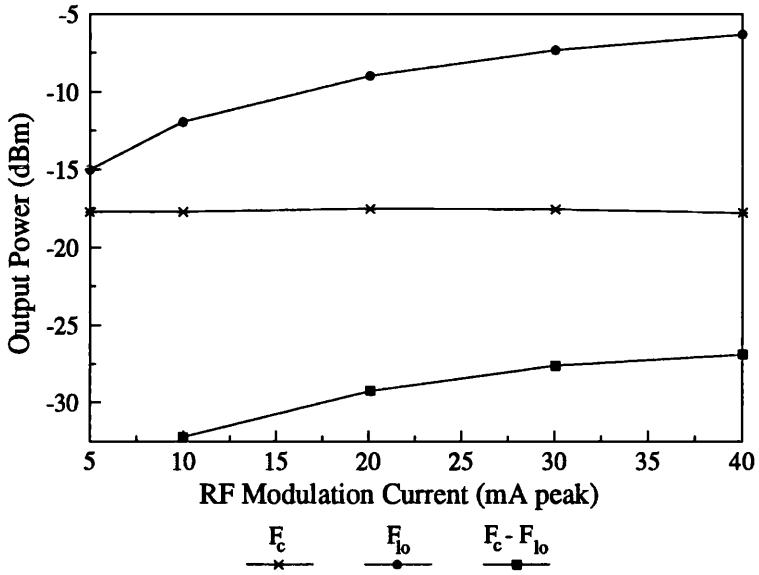

(a)

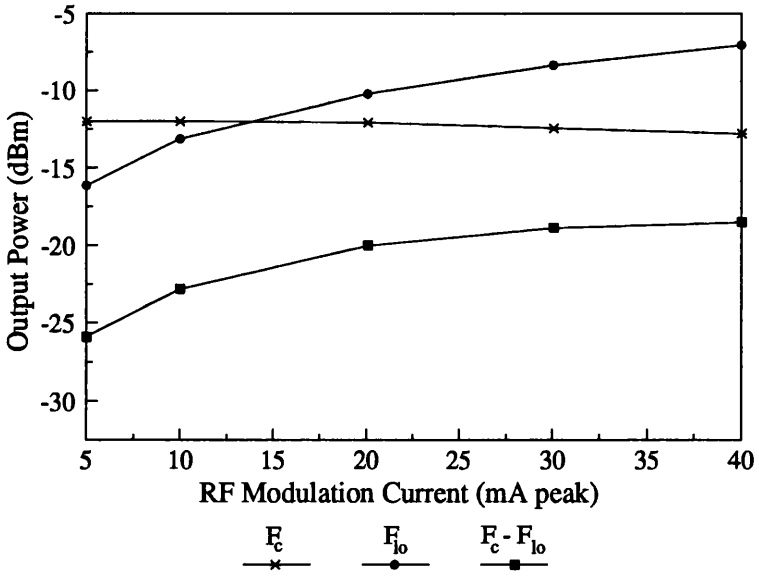

(b)

Figure 7.24 Dependence upon SOA modulation current of output power components at the carrier, LO and difference frequencies. Conditions as figure 7.22 except laser temperature (a) 16.5 °C (b) 18.5 °C.

Figure 7.24 shows the dependence upon the magnitude of the rf modulating current of the output power at the carrier frequency, the LO frequency and the difference frequency, for both signal wavelengths.

In both cases the application of the rf modulation has no significant effect on the output at the signal frequency; the decline in power observed in figure 7.24(b) is due to temperature effects in the rf source used to modulate the laser. The output at the LO frequency increases with rf modulation current, but shows signs of saturation at higher currents, as does the power in the difference frequency component. Where the signal wavelength corresponds to a peak gain wavelength (7.24(b)), higher power is obtained at the difference frequency; the variation with wavelength observed here is more than 5 dB.

7.4.3 All-Optical Frequency Downconversion

In this case the dfb is modulated at 2 GHz to represent the optical carrier, and the multimode laser is modulated at 1.5 GHz to act as the local oscillator. The two signals are mixed in the fibre coupler, before entering the SOA. Two dfb wavelengths are again used, to investigate the effect of signal wavelength.

Figure 7.25 shows input and output power spectra for the following conditions: SOA dc bias 80 mA; SOA temperature 17 °C; dfb temperature 16.5 °C; dfb average power -18.65 dBm; dfb omi 77 %; multimode laser average power -12.58 dBm; omi 60.11 %. The input spectrum, figure 7.25(a), shows the two frequency components of the input signal. A weak mixing component is visible at 3.5 GHz ($f_c + f_{lo}$). The ripples in the spectrum around 2 GHz are produced by the multimode laser when directly modulated.

In the output spectrum, figure 7.25(b), several sum and difference and harmonic terms may be seen. The power obtained at the difference frequency, 0.5 GHz, is -22.08 dBm.

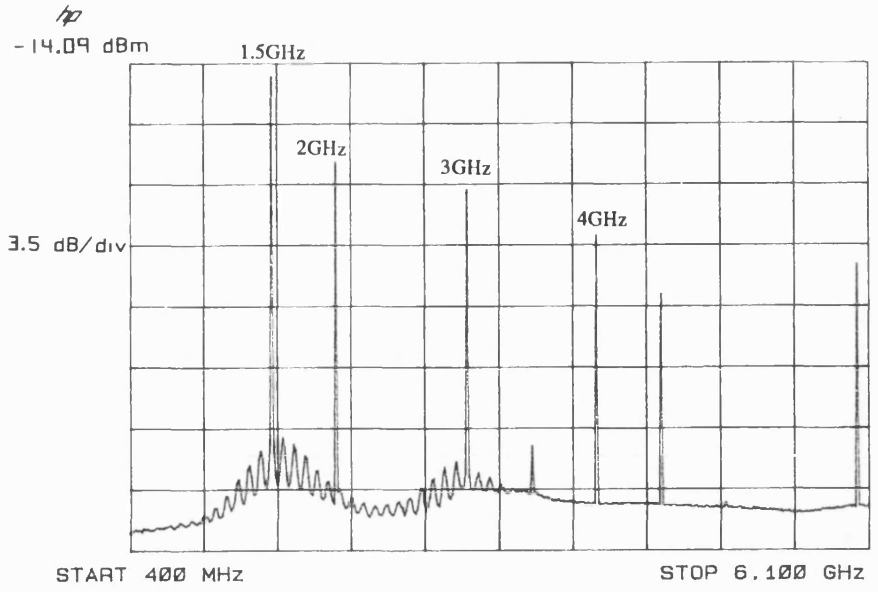

(a)

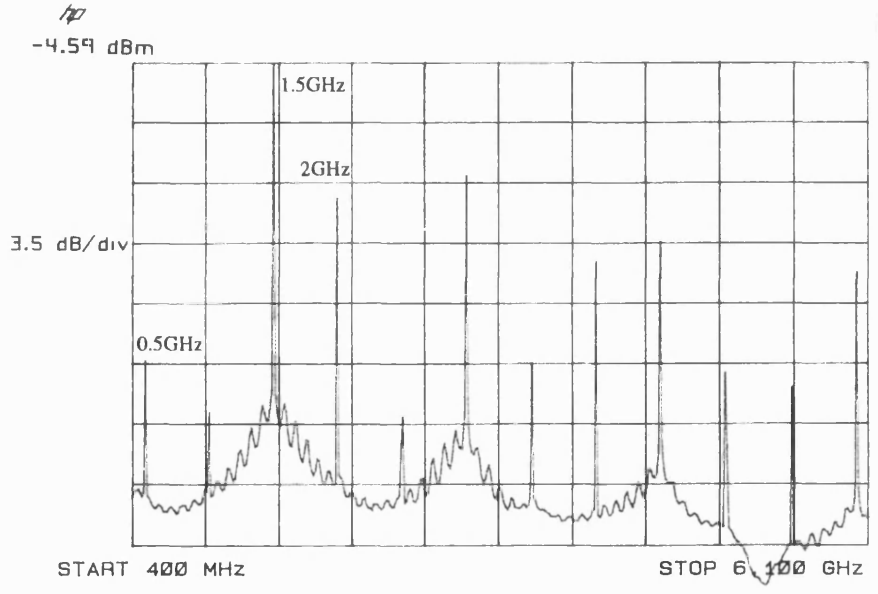

(b)

Figure 7.25 Electrical frequency spectra of (a) input signal and (b) SOA output for all-optical frequency mixing. SOA dc bias 80 mA, temperature 17 °C, dfb temperature 16.5 °C, average power -18.65 dBm, omi 77 %, multimode laser average power -12.58 dBm, omi 60.11 %.

The power in the difference frequency is slightly higher when a dfb temperature of 18.5 °C is used (figure 7.26), not surprisingly since this represents a peak optical gain wavelength.

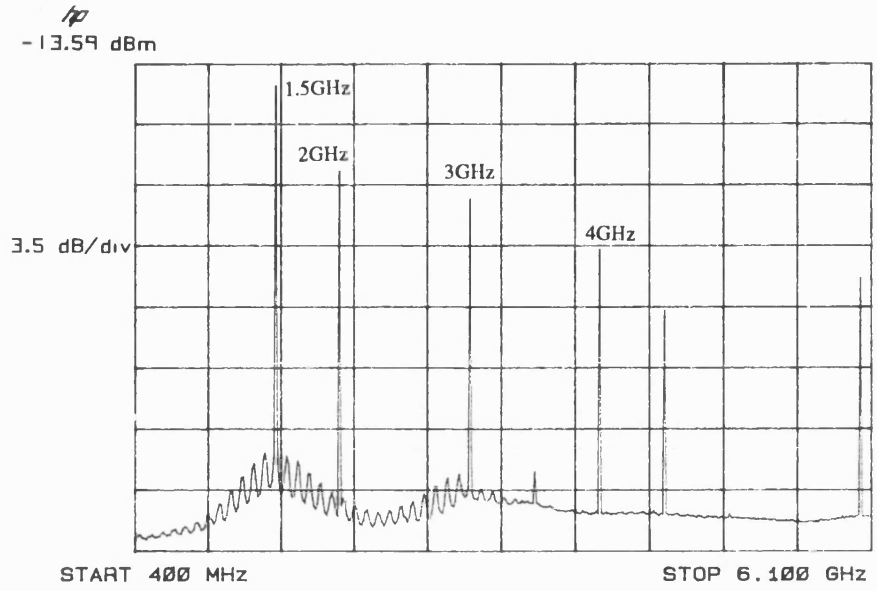

(a)

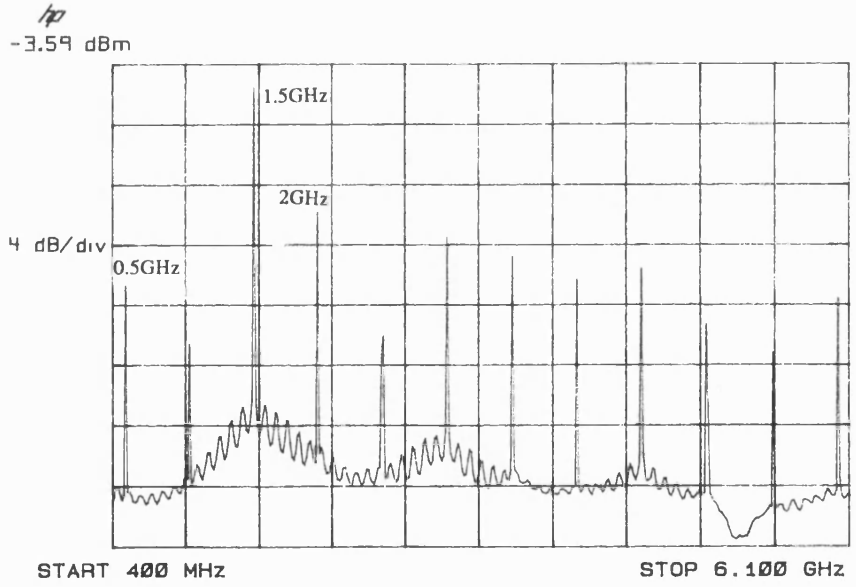

(b)

Figure 7.26 Electrical spectra of (a) input signal and (b) SOA output for all-optical frequency mixing. Conditions as figure 7.25 except dfb temperature 18.5 °C.

The output power at the difference frequency may be greatly enhanced if the SOA bias current is modulated at this frequency, as shown in figures 7.27(a) and (b) for the conditions used in figures 7.25 and 7.26, and a modulating current of 5 mA peak. This

is not a practical systems solution, however, since all three modulation frequencies would require very tight control, as would the phase of the modulating current with respect to the difference frequency signal generated inside the amplifier.

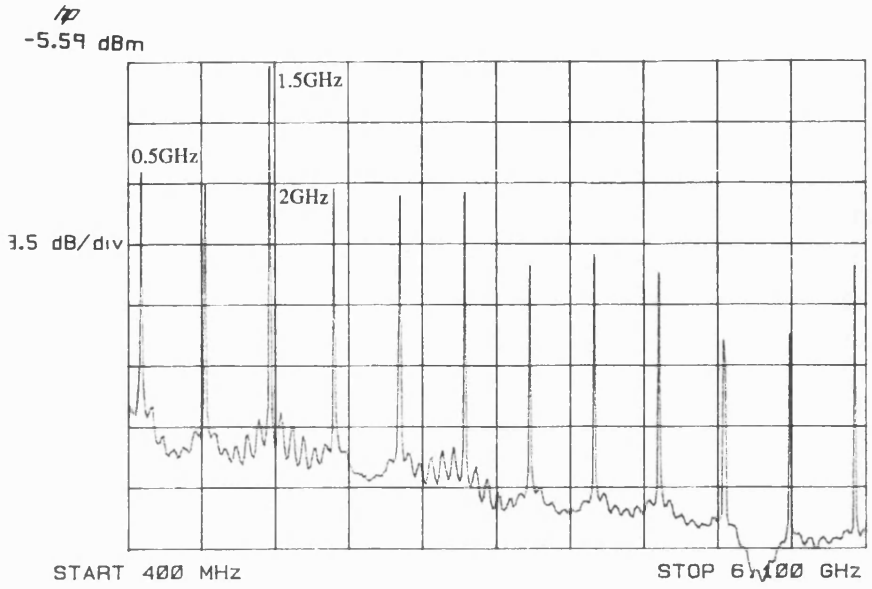

(a)

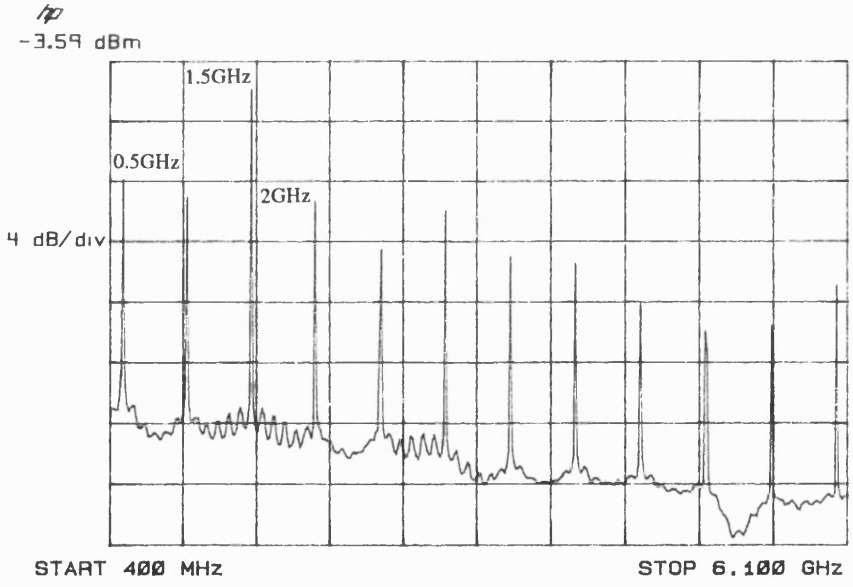

(b)

Figure 7.27 Electrical frequency spectra of the SOA output power for all-optical frequency mixing enhanced by direct modulation of the SOA bias current. (a) conditions as figure 7.25 with SOA rf modulating current 5 mA peak at 0.5 GHz, (b) conditions as figure 7.26 with SOA rf modulating current 5 mA peak at 0.5 GHz.

Figure 7.28 shows the output power obtained at the signal, LO and difference frequencies, as a function of local oscillator optical modulation index.

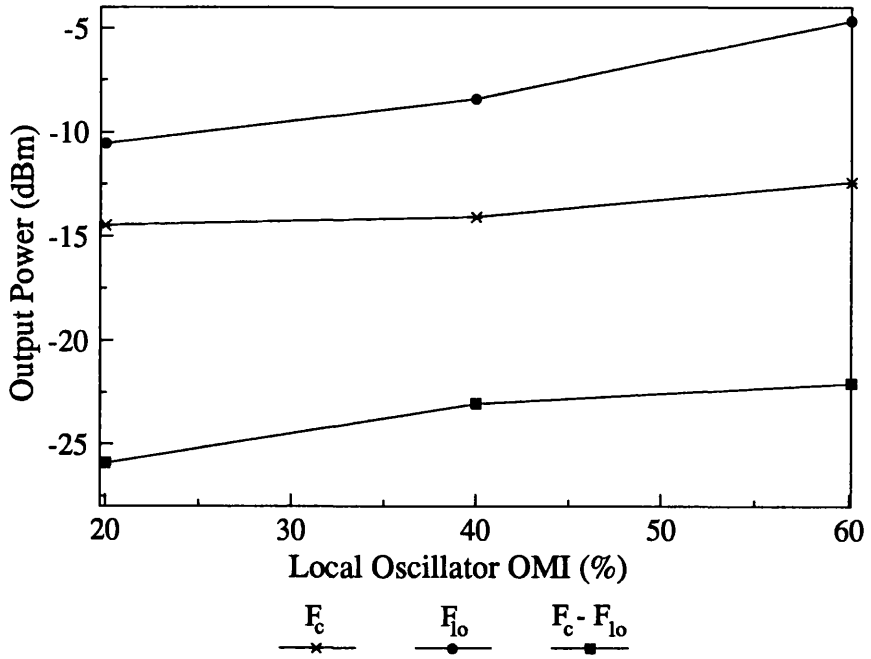

(a)

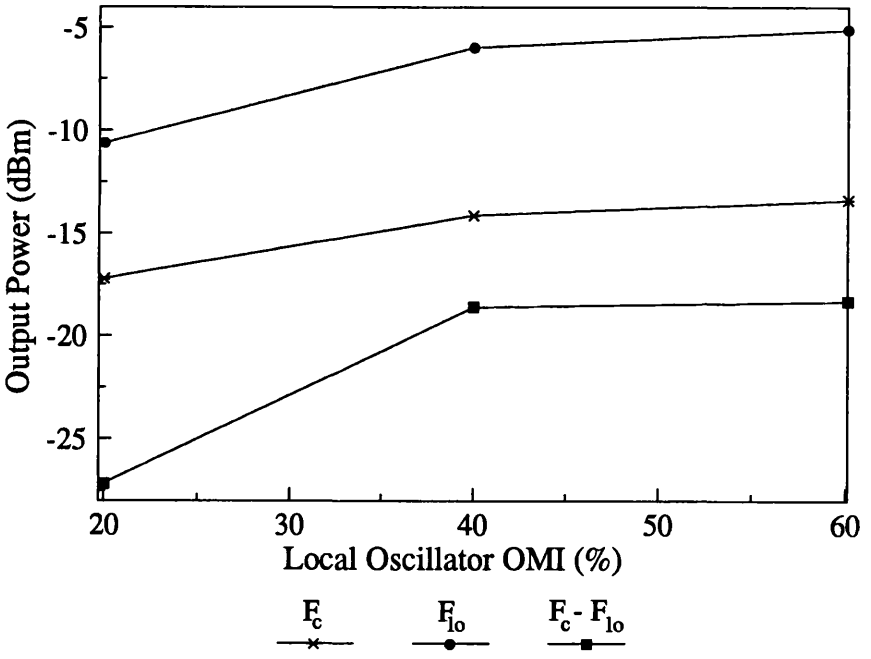

(b)

Figure 7.28 Dependence upon local oscillator optical modulation index of SOA output power at carrier, LO and difference frequencies. Conditions as figure 7.24 except dfb temperature (a) 16.5 °C and (b) 18.5 °C.

There is a small variation in power at the signal frequency due to the increased omi of the LO signal; this is due to variations in the input signal to the SOA. Again, there is evidence of saturation of the power at the difference frequency as the LO signal is increased. At the peak wavelength (18.5 °C), the difference signal may be made comparable to that obtained using electro-optic mixing (figure 7.24(b)); at the trough wavelength (16.5 °C), the difference signal is considerably higher than for electro-optic mixing under comparable conditions.

7.4.4 Discussion

Two types of modulation frequency conversion have been investigated; electro-optic and all-optical. It has been found that the signal wavelength has a strong effect on the output spectrum of the SOA, due to the high facet reflectivity of the device, and so eventual use of this method in SCM systems will require a travelling-wave or near travelling-wave device. All-optical frequency mixing, in which the signal and local oscillator frequencies are both optically transmitted, is shown to be more effective than the electro-optic method, and may be enhanced further if the SOA bias current is modulated at the required frequency.

7.5 Laser Linewidth Measurement

7.5.1 Introduction and Experimental Details

For the long-haul, high bit rate optical communication systems of the future, very narrow line sources are required. The linewidths of these lasers, which may be of the order of kilohertz, cannot be measured by monochromators or Fabry-Perot interferometers. However, the Mach-Zehnder interferometer, which has long been used to analyse laser phase noise [2], has proved itself equal to the task [3].

In an unbalanced Mach-Zehnder interferometer, the input signal is split into two paths, one being delayed with respect to the other, and recombined at the output. The interference between the two components of the signal converts the optical phase noise at the input of the device to intensity noise at the output. Thus, the electrical spectrum of the output, viewed on a spectrum analyzer, represents the optical spectrum at the input.

Because the interference signal at the output of the interferometer is centred at 0 Hz, however, it is necessary in many situations to shift it up in frequency, using for example an acousto-optical modulator. However, modulators introduce loss into the system, and in an unbalanced high resolution system one path could conceivably be several kilometres long. Here, optical gain may be required to enhance fringe visibility at the output.

In this case, the linewidth to be measured is that of the dfb laser, and it is proposed that the optical amplifier resonant feedback system could be used to provide frequency shifting of the interference signal from 0 Hz to 2.37 GHz. The experimental system used to assess the feasibility of this technique is shown in figure 7.29. The input to the spectrum analyser used in this experiment has a capacitor to block any dc signal; for this reason, the spectrum between ±10 MHz is unreliable, and thus the frequency shift is necessary in this case for an accurate observation of the laser spectrum.

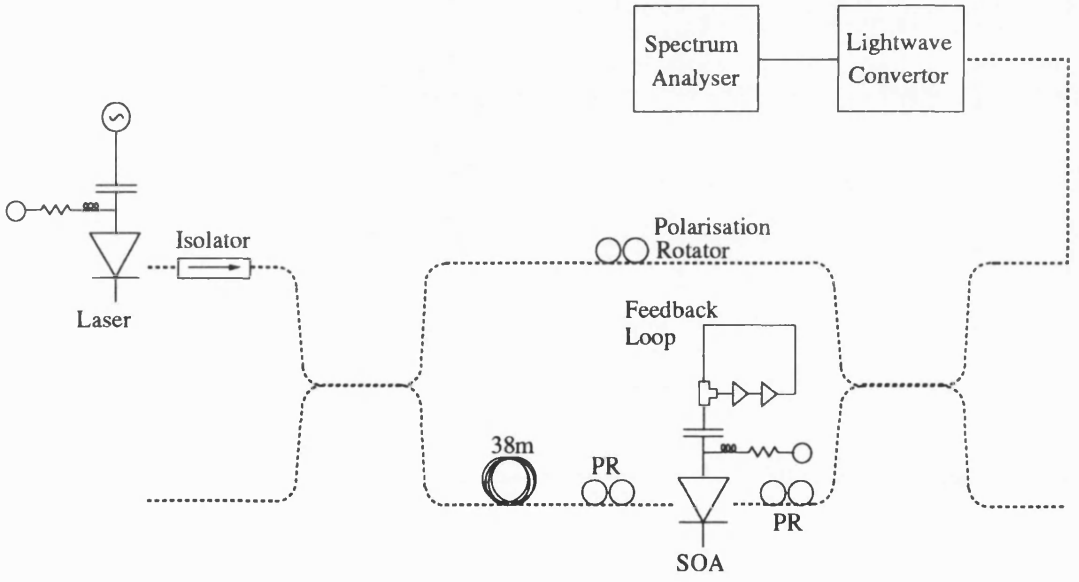

Figure 7.29 Laser linewidth measurement system, consisting of singlemode fibre unbalanced Mach-Zehnder interferometer and semiconductor optical amplifier with resonant electrical feedback.

The Mach-Zehnder is an unbalanced singlemode fibre device, with a 38 m delay line, corresponding to a delay time of approximately 0.19 μs, which gives a measurement resolution of approximately 5.26 MHz. The optical amplifier is inserted into the long arm of the interferometer, where it can perform frequency shifting, using the resonant

electrical feedback circuit, and also compensate for any losses induced by the delay line. The measurement should also be possible with the SOA circuit either before or after the interferometer.

7.5.2 Results

The laser linewidth has been measured under cw conditions, as the modulated output from the SOA obscures the effects of chirp. This is a disadvantage of this method, which it should be possible to overcome with further research.

Figure 7.30 shows sample frequency spectra of the interferometer output, obtained both without and with the SOA in the interferometer. The conditions are as follows: SOA dc bias 80 mA; SOA temperature 17 °C; dfb temperature 18 °C; Mach-Zehnder input power -8.26 dBm. The blue line represents the spectrum obtained without the SOA present in the interferometer, the red line that observed with the addition of the SOA and feedback circuit.

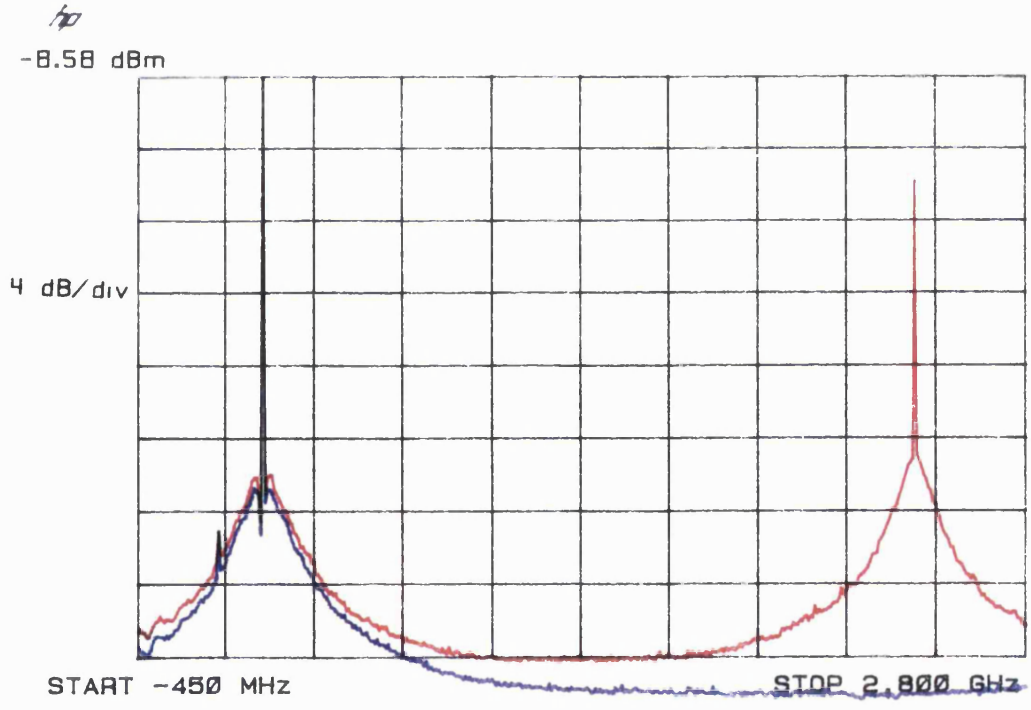

Figure 7.30 Frequency spectra of Mach-Zehnder interferometer output signal, with and without the SOA as frequency shifter. SOA dc bias 80 mA, temperature 17 °C, Mach-Zehnder input power -8.26 dBm, laser temperature 18 °C.

The sharp spike at 0 Hz, and that at approximately -150 MHz, are generated by the dc source inside the spectrum analyser; that at 2.37 GHz is the narrow line emitted by the SOA due to the modulation of the resonant feedback. Measurement of the linewidth of this frequency component is limited by the minimum resolution of the spectrum analyser, which is 1 kHz, and so this line is not expected to interfere with laser linewidth measurements.

It may be observed from this spectrum that the addition of the SOA with resonant electrical feedback has no significant effect on the spectrum around 0 Hz, also that the laser phase noise spectrum has been reproduced at 2.37 GHz, enabling measurement of the linewidth. The use of resonant feedback, as opposed to direct modulation of the SOA bias current to produce the frequency shift, has the added advantages of low output noise and distortion, increased depth of modulation, and a narrow linewidth.

As the delay in the long arm of the interferometer is longer than the laser coherence time (approximately equal to the inverse of the linewidth), the phase noise spectrum at the output of the interferometer is expected to be Lorentzian in shape [3]. A simple comparison between experimental lineshapes and a pure Lorentzian function has confirmed this to be the case, and thus it may be assumed that the observed linewidth is twice the real value [3].

The linewidth of the dfb has been measured for four different laser temperatures (wavelengths), and the results are plotted in figure 7.31, as a function of the inverse of the fibre output power. The SOA dc bias is again 80 mA, and its temperature 17 °C. The dfb bias current is varied to alter the output power.

The function has the classic form [4], the linewidth decreasing linearly with inverse output power until a minimum is reached, after which it begins to rise again. As the minimum linewidth measured is of the order of 50 MHz, the measurement is not limited by the resolution of the interferometer.

7.5.3 Discussion

Measurement of laser linewidth, using a Mach-Zehnder interferometer and an optical amplifier with resonant electrical feedback, has been demonstrated. It has been shown that the insertion of the SOA circuit has no appreciable effect on the observed linewidth,

and that it acts as an efficient frequency shifter. The linewidth of a dfb laser has been measured, at four different wavelengths, as a function of inverse fibre output power. The plots have the expected shape, and the measurement is not resolution-limited.

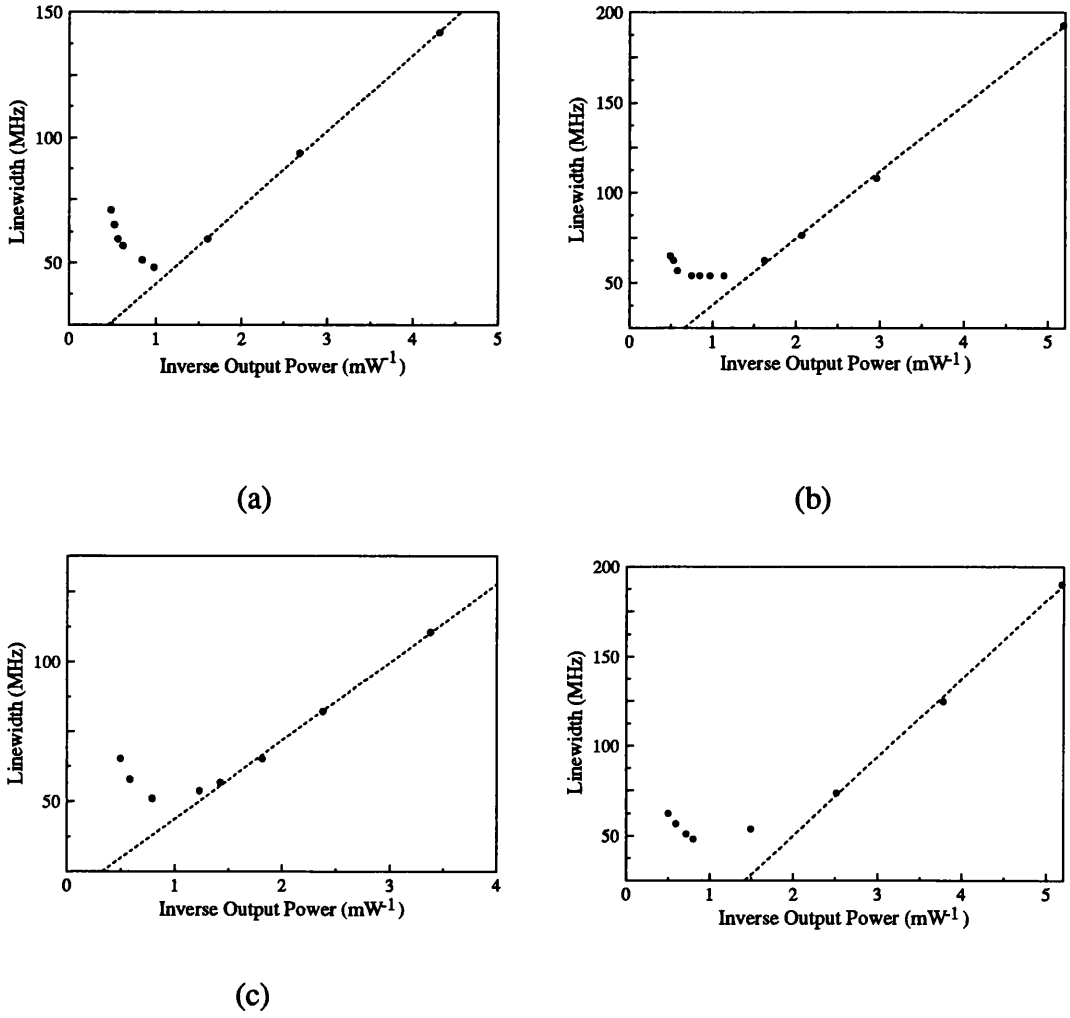

Figure 7.31 DFB laser linewidth as a function of inverse output power measured by Mach-Zehnder interferometer using an SOA and resonant feedback circuit as frequency shifter. SOA dc bias 80 mA, temperature 17 °C, dfb temperature (a) 17 °C (b) 18 °C (c) 19 °C (d) 20 °C.

7.6 Conclusions

This chapter has investigated several different methods of frequency conversion, using an optical amplifier. Frequency upconversion has been achieved using direct modulation of the bias current of the SOA, in conjunction with a modulated optical input signal. It is shown that the SOA can be modulated at frequencies up to 3.8 GHz, with a 3 dB down frequency of 1.2 GHz. The output power at the electrical modulation frequency, and the form of the electrical frequency spectrum, depend upon the signal wavelength, due to the high facet reflectivities of this device.

Frequency upconversion has also been demonstrated using the 2.37 GHz signal generated by the SOA electrical feedback loop. Effective conversion of the 140 MHz optical signal is demonstrated up to a centre frequency of 14.22 GHz, the sixth harmonic of the feedback resonance signal. The use of resonant feedback produces higher output power at 2.37 GHz than direct bias current modulation of the same rf power, due to the reinforcing effect of the bias current feedback signal. Wavelength conversion is also demonstrated, an effect which could find applications in dense WDM systems. This effect is not observed under conditions of direct bias current modulation, confirming that the resonant feedback method provides more effective modulation of the SOA gain. DC gain suppression is confirmed as the mechanism of noise reduction reported in chapter 6.

Modulation frequency downconversion, expected to find applications in SCM receivers, has been investigated using electro-optic and all-optical techniques. Again, the effectiveness of the conversion depends upon the signal wavelength. All-optical mixing is found to be more effective than the electro-optic technique, and may be reinforced by direct modulation of the SOA bias current.

The frequency conversion provided by the resonant feedback circuit has been used to shift the output from a Mach-Zehnder interferometer from 0 Hz to 2.37 GHz, and thus permit measurement of the linewidth of a dfb laser. The insertion of the SOA circuit into the interferometer makes no appreciable difference to the observed linewidth, due to the low noise, low distortion characteristics of the SOA with feedback.

7.7 References

1. T E Darcie, S O'Brien, G Raybon, C A Burrus: "Optical mixer-preamplifier for lightwave subcarrier systems", *Electron. Lett.* **24**, pp. 179-180, 1988.
2. J A Armstrong: "Theory of interferometric analysis of laser phase noise", *J. Opt. Soc. Am*, 1966, **56**, pp.1024-1031, 1966.
3. T Okoshi, K Kikuchi, A Nakayama: "Novel method for high resolution measurement of laser output spectrum", *Electron. Lett.*, 1980, **16**, pp. 630-631, 1980.
4. J Buus, "Single Frequency Semiconductor Lasers", pub. SPIE, 1ed (USA 1991) chapter 6.

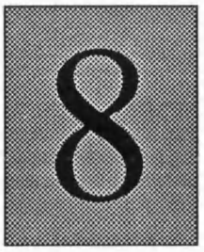

Conclusions

This dissertation is concerned with the use of semiconductor optical amplifiers in analogue amplitude modulated systems, their advantages and disadvantages, and how their performance may be improved.

Future widespread use of optical fibre systems has exciting implications for the worlds of entertainment, communications and computing. The wide bandwidths and high data rates offered by lightwave systems are expected to enable the provision of a wide range of facilities and services not presently available. These new systems will rely on optical amplification, whether to boost the signal at the transmitter, to overcome fibre and branching losses, or to preamplify a weak signal prior to detection. Although doped fibre amplifiers have the advantages of high gain and low distortion at 1.5 μm, semiconductor optical amplifiers have the ability to perform signal manipulation and processing, in addition to providing optical gain.

However, the same mechanisms which enable the SOA to carry out switching, multiplexing and frequency conversion also cause high levels of signal distortion, a major disadvantage in analogue systems. Before SOAs can be used in such systems, therefore, the distortion mechanisms must be understood, with a view to optimising device performance.

To this end, two computer models have been developed to predict the response of an SOA to a wide variety of stimuli, and these are described in chapter 3. Using the rate equation as a starting point, the model includes the effects of Fabry-Perot resonance, spontaneous emission, nonradiative and Auger recombination, gain spectral effects, electrical heating and current leakage. The data obtained from the computer programs agrees well with experimental results from a bulk buried heterostructure optical

amplifier. It has been found that the level of distortion generated by a particular device depends in part upon the saturation power of the device, also that Fabry-Perot resonance caused by the reflective end facets strongly influences the distortion levels.

Chapter 4 explores the design of a low distortion device, having high input saturation power. A multi-quantum-well structure is used, and the effect on the saturation input power of varying each of the physical dimensions is investigated. It is concluded that a high saturation power device needs to have a short cavity, offset by a large electrical thickness to provide the necessary gain, and a large optical volume to increase the output power obtained for a given intensity. Theoretical and experimental data have established both that MQW devices can outperform bulk devices, and that SOAs need to be specially designed for specific applications.

It is not always feasible to design a new device for a particular application, and chapter 5 proposes a novel method of improving the harmonic performance, with the use of an electrical feedback loop to reduce the modulation of the cavity carrier concentration by the optical input signal. Mathematical analysis and computer simulation predict significant reduction in phase and harmonic distortion using this technique, and this is borne out by the experimental results presented in chapter 6. Harmonic distortion has been reduced by up to 18 dB using electrical feedback, and low frequency noise has been reduced by up to 15 dB. The rf gain may also be enhanced using this method; increases of up to 5.5 dB have been obtained. The effects of feedback are wavelength-dependent, since the device under study has relatively high values of facet reflectivity.

One of the processing applications to which the SOA is admirably suited is modulation frequency conversion. This has been investigated in chapter 7, for both up and down-conversion of the frequency of an optical signal. Using direct modulation of the amplifier bias current, a 140 MHz optical subcarrier has been mixed with a high frequency carrier, for carrier frequencies of up to 3.8 GHz. The efficiency of the conversion, and the purity of the spectrum, are strongly wavelength-dependent. The electrical feedback loop used previously to reduce distortion can also be used to modulate the amplifier, using a 2.37 GHz resonance signal generated by the electronics in the loop. Using this method, the 140 MHz signal can be shifted up to a carrier frequency of up to 14.22 GHz, the sixth harmonic of the feedback resonance signal. Wavelength conversion is also observed, by up to 7.11 GHz, an effect which could find applications in dense WDM systems, in

which the channels are closely spaced. Downconversion of a high frequency optical carrier, of possible use in SCM receivers, has been demonstrated using both electrical and optical local oscillator signals. More efficient conversion is obtained using an all-optical technique, than when an electro-optic method is used. Lastly, the modulation provided by the resonant feedback circuit is used to shift the output from a Mach-Zehnder interferometer from 0 Hz, and thus enable measurement of the cw linewidth of a distributed feedback laser.

The final conclusions of this work are as follows. Firstly, that for high performance optical amplification in an analogue system, a device with a high input saturation power is needed to reduce harmonic distortion. If it is not possible to acquire a specially designed device, the distortion may be reduced with the use of electrical feedback to reduce the modulation of the carrier density by the optical signal. SOAs can be used to provide efficient modulation frequency conversion of an optical signal by electro-optic or all-optical methods, by several gigahertz, a capability which may be enhanced by the presence of electrical feedback. All of the experiments carried out in the course of this study have exhibited strong wavelength dependence of the SOA response; this confirms that travelling wave devices are vital for most commercial applications.

This work has left some questions unanswered, and there is scope for further research into this subject. Given the efficient modulation of the SOA by the high frequency resonance frequency produced by the feedback loop, it would be useful to determine the maximum fundamental frequency at which this effect operates. This could be done by altering the effective length of the feedback loop to change the resonance frequency. More work could also be done to optimise the electro-optic and all-optical frequency downconversion, with a view to fulfilling applications in SCM systems. The insertion of the SOA with resonant feedback into the Mach-Zehnder interferometer was very successful, but it is not yet possible to measure chirped linewidths, as the modulation on the SOA output signal obscures the linewidth measurement.